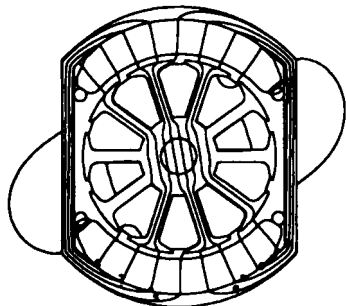
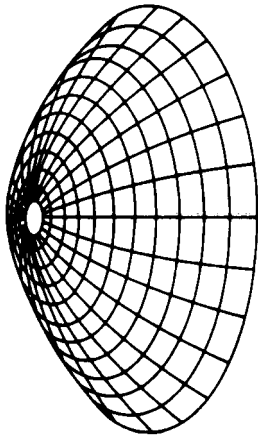


Applied Computational Electromagnetics Society Journal

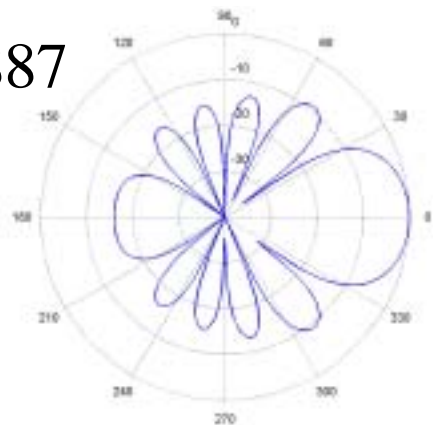
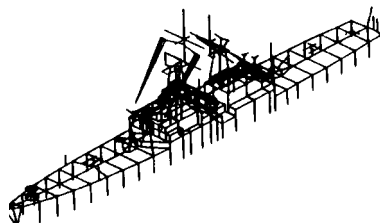
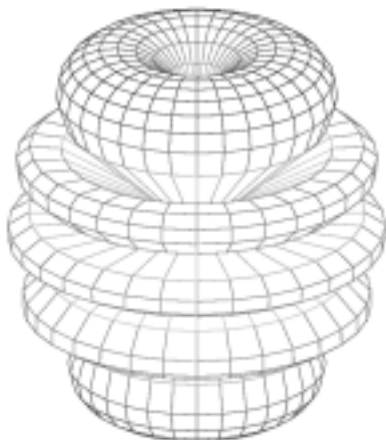


Special Issue on
ACES 2003 Conference
Part I



Editor-in-Chief
Atef Z. Elsherbeni

November 2003
Vol. 18 No. 4
ISSN 1054-4887



GENERAL PURPOSE AND SCOPE: The Applied Computational Electromagnetics Society (*ACES*) Journal hereinafter known as the *ACES Journal* is devoted to the exchange of information in computational electromagnetics, to the advancement of the state-of-the art, and the promotion of related technical activities. A primary objective of the information exchange is the elimination of the need to “re-invent the wheel” to solve a previously-solved computational problem in electrical engineering, physics, or related fields of study. The technical activities promoted by this publication include code validation, performance analysis, and input/output standardization; code or technique optimization and error minimization; innovations in solution technique or in data input/output; identification of new applications for electromagnetics modeling codes and techniques; integration of computational electromagnetics techniques with new computer architectures; and correlation of computational parameters with physical mechanisms.

SUBMISSIONS: The *ACES Journal* welcomes original, previously unpublished papers, relating to applied computational electromagnetics. Typical papers will represent the computational electromagnetics aspects of research in electrical engineering, physics, or related disciplines. However, papers which represent research in applied computational electromagnetics itself are equally acceptable.

Manuscripts are to be submitted through the upload system of *ACES* web site <http://aces.ee.olemiss.edu> See “Information for Authors” on inside of back cover and at *ACES* web site. For additional information contact the Editor-in-Chief:

Dr. Atef Elsherbeni

Department of Electrical Engineering
The University of Mississippi
University, MS 386377 USA
Phone: 662-915-5382 Fax: 662-915-7231
Email: atef@olemiss.edu

SUBSCRIPTIONS: All members of the Applied Computational Electromagnetics Society who have paid their subscription fees are entitled to receive the *ACES Journal* with a minimum of three issues per calendar year and are entitled to download any published journal article available at <http://aces.ee.olemiss.edu>.

Back issues, when available, are \$15 each. Subscriptions to *ACES* is through the web site. Orders for back issues of the *ACES Journal* and changes of addresses should be sent directly to *ACES* Executive Officer:

Dr. Richard W. Adler

ECE Department, Code ECAB
Naval Postgraduate School
833 Dyer Road, Room 437
Monterey, CA 93943-5121 USA
Fax: 831-649-0300
Email: rwa@attglobal.net

Allow four week’s advance notice for change of address. Claims for missing issues will not be honored because of insufficient notice or address change or loss in mail unless the Executive Officer is notified within 60 days for USA and Canadian subscribers or 90 days for subscribers in other countries, from the last day of the month of publication. For information regarding reprints of individual papers or other materials, see “Information for Authors”.

LIABILITY. Neither *ACES*, nor the *ACES Journal* editors, are responsible for any consequence of misinformation or claims, express or implied, in any published material in an *ACES Journal* issue. This also applies to advertising, for which only camera-ready copies are accepted. Authors are responsible for information contained in their papers. If any material submitted for publication includes material which has already been published elsewhere, it is the author’s responsibility to obtain written permission to reproduce such material.

APPLIED COMPUTATIONAL ELECTROMAGNETICS SOCIETY JOURNAL

Special Issue on
**ACES 2003 Conference
Part I**

Editor-in-Chief
Atef Z. Elsherbeni

November 2003
Vol. 18 No. 4
ISSN 1054-4887

The ACES Journal is abstracted in INSPEC, in Engineering Index, and in DTIC.

The first, fourth, and sixth illustrations on the front cover have been obtained from the Department of Electrical Engineering at the University of Mississippi.

The third and fifth illustrations on the front cover have been obtained from Lawrence Livermore National Laboratory.

The second illustration on the front cover has been obtained from FLUX2D software, CEDRAT S.S. France, MAGSOFT Corporation, New York.

THE APPLIED COMPUTATIONAL ELECTROMAGNETICS SOCIETY

<http://aces.ee.olemiss.edu>

ACES JOURNAL EDITORS

EDITOR-IN-CHIEF/ACES/JOURNAL

Atef Elsherbeni

University of Mississippi, EE Dept.
University, MS 38677, USA

EDITORIAL ASSISTANT

Matthew J. Inman

University of Mississippi, EE Dept.
University, MS 38677, USA

EDITOR-IN-CHIEF, EMERITUS

David E. Stein

USAF Scientific Advisory Board
Washington, DC 20330, USA

ASSOCIATE EDITOR-IN-CHIEF

Alexander Yakovlev

University of Mississippi, EE Dept.
University, MS 38677, USA

EDITOR-IN-CHIEF, EMERITUS

Ducan C. Baker

EE Dept. U. of Pretoria
0002 Pretoria, South Africa

EDITOR-IN-CHIEF, EMERITUS

Allen Glisson

University of Mississippi, EE Dept.
University, MS 38677, USA

MANAGING EDITOR

Richard W. Adler

833 Dyer Rd, Rm 437 EC/AB
NPS, Monterey, CA 93943-5121, USA

EDITOR-IN-CHIEF, EMERITUS

Robert M. Bevensee

Box 812
Alamo, CA 94507-0516, USA

EDITOR-IN-CHIEF, EMERITUS

Ahmed Kishk

University of Mississippi, EE Dept.
University, MS 38677, USA

ACES JOURNAL ASSOCIATE EDITORS

Giandomenico Amendola

Universita' della Calabria
Rende , Italy

John Beggs

NASA Langley Research Center
Hampton, VA, USA

John Brauer

Ansoft Corporation
Milwaukee, WI, USA

Magda El-Shenawee

University of Arkansas
Fayetteville AR, USA

Pat Foster

Microwave & Antenna Systems
Gt. Malvern, Worc. UK

Cynthia M. Furse

Utah State University
Logan UT, USA

Christian Hafner

Swiss Federal Inst. of Technology
Zurich, Switzerland

Michael Hamid

University of South Alabama,
Mobile, AL, USA

Andy Harrison

Radiance
Huntsville, AL

Chun-Wen Paul Huang

Anadigics, Inc.
Warren, NJ, USA

Todd H. Hubing

University of Missouri-Rolla
Rolla, MO, USA

Nathan Ida

The University of Akron
Akron, OH, USA

Yasushi Kanai

Niigata Institute of Technology
Kashiwazaki, Japan

Leo C. Kempel

Michigan State University
East Lansing MI, USA

Andrzej Krawczyk

Institute of Electrical Engineering
Warszawa, Poland

Stanley Kubina

Concordia University
Montreal, Quebec, Canada

Samir F. Mahmoud

Kuwait University
Safat, Kuwait

Ronald Marhefka

Ohio State University
Columbus, OH, USA

Edmund K. Miller

LASL
Santa Fe, NM, USA

Krishna Naishadham

Wright State University
Dayton, OH, USA

Giuseppe Pelosi

University of Florence
Florence, Italy

Vicente Rodriguez

ETS-Lindgren
Cedar Park, TX, USA

Harold A. Sabbagh

Sabbagh Associates
Bloomington, IN, USA

John B. Schneider

Washington State University
Pullman, WA, USA

Abdel Razek Sebak

University of Manitoba
Winnipeg, MB, Canada

Amr M. Sharawee

American University
Cairo, Egypt

Norio Takahashi

Okayama University
Tsushima, Japan

THE APPLIED COMPUTATIONAL ELECTROMAGNETICS SOCIETY

JOURNAL

SPECIAL ISSUE ON ACES 2003 CONFERENCE

Part I

November 2003

TABLE OF CONTENTS

“The Marvels of Electromagnetic Band Gap (EBG) Structures” Y. Rahmat-Samii.....	1
“A Decompose-Solve-Recompose (DSR) Technique for Large Phased Array Antenna Analysis” K. Y. Sze, K. F. Sabet, and D. Chun.....	11
“A 2-Pin Loaded Patch as a Multiband Antenna for Wireless Communication” S. F. Mahmoud and A. F. Almutairi.....	19
“Antenna Design and Radiation Pattern Visualization” A. Z. Elsherbeni and M. J. Inman	26
“Aperture-Coupled Stripline-to-Waveguide Transitions for Spatial Power Combining” C. W. Hicks, A. B. Yakovlev, and M. B. Steer	33
“Accuracy of Three Unconditionally-Stable FDTD Schemes for Solving Maxwell’s Equations” G. Sun and C. W. Trueman.....	41
“Accelerating Computations with a MoM-Based Computer Program using a Model-Based Parameter Estimation Algorithm” M. Schick and F. M. Landstorfer.....	48
“Performance of Preconditioned Krylov Iterative Methods for Solving Hybrid Equations in Electromagnetics” J. Lee, J. Zhang, and C. Lu.....	54
“Analysis of Scattering Problems by MOM with Intervallic Wavelets and Operators” S. Barmada and M. Raugi.....	62
“On the Construction and Use of Two-Dimensional Wavelet-Like Basis Functions” W. E. Hutchcraft and R. K. Gordon.....	68
“Transient Modeling of Magnetoelastic Problems in Electric Machinery” O. A. Mohammed, T.E. Calvert, L. Peterson, and R. McConnell.....	77

“Multimode Hybrid Junctions” M. Hamid.....	84
“Electromagnetic Scattering by a System of Dielectric Spheres Coated with a Dielectric Shell” A-K. Hamid, M. I. Hussein, and M. Hamid.....	91
“A Fast Forward Model for Simulating EMI Scattering with Realistic Sensors and Elongated Objects” K. Sun, K. O’Neill, I. Shamatava, F. Shubitidze, and K. D. Paulsen.....	97
“Computation of SAR in Cell Culture Flasks Exposed to 900 MHz GSM Type Signals in a Modified TEM Cell” R. L. McIntosh, R. J. McKenzie, S. Iskra, A. Carratelli, and P. Standaert.....	107

The Marvels of Electromagnetic Band Gap (EBG) Structures

Y. Rahmat-Samii
Electrical Engineering Department
University of California at Los Angeles
Los Angeles, CA, 90095-1594, U. S. A.
rahmat@ee.ucla.edu

1. INTRODUCTION

Artists and scientists alike have been fascinated by the existence of periodic structures in nature. When these structures interact with electromagnetic waves many unique features result. Observables are characteristics such as frequency stop-bands, pass-bands, and band-gaps. Various terminology have been used to classify these structures depending on the domain of the applications in filter designs, gratings, frequency selective surfaces (FSS), photonic crystals and band-gaps (PBG), etc. We prefer to classify them under the broad terminology of “Electromagnetic Band-gaps (EBG)”. Recently, many researchers have adopted this terminology. Broadly speaking, EBG structures are 3-D periodic objects that prevent the propagation of the electromagnetic waves in a specified band of frequency for *all* angles of arrival and for *all* polarization states of electromagnetic waves. In practice, however, it is very difficult to obtain such complete band-gap structures and partial band-gaps are achieved. Filters typically cover the scalar situation and single angle of arrival. FSS typically cover limited angles of arrival and respond differently to polarization states. PBG typically cover in-plane angles of arrival and also sensitive to polarization states. Surveying the literature, one finds that FSS terminology has been widely used in the microwave community while PBG terminology has been widely applied in the optical community. This overview paper presents a powerful computational engine utilizing Finite Difference Time Domain (FDTD) technique integrated with

novel extrapolating algorithms to illustrate the marvels of EBG structures. The paper addresses structures such as (a) FSS structures, (b) PBG crystals, (c) smart surfaces for communication antenna applications, (d) surfaces with perfectly magnetic conducting properties (PMC), (e) creation of materials with negative permittivity and negative permeability, (f) surfaces with reduced edge diffraction effects and (g) reduction of mutual coupling among array antenna elements. Some representative applications of these structures are highlighted. In the last several years, there have been numerous published conference papers and journal articles dealing with the characterizations and applications of EBG structures. This paper is based on some of the results published by the author and his co-workers in the cited references. The reader is encouraged to perform detailed literature search to learn more about this area.

2. UCLA-FDTD CHARACTERIZATION OF EBG STRUCTURES

To perform an in-depth assessment of the performance characteristics of the complex EBG structures the FDTD technique with Periodic Boundary Condition/Perfectly Matched Layer (PBC/PML) is developed by modifying previously developed and well tested FDTD code without periodic boundary conditions, Jensen and Rahmat-Samii [1]. The split-field approach detailed in the book by Taflove [2], is incorporated to discretize the Floquet transformed Maxwell's equations, Mosallaei and Rahmat-

Samii [3]. The broadband analysis capabilities of the FDTD technique provide great computational efficiency and accuracy when one requires determining the frequency response of complex structures. Extrapolation schemes such as Prony method (Mosallaei and Rahmat-Samii [4]) and Auto Regressive Moving Average (ARMA) method (Yang and Rahmat-Samii [5]) are also incorporated to increase the efficiency of the computational technique. The key components of this powerful computational engine are briefed in Fig. 1.

The developed FDTD/Prony/ARMA technique has been effectively applied to the characterization of a variety of complex periodic EBG structures illustrated in Fig. 2. Representative examples are discussed to highlight unique features of the results and application areas.

2. ULTRA BROADBAND MULTI-LAYERED TRIPOD FSS

This section focuses on the performance evaluation of the electromagnetic band-gap multi-layered tripod FSS (Barlevy and Rahmat-Samii [6]) with ultra wideband characteristics. Fig. 3(a) shows the geometry of a single layer tripod FSS. The FDTD/Prony technique is applied to analyze the structure, and the results for the normal incidence (E_z) reflected power is presented in Fig. 3(b). This structure exhibits resonance behavior around $f_0 = 145 \text{ GHz}$.

The resonance and bandwidth frequency of this structure can be controlled using a 2-layer tripod

FSS, as depicted in Fig. 4(a). The second layer is rotated 180° with respect to the first layer, and is shifted along the z -axis in such a way that all three legs of each tripod overlap a leg of a tripod in the first layer. The overlap region creates a capacitor, which is used to tune the frequency for 100% reflection. The reflected power of the normal incident plane wave is presented in Fig. 4(b) showing that for the 2-layer tripod the resonance frequency is shifted down.

To further broaden the 100% reflection bandwidth, a 4-layer tripod FSS is introduced in Fig. 5(a). This is a rather complex structure composed of two sets of the FSS shown in Fig. 4(a). The geometry allows two degrees of freedom, d and D . The capacitance governed by the small distance d controls the lower edge of the rejection band, where the large inter-capacitor spacing D controls the upper edge of the band. The reflected power for both the normal and 30° oblique incidence ($\theta^i = 90^\circ, \phi^i = 150^\circ$) for TE (E_z) and TM (H_z) polarization cases are presented in Fig. 5(b). One notices that by increasing the bandwidth of the 100% reflection, an EBG structure utilizing the multiple coupled tripod arrays is designed. For the angles near to the grazing, the TM waves are almost normal to surface of tripods and the FSS cannot reject them. Incorporating interconnecting vias between tripods helps to reject the normal components. This design approaches a complete band-gap structure as demonstrated by Barlevy and Rahmat-Samii [6].

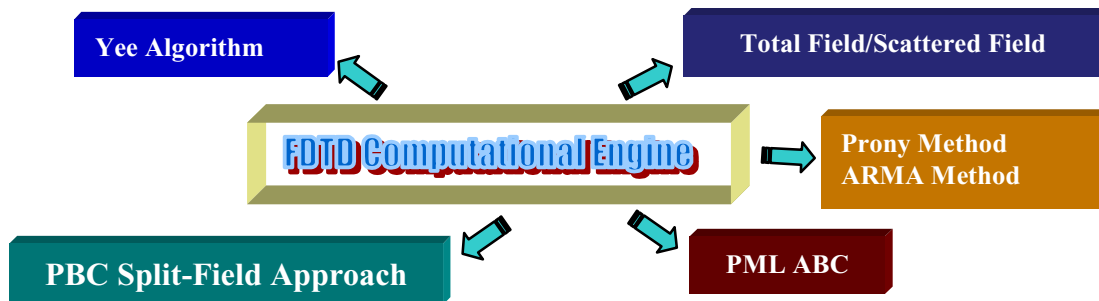


Fig. 1: Schematic of the UCLA-FDTD/Prony/ARMA computational technique.

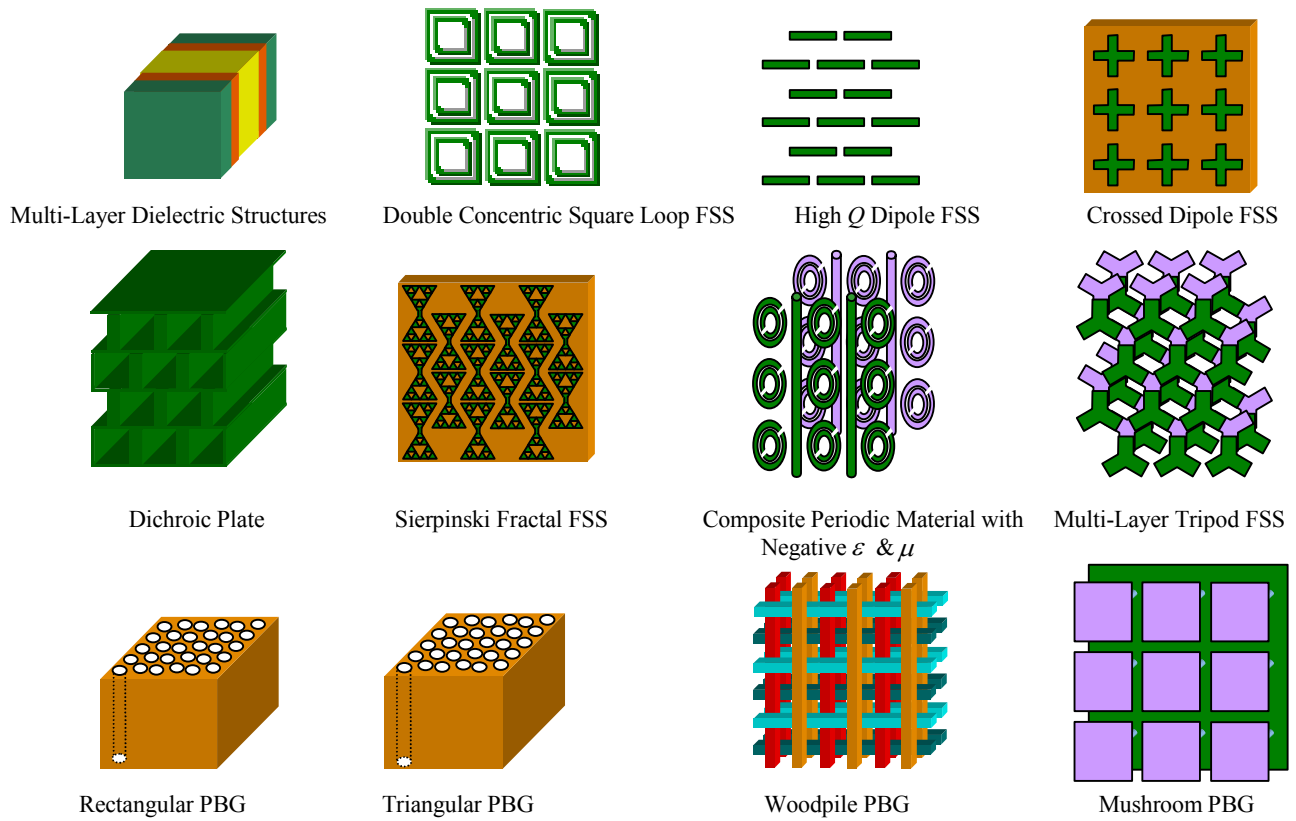


Fig. 2: Different classes of complex EBG structures characterized by the FDTD/Prony/ARMA technique.

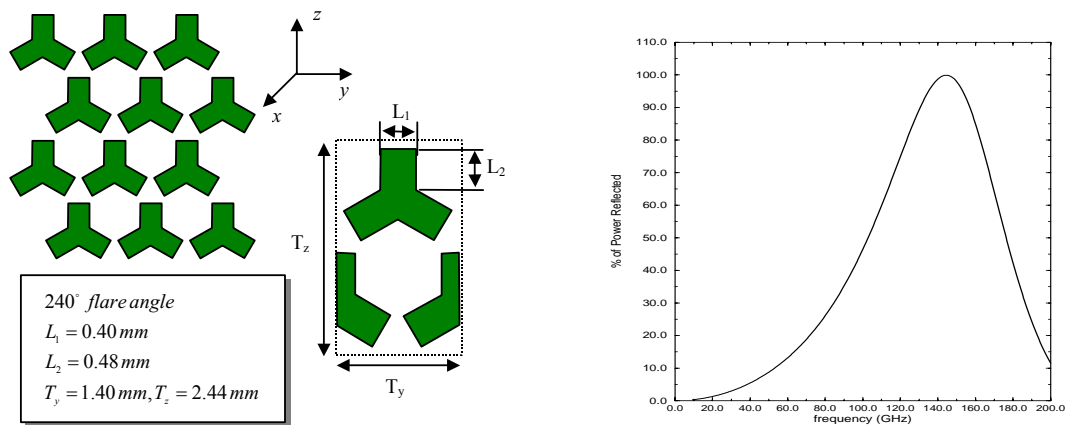


Fig. 3: 1-Layer tripod FSS, (a) Periodic structure, (b) Normal incident reflected power.

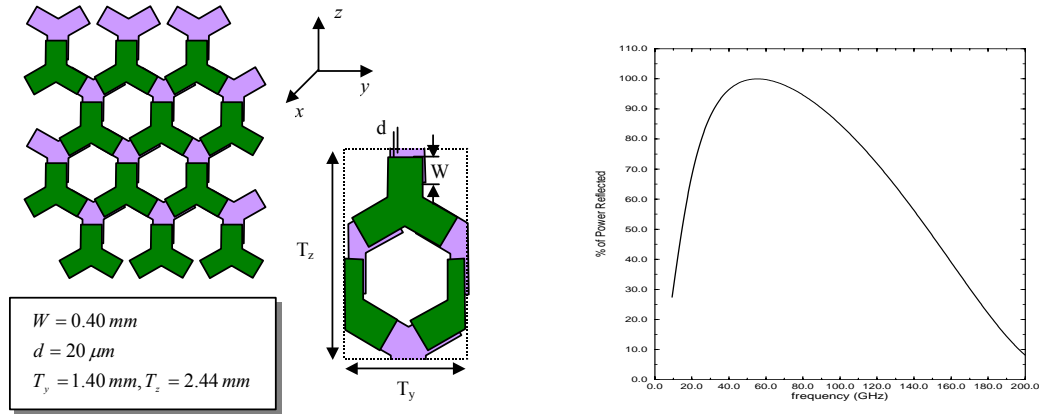


Fig. 4: 2-Layer tripod FSS, (a) Periodic structure, (b) Normal incident reflected power.

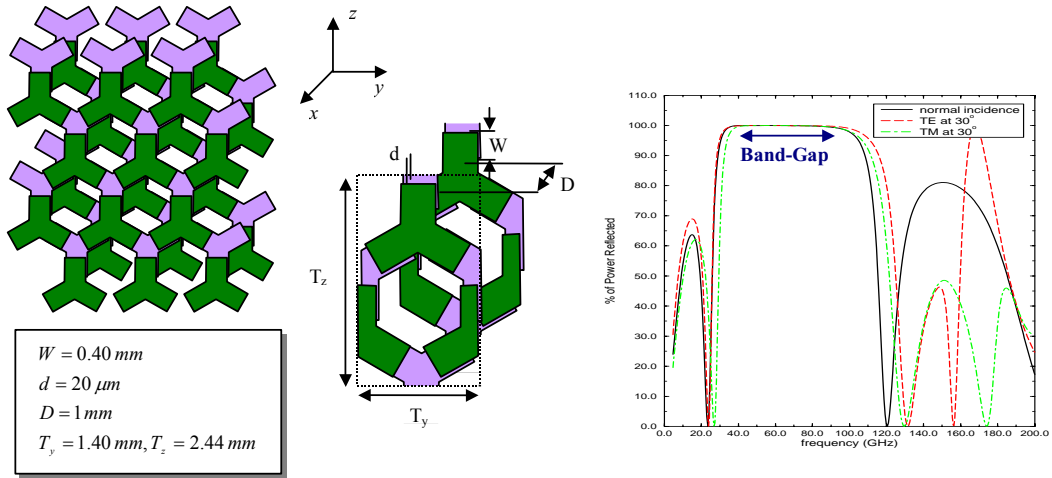


Fig.5: 4-Layer tripod FSS, (a) Periodic structure, (b) Normal and oblique (TE/TM) incidence reflected power.

3. PBG CRYSTALS FOR OPTICAL APPLICATIONS

This section addresses utilization of EBG structures in optical regime and classifies them as the photonic band-gap (PBG) crystals (Coccioli et al. [7]). The UCLA-FDTD technique is applied to obtain the reflection coefficient of the plane wave incident on various PBG structures. The plane wave approach has some distinct advantageous compared to the dispersion diagram method as listed below:

- Presenting phase and polarization information of the scattered fields,
- Obtaining reflection and transmission coefficients outside the band-gap regime,
- Ease of implementation.

For a 5-layer 2-D rectangular PBG structure of air holes in the dielectric material and for both normal and oblique incidence plane waves, Fig. 6 shows the reflection coefficients. There is a complete band-gap region for the z -polarized (TE) waves for the normalized frequencies $0.21 \leq a/\lambda_0 \leq 0.28$. The region of the band-gap frequency band has an excellent agreement with the data presented in

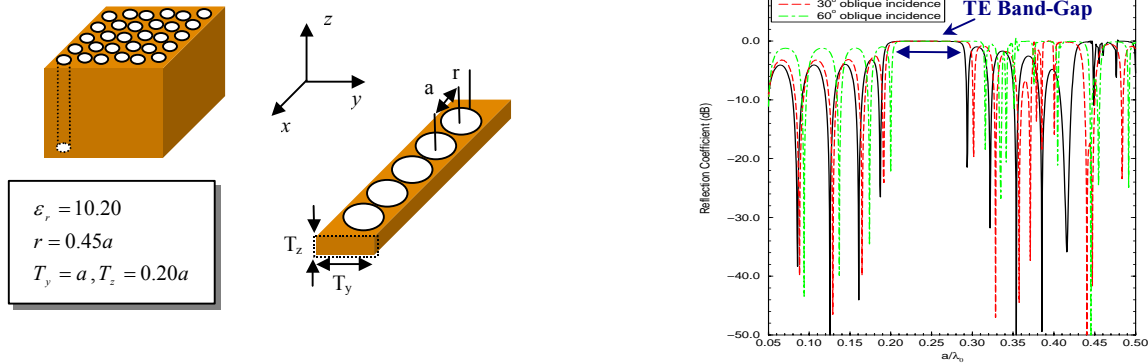


Fig.6: 5-Layer rectangular PBG, (a) Periodic structure, (b) Normal and oblique incidence reflection coefficient.

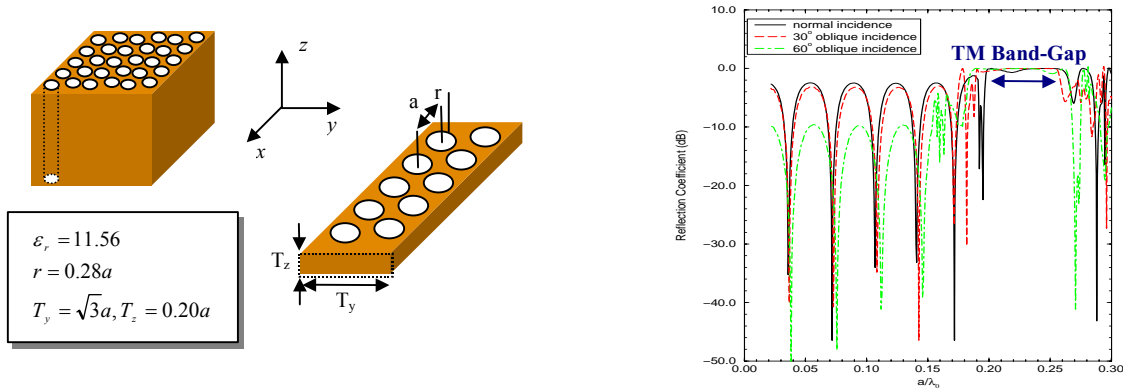


Fig.7: 5-Layer triangular PBG, (a) Periodic structure, (b) Normal and oblique incidence reflection coefficient.

Joannopoulos et al [8] based on the dispersion diagram. The PBG structure can be also created to generate a TM band-gap region using a triangular array of holes (5-layer) in the dielectric material, as shown in Fig. 7. The electric field is polarized in the plane normal to the axis of holes. One observes that there is a TM band-gap region in the normalized frequency range $0.20 \leq a/\lambda_0 \leq 0.25$. Ho et al [9] proposed a novel PBG structure that has the potential of generating a complete band-gap region for all angles of incidence and for all polarizations (an ideal EBG structure). The geometry of a 2-layer woodpile PBG is depicted in Fig. 8(a). The symmetric arrangement of the structure forbids propagation in almost all the wave vector directions. Fig. 8(b) presents the

reflection coefficient for the normal, 30° oblique/TE, and arbitrary incident wave $\theta^i = 40^\circ, \phi^i = 150^\circ$ with 45° polarization angle (between the electric field and reference direction $\hat{k}^i \times \hat{z}$). As observed, the structure is able to generate an almost complete band-gap region. The reflected phase on the surface of the structure for 30° oblique wave in obtained in Fig. 8(c). It is interesting to note that within the band gap region the phase has an almost linear frequency variation. This means that the woodpile can be represented as a Perfect Electric Conductor (PEC) where the location of the PEC is variable instead to be fix at the front surface of PBG.

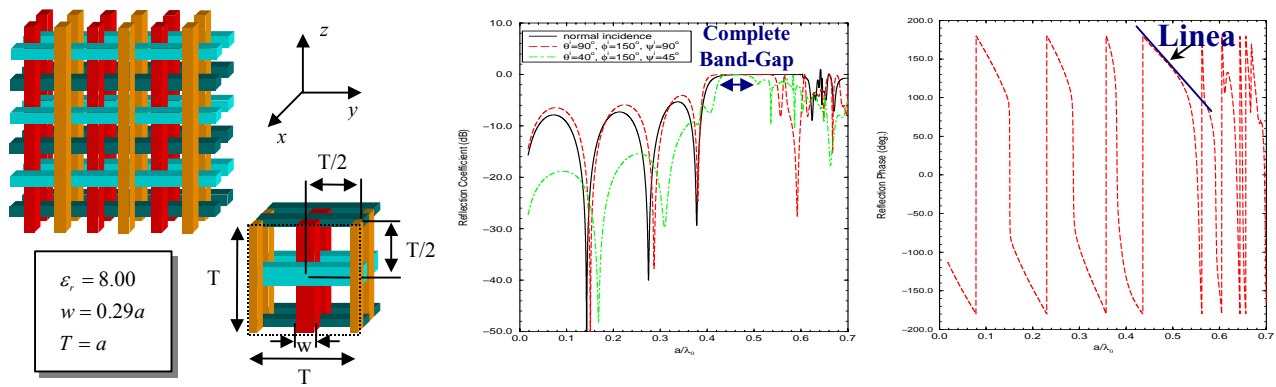


Fig.8: 2-Layer woodpile PBG, (a) Periodic structure, (b) Normal and oblique incidence reflection coefficient, (c) Reflection phase for the 30° /TE incidence wave.

4. VARIOUS APPLICATIONS OF EBG

One may wonder how some of those novel characteristics of EBG structures can be used in engineering designs. This section discusses utilization of the EBG structures into some potential applications such as nanocavities, waveguides, and patch antennas, as shown in Fig. 9. Some practical antenna examples using EBG structures have also been fabricated and tested.

4.1 High Q nanocavities. To create a high Q cavity for distributed laser applications a finite thickness 2-D PBG structure is used to localize the electromagnetic waves inside a defect region in three directions. The confinement is based on the PBG gap/total internal reflections properties of the structure. The defect-excited mode (inside

the gap region) becomes localized in the transverse plane utilizing the PBG crystal. In the vertical direction, the dielectric contrast between the impurity and outside air region produces the total internal reflections trapping the waves in this direction (Coccioli et al. [7]).

4.2 Guiding the light in sharp bends. Another useful application of the PBG is for guiding the light in sharp bends. This is achieved by an array of the PBG holes removed in the guiding direction as shown in Fig. 9(b). In the frequency range within the gap-region, light is confined through the channel, and cannot be scattered through the PBG. This is even the case at tight corners. It has been shown that by appropriate shaping of the bend one can reduce scattering of

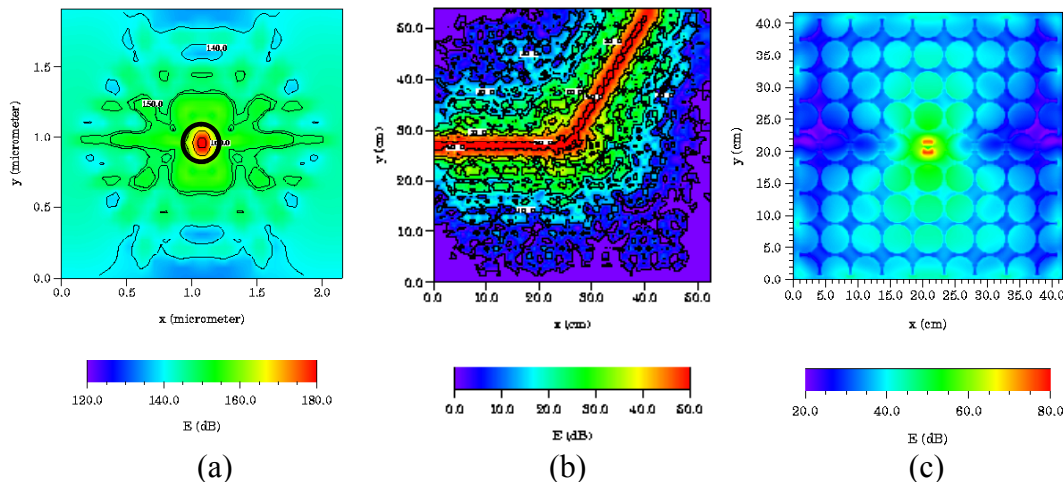


Fig.9: Potential applications of the PBG structures in (a) High Q nanocavities, (b) Guiding the EM waves in sharp bends, and (c) Miniaturized microstrip patch antennas.

the light waves at sharp corners.

4.3 Miniaturized microstrip patch antennas.

Miniaturized patch antennas can be constructed using the EBG as the substrate surrounding the patch as shown in Fig. 9(c). This results into suppression of the surface waves. Although, in general, this EBG structure *cannot* generate a complete surface wave band-gap, it still has the capability of suppressing surface waves, and improving the radiation performance of the patch antenna (Colburn and Rahmat-Samii [10]).

4.4 Low profile CP curl antenna design.

The curl antenna was originally proposed as a simple radiator to generate circular polarized electromagnetic waves. This antenna concept does not function efficiently when it is placed close to a finite PEC ground plane due to the

reverse image. Therefore, the mushroom EBG surface, which shows an in-phase reflection feature inside its band gap, provides a good alternate to the PEC ground plane to build a low profile structure as well as the circular polarization (Yang and Rahmat-Samii [11]).

Fig. 10(a) shows a photo of a curl antenna designed by the UCLA-FDTD computational tools. The height of the antenna is only 3 mm, which is about 0.07λ at 7 GHz. Compared to a curl on the PEC ground plane, the curl on the EBG ground plane has a much better input match as shown in Fig. 10(b). The axial ratio of the antenna is also measured and plotted in Fig. 10(c). A good axial ratio of 0.9 dB is achieved at 7.18 GHz.

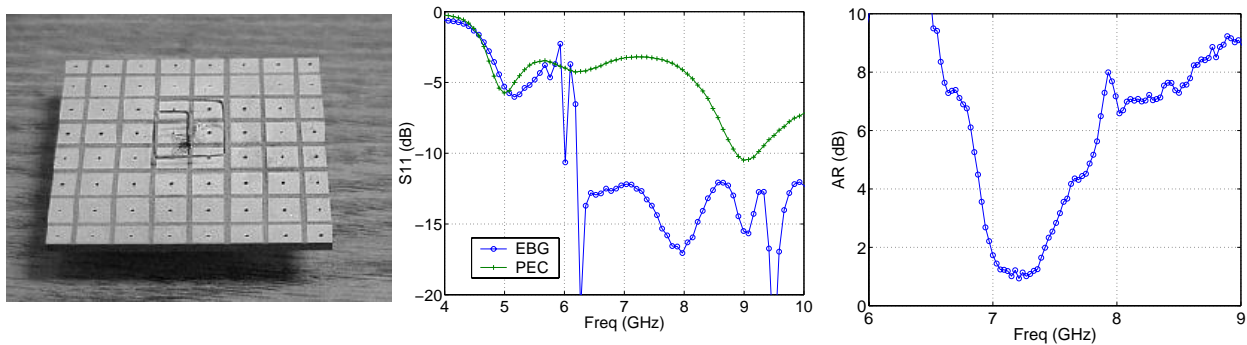


Fig. 10: A low profile circularly polarized curl antenna on a finite mushroom EBG surface: (a) a photo of the design, (b) return loss of the curl on the EBG compared to that of a curl on a PEC surface, and (c) axial ratio (AR) of the curl antenna.

4.5 Microstrip antenna element within an EBG for enhanced performance.

Applications of microstrip antennas on high dielectric constant substrates are of growing interest due to their compact size and conformability with monolithic microwave integrated circuit (MMIC). However, there are some drawbacks with the utilization of high dielectric constant substrates such as a narrow bandwidth and pronounced surface waves. The bandwidth can be recovered using a thick substrate; however, this excites severe surface waves, which will decrease the antenna

efficiency, degrade the antenna pattern and increase the mutual coupling. Because the mushroom EBG structure exhibits a surface-wave suppression feature, it is applied to the patch antenna and array to improve their performance.

Fig. 11(a) shows a photo of a microstrip antenna surrounded by four rows of EBG patches and Fig. 11(b) presents the E plane radiation pattern of the antenna compared to other conventional microstrip antenna designs (Yang and Rahmat-Samii [12]). It is observed that the radiation

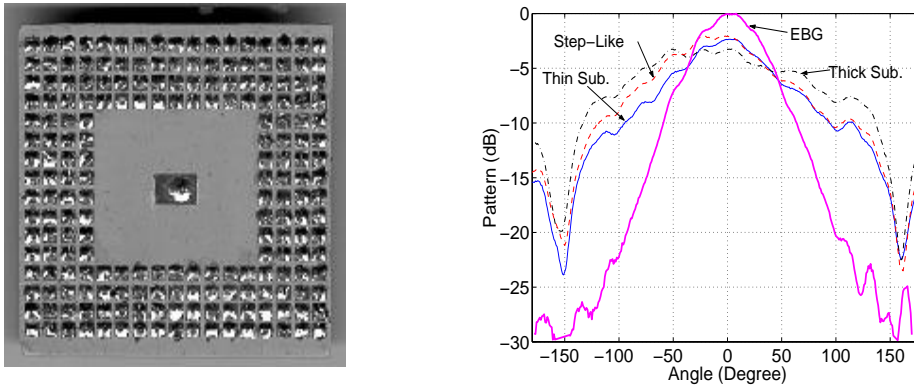


Fig. 11: Enhanced performance microstrip antenna with EBG around: (a) a photo of the design and (b) measured radiation patterns of various microstrip antenna designs. It is noticed that the microstrip antenna with EBG around has the highest gain and lowest back lobe.

performance of the antenna with EBG around is the best: its front radiation is the highest that is about 3 dB higher than the thick case while its

back lobe is the lowest which is more than 15 dB lower than other cases.

4.6 Microstrip antenna array with EBG in between for reduced mutual coupling. Above experiments have demonstrated that the EBG structure can suppress surface waves successfully so that the performance of an antenna element is significantly improved. This approach has also been extended to array applications (Yang and Rahmat-Samii [13]). Two pairs of microstrip antenna arrays were fabricated on Roger RT/Duroid 6010 substrates. Fig. 12(a) shows a photograph of the fabricated antenna arrays with and without EBG in between.

and EBG parameters are carefully designed by the UCLA-FDTD tools. The measured results are plotted in Fig. 12(b). It is noticed that both antennas resonate at 5.86 GHz with impedance matches better than -10 dB. For the antennas without the EBG structure, the mutual coupling at 5.86 GHz is -16.8 dB. As a comparison, the mutual coupling of the antennas with the EBG in between is only -24.6 dB. About 8 dB reduction of mutual coupling is achieved at the resonant frequency. From this experimental demonstration, it can be concluded that the EBG structure can be

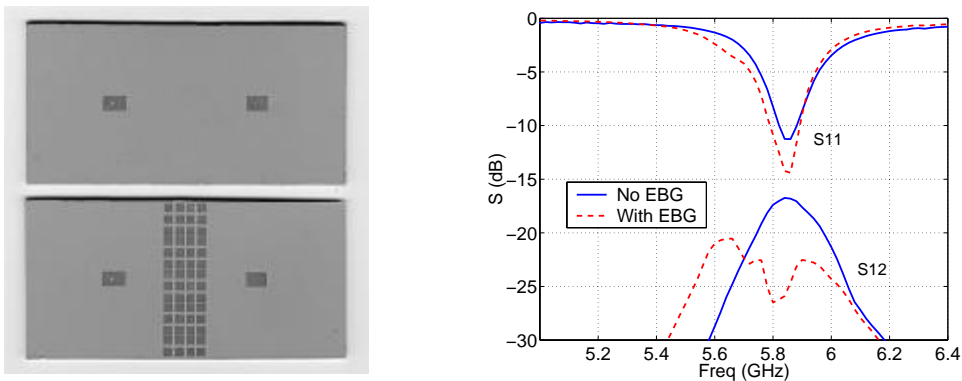


Fig. 12: Microstrip antenna array with reduced mutual coupling: (a) photos of microstrip antenna arrays with and without EBG in between and (b) measured return loss and mutual coupling results of the arrays. It is observed that the mutual coupling is greatly reduced when the EBG is inserted between patch elements.

utilized to reduce the mutual coupling between elements of antenna arrays.

5. CONCLUSIONS

This invited plenary session paper provides an overview of research activities at author's laboratory at UCLA in the area of EBG structures. As such, it is based on some of the results published by the author and his co-workers in the cited references. Computational tools of FDTD/Prony/AMRA are discussed. Ample representative examples are provided to highlight the marvels of EBG structures for both microwave and optical applications. Characterizations of EBG structures and related meta-materials are interesting research frontiers with potential electromagnetic engineering system applications.

ACKNOWLEDGMENTS

The author would like to thank assistance from many of his current and past students who performed research in the area of EBG structure under his supervision. He also acknowledges fruitful discussions with many of his colleagues interested in EBG research activities.

REFERENCES

- [1] M. A. Jensen and Y. Rahmat-Samii, "Performance Analysis of Antennas for Hand-Held Transceivers using FDTD", *IEEE Trans. Antennas and Propagation*, Vol. 42, No. 8, pp. 1106-1113, August 1994.
- [2] A. Taflove, 1998, "Advances in Computational Electrodynamics", Artech House, MA, 1998.
- [3] H. Mosallaei and Y. Rahmat-Samii, "Characterization of Complex Periodic Structures: FDTD Analysis based on Sin/Cos and Split-Field Approaches", *URSI Electromagnetic Symposium*, pp. 13-17, Canada, May, 2001.
- [4] H. Mosallaei and Y. Rahmat-Samii, "Grand Challenges in Analyzing EM Band-Gap Structures: An FDTD/Prony Technique based on the Split-Filed Approach", *IEEE Antennas and Propagation Society International Symposium*, Vol. 2, pp. 47-50, Boston, MA, July 8-13, 2001.
- [5] F. Yang and Y. Rahmat-Samii, "Microstrip antenna Analysis using Fast FDTD Methods: A Comparison of Prony and ARMA Techniques", *Proceedings of the 3rd International Conference on Microwave and Millimeter-wave Technology*, pp. 661-664, Beijing, China, August 17-19, 2002.
- [6] A. S. Barlevy and Y. Rahmat-Samii, "Characterization of Electromagnetic Band-Gaps Composed of Multiple Periodic Tripods with Interconnecting Vias: Concept, Analysis, and Design", *IEEE Trans. Antennas and Propagation.*, Vol. AP-49, no. 3, pp. 343-353, March 2001.
- [7] R. Coccioli, M. Boroditsky, K. W. Kim, Y. Rahmat-Samii, and E. Yablonovitch, "Smallest Possible Electromagnetic Mode Volume in a dielectric Cavity", *IEE Proc. Optoelectron*, vol.145, no.6, p.391-397, Dec. 1998.
- [8] J. D. Joannopoulos, R. D. Meade, and J. N. Winn, "Photonic Crystals", Princeton U. Press, NJ, 1995.
- [9] K. M. Ho, C. T. Chan, C. M. Soukoulis, R. Biswas, and M. Sigalas, *Solid State Communication*, Vol. 89, pp. 413-416, 1994.
- [10] J. S. Colburn and Y. Rahmat-Samii, "Patch Antennas on Externally Perforated High Dielectric Constant Substrates", *IEEE Transactions on Antennas and Propagation*, Vol. 47, No. 12, pp.1785-1794, Dec. 1999.
- [11] F. Yang, and Y. Rahmat-Samii, "A Low Profile Circularly Polarized Curl Antenna over Electromagnetic Band-Gap (EBG) Surface", *Microwave and Optical Technology Letter*, Vol. 31, pp. 165-168, 2001.
- [12] F. Yang and Y. Rahmat-Samii, "Step-Like Structure and EBG Structure to Improve the Performance of Patch Antennas on High Dielectric Substrate", *Digest of 2001 IEEE*

AP-S International Symposium, Vol. 2, pp. 482-485, 2001.

- [13] F. Yang and Y. Rahmat-Samii, "Mutual Coupling Reduction of Microstrip Antennas Using Electromagnetic Band-Gap Structure", *Digest of 2001 IEEE AP-S International Symposium*, Vol. 2, pp. 478-481, 2001



Yahya Rahmat-Samii is a Professor and the Chairman of the Electrical Engineering Department at the University of California, Los Angeles (UCLA). He was a Senior Research Scientist at NASA's Jet Propulsion Laboratory, California Institute of Technology before joining

UCLA in 1989. He was a Guest Professor at the Technical University of Denmark (TUD) in the summer of 1986. He has also been a consultant to many aerospace companies. He received the M.S. and Ph.D. degrees in Electrical Engineering from the University of Illinois, Urbana-Champaign.

Dr. Rahmat-Samii was the elected 1995 President and 1994 Vice-President of IEEE Antennas and Propagation Society. He was appointed an IEEE Antennas and Propagation Society Distinguished Lecturer and presented lectures internationally. Dr. Rahmat-Samii was elected as a Fellow of IEEE in 1985, and a Fellow of IAE in 1986. He was also a member of the Strategic Planning and Review Committee (SPARC) of IEEE. He was the IEEE AP-S Los Angeles Chapter Chairman (1987-1989) and his chapter won the best chapter awards in two consecutive years. He has been the plenary and millennium session speaker at many national and international symposia. He was one of the directors and Vice President of the Antennas Measurement Techniques Association (AMTA) for three years. He has been editor and guest editor of many technical journals and book publication entities. He has also served as Chairman and Co-Chairman of several national and international symposia. Dr. Rahmat-Samii was also a member of UCLA's Graduate council for a period of three years.

Prof. Rahmat-Samii has authored and co-authored over 500 technical journal articles and conference papers and has written seventeen book chapters. He is

the co-author of two books entitled, *Electromagnetic Optimization by Genetic Algorithms*, and *Impedance Boundary Conditions in Electromagnetics* published in 1999 and 1995, respectively. He is also the holder of several patents. He has had pioneering research contributions in diverse areas of electromagnetics, antennas, measurement and diagnostics techniques, numerical and asymptotic methods, satellite and personal communications, human/antenna interactions, frequency selective surfaces, electromagnetic band gap structures and the applications of the genetic algorithms, etc., (visit <http://www.antlab.ee.ucla.edu>). On several occasions, Prof. Rahmat-Samii's work has made the cover of many magazines and has been featured on several TV News casts.

For his contributions, Dr. Rahmat-Samii has received numerous NASA and JPL Certificates of Recognition. In 1984, Prof. Rahmat-Samii received the coveted Henry Booker Award of URSI from the International Union of Radio Science which is given triennially to the most outstanding young radio scientist in North America. Since 1987, he has been designated every three years as one of the Academy of Science's Research Council Representatives to the URSI General Assemblies held in various parts of the world. In 1992 and 1995, he was the recipient of the Best Application Paper Prize Award (Wheeler Award) for papers published in the 1991 and 1993 IEEE AP-S Transactions. In 1993, 94 and 95, three of his Ph.D. students were named the Most Outstanding Ph.D. Students at UCLA's School of Engineering and Applied Science. Seven others received various Student Paper Awards at the 1993-2002 IEEE AP-S/URSI Symposia. Dr. Rahmat-Samii is a member of Commissions A, B, J and K of USNC/URSI, AMTA, Sigma Xi, Eta Kappa Nu and the Electromagnetics Academy. He is listed in Who's Who in America, Who's Who in Frontiers of Science and Technology and Who's Who in Engineering. In 1999, he was the recipient of the University of Illinois ECE Distinguished Alumni Award. In 2000, Prof. Rahmat-Samii was the recipient of IEEE Third Millennium Medal and AMTA Distinguished Achievement Award. In 2001, Rahmat-Samii was the recipient of the Honorary Doctorate in physics from the University of Santiago de Compostela, Spain. In 2001, he was elected as the Foreign Member of the Royal Academy of Belgium for Science and the Arts.

A Decompose-Solve-Recompose (DSR) Technique for Large Phased Array Antenna Analysis

K. Y. Sze¹, K. F. Sabet² and D. Chun³

Abstract: A novel spatial Decompose-Solve-Recompose (DSR) technique is demonstrated to be very attractive for analyzing uniform and non-uniform large phased array (LPA) antennas, because it can accurately account for array edge effects. A simple concurrent periodic/non-periodic analysis scheme, similar to that utilized in the Progressive Numerical Method (PNM), is presented for the modeling of planar large phased array antennas. The resulting 2D spatial DSR technique, known as the Hybrid Edge-Periodic DSR technique, requires the decomposition of a large planar array into an outer edge “ring” array and a central periodic array block.

Index Terms: spatial DSR, large phased array (LPA) antenna, PNM, periodic, non-periodic, Hybrid Edge-Periodic, uniform array, non-uniform array.

I. INTRODUCTION

The full-wave analysis of large-scale phased array systems poses a very challenging computational electromagnetic problem. Conventional full-wave techniques such as the Method of Moments (MoM) can handle small- to medium-scale problems relatively easily. When the size of the array exceeds a hundred elements, full-wave techniques reach their limit of applicability. For larger arrays, periodic simulators are often utilized, whereby the array is assumed to have an infinite extent. However, periodic techniques cannot predict edge effects due to the radiating elements located at the boundary of the finite-size array structure. Therefore, it is essential to develop a technique that utilizes the full-wave analysis of the array in an efficient manner while being able to recognize the finite size of the array and account for the edge effects.

Several techniques are presently available in the literature on the analysis and design of large phased arrays. The truncated Floquet Wave/GTD formulation [1], [2] utilizes a Floquet mode truncation method to model a plane wave illumination of a large array of dipole elements in conjunction with the GTD technique to account for edge element

diffractions. This approach was also extended to include a mildly tapered plane wave illumination of the dipole array [3]. Another new hybrid technique, the Discrete Fourier Transform/Moment Method (DFT-MoM) [4], also incorporates the high frequency GTD analysis to include edge diffractions. Additionally, for a large scatterer analysis, a relatively similar technique used is one that is based on MoM and combined with a new asymptotic formulation known as the asymptotic phase-front extraction (APE) [5]. This technique utilizes results from low frequency simulations to predict solutions at higher frequencies, so that computational effort and memory requirements are significantly reduced. Nevertheless, all these asymptotic techniques are generally very complex and are presently applicable only to simple geometries. In addition, a somewhat new matrix decomposition technique was introduced in [6], using the Generalized Forward-Backward Method (GFBM), in which the global impedance matrix is decomposed into forward and backward components instead of the submatrices. Although this is proven to be accurate and efficient for rough surface scattering problems, further studies are necessary to confirm its accuracy, efficiency and robustness applicable to large phased array analyses.

On the issue of mutual coupling in a non-uniform (aperiodic) array, papers [11]-[14] discussed some analysis methods using periodic sources for modeling a single source in an otherwise large uniform array, which is a singly-perturbed non-uniform array problem. Nevertheless, there is still a great demand for a more generalized method that handles a multiply-perturbed non-uniform array problem, and this is thus the focus of this paper.

In this paper, a brief overview is given of a proposed simpler concurrent periodic/non-periodic analysis scheme, the *Decompose-Solve-Recompose* (DSR) technique [7], adapted to the modeling of planar large phased array (LPA) systems. The resulting 2D spatial DSR technique, known as the Hybrid Edge-Periodic DSR technique, requires the decomposition of a large planar array into an outer edge “ring” array and a central periodic array block. In addition, its computation speed and efficiency may be further enhanced by means of a 2D Progressive Numerical Method (PNM) like algorithm described in [8]-[10]. An analysis using the Hybrid Edge-Periodic DSR technique is

The authors are with EMAG Technologies, Inc., 1340 Eisenhower Place, Ann Arbor, MI 48108-3282, USA.

Phone: (734) 973-6600. Fax: (734) 973-7220.

E-mails: kinsze@msm.umr.edu¹, ksabet@emagtechnologies.com² and donghoon@emagtechnologies.com³.

presented for uniform and non-uniform LPA examples, similar to that for the uniform 12x12-element LPA reported in [7]. These studies are part of an effort to understand the characteristics of the Hybrid Edge-Periodic DSR technique for applications to more general uniform and non-uniform LPA analyses and designs. Traditional approaches, such as, that computed by a brute force Method of Moments (MoM) technique, and a simpler approximation approach using the periodic array windowing approach, are employed for comparisons.

II. HYBRID EDGE-PERIODIC DSR TECHNIQUE

A 2D spatial DSR analysis, using the Hybrid Edge-Periodic DSR technique, is employed for the modeling of a planar array of dipoles depicted schematically in Fig. 1. This DSR technique is new, and involves the decomposition of an LPA into an outer edge “ring” array and a central block of periodic array, as shown in the figure. Each of these decomposed arrays are solved independently using the full-wave MoM (or any other full-wave analysis methods), and subsequently, recomposed back as a solution to the original problem.

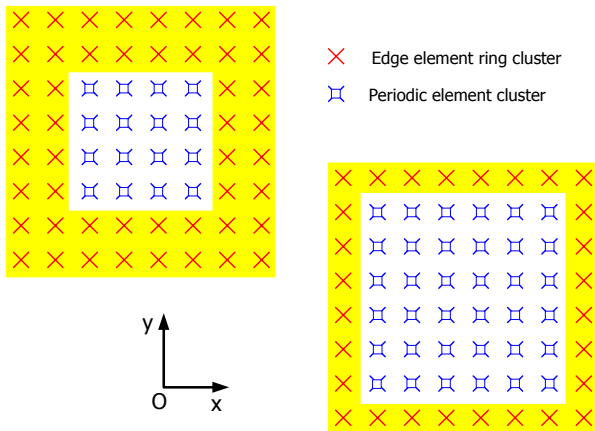


Fig. 1: Discarding an edge element ring for an 8x8 planar array using the Hybrid Edge-Periodic DSR technique. The original edge element ring cluster (top left) is 2 rings wide, and with the second ring in the cluster discarded (i.e. overlapped by the periodic element cluster), only the first ring is retained (bottom right).

Additional improvements of the Hybrid Edge-Periodic DSR technique may be achieved through the use of region “overlapping” between edge rings and the periodic array block, as implemented similarly in a PNM algorithm in [8]. An optimal choice of edge element ring width can also yield better accuracy. The mechanism of region “overlap-

ping” requires that inner edge rings be discarded and outer rings retained during the recomposition of solution. Periodic elements are then substituted in their place so that the final solution will still represent the correct number of array elements and their spatial positions in Euclidean space, as illustrated in Fig. 1. That is,

$$\text{Total Rings} = \text{Rings Retained} + \text{Rings Discarded.} \quad (1)$$

These discarded rings actually served as “pawns” for approximating the mutual coupling effects on the rings retained.

Fig. 2 shows a matrix block representation of a decomposed full-wave MoM impedance matrix, consisting of different submatrix blocks. These blocks are $[A_a]$, $[A_b]$, $[A_c]$, $[A_{ctr}]$ and $[A_{edg}]$, which respectively represent couplings (interactions between basis and test functions) between elements in the overlap and edge ring regions, overlap and central block regions, overlap region only, central block region only, and edge ring region only.

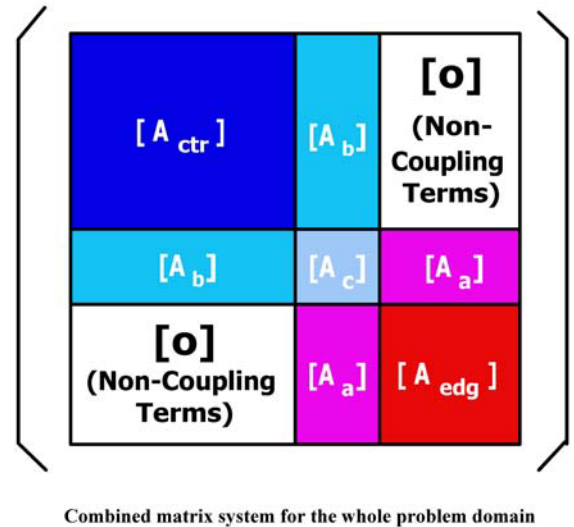


Fig. 2: Decomposed matrix blocks of the full-wave MoM impedance matrix.

However, this combined matrix system is not directly solved as a single matrix system, but rather, as two separate smaller matrix problems. In particular, one solution is computed for the central block of periodic array, and another for the edge ring array. Mathematically, this method may also be considered as a form of matrix decomposition technique, with its methodology based on physical 2D spatial decomposition. Further detailed mathematical formulations are found in [9], [10].

For the central block region, with the solution (current) vector assumed as $[c_{ctr} \ c_b]^{-1}$ and the voltage vector represented as $[b_{ctr} \ b_c]^{-1}$, the submatrix equation becomes

$$[A_{ctr}][c_{ctr}] + [A_b][c_b] = [b_{ctr}], \quad (2)$$

$$[A_b][c_{ctr}] + [A_c][c_b] = [b_c]. \quad (3)$$

Similarly, for the edge ring region, with solution (current) vector $[c_a \ c_{edg}]^{-1}$ and voltage vector $[b_c \ b_{edg}]^{-1}$, the submatrix equation becomes

$$[A_c][c_a] + [A_a][c_{edg}] = [b_c], \quad (4)$$

$$[A_a][c_a] + [A_{edg}][c_{edg}] = [b_{edg}]. \quad (5)$$

Subsequently, by recomposing the solution vectors of (2) through (5) into a new single solution vector, which becomes $[c_{ctr} \ c_b \ c_{edg}]^{-1}$, with the subvector $[c_a]$ discarded.

For the modeling of an LPA on a platform in the vicinity of objects such as screws, fasteners and pins, as schematically depicted in Fig. 3, the Hybrid Edge-Periodic DSR technique can be employed, with additional considerations for adjacent objects to be solved as part of the edge element array in the DSR algorithm. For the ease of developing the DSR technique, however, uniform and non-uniform LPAs are utilized as simple test examples in the proving of concepts in this paper, since their radiation behaviors are generally well understood.

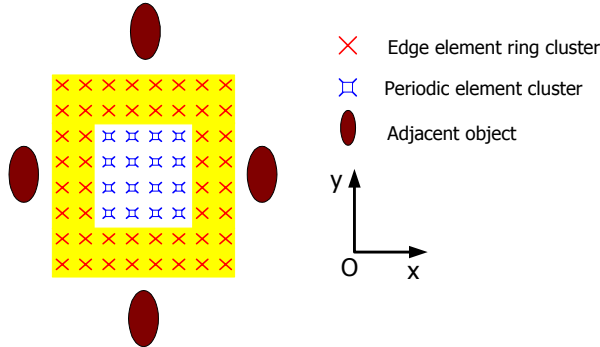


Fig. 3: Schematic of a Hybrid Edge-Periodic DSR model for the analysis of an LPA in the vicinity of other objects.

III. LARGE PHASED ARRAY MODELS

In this analysis, a uniformly-excited 8x8-element array of microstrip dipoles etched on a foam substrate ($\epsilon_r=1.03$) of thickness $0.19\lambda_0$ is employed, with dipole length and width being $0.39\lambda_0$ and $0.002\lambda_0$, respectively, and element spacings in the x- and y-directions being $0.5\lambda_0$ and $0.333\lambda_0$, respectively. The accuracy of this spatial DSR

technique over the traditional periodic array windowing approach is also investigated for a 24x24-element uniform array of microstrip dipoles etched on a $\epsilon_r=2.2$ substrate of thickness $0.188\lambda_d$, where $\lambda_d = \lambda_0/\sqrt{\epsilon_r}$. The array dipoles are center-fed, each having a length and width of $0.578\lambda_d$ and $0.003\lambda_d$, respectively, and their center-to-center element spacings in the x- and y-directions are $0.742\lambda_d$ and $0.494\lambda_d$, respectively. These dipoles are oriented parallel to the x-axis, giving an E_x field polarization. The full-wave MoM solutions are computed using *EMPiCASSO*, a well-established commercial EM CAD software tool from EMAG Technologies, Inc.

For the 24x24-element array, the full-matrix solution is equivalent to the case having a total of 12 square rings with no rings discarded (i.e. with no periodic element utilized in the DSR modeling), while the periodic array windowing solution is equivalent to that without any rings (i.e. with only periodic elements utilized in the DSR simulation). For example, a zero number of rings corresponds to a windowed periodic array solution. For a total number of rings between these two extremes, results obtained are from combinations of solutions for both edge rings and inner periodic elements. The amount of region overlap is thus implicitly represented by the number of rings discarded.

Extending the modeling to a non-uniform LPA, the uniform 24x24-element LPA is subsequently modified to consist of 48 cross-polarized dipoles arranged alternately at the array edge. A similar DSR procedure is then utilized for this non-uniform case.

IV. FAR-FIELD RADIATION CHARACTERISTICS

Far-field radiation characteristics for the uniform 8x8-element LPA are computed using the full-matrix (full-wave exact solution), periodic array windowing and Hybrid Edge-Periodic DSR (using 2 and 3 edge element rings without any region overlap) techniques. Thus, directivities computed for this LPA are 21.670dBi, 21.590dBi, 21.644dBi and 21.671dBi, respectively. These techniques all exhibit good accuracy, with the 3-element ring Hybrid Edge-Periodic approach producing the best accuracy. Fig. 4 illustrates the far-field radiation patterns of this LPA. The Hybrid Edge-Periodic technique with both 2- and 3-element rings shows excellent agreement with the full-matrix solution. Although results for the periodic array windowing technique indicate relatively good accuracy for near broadside observation angles, its predictions of side-lobe levels (SLL) at far observation angles incur large errors. The Hybrid Edge-Periodic technique, on the other hand, significantly improves this discrepancy.

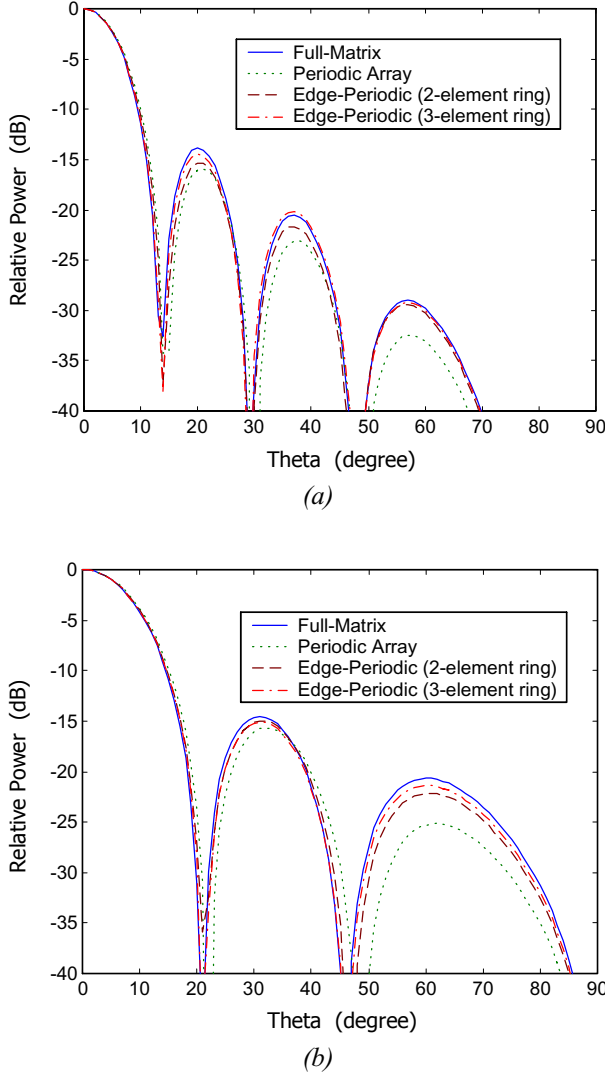


Fig. 4: Far-field radiation patterns of a uniform 8×8 -element array of microstrip dipoles etched on a foam substrate ($\epsilon_r=1.03$) of thickness $0.19\lambda_0$: (a) E-plane, and (b) H-plane. Dipole lengths and widths are $0.39\lambda_0$ and $0.002\lambda_0$, respectively, and element spacings in the x - and y -directions are $0.5\lambda_0$ and $0.333\lambda_0$, respectively.

Far-field radiation characteristics for the uniform 24×24 -element LPA are computed using the same full-matrix, periodic array windowing and Hybrid Edge-Periodic DSR techniques described above. Their far-field radiation patterns are shown in Fig. 5, and their corresponding directivities are 30.89dBi, 30.94dBi and 30.87dBi, respectively. For the Hybrid Edge-Periodic modeling, radiation patterns are obtained using a total of 7 edge element rings with a 4-ring overlap. With realistic array edge effect incorporated into the analysis, this model pre-

dicts pattern SLL with good accuracy. More accurate SLL may be obtained through the use of an optimal choice of the number of edge rings and overlapping. For the periodic array windowing approach, on the other hand, distinct nulls are predicted which are especially unrealistic in the H-plane.

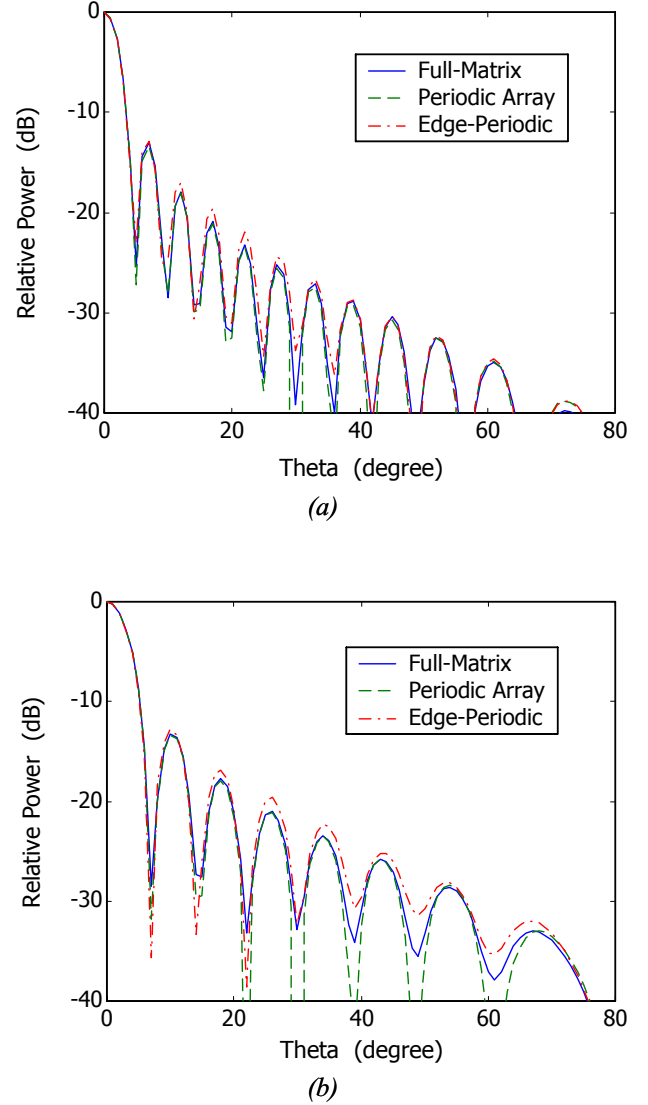


Fig. 5: Far-field radiation patterns of a uniform 24×24 -element array of microstrip dipoles etched on a $\epsilon_r=2.2$ substrate of thickness $0.188\lambda_d$ (where $\lambda_d = \lambda_0/\sqrt{\epsilon_r}$), obtained using different techniques: (a) E-plane, and (b) H-plane. Oriented parallel to the x -axis, the dipoles have lengths and widths $0.578\lambda_d$ and $0.003\lambda_d$, respectively, and element spacings in the x - and y -directions are $0.742\lambda_d$ and $0.494\lambda_d$, respectively. The Hybrid Edge-Periodic results are computed using a total of 7 edge element rings with a 4-ring overlap.

In addition, the Hybrid Edge-Periodic DSR technique is capable of accurately predicting far-field radiation characteristics of a non-uniform 24x24-element LPA, as illustrated in Fig. 6 and Fig. 7. For this case, directivities for the full-matrix and Hybrid Edge-Periodic techniques are 30.48dBi and 30.51dBi, respectively, and their cross-polarized “main” lobes are 18.90dB (for full-matrix approach) and 18.49dB (for Hybrid Edge-Periodic technique) below their co-polarized counterparts, respectively.

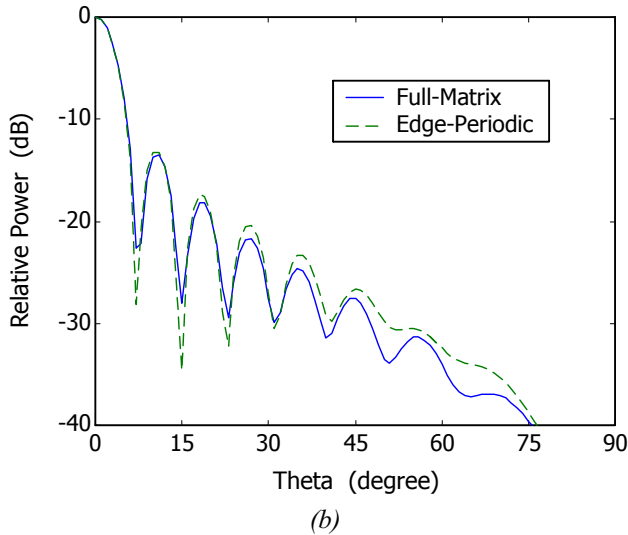
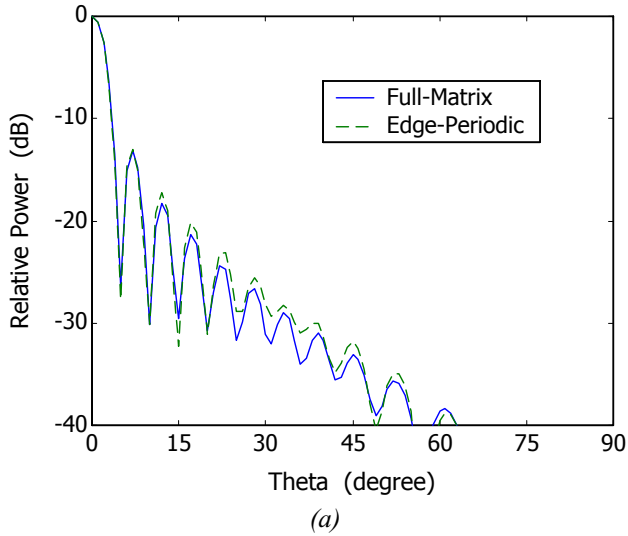


Fig. 6: Co-polarized far-field radiation patterns of a non-uniform 24x24-element array of microstrip dipoles: (a) E-plane, (b) H-plane. Hybrid Edge-Periodic plots are non-optimal results computed using a total of 7 edge element rings with a 4-ring overlap, while all other array parameters are the same as in Fig. 5.

Fig. 7 also demonstrates that very accurate cross-polarization results can be achieved through the Hybrid Edge-Periodic technique. This is attributed to the cross-polarized fields, which are contributed only by the y-directed dipoles at the array edge, as being solved using the full-wave MoM as part of the edge ring array, and that, there is no coupling of these y-directed dipoles with elements beyond a 6-element distance. Furthermore, with a proper choice of the number of edge rings and overlapping utilized, co-polarized radiation patterns can be further improved as well.

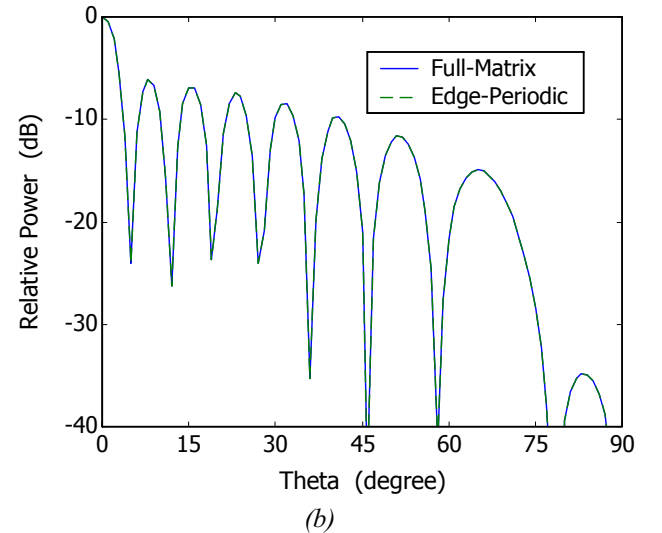
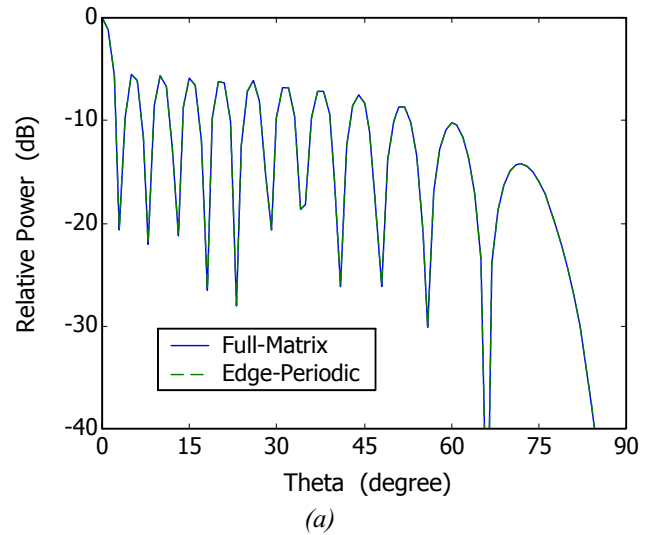


Fig. 7: Cross-polarized far-field radiation patterns of a non-uniform 24x24-element array of microstrip dipoles: (a) E-plane, (b) H-plane. All array parameters are the same as in Fig. 6.

V. COMPUTATIONAL PERFORMANCE

CPU times and memory storage requirements for simulations of the uniform 12x12- and 24x24-element LPAs are briefly investigated in this section. More rigorous quantitative studies and benchmarkings of these are necessary, which will be addressed separately.

A cost function analysis using the Hybrid Edge-Periodic DSR technique is also presented in this section for the non-uniform 24x24-element LPA described in Section IV. A similar analysis for the uniform 12x12-element LPA was reported in [7]. These are part of an effort to determine the accuracy of the solutions obtained and to understand the convergence characteristics of the DSR technique.

Table 1 compares the CPU times for modeling a uniform 12x12-element LPA using the Hybrid Edge-Periodic DSR technique, with 23 mesh segmentations on each dipole element. As compared to that of the full-matrix MoM simulation (full-wave MoM simulation), the number of unknowns required using this technique is reduced by approximately 25%, and its CPU time is decreased by more than 55%. From Table 2, its memory storage size is also decreased by more than 40%. Nonetheless, the conventional periodic array windowing technique (which does not account for finite array edge effects) is still the most computationally cost efficient technique of the 3 cases investigated, if array edge effects can be neglected.

Table 1: Comparisons of CPU times and the number of unknowns required for simulating a uniform 12x12-element LPA at 23 mesh segmentations per dipole element.

Computational technique	Number of unknowns*	CPU time* (minutes)
Full-matrix MoM	3312 (100%)	187.8 (100%)
Periodic array	23 (0.69%)	0.02 (0.01%)
Hybrid Edge-Periodic (3 edge element rings, with 1-ring overlap)	2507 (75.69%)	80.3 (42.76%)

* Values in parentheses are relative percentages to that of the full-matrix MoM simulation.

Table 2: Comparisons of memory storage sizes for simulating a uniform 12x12-element LPA at 23 mesh segmentations per dipole element.

Computational technique	Memory* (MB)
Full-matrix MoM	822 (100%)
Periodic array	0.04 (0.005%)
Hybrid Edge-Periodic (3 edge element rings)	471.1 (57.31%)

* Values in parentheses are relative percentages to that of the full-matrix MoM simulation.

As for the uniform 24x24-element LPA, modeled using 8 mesh segmentations per dipole element, the number of unknowns required is reduced by more than 55%, and more than 15%, for the case of 3 and 7 edge element rings, respectively. These results are as presented in Table 3. Their memory storage sizes are also decreased by more than 80%, and more than 30%, respectively (also shown in Table 3).

These observations of results from Table 1 through Table 3 indicate, that, the larger the array size is, the greater is the computational cost saving in terms of CPU time and memory storage requirements.

Table 3: Comparisons of memory storage sizes times and the number of unknowns required for simulating a uniform 24x24-element LPA at 8 mesh segmentations per dipole element.

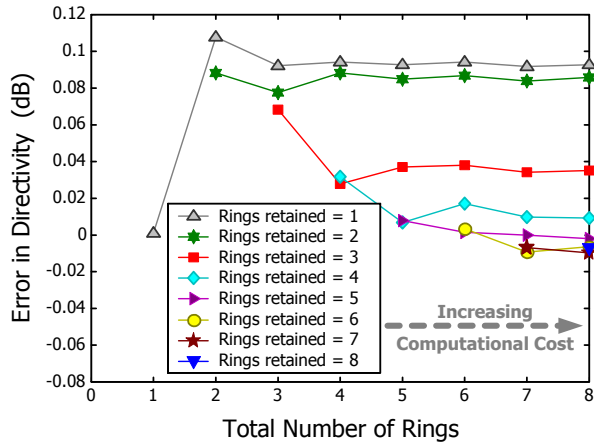
Computational technique	Number of unknowns*	Memory* (MB)
Full-matrix MoM	4608 (100%)	1590.9 (100%)
Hybrid Edge-Periodic (3 edge element rings)	2024 (43.92%)	307.1 (19.30%)
Hybrid Edge-Periodic (7 edge element rings)	3816 (82.81%)	1091.1 (68.58%)

* Values in parentheses are relative percentages to that of the full-matrix MoM simulation.

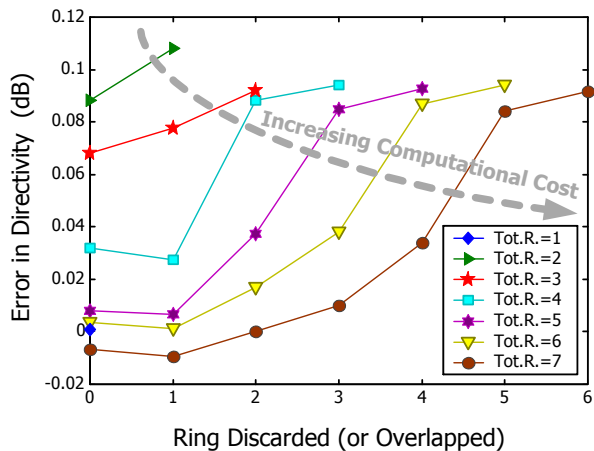
For the non-uniform 24x24-element LPA, its cost function analysis results are illustrated in Fig. 8. A full-matrix solution (full-wave MoM solution) is used as exact solutions for comparing the errors in directivity. For instance, for the DSR modeling results shown in Fig. 6, the error in directivity is 0.03dB, which can be further improved if necessary. Although this error in directivity is relatively small, errors in its far-field radiation patterns can be significant.

The directivity sensitivities to total number of rings used, retained and discarded (overlapped) are also illustrated in Fig. 8. That is, the directivity becomes less sensitive as more rings are retained (or, less rings are discarded/overlapped), and the total number of rings utilized is increased. However, the computational cost is also increased. Nonetheless, two types of convergence behaviors are observed in the figures. Namely, a convergence occurs for an increasing total number of rings utilized, and another, for an increasing number of rings retained (or, for a decreasing number of rings discarded/overlapped). The cost function curves also appear to indicate a convergence to a non-zero dB error, which is mostly attributed to numerical round-off errors in the directivity computations. Thus, based on these observations, optimal DSR parameters for a best accuracy at minimal cost can easily be obtained from data in the figures.

The cost function analysis results for the uniform 24x24-element LPA, described in Section IV, can also be similarly determined. Nevertheless, the discarding of edge element rings is generally more expensive since more rings are necessary and the computational cost increases with the increasing number of total rings (due to the use of full-wave technique for the edge array computation).



(a)



(b)

Fig. 8: Hybrid Edge-Periodic cost function curves for a non-uniform 24x24-element array: (a) effect of increasing number of rings retained, and (b) effect of overlapping regions, represented as rings discarded (where Tot.R. \equiv Total Rings), for a particular total number of rings. All other array parameters are the same as in Fig. 5.

VI. CONCLUSION

A region overlap mechanism, similar to that utilized in PNM, is implemented into a newly proposed Hybrid Edge-

Periodic DSR technique for the 2D spatial DSR analysis of planar LPA systems. Simulations of the uniform 8x8- and 12x12-element LPAs, and both uniform and non-uniform 24x24-element LPAs, provide very good results and also demonstrate high computational efficiency. Although the periodic array windowing approach produces unrealistic distinct nulls in its far-field radiation patterns, but yields acceptable accuracy for a uniform LPA, the Hybrid Edge-Periodic DSR technique has proven to be more superior for a large-scale non-uniform LPA, and may be its only practical modeling solution. In essence, pattern improvements in the Hybrid Edge-Periodic method are generally attributed to the choice of optimal total number of edge rings and overlapping, which serve as important simulation criteria.

VII. ACKNOWLEDGEMENTS

This research work was in part supported by the U.S. Navy SBIR Programs, contract numbers N00178-02-C-3001 and N68335-02-C-0437.

VIII. REFERENCES

- [1] Filippo Capolini, Matteo Albani, Stefano Maci and Leopold B. Felsen, "Frequency-domain Green's function for a planar periodic semi-infinite phased array -- Part I: Truncated Floquet wave formulation," *IEEE Trans. Antennas and Propag.*, vol. 48, no. 1, pp. 67-74, January 2000.
- [2] Filippo Capolini, Matteo Albani, Stefano Maci and Leopold B. Felsen, "Frequency-domain Green's function for a planar periodic semi-infinite phased array -- Part II: Diffracted wave phenomenology," *IEEE Trans. Antennas and Propag.*, vol. 48, no. 1, pp. 75-85, January 2000.
- [3] F. Mariottini, F. Capolino, S. Maci and L. B. Felsen, "High frequency Green's function for a rectangular array of dipoles with weakly varying tapered excitation," *2001 IEEE Antennas and Propag. Society International Symp.*, vol. 3, Boston, MA, pp. 796-799; July 2001.
- [4] Hsi-Tseng Chou, Hsien-Kwei Ho, P. H. Pathak, P. Nepa and O. A. Civi, "A hybrid discrete Fourier transform – moment method for the fast analysis of large rectangular phased arrays," *2001 IEEE Antennas and Propag. Society International Symp.*, vol. 4, Boston, MA, pp. 314-317, July 2001.
- [5] Do-Hoon Kwon, Robert J. Burkholder and Prabhakar H. Pathak, "Efficient method of moments formulation for large PEC scattering problems using asymptotic phasefront extraction (APE)," *IEEE Trans. Antennas and Propag.*, vol. 49, no. 4, pp. 583-591, April 2001.
- [6] H.-T. Chou, "Extension of the forward-backward method using spectral acceleration for the fast analysis of large array problems," *IEE Proc. Microwaves*,

Antennas and Propag., vol. 147, no. 3, pp. 167-172, June 2000.

- [7] K. Y. Sze, K. F. Sabet, T. Özdemir and D. Chun; "A spatial decomposition technique for large phased arrays using region overlap," *2002 Symp. on Antenna Technology and Applied Electromagnetics (ANTEM 2002)*, Montréal, Canada, pp. 502-505, July/August 2002.
- [8] K. Y. Sze, K. F. Sabet, T. Özdemir and D. Chun, "A PNM implementation for large phased arrays," *2002 Symp. on Antenna Technology and Applied Electromagnetics (ANTEM 2002)*, Montréal, Canada, pp. 514-517, July/August 2002.
- [9] L. Shafai; "A progressive numerical method and its application to large field problems in antennas and electromagnetic scattering," *Can. J. Elect. Eng.*, vol. 2, no. 4, pp.17-23, 1977.
- [10] Qiubo Ye; "Electromagnetic scattering by numerical methods applicable for large structures," *Ph. D. Thesis*, University of Manitoba, Winnipeg, Manitoba; July 2000.
- [11] Hung-Yu David Yang and Jianpei Wang; "Surface waves of printed antennas on planar artificial periodic dielectric structures," *IEEE Trans. Antennas and Propag.*, vol. 49, no. 3, pp. 444-450, March 2001.
- [12] Hung-Yu David Yang; "Theory of microstrip lines on artificial periodic substrates"; *IEEE Trans. Microwave Theory and Techn.*, vol. 47, no. 5, pp. 629-635, May 1999.
- [13] B. A. Munk and G. A. Burrell; "Plane-wave expansion for arrays of arbitrarily oriented piecewise linear elements and its application in determining the impedance of a single linear antenna in a lossy half-space," *IEEE Trans. Antennas and Propag.*, vol. AP-27, no. 3, pp. 331-343; May 1979.
- [14] V. Galindo; "A generalized approach to a solution of aperiodic arrays and modulated surfaces," *IEEE Trans. on Antennas and Propag.*, vol. AP-16, no. 4, pp. 424-429, July 1968.



Kin Y. Sze received the B.S.E.E. degree from the University of Missouri-Rolla, USA, in 1989, the M.S.E.E. degree from the Ohio State University, USA, in 1991, and the Ph.D. degree in Electrical Engineering from the University of Manitoba, Canada, in 2001. He is formerly with the Department of Electrical and Computer Engineering of the University of Manitoba, as a Research Assistant as well as a Teaching

Assistant. While there, he worked on the analysis and design of conformal, high-gain (up to 35dBi), microstrip reflectarray antennas for DBS and LMDS applications. Prior to that, he worked as a Graduate Research Assistant at the ElectroScience Laboratory of the Ohio State University, where he was involved in a NASA-

sponsored project on the development of the *Helicopter Antenna Radiation Prediction (HARP)* Code, a comprehensive, integrated software package for analyzing the far-field radiation and scattering phenomena of an antenna mounted on a helicopter. Dr. Sze joined EMAG Technologies, Inc., USA, as a full-time Senior Research Engineer in June 2001, where he worked on the development and parallelization of *EMPiCASSO*, a software package for computer aided design of printed circuit and antenna systems, and *EMRENOIR*, a highly advanced design tool for reconfigurable antenna arrays. Additionally, he is the principal investigator for three US DoD-funded SBIR projects. He is also a member of Tau Beta Pi, Eta Kappa Nu and Kappa Mu Epsilon honor societies as well as IEEE.

Kazem F. Sabet received the B.S.E.E. degree from the University of Science and Technology, Iran, in 1987, the M.S.E.E. degree from the Polytechnic University, USA, in 1990, and the Ph.D. degree in Electrical Engineering from the University of Michigan, USA, in 1995. He worked at Compact Software, Inc., in Paterson, USA, as a CAD engineer, prior to his graduate study. In 1991, he joined the Radiation Laboratory of the University of Michigan, where he was involved in the development of novel numerical techniques for electromagnetic problems. His Ph.D. thesis at the University of Michigan was concerned with the efficient full-wave modeling of planar circuits and antennas for microwave and millimeter-wave applications. In 1994, Dr. Sabet founded EMAG Technologies, Inc., USA, with two other principals from the University of Michigan. He has since served as the president of EMAG. Dr. Sabet is a member of IEEE, Optical Society of America and Tau Beta Pi. He has directed numerous R&D contracts including two Phase II SBIR contracts with the US Department of Army and other projects funded by DARPA, US Air Force and CECOM.



Donghoon Chun received the B.S. and M.S. in Electronics degrees from the Dong-A University, Korea, in 1988 and 1992, respectively, and the M.S. and Ph.D. degrees in Electrical Engineering from the University of Michigan, USA, in 1997 and 2000, respectively. He began his work in the area of computational electromagnetics in 1990 when he was pursuing his M.S. degree at Dong-A University. During past 10 years, he was involved

in a variety of numerical modeling and characterization of MMIC and large phased array antennas using Method of Moments (MoM), Finite Element Method (FEM) and Hybrid MoM/FEM technique. Subsequently, he joined EMAG Technologies, Inc., USA, as a full-time Senior Research Engineer. He is presently responsible for the development of fast and efficient parallel Hybrid MoM/FEM solvers for large-size complex antenna systems and the management of US DoD-funded HPC projects at EMAG. He has been involved in these HPC projects since 1995.

A 2-PIN LOADED PATCH AS A MULTIBAND ANTENNA FOR WIRELESS COMMUNICATION

Samir F. Mahmoud and Ali F. Almutairi
EE Department, Kuwait University
P.O.Box 5969, Safat 13060, Kuwait

ABSTRACT

A new microstrip patch antenna, capable of dual or triple band operation is proposed. The patch is circular in shape and is loaded by two shorting pins having a certain angular separation of 2α . The dominant cavity modes of the patch antenna are studied using a developed rigorous theory. It is found that the first three dominant modes of the loaded patch can act as good radiators with distinct resonant frequencies, hence providing dual or triple-band operation. Salient mode characteristics such as the resonant frequency, radiation power, and the radiation quality factors are derived. Numerical results showing the dependence of these parameters on the angular separation angle 2α and the patch geometry are presented and compared with several simulations obtained by Zealand IE3D software.

I. INTRODUCTION

With the growing interest in wireless communication and the emergence of new generations there has been a need to use the same antenna for more than one band. Several approaches have been proposed for single feed dual frequency operation. These include the annular slot antenna with capacitor loading [1], the compact PIFA [2] and the H- microstrip antenna [3]. Here we propose a new patch antenna configuration that can achieve dual or multiband operation. The proposed antenna is a circular patch loaded with two shorting pins as depicted in Fig.1. The case of a circular patch with a single shorting pin has been studied by several authors [e.g.4-6] and is proved to provide a significant size reduction when operated in the dominant mode. However a single pin loaded patch suffers from the necessity to keep close proximity between the pin and the feeding probe, which raises a mechanical difficulty. The use of a patch with two shorting pins with a given angular

separation should alleviate this difficulty, besides providing multiband operation with controlled ratio of resonant frequencies.

In this paper we consider a circular patch with two shorting pins. The aim is to deduce the characteristics of the first few cavity modes in terms of their resonant frequencies and their radiation behavior. To our knowledge, no analysis has been presented for this patch configuration. So, we introduce here a rigorous analysis to determine the resonant frequencies, field distribution and radiation character of the dominant modes. In the next section we briefly derive the modal equation for the cavity modes and obtain their modal fields. In section 3, modal radiation fields and power are addressed. We compare numerical results obtained by theory with some simulations performed on the Zealand IE3D software in section 4.

II. CAVITY MODES OF A 2-PIN-LOADED CIRCULAR PATCH

We consider a circular patch of a radius ' a ' on a grounded dielectric layer of thickness ' h ' and relative dielectric constant ' ϵ_r ' with z axis coinciding with the patch axis. Two thin shorting pins, each of radius ' b ' are placed at $(r_0, \phi = \pm\alpha)$ as shown in Fig.1. Adopting the cavity model for the patch, the boundary $r=a$ is considered to behave as a magnetic wall. We wish to find the fields and the resonant frequencies of the normal cavity modes in the presence of the two shorting pins. We start by assuming z -oriented currents $I_{1,2} \exp(j\omega t)$ flowing in the two pins, where ω is the (so far unknown) modal resonant frequency. For even modes (having E_z even function of ϕ), we have $I_1 = I_2 = I$. Conversely, for odd modes, $I_1 = -I_2 = I$. Due to the smallness of the pins

radii, the currents can be considered to be concentrated on the axes of the pins.

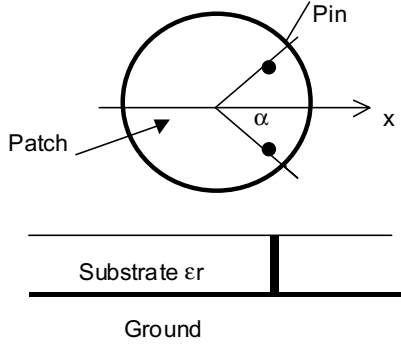


Fig.1: A circular patch, of radius a with two shorting pins of radii b and angular distance 2α ; r_0 is the radial position of the pins.

Following the authors' work in [6], such modal pin currents produce a modal electric field given by:

$$E_z(r, \phi) = \sum_{n=0}^{\infty} E_n J_n(kr) \begin{bmatrix} \cos n\phi \\ \sin n\phi \end{bmatrix} \quad (1)$$

for $0 \leq r \leq r_0$, and,

$$= \sum_{n=0}^{\infty} E_n J_n(kr_0) \begin{bmatrix} \cos n\phi \\ \sin n\phi \end{bmatrix} \frac{J_n(kr)Y_n'(ka) - Y_n(kr)J_n'(ka)}{J_n(kr_0)Y_n'(ka) - Y_n(kr_0)J_n'(ka)} \quad (2)$$

for $r_0 \leq r \leq a$, where the \cos and \sin functions relate to even and odd modes about $\phi=0$ respectively. The functions $J_n(\cdot)$ and $Y_n(\cdot)$ are the Bessel functions of first and second kind; the prime denotes differentiation with respect to the argument and $k = \omega_r \sqrt{\epsilon_r} / c$, with c the wave velocity in free space. Note that E_z is readily continuous at $r=r_0$, while $H_\phi \propto \partial E_z / \partial r = 0$ at $r = a$ satisfying the boundary condition at the magnetic wall. Next, we use the discontinuity of H_ϕ due to the pin currents at $r=r_0$. The latter can be expressed as:

$$J_z(r, \phi) = (I / r_0) \delta(r - r_0) [\delta(\phi - \alpha) \pm \delta(\phi + \alpha)] \\ = (2I / \pi r_0) \delta(r - r_0) \sum_{n=0}^{\infty} \chi_n \begin{pmatrix} \cos n\phi \cos n\alpha \\ \sin n\phi \sin n\alpha \end{pmatrix} \quad (3)$$

and the discontinuity of H_ϕ by this current leads to the determination of the coefficients E_n as:

$$E_n = -j\omega\mu_0 I \chi_n \begin{pmatrix} \cos n\alpha \\ \sin n\alpha \end{pmatrix} \frac{J_n(kr_0)Y_n'(ka) - J_n'(ka)Y_n(kr_0)}{J_n'(ka)} \quad (4)$$

where $\chi_n = 1$ for $n \geq 1$, and $\chi_0 = 1/2$ for $n=0$.

Now, the modal equation for the resonant frequency is obtained by imposing the boundary condition of vanishing E_z at the pin surface. Since the pin radius ' b ' is assumed very small relative to the field variation, we are allowed to satisfy the vanishing E_z at one line on the pin surface; say the line ($r=r_0-b$, $\phi=\alpha$) to get, after some manipulations:

$$Y_0(kb) \pm Y_0(kd) - 4 \sum_{n=0}^{\infty} \chi_n [J_n(k(r_0 - b))J_n(kr_0)] \\ \begin{cases} \cos^2 \alpha \\ \sin^2 \alpha \end{cases} Y_n'(ka) / J_n'(ka) = 0 \quad (5)$$

where d is the distance between the two pins and the upper/ lower terms correspond to even/odd modes respectively. The resonant frequencies are obtained by solving the modal equation (5) for the set of discrete values of $ka = \omega_r a \sqrt{\epsilon_r} / c$, with $\omega_r = \omega_{r1}, \omega_{r2} \dots$ which are the modal resonant frequencies. Universal curves for the normalized resonant frequency ka of the first two even modes and the first odd mode are given versus half pin separation angle ' α ', for fixed r_0/a and b/a in Fig.2. These modes are the dominant modes that are expected to have good radiation efficiency. Here ' a ' should be taken as the effective radius of the patch after accounting for field fringing. It is seen that dual or triple band operation is possible if the feed excites efficiently the corresponding modes. It is useful to note here that the placement of the feeding probe in the plane $\phi=0$ will excite the even modes only,

leading to dual band operation. Setting the feed at $\phi_f \neq 0$ will excite the odd mode as well. In Fig 3, we show the ratio of the resonant frequency of the first two even modes versus the angle α . It is seen that dual band operation with frequency ratio ranging

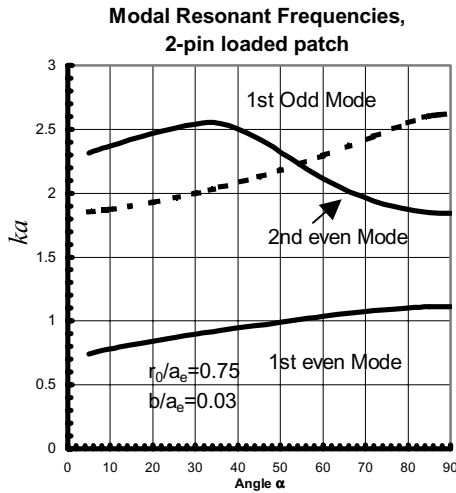


Fig.2: Normalized resonant frequency ka for first 2 even modes and the first odd mode versus angle α . Here $b/a_e=0.03$ and $r_0/a_e=0.75$.

from ~ 1.6 to 3 is possible by the right choice of ' α '. For example dual band operation at the second generation GSM (2G) centered at 925 MHz and the third generation (3G) IMT-2000 centered at 2035 MHz is possible by the choice $\alpha=56^\circ$. In this case, the effective patch radius $=35.2\text{mm}$ on a substrate with $\epsilon_r=2.2$. Note that the actual patch radius will be less because of field fringing. In the above example, the required radius $a=31.6\text{mm}$ when the substrate height $h=7.04\text{mm}$. Another point that can be inferred from Fig.2 is that the first even mode, which is the dominant cavity mode of the patch, possesses the least resonant frequency. This means that for a given operating frequency, this mode provides patch area saving. This agrees with results obtained earlier [6] for the dominant mode of a single pin loaded patch.

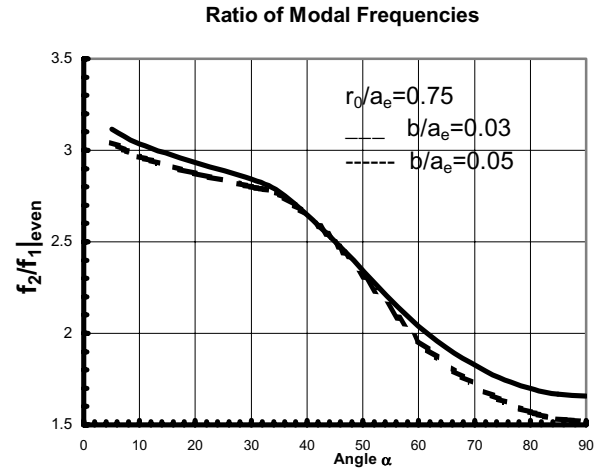


Fig.3 : Ratio of resonant frequencies of the second to first even modes versus angle α .

III. RADIATION CHARACTER OF THE MODES

In this section we derive the radiation fields and power of each of the natural modes of the patch. The starting point is to find the aperture field E_z at $r=a$. Using (2) and (4) with $r=a$, we get:

$$E_{za}(a, \phi) = \sum_{n=0}^{\infty} E_{an} \begin{pmatrix} \cos n\phi \\ \sin n\phi \end{pmatrix} = \frac{-2\omega_r \mu_0 I}{\pi ka} \sum_{n=0}^{\infty} \chi_n \frac{J_n(kr_0)}{J'_n(ka)} \begin{pmatrix} \cos n\alpha \cos n\phi \\ \sin n\alpha \sin n\phi \end{pmatrix} \quad (6)$$

where the E_{an} factors are defined by (6) for even and odd modes. The fields excited by this aperture field in the outer region $r > a$ and $z > h$ have been derived in [6]. In the far zone fields are derived as:

$$E_{\theta}(R, \theta, \phi) \approx -k_0 ah (e^{-jk_0 R} / R) \sum_n j^n E_{an} J'_n(k_0 a \sin \theta) \begin{pmatrix} \cos n\phi \\ \sin n\phi \end{pmatrix} \quad (7)$$

$$E_\phi(R, \theta, \phi) = k_0 a h (e^{-jk_0 R} / R) \cos \theta$$

$$\sum_n j^n E_{an} n \frac{J_n(k_0 a \sin \theta)}{k_0 a \sin \theta} \begin{pmatrix} \sin n\phi \\ -\cos n\phi \end{pmatrix} \quad (8)$$

where (R, θ, ϕ) are the usual spherical coordinates, $k_0 = \omega \sqrt{\mu_0 \epsilon_0}$, and $k_0 R \gg 1$. The total radiated power is given by :

$$P_r = \frac{\pi h^2}{\omega_r \mu_0 a} \sum_{n=0}^{\infty} (|E_{an}|^2 / \chi_n) I; \text{ where}$$

$$I = \int_{g=0}^{k_0} \left[k_0^2 a^2 \frac{g}{\sqrt{k_0^2 - g^2}} J_n'^2(ga) + \frac{n^2 \sqrt{k_0^2 - g^2}}{g} J_n^2(ga) \right] g da \quad (9)$$

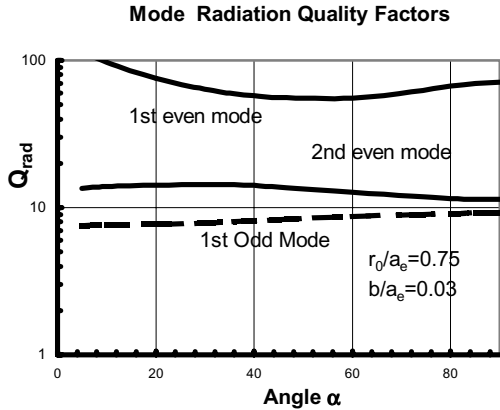


Fig.4: Radiation Quality factor of the first two even modes and the first odd mode.

The integration is taken over the radial wavenumber g in the range $\{0-k_0\}$ and can be readily evaluated numerically. The sum can be truncated at $n=3$ or 4 with no significant error. The energy stored ' W ' in the patch cavity for a given mode at resonance can be obtained by integrating ϵE_z^2 in (1-2) over the cavity volume. Now, the mode radiation quality factor Q_r is

obtained as $Q_r = \omega_r W / P_r$. The quality factors for the first two even modes and the first odd mode of a 2-pin loaded patch are plotted versus the angle α in Fig.4. It is clear that the quality factor of the first even mode is significantly higher than those of the second even and first odd mode. This means that the first even mode is a less efficient radiator than the other two modes.

IV. SIMULATION RESULTS

In order to support the presented theory several simulations are carried out using Zealand IE3D software. The geometry considered is that shown in Fig.1 and the geometry parameters are summarized for four simulation cases in Table 1. The magnitude of the reflection coefficient S_{11} , relative to a 50Ω feed line, is shown in dB versus frequency in Figures 5-7. The angle α is taken equal to 30° in Fig.5, 60° in Fig. 6, and 72° in Fig.7. In all simulations, $\epsilon_r = 2.2$, $r_0/a_e = 0.75$, $b/a_e = 0.03$, and $h/a_e = 0.2$, where a_e is the effective patch radius taking the field fringing into account [7].

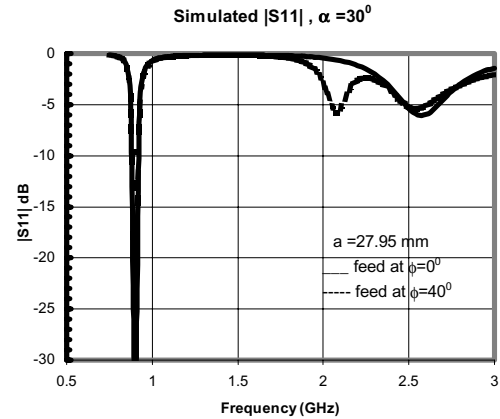


Fig.5: $|S_{11}|$ in dB for $\alpha=30^\circ$ and two feed positions

We have chosen the actual patch radius such that the first mode resonates at 925 MHz. With $\alpha = 30^\circ$, the feed is located at $(r_0, \phi_f = 0)$ in for the solid curve where the first two even modes appear at ~ 900 MHz and 2575 MHz. As expected, no odd mode is excited

in this case since the feed is located at a null for these modes. When the feed is moved to $(r_0, \phi_f = 40^\circ)$ for the dashed curve in Fig.5, the first odd mode is excited at a resonant frequency $f_{1,odd} = 2062$ MHz, in addition to the first two even modes.

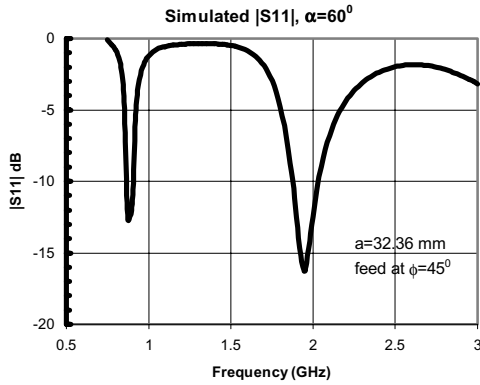


Fig.6: $|S_{11}|$ for $\alpha=60^\circ$ and feed at $(r_0, 45^\circ)$

Next consider the simulations for $\alpha=60^\circ$ and 72° in Fig. 6 and 7 respectively. For such large values of α , the modal currents are small near the axis $\phi=0$. So, if the feed were located at $\phi=0$, the input impedance would be too high to achieve matching. We therefore choose $\phi_f = 45^\circ$ and 50° in Fig.6 and 7. In Fig.6 for $\alpha=60^\circ$, only two modes appear since the second even mode and the first odd mode have their resonant frequencies so close (see Fig.2) that they appear as one mode. For $\alpha=72^\circ$, three modes appear with the odd mode having a resonant frequency higher than that of the second even mode in agreement with theoretical results of Fig.2.

The simulated resonant frequencies are compared with the theoretical values in the first row of Table 2 and it is seen that the difference between simulated and theoretical results ranges from 0.3% and 3%. This is largely caused by the definition of the effective patch radius a_e based on electrostatic analysis [7] while it is expected that it must change with frequency from one mode to another.

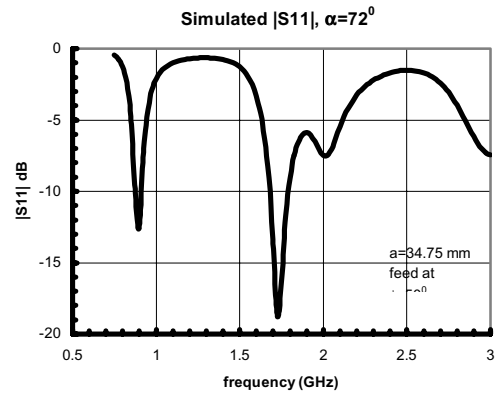


Fig.7: $|S_{11}|$ for $\alpha=72^\circ$ and feed at $(r_0, 50^\circ)$

It is clear that for the chosen feed location ($\phi_f=50^\circ$), the odd mode is not well matched. There was no attempt to optimize the feed location, but it is probably difficult to achieve matching for the three modes with a single feed. For example, it may be necessary to use a matching circuit for the odd mode in Fig.7. Matching techniques as described in [8] may then be applied.

Considering the bandwidths of the modes in Fig.6, we find that the -10 dB bandwidth of the 900 MHz mode is about 36 MHz which amounts to 4%. The bandwidth of the second mode is about 175 MHz around a center frequency of 1950 MHz which is

Table 1
Geometrical parameters of Simulation cases

No.	Angle α	a (mm)	$a_{effective}$ (mm)	h (mm)	Feed at (r_f, ϕ_f)
1	30	27.95	31.11	6.19	$(23.3, 0^\circ)$
2	30	27.95	31.11	6.19	$(23.3, 40^\circ)$
3	60	32.36	36.04	7.21	$(27.0, 45^\circ)$
4	72	33.77	37.61	7.52	$(28.2, 50^\circ)$

equivalent to $\sim 9\%$. These bandwidths are adequate for dual band operation for the 2G GSM and IMT-2000 provided that the second center frequency is shifted to 2035MHz by changing α to 56° as stated earlier.

Table 2
Theoretical versus Simulated results
on modal resonant frequencies

Angle α^0	f_{1e}^{TH}/f_{1e}^{SIM} (MHz)	f_{2e}^{TH}/f_{2e}^{SIM} (MHz)	f_{1o}^{TH}/f_{1o}^{SIM} (MHz)
30^0	925/900	2629/2575	2068/2062
60^0	925/912	1887/1937	2047/1937
72^0	925/900	1661/1712	2088/2025

V. CONCLUSIONS

The cavity modes on a circular microstrip patch antenna loaded by 2 shorting identical pins have been rigorously treated. The resonant frequencies of the even and odd modes are obtained as the solution of a derived modal equation and it is found that the lowest two even modes and the first odd mode provide the possibility of dual or triple band operation. The pin separation angle 2α acts a controlling parameter for the modal resonant frequencies and therefore determines the ratios between the operating bands in dual or triple band operation. Simulations performed on the Zealand IE3D software support the theoretical results. As expected, the position of the feeding probe determines the relative excitation of modes and input impedance at their resonant frequencies. Results show that it is feasible to have a dual band operation with good matching using a single feed. It may be difficult though to achieve good matching for the three modes in a triple band operation, whence it may be necessary to use some matching technique at one of the modes. The results are pertinent to antenna design for wireless communication.

REFERENCES

- [1] C.S.Hong, "Small annular slot antenna with capacitive loading", *Electronic Letters*, vol. 36, 2000, p.110-111.
- [2] C.R. Rowell and R.D. Murch, "A compact PIFA suitable for dual frequency 900/1800-MHz operation", *IEEE Trans. On AP*, vol.46, 1998, p. 596-598.
- [3] A.F. Sheta, A. Mohra and Samir.F. Mahmoud, "Multi-band Operation of a Compact H-Shaped Microstrip Antenna", *Microwave and Optical Technology Letters*, Vol.35, No.5, December 5, 2002, PP.363-367.
- [4] Waterhouse,R.B., "Small microstrip patch antenna", *Electronics Letters*, 13th April, 1995, Vol. 31, no. 8, pp. 604-605.
- [5] Waterhouse, R.B, S.D.Targonski, and D.M. Kokotoff, "Design and performance of small printed antennas", *IEEE Trans. Antennas Propagat.*, 1998, vol46, no.11, pp.1629-1633.
- [6] Samir F. Mahmoud and Rabih K. Deeb, "Characteristics of a circular microstrip patch antenna with a shorting post", *Journal of Electromagnetic Waves and Applications (JEMWA)*, Vol. 16, no.2, pp.213-226, 2002.
- [7] Garg, R., P. Bhartia, I. Bahl and A. Ittipiboon, "Microstrip Antenna Design Handbook", Artech House, 2001, Chapter 2, p.149.
- [8] Peter A. Rizzi, "Microwave Engineering; Passive Circuits", Prentice Hall, New Jersey, 1988, Section 4.1.

ACKNOWLEDGEMENT

The authors acknowledge the support of the Research Administration of Kuwait University under a research project. The authors wish to thank Mr. Rabih Deeb for helping with numerical work.



Samir F. Mahmoud graduated from the Electronic Engineering Department, Cairo university, Egypt in 1964. He received the M.Sc and Ph.D. degrees in the Electrical Engineering Department, Queen's university, Kingston, Ontario, Canada in 1970 and

1973. During the academic year 1973-1974, he was a visiting research fellow at the Cooperative Institute for Research in Environmental Sciences (CIRES), Boulder, CO, doing research on Communication in Tunnels. He spent two sabbatical years, 1980-1982, between Queen Mary College, London and the British Aerospace, Stevenage, where he was involved in design of antennas for satellite communication. Currently Dr. Mahmoud is a full professor at the EE Department, Kuwait University. Recently, he has visited several places including Interuniversity Micro-Electronics Centre (IMEC), Leuven, Belgium and spent a sabbatical leave at Queen's University and the royal Military College, Kingston, Ontario,

Canada in 2001-2002. His research activities have been in the areas of antennas, geophysics, tunnel communication, e.m wave interaction with composite materials and microwave integrated circuits. Dr. Mahmoud is a Fellow of IEE and one of the recipients of the best IEEE/MTT paper for 2003.



Ali Almutairi Received the B.S. degree in electrical engineering from the University of South Florida, Tampa, Florida, in 1993. In December 1993, he has been awarded a full scholarship from Kuwait University to pursue his graduate studies. He received M.S. and Ph.D. degrees in electrical engineering from the University of Florida, Gainesville, Florida, in 1995 and 2000, respectively.

At the present, he is an assistant professor at Electrical Engineering Department, Kuwait University and director of the Wireless Communication Networks Laboratory. His current research interests include CDMA system, multiuser Detection, cellular networks performance issues, coding and modulation.

Dr. Almutairi is a member of IEEE and other professional societies and served as a reviewer for many technical publications.

ANTENNA DESIGN AND RADIATION PATTERN VISUALIZATION

Atef Z. Elsherbeni and Matthew J. Inman

atef@olemiss.edu

Center of Applied Electromagnetics Systems Research

Electrical Engineering Department

The University of Mississippi

University, MS 38677

Abstract: Characteristics and radiation patterns of many antenna geometries and antenna arrays can be evaluated but not easily visualized. This paper presents a software package that has been developed to allow for 2D and 3D visualization of the radiation patterns for many different types of antennas and antenna arrays. The package allows the user to visualize the field patterns for a given type of antenna, and to display the constituent parameters (input impedance, directivity, gain, etc). The user may inspect the field pattern for a single element of many different types of antennas (such as dipole, loop, aperture) or for arrays of common elements. The parameters for these antennas or arrays may be varied manually or via an automated swept parameter menu. The program allows for the design and study of diverse antenna arrays. Common types of 1-D, 2-D, and 3-D arrays are available, as well as a builder for an arbitrary system of elements. Synthesis and simulation tools are also integrated into the package to allow for automatically determining the best configuration for an array or an element to meet a predetermined radiation characteristic.

1. Introduction

In the course of designing an antenna element or an array of elements it often becomes useful to have a method of visualizing the radiation pattern and for determining the constituent

parameters of the antenna system. This program allows for the design and visualization of both single elements and of arrays of common elements. The visualization option in the program allows for the inspection of the radiation pattern in full 3-D or in multiple 2-D and 3-D plane cuts. A great advantage is gained by being able to quickly and efficiently examine the radiation pattern in various manners. The ability to examine the field structure for many common types of antennas and antenna arrays enhances the educational and research value of this package. In addition to being able to examine the field structure of the antenna element or array, the package also allows for certain observational calculations to be displayed as well.

2. Single Element Simulation

Since the radiation patterns and constituent parameters for many common types of elements are well known, calculating the radiation patterns is performed in a straightforward manner. The user first selects one of the element types given (dipole, loop, helix, infinite biconical, aperture, or corner reflector). This will bring up the appropriate basic pattern and initial parameters for this type of element. Many of the element types have various configurations and sub-types available in the program. For example if a dipole is selected, the user may choose the

type of dipole (thin wire, thick cylindrical, small vertical with ground plane, or small horizontal with ground plane), and then set the parameters for the dipole (frequency/wavelength, dipole

length, maximum current, and far field distance). All these parameters will be used to calculate the field pattern to be displayed and its calculated parameters (gain, directivity, etc.), in separate

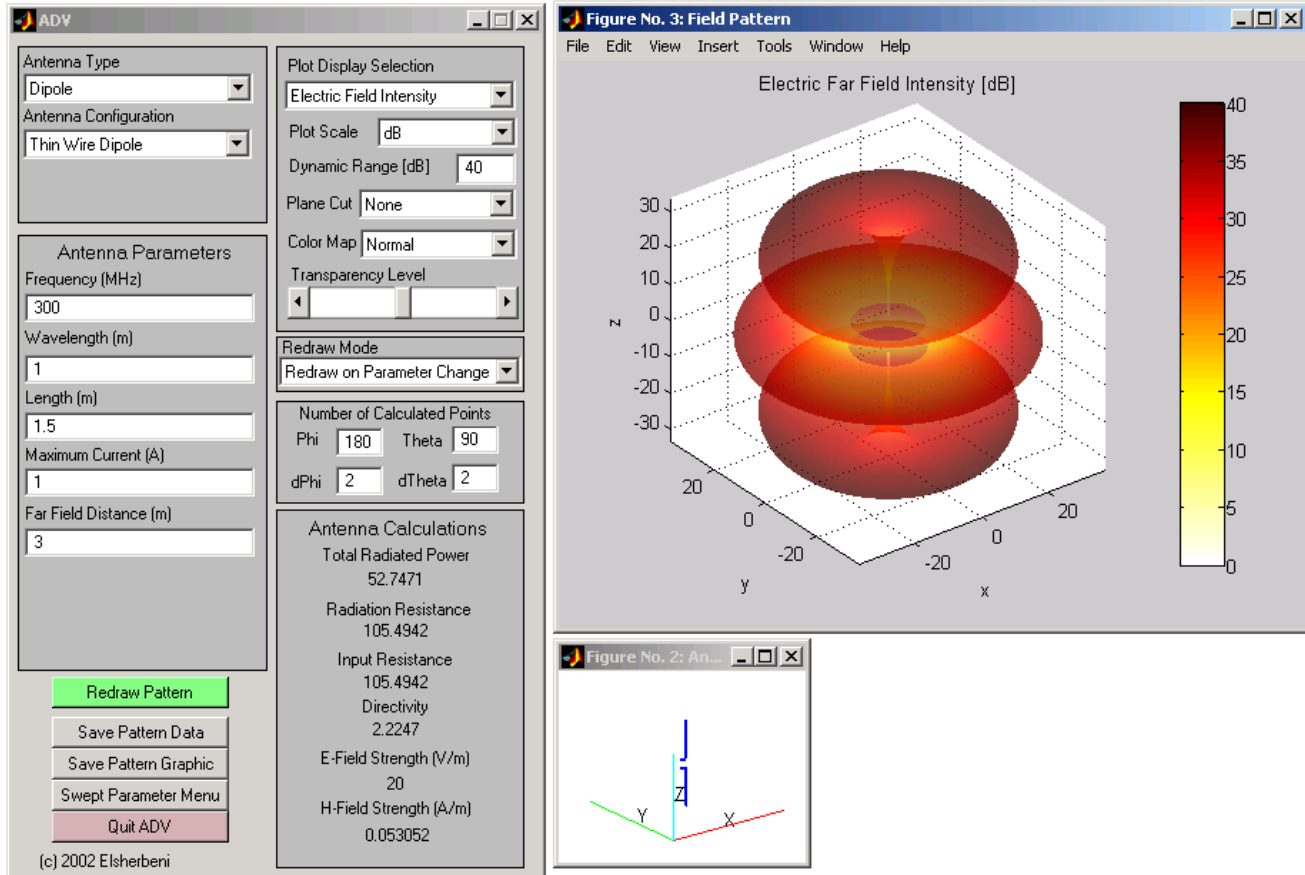


Figure 1. The program windows showing a dipole pattern for $L=1.5\lambda$.

windows, as seen in Figure 1.

Once the antenna type has been selected and the parameters for the antenna have been entered, the program calculates the E and H field patterns from this information. The main program passes off the entered parameters into the appropriate module to perform the field and parameters calculations. By using a modular system, adding new features such as new elements or arrays, becomes a simple matter of loading the appropriate module. The program then calculates the magnitude and phases of each field component at a user selectable number of points in θ (elevation) and ϕ (azimuth) from the

gathered information. By varying the number of points or the step size in each direction, the user may increase or decrease the resolution of the pattern being generated. This saves computational time when the pattern is relatively smooth, and allows for fine detail when the pattern is more complex.

In the main window along with the antenna parameters, are the visualization parameters. These allow for the user to select the type and way the pattern is viewed. The user may select from a list of available patterns and field components (Total E Field, Total H Field, E-Theta, E-Phi, H-Theta, H-Phi, Radiation Intensity, etc.), which allows the user to examine

both the total field characteristics and the individual directional characteristics as well. The user may also choose which format they wish to see the pattern displayed in, either in a linear relative format or in a normalized dB format. When the normalized dB format is selected, the user may enter the Dynamic Range for data to be shown. Since in dB format the data can range from 0 down to $-\infty$, the range is a useful tool to examine either the major features of the field pattern or can be varied down to show even small fluctuations. One of the most useful tools in the package allows for the combination of

plane cuts and transparency settings for the displayed pattern. When the full pattern is displayed, the transparency slider sets the transparency for the whole figure from completely transparent to completely opaque. When one of the 3-D plane cuts is selected, the slider will go from just showing a small slice of the pattern as seen in Figure 2, to showing a slightly transparent half of the pattern at the halfway point, and up to a completely opaque figure at its highest setting. Likewise the program has the ability to show plain 2-D cuts as well for any figure type.

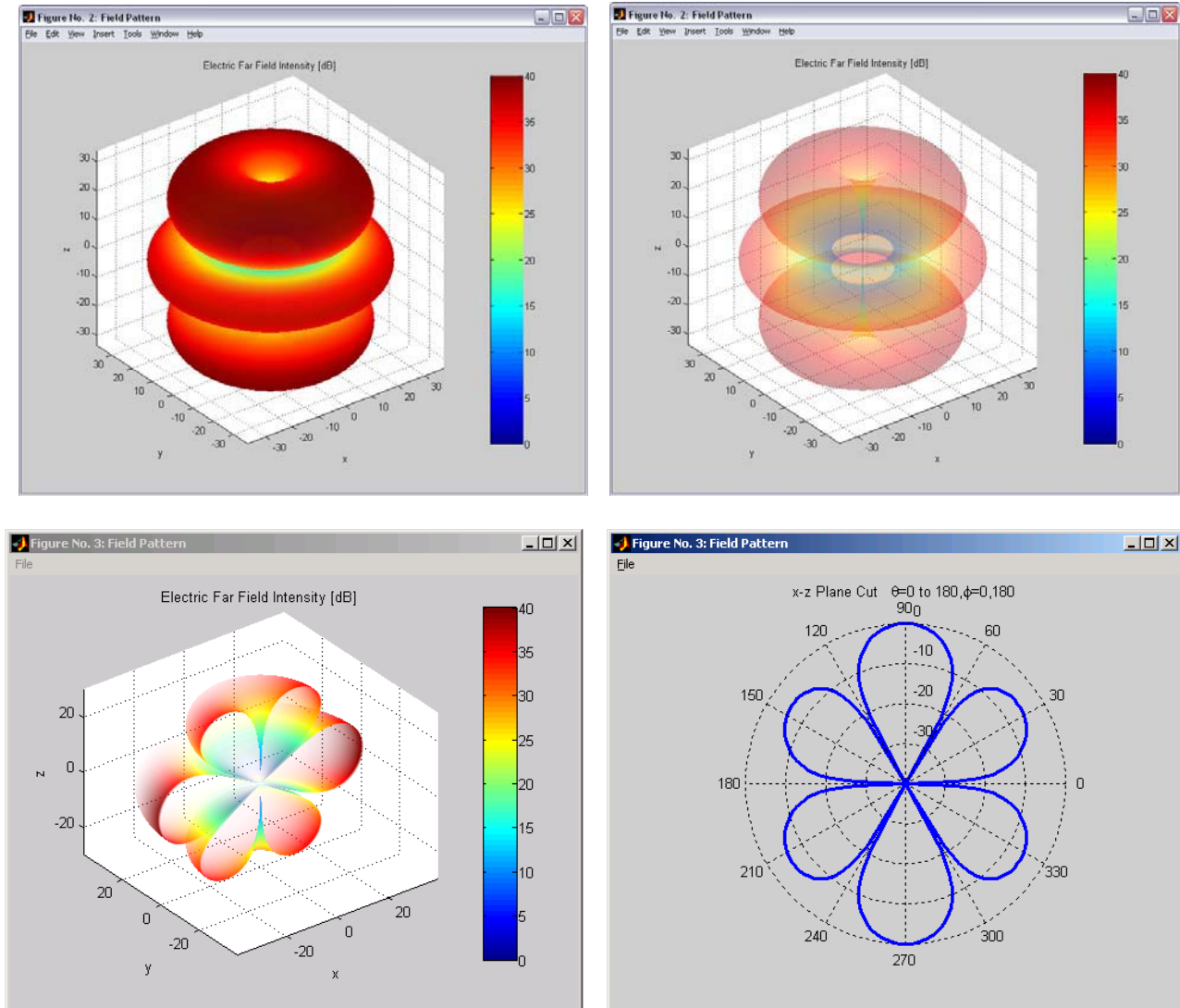


Figure 2. The pattern window showing various 3-D and 2-D plots.

3. Swept Parameters

A very useful tool in antenna design and simulation allows for the program to sweep over a set range of parameters. With the Swept Parameter tool the user may select any one of the active parameters to sweep across. The user then selects the starting and ending points for a parameter to sweep across and also enters the number of increments to be used. When started the program will begin to sweep across this

parameter and display the results either as an animated figure in the pattern window (for the type of plot being displayed) or they may step through the sweep one point at a time to examine the results. This ability not only aids in the fine tuning of a desired element by showing the changes in the pattern for small increments, but also adds to the software packages educational value as well.

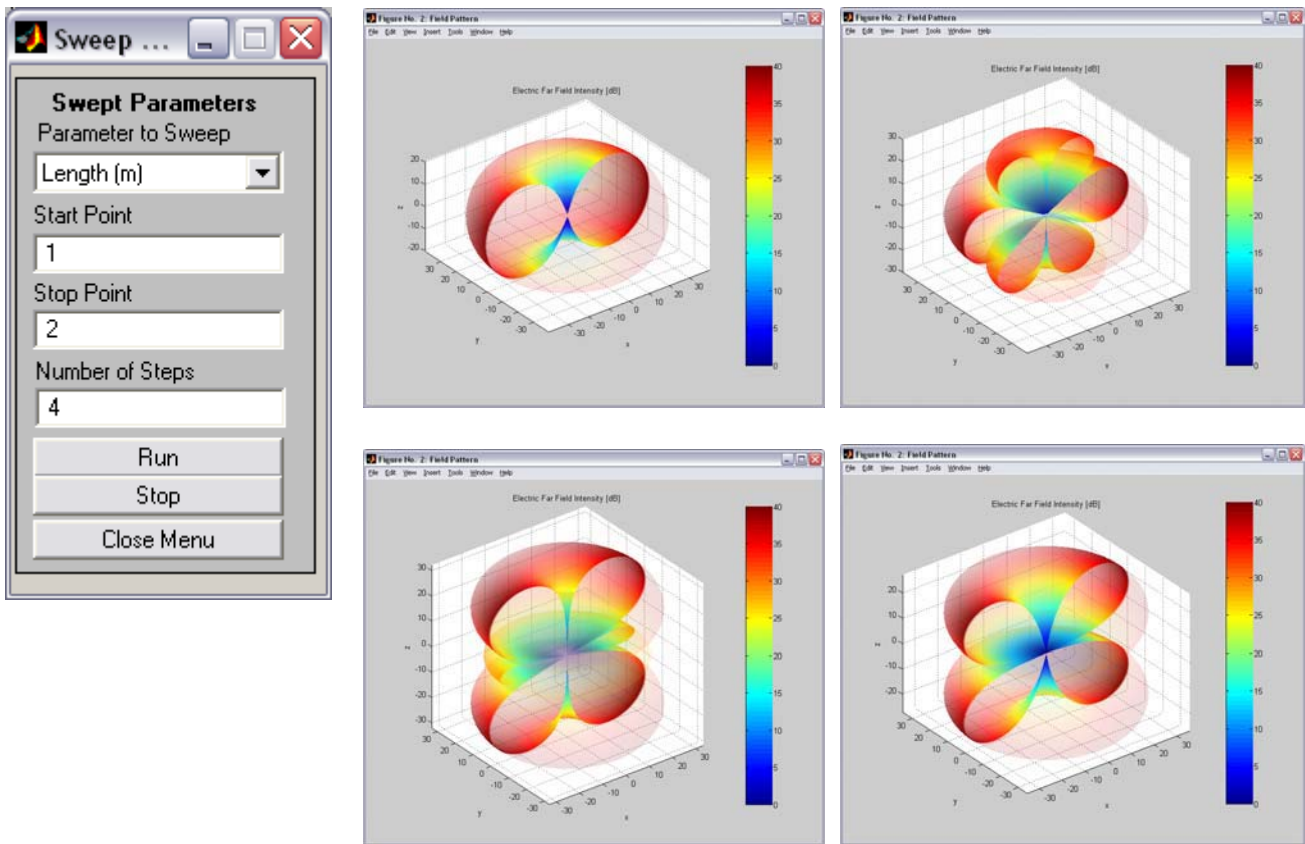


Figure 3. Sweeping a dipole from $L=1\text{m}$ to 2m ($\lambda=1\text{m}$).

4. Antenna Arrays

One of the main features of the program allows for the design of any type of array of common elements. From the main window the user may select any one of the 1-D, 2-D, or 3-D, array types. These include Linear, Circular, Planar, Cubical, Spherical, or the completely arbitrary array. In all but the arbitrary array the user simply selects the desired array, enters the number of elements, the relative amplitudes and

phases of the elements (either single elements, rows of elements, or planes of elements depending on the array type) and the corresponding array factor is generated. The array factor itself may be viewed or a composite pattern of the array made with a selected element can be viewed. When an array is chosen an element pattern window will open allowing the user to choose which antenna will be used for the individual elements.

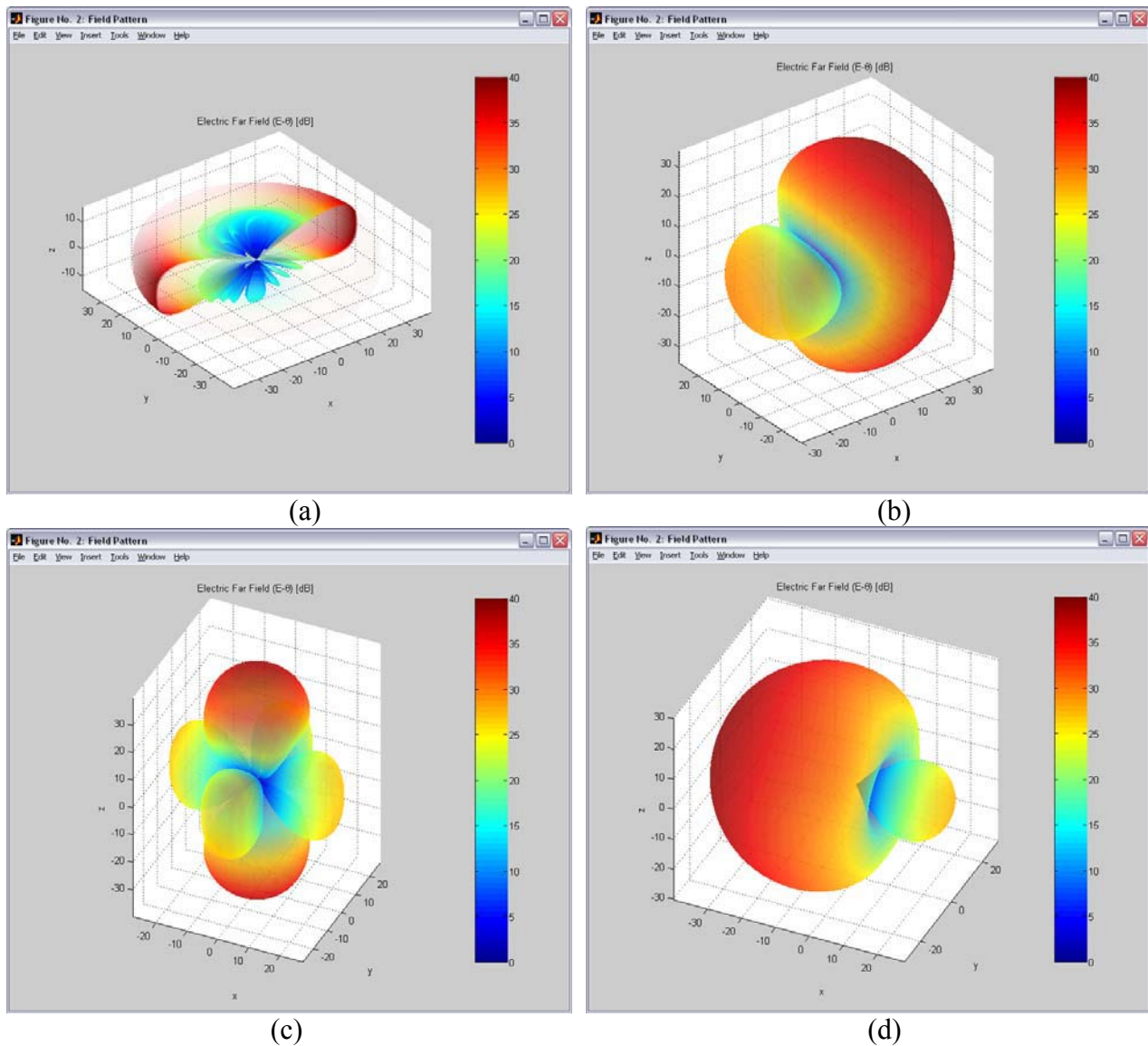


Figure 4. Radiation patterns for arrays of isotropic elements for, (a) Fourier synthesized 1-D array, (b) circular 2-D array, (c) planar array, and (d) spherical array.

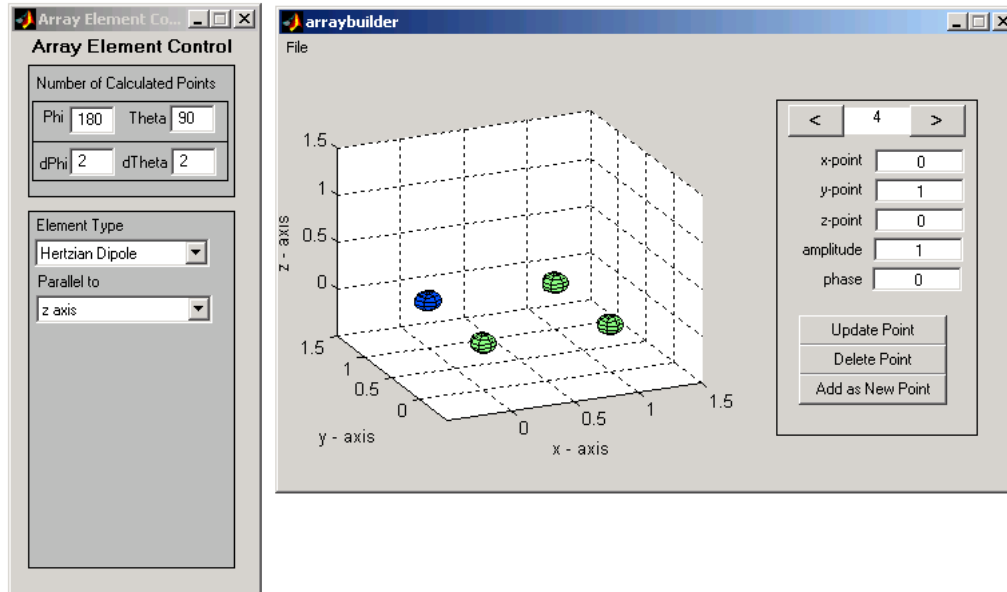


Figure 5. The array element window and arraybuilder window.

A few common types of antenna elements are available here as a matter of convenience, as well as an option for the user to load a pattern file. This file may be generated by this program earlier while designing a single element or may contain data generated elsewhere. This allows for the use of the patterns generated from other programs or gathered from real antennas on an antenna range to be used as elements when analyzing arrays.

Alternatively the program allows for the analysis and visualization of completely arbitrary arrays of elements. In order to accomplish this, the program includes what is known as the arraybuilder. This is a small subprogram that allows for the layout and viewing of the array elements. The user may choose the location in x, y, and z directions (all points are relative to each other and the distance is measured in wavelengths) and the relative amplitude and phase of each element. The arraybuilder allows for the interactive placement and updating of these elements, as changes are shown immediately in the arraybuilder window shown in Figure 3. Elements may be added, updated or deleted at will, and as can be seen in the figure,

the currently selected element is highlighted in blue.

5. Conclusions

The program successfully allows the user to interactively design and visualize many common types of antennas as well as arrays of elements. It has great utility not only in its use as a design program for antennas, but as a learning tool as well. It can allow the user to interactively explore antenna patterns and its properties and promotes greater understanding of antenna design. The element design features provide a good platform for design and visualization. The array features allow for the interactive design and visualization of many different types of arrays and allow for the testing and verification of array designs.

References

- [1] W. L. Stutzman, "Antenna Theory and Design", 2nd Edition. John Wiley & Sons, Inc, 1997.
- [2] C. A. Balanis, "Antenna Theory: Analysis and Design", 2nd Edition. John Wiley & Sons, Inc, 1996.



Atef Z. Elsherbeni joined the faculty at the University of Mississippi in August 1987 as an Assistant Professor of Electrical Engineering. He advanced to the rank of Associate Professor on July 1991, and to the rank of Professor on July 1997. He spent a sabbatical term in 1996 at the Electrical Engineering Department,

University of California at Los Angeles (UCLA).

Dr. Elsherbeni received The Mississippi Academy of Science 2003 Outstanding Contribution to Science Award, The 2002 IEEE Region 3 Outstanding Engineering Educator Award, The 2002 School of Engineering Outstanding Engineering Faculty Member of the Year Award, the 2001 Applied Computational Electromagnetic Society (ACES) Exemplary Service Award for leadership and contributions as Electronic Publishing managing Editor 1999-2001, the 2001 Researcher/Scholar of the year award in the Department of Electrical Engineering, The University of Mississippi, and the 1996 Outstanding Engineering Educator of the IEEE Memphis Section.

Dr. Elsherbeni has conducted research in several areas such as: scattering and diffraction by dielectric and metal objects, inverse scattering, finite difference time domain analysis of passive and active microwave devices, field visualization and software development for EM education, dielectric resonators, interactions of electromagnetic waves with human body, and development of sensors for soil moisture and for monitoring of airports noise levels, reflector antennas and antenna arrays, and analysis and design of printed antennas for wireless communications and for radars and personal communication systems. His recent research has been on the application of numerical techniques to microstrip and planar transmission lines, antenna measurements, and antenna design for radar and personal communication systems. He has published 65 technical journal articles and 12 book chapters on applied electromagnetics, antenna design, and microwave subjects, and contributed to 210 professional presentations. He is the coauthor of the book entitled "MATLAB Simulations for Radar Systems Design", CRC Press, 2003 and the main author of the chapters "Handheld Antennas" and "The Finite Difference

Time Domain Technique for Microstrip Antennas" in Handbook of Antennas in Wireless Communications, CRC Press, 2001.

Dr. Elsherbeni is a senior member of the Institute of Electrical and Electronics Engineers (IEEE). He is the Editor-in-Chief for the Applied Computational Electromagnetic Society (ACES) Journal, an Associate Editor to the Radio Science Journal, and the electronic publishing managing editor of ACES. His honorary memberships include the Electromagnetics Academy and the Scientific Sigma Xi Society. He serves on the editorial board of the Book Series on Progress in Electromagnetic Research, the Electromagnetic Waves and Applications Journal, and the Computer Applications in Engineering Education Journal. He is the Chair of the Engineering and Physics Division of the Mississippi Academy of Science and the past Chair of the Educational Activity Committee for the IEEE Region 3 Section. Dr. Elsherbeni's home page can be found at <http://www.ee.olemiss.edu/atef> and his email address is Elsherbeni@ieee.org.



Matthew Joseph Inman was born in Dayton, Ohio on Feb 7th, 1978. He received his B.S. and M.S. in Electrical Engineering from the University of Mississippi in 2000 and 2003, respectively. He currently is currently pursuing a Ph.D. degree in

electromagnetics there. He is currently employed at the University as research assistant and graduate instructor teaching a number of undergraduate courses. His interests involve electromagnetic theories, numerical techniques, antenna design and visualization.

Aperture-Coupled Stripline-to-Waveguide Transitions for Spatial Power Combining

Chris W. Hicks*, Alexander B. Yakovlev#, and Michael B. Steer⁺

*Naval Air Systems Command, RF Sensors Division 4.5.5, Patuxent River, MD 20670

#Department of Electrical Engineering, The University of Mississippi, University, MS 38677-1848

⁺Department of Electrical and Computer Engineering, North Carolina State University, Raleigh, NC 27695-7914

Abstract

A full-wave electromagnetic model is developed and verified for a waveguide transition consisting of slotted rectangular waveguides coupled to a strip line. This waveguide-based structure represents a portion of the planar spatial power combining amplifier array. The electromagnetic simulator is developed to analyze the stripline-to-slot transitions operating in a waveguide-based environment in the X-band. The simulator is based on the method of moments (MoM) discretization of the coupled system of integral equations with the piecewise sinusoidal testing and basis functions in the electric and magnetic surface current density expansions. Electric and magnetic dyadic Green's functions used in this integral equation formulation are developed for an infinite rectangular waveguide in the form of partial expansion over the complete system of eigenfunctions of a transverse Laplacian operator. Numerical results are obtained and compared with a commercial microwave simulator for a few representative structures, including various configurations and planar arrays of slotted waveguide modules coupled to a strip line.

I. Introduction

Military and civilian applications require sizable power at microwave and millimeter-wave frequencies. Medium to high power levels are needed for applications such as communications, active missile seekers, radar, and millimeter-wave imaging. To meet this need, klystrons, traveling-wave tubes, and gridded tubes are heavily utilized to generate medium to high

power. However, tubes are bulky, costly, require high operating voltages, and have a short lifetime. As an alternative, solid-state devices offer several advantages such as, lightweight, smaller size, wider bandwidths, and lower operating voltages. These advantages lead to lower cost because systems can be constructed using planar fabrication techniques. However, as the frequency increases, the output power of solid-state devices decreases due to their small physical size. Therefore, to achieve sizable power levels that compete with those generated by vacuum tubes, several solid-state devices can be combined in an array. Conventional power combiners are effectively limited in the number of devices that can be combined. To overcome these limitations and produce high power levels at microwave and millimeter-wave frequencies, in a past few years there has been a considerable activity in developing spatial power combining systems [1], [2], [3]. The output power of individual solid-state devices in a planar array is combined to produce moderate-to-high power levels. It is desirable to utilize a single solid-state amplifier, however, as frequency increases, the output power levels become low due to the $1/f^2$ fall-off of available power [4]. By utilizing power combining techniques light-weight, reliable, and low cost amplifiers and oscillators can be potentially designed to meet the demand of military and civilian applications.

Fundamental understanding of spatial power combining systems has primarily been done by experimental investigation. Several experimental free space and dielectric quasi-optical power combiners and waveguide spatial power combiners have been successful at demonstrating the fundamental concept of generating usable output power levels using spatial and quasi-optical techniques. Although great strides have been

made, to date, quasi-optical/spatial power combining systems have not yet out performed conventional power combiners. In order to capture the full potential of quasi-optical/spatial systems to generate high power levels, numerical modeling and computer aid engineering tools are needed to fully understand these systems [5]. The development of computer models helps to reduce the cost and time associated with experimental work, and computer models assist with designing efficient quasi-optical/spatial power combining systems. Modeling a quasi-optical/spatial power combining system is complex and challenging. There are several major system components that must be modeled such as, the input and output sources, which are typically waveguide horns with optical lenses inside, the input and output antennas with associated transmission lines and control components, and the active integrated amplifier circuitry.

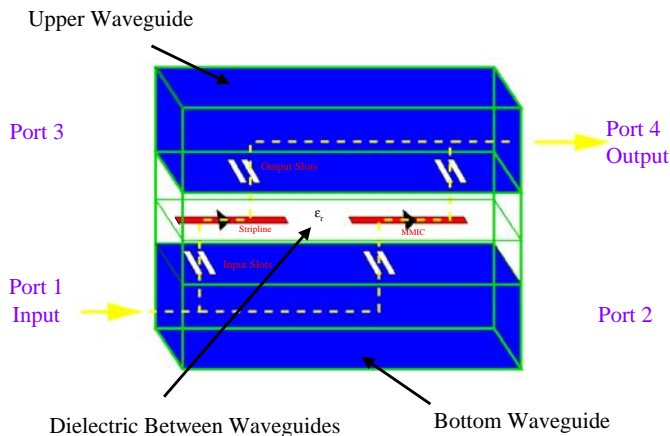


Fig. 1. Aperture-coupled stripline-to-waveguide transition.

In this paper, an electromagnetic modeling environment is developed for an aperture-coupled stripline-to-waveguide transition (with geometry shown in Fig. 1). This transition is the fundamental building block for two-dimensional spatial power combining amplifier arrays shown in Fig. 2 and, in turn, for the planar quasi-optical power combining systems. The transition consists of three infinite aperture-coupled rectangular waveguides. The lower slots (apertures) are located on the surface between the lower and middle waveguides, and the upper slots are located on the surface

between the middle and upper waveguides. The strips are located inside of the middle waveguide region. The objective of stripline-to-waveguide transition is to efficiently couple energy from the lower waveguide to the upper waveguide. An incident electromagnetic field is illuminated at the input port of the lower waveguide. This signal travels into the lower waveguide and induces magnetic currents on the lower slots where the slots scatter energy into the lower, middle, and upper waveguides. In the middle waveguide region the scattered fields induce electric currents and standing waves along the strips. The scattered energy from the strips along with the scattered energy from the lower slots induce magnetic currents in the upper slots. The magnetic currents in the upper slots cause scattered fields back into the middle waveguide and into the upper waveguide region. Optimum performance is achieved by varying the distance between the slots, adjusting the slot dimensions, rotating the slots, or varying the stripline dimensions.

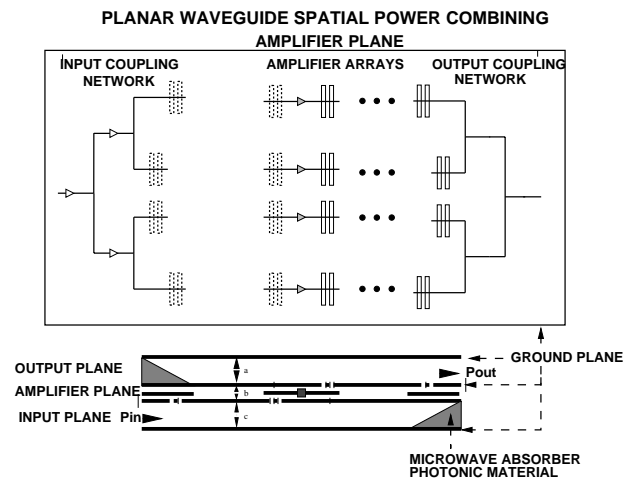


Fig. 2. Aperture-coupled planar waveguide amplifier array.

A full-wave electromagnetic model is developed for a structure that couples a waveguide to a stripline through a set of slots and from the stripline through another set of slots into a second waveguide. The system modeling is based on an integral equation formulation for the induced electric and magnetic surface current densities resulting in a coupled set of integral equations discretized via the method of moments (MoM). The scattered electric and magnetic fields are

expressed in terms of dyadic Green's functions and the electric and magnetic surface currents. Electric and magnetic dyadic Green's functions are developed for an infinite rectangular waveguide in the form of partial expansion over the complete system of eigenfunctions of a transverse Laplacian operator. The surface currents are discretized by overlapping piecewise sinusoidal subdomain basis functions in order to accurately model narrow longitudinal strips and transverse slots. In this formulation, a MoM matrix includes all possible self and mutual coupling effects between the slots and strips. The transition is excited with the TE₁₀ dominant waveguide mode, and the scattering parameters are calculated from the forward and backward coupling coefficients in the waveguide regions.

Numerical results of the scattering characteristics are obtained and compared with a commercial microwave simulator for a few representative structures, including a single slot-strip-slot waveguide transition, multiple slot-strip-slot waveguide transitions, and planar arrays of slotted waveguide modules coupled to strip lines.

II. Theory

A general electromagnetic formulation for a closed-boundary waveguiding structure containing arbitrarily shaped apertures and conducting strips (see Fig. 3) is presented in this section. This structure is a general building block of the aperture-coupled stripline-to-waveguide transition shown in Fig. 1. The formulation is based on the integral representation of incident and scattered electric and magnetic fields in terms of dyadic Green's functions [6], [7]. Dyadic Green's functions represent the electric and magnetic fields at an observation point inside a volume due to an arbitrarily oriented point source. Fig. 3 shows an arbitrary volume V enclosed by the surface $\tilde{S} = S \cup S_m$, where S represents an electric-type boundary surface and S_m represents the surface of apertures (magnetic-type surface). The volume V encloses an impressed electric volume current source $\bar{J}_{imp} \in V_{imp}$ and an electric current source \bar{J}_{ind} induced on the surface of conducting strips S_e (electric-type surface).

The integral representations for the total electric and magnetic fields in volume V due to the impressed and induced currents are obtained as follows

$$\bar{E}(\vec{r}) = -j\omega\mu \int_{V_{imp}} \bar{\bar{G}}_{EJ}(\vec{r}, \vec{r}') \cdot \bar{J}_{imp}(\vec{r}') dV'$$

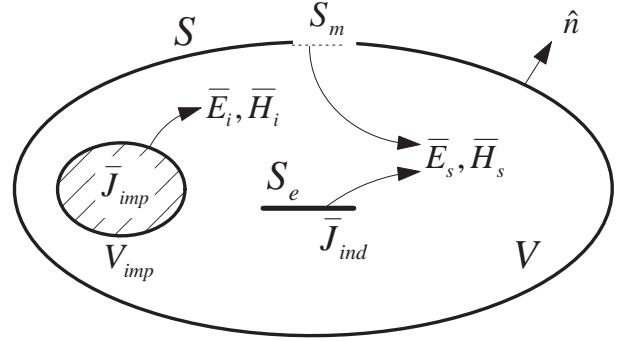


Fig. 3. Geometry of a closed-boundary waveguiding structure containing apertures and conducting strips in the presence of an impressed electric current source.

$$\begin{aligned} & -j\omega\mu \int_{S_e} \bar{\bar{G}}_{EJ}(\vec{r}, \vec{r}') \cdot \bar{J}_{ind}(\vec{r}') dS' \\ & - \int_{S_m} \bar{\bar{G}}_{EM}(\vec{r}, \vec{r}') \cdot \bar{M}(\vec{r}') dS' \end{aligned} \quad (1)$$

$$\begin{aligned} \bar{H}(\vec{r}) = & \int_{V_{imp}} \bar{\bar{G}}_{HJ}(\vec{r}, \vec{r}') \cdot \bar{J}_{imp}(\vec{r}') dV' \\ & + \int_{S_e} \bar{\bar{G}}_{HJ}(\vec{r}, \vec{r}') \cdot \bar{J}_{ind}(\vec{r}') dS' \\ & - j\omega\epsilon \int_{S_m} \bar{\bar{G}}_{HM}(\vec{r}, \vec{r}') \cdot \bar{M}(\vec{r}') dS' \end{aligned} \quad (2)$$

where

$$\bar{\bar{G}}_{HJ}(\vec{r}, \vec{r}') = \nabla \times \bar{\bar{G}}_{EJ}(\vec{r}, \vec{r}'), \quad (3)$$

$$\bar{\bar{G}}_{EM}(\vec{r}, \vec{r}') = \nabla \times \bar{\bar{G}}_{HM}(\vec{r}, \vec{r}'). \quad (4)$$

Here, the electric-electric dyadic Green's function, $\bar{\bar{G}}_{EJ}(\vec{r}, \vec{r}')$, relates the electric field in volume V enclosed by surface \tilde{S} to the impressed electric current source $\bar{J}_{imp}(\vec{r}') \in V_{imp}$ and the induced electric surface current $\bar{J}_{ind}(\vec{r}') \in S_e$; the electric-magnetic dyadic Green's function, $\bar{\bar{G}}_{EM}(\vec{r}, \vec{r}')$, relates the electric field in the volume V to the equivalent magnetic surface current $\bar{M}(\vec{r}') \in S_m$; the magnetic-magnetic dyadic Green's function, $\bar{\bar{G}}_{HM}(\vec{r}, \vec{r}')$, relates the magnetic field in the volume V to the equivalent magnetic surface current $\bar{M}(\vec{r}') \in S_m$, and the magnetic-electric dyadic Green's function, $\bar{\bar{G}}_{HJ}(\vec{r}, \vec{r}')$, relates the magnetic field in the volume V to the impressed electric current source

$\bar{J}_{imp}(\vec{r}') \in V_{imp}$ and the induced electric surface current $\bar{J}_{ind}(\vec{r}') \in S_e$. These electric and magnetic dyadic Green's functions are developed for an infinite rectangular waveguide in the form of partial expansion over the complete system of eigenfunctions of a transverse Laplacian operator [8].

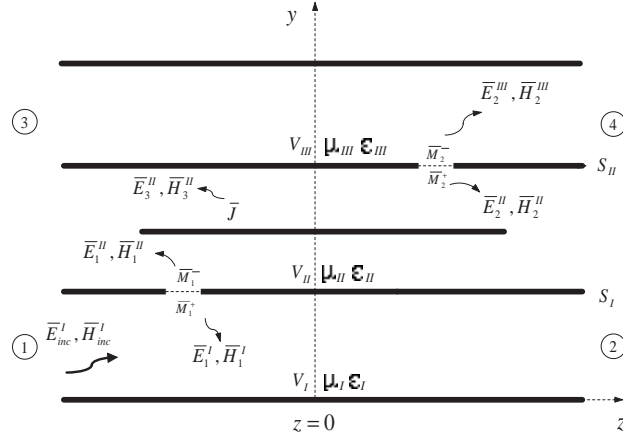


Fig. 4. Field analysis in terms of incident and scattered electric and magnetic fields due to induced electric and magnetic surface currents in the aperture-coupled stripline-to-waveguide transition.

The integral equation formulation discussed above was applied for the analysis of a structure that couples the lower waveguide (region V_I) to the stripline (region V_{II}) through a set of slots and from the stripline through another set of slots into the upper waveguide (region V_{III}) (Fig. 4). The geometry shown in Fig. 4 is a unit cell of a general topology of the aperture-coupled stripline-to-waveguide transition (Fig. 1). Fig. 4 shows a field analysis in terms of incident and scattered electric and magnetic fields in three different regions due to induced electric and magnetic surface currents. A coupled system of equations is obtained by imposing a continuity of tangential magnetic fields across the surfaces of lower and upper slots, S_1 and S_2 , respectively, and an electric-field boundary condition on the surface of the strip, S_3 ,

$$\hat{y} \times \bar{H}_{inc}^I(\vec{r}) = \hat{y} \times [\bar{H}_1^{II}(\vec{r}) - \bar{H}_1^I(\vec{r}) + \bar{H}_2^{II}(\vec{r}) + \bar{H}_3^{II}(\vec{r})], \quad \vec{r} \in S_1 \quad (5)$$

$$0 = \hat{y} \times [\bar{H}_1^{II}(\vec{r}) + \bar{H}_2^{II}(\vec{r}) - \bar{H}_2^{III}(\vec{r}) + \bar{H}_3^{II}(\vec{r})], \quad \vec{r} \in S_2 \quad (6)$$

$$0 = \hat{y} \times [\bar{E}_1^{II}(\vec{r}) + \bar{E}_2^{II}(\vec{r}) + \bar{E}_3^{II}(\vec{r})], \quad \vec{r} \in S_3 \quad (7)$$

or it can be written in the integral form in terms of corresponding dyadic Green's functions and impressed and induced surface current densities

$$\begin{aligned} \hat{y} \times \bar{H}_{inc}^I(\vec{r}) = & \hat{y} \times [j\omega\epsilon_{II} \int_{S_1} \bar{G}_{HM}^{=II}(\vec{r}, \vec{r}') \cdot \bar{M}_1(\vec{r}') dS' \\ & - j\omega\epsilon_I \int_{S_1} \bar{G}_{HM}^{=I}(\vec{r}, \vec{r}') \cdot \bar{M}_1(\vec{r}') dS' \\ & - j\omega\epsilon_{II} \int_{S_2} \bar{G}_{HM}^{=II}(\vec{r}, \vec{r}') \cdot \bar{M}_2(\vec{r}') dS' \\ & + \int_{S_3} \bar{G}_{HJ}^{=II}(\vec{r}, \vec{r}') \cdot \bar{J}(\vec{r}') dS'], \quad \vec{r} \in S_1 \end{aligned} \quad (8)$$

$$\begin{aligned} 0 = \hat{y} \times [j\omega\epsilon_{II} \int_{S_1} \bar{G}_{HM}^{=II}(\vec{r}, \vec{r}') \cdot \bar{M}_1(\vec{r}') dS' \\ - j\omega\epsilon_{II} \int_{S_2} \bar{G}_{HM}^{=II}(\vec{r}, \vec{r}') \cdot \bar{M}_2(\vec{r}') dS' \\ + j\omega\epsilon_{III} \int_{S_2} \bar{G}_{HM}^{=III}(\vec{r}, \vec{r}') \cdot \bar{M}_2(\vec{r}') dS' \\ + \int_{S_3} \bar{G}_{HJ}^{=II}(\vec{r}, \vec{r}') \cdot \bar{J}(\vec{r}') dS'], \quad \vec{r} \in S_2 \end{aligned} \quad (9)$$

$$\begin{aligned} 0 = \hat{y} \times [\int_{S_1} \bar{G}_{EM}^{=II}(\vec{r}, \vec{r}') \cdot \bar{M}_1(\vec{r}') dS' \\ + \int_{S_2} \bar{G}_{EM}^{=II}(\vec{r}, \vec{r}') \cdot \bar{M}_2(\vec{r}') dS' \\ + j\omega\mu_{II} \int_{S_3} \bar{G}_{EJ}^{=II}(\vec{r}, \vec{r}') \cdot \bar{J}(\vec{r}') dS'], \quad \vec{r} \in S_3. \end{aligned} \quad (10)$$

Here, $\bar{H}_{inc}^I(\vec{r})$ is the incident magnetic field generated in the lower waveguide; $\bar{M}_1(\vec{r}')$ and $\bar{M}_2(\vec{r}')$ are the equivalent magnetic surface currents induced on the surfaces of the lower and upper slots, S_1 and S_2 , respectively; $\bar{J}(\vec{r}')$ is the electric surface current induced on the surface of the strip, S_3 ; $\bar{G}_{HM}(\vec{r}, \vec{r}')$, $\bar{G}_{HJ}(\vec{r}, \vec{r}')$, $\bar{G}_{EM}(\vec{r}, \vec{r}')$, and $\bar{G}_{EJ}(\vec{r}, \vec{r}')$ are the electric and magnetic Green's dyadics of the corresponding waveguides (regions V_I , V_{II} , and V_{III}). The surface currents are discretized by overlapping piecewise sinusoidal subdomain basis functions. In this formulation, a MoM matrix includes all possible self and mutual coupling effects between the slots and strips. The transition is excited with the TE₁₀ dominant waveguide mode and the scattering parameters are calculated from the forward and backward coupling coefficients

in the waveguide regions. The details of the method of moments discretization technique of the slotted waveguide transitions and dyadic Green's functions applied in this formulation can be found in [8].

III. Numerical Results and Discussions

Numerical results of the scattering characteristics were obtained and compared with a commercial microwave simulator for a few representative structures shown in Fig. 5, including a single slot-strip-slot waveguide and multiple slot-strip-slot waveguide transitions. Also, planar arrays of slotted waveguide modules coupled to a strip line (with geometries shown in Figs. 8 and 10) are investigated.

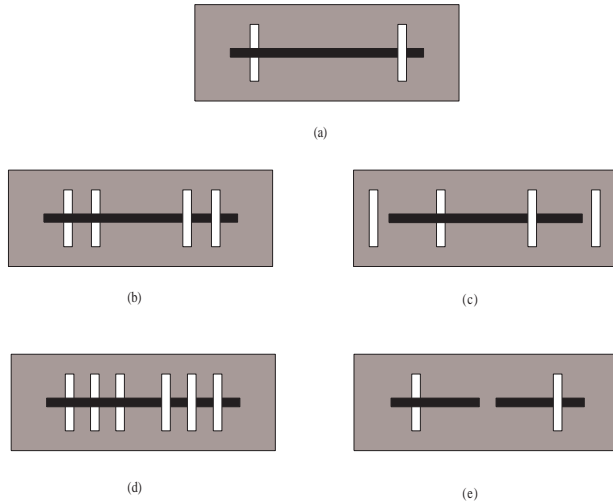
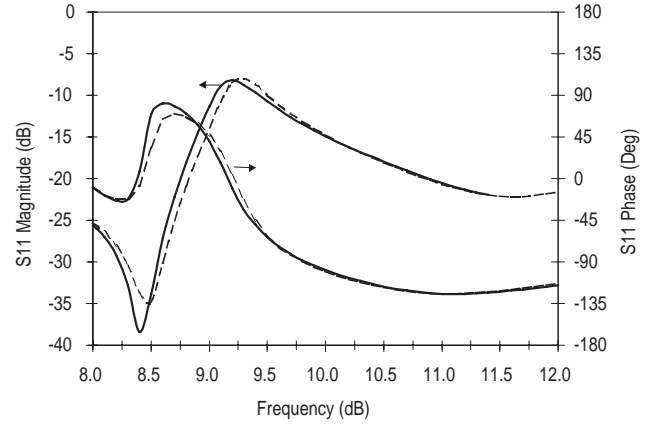
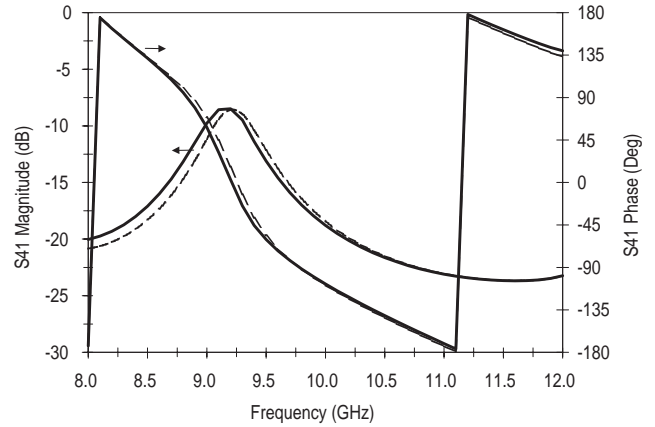


Fig. 5. Top view: (a) one lower slot, one strip, and one upper slot; (b) two lower slots, one strip, and two upper slots; (c) same as (b) but one lower slot and one upper slot are offset, (d) three lower slots, one strip, and three upper slots; and (e) one lower slot, two strips, and one upper slot.

Here we present numerical results of the scattering characteristics for the examples of the double slot-strip-slot waveguide transition with two shifted slots (case (c) in Fig. 5) and two strips coupled to two slots (case (e) in Fig. 5). In both examples, the upper and lower X-band waveguide dimensions are $22.86 \text{ mm} \times 10.16 \text{ mm}$, $\epsilon_I = \epsilon_{III} = 1.0$, while the middle waveguide dimensions are $22.86 \text{ mm} \times 1.5748 \text{ mm}$ (62 mils), and $\epsilon_{II} = 1.0$. In the case shown in Fig. 5(c), the spacing between the lower and upper slots is 19 mm, while the



(a)

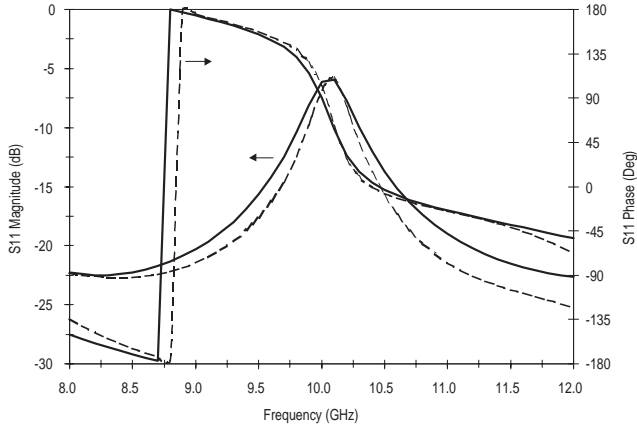


(b)

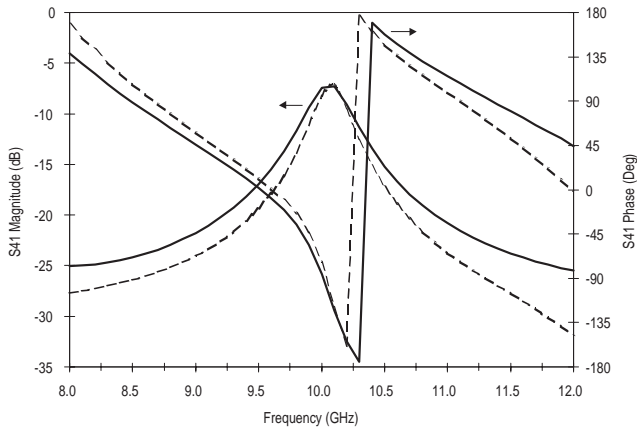
Fig. 6. MoM (solid line) and HFSS (dashed line) comparison for the scattering parameters (reflection and coupling coefficients) for the double slot-strip-slot waveguide transition with two offset slots. Magnitude and phase: (a) S_{11} and (b) S_{41} .

inter-spacing between the two lower slots and two upper slots is 10 mm. The length of the strip is 30 mm, the width of the strip is 1 mm, the length of the slots is 13 mm, and the width of the slots is 1 mm. The reflection coefficient S_{11} and the coupling coefficient S_{41} computed using the MoM technique presented here and the HFSS commercial program are compared in Fig. 6. The coupling of -8.6 dB occurs at approximately 9.2 GHz.

In the second example with geometry shown in Fig. 5(e), the longitudinal strip is divided into two strips



(a)



(b)

Fig. 7. MoM (solid line) and HFSS (dashed line) comparison of the scattering parameters for one lower slot, two strips, and one upper slot waveguide transition. Magnitude and phase: (a) S_{11} and (b) S_{41} .

each 10 mm in length. The length of the lower and upper slots is changed to 15 mm. In the method of moments program, the slots and strips are discretized in 1 mm cells. Both scattering parameters peak at 10 GHz (Fig. 7), and both magnitudes of S_{11} and S_{41} reach a peak value of approximately -5.5 dB and -7.2 dB, respectively.

Fig. 8 shows the geometry of the 1×2 waveguide coupler array which consists of 2 transitions in series shown in Fig. 5(a). Transitions are separated by 40

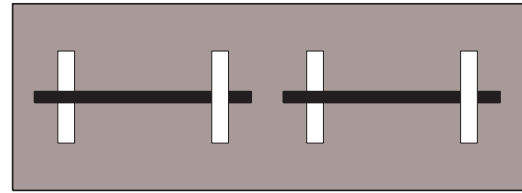
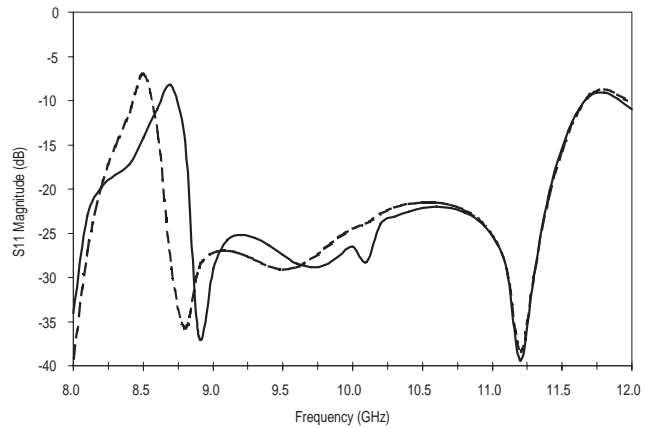
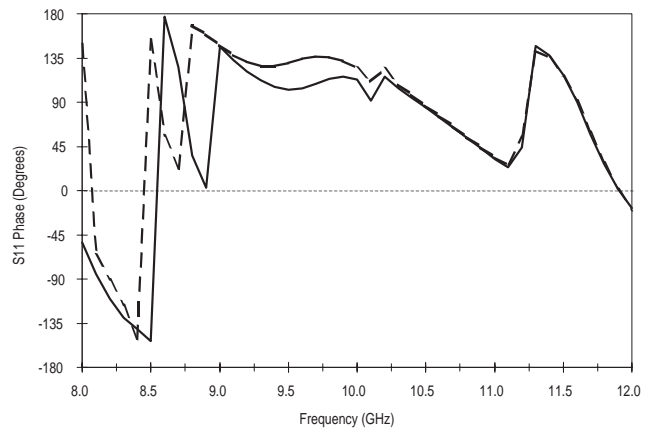


Fig. 8. Top view of the slotted 1×2 waveguide array with a unit cell shown in Fig. 5(a) consisting of one lower slot, one strip, and one upper slot.



(a)



(b)

Fig. 9. MoM (solid line) and HFSS (dashed line) comparison of S_{11} for the 1×2 one lower slot, one strip, and one upper slot waveguide coupler array. (a) Magnitude and (b) phase.

mm with respect to the center, the waveguide length is 90 mm, and $\epsilon_I = \epsilon_{II} = \epsilon_{III} = 1.0$.

Fig. 9 compares the MoM simulations and HFSS results for the magnitude and phase of the reflection coefficient S_{11} . The maximum and minimum values, -8.3 dB and -39.5 dB, of the reflection coefficient occur at 8.7 GHz and 11.2 GHz, respectively.

Fig. 10 shows the 2×2 slotted waveguide array which consists of four transitions with the geometry of a unit cell shown in Fig. 5(a). The 2×2 array represents two waveguide couplers separated by a distance of 23 mm. The length and width of the slots are 13 mm \times 1 mm, and the length and width of the strip are 30 mm \times 1 mm, respectively. Both the lower and upper waveguide width and height dimensions are 46.0 mm \times 10.16 mm and $\epsilon_I = \epsilon_{III} = 1.0$. The middle waveguide dimensions are 46.0 mm \times 1.5 mm and $\epsilon_{II} = 2.2$.

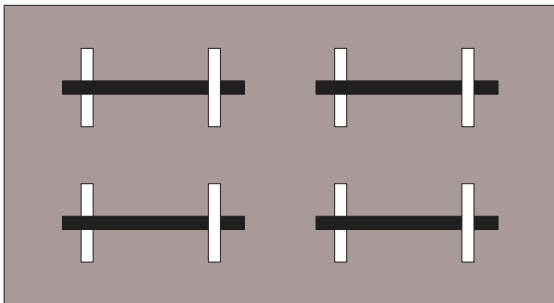


Fig. 10. Top view of a 2×2 one lower slot, one strip, and one upper slot waveguide array.

Fig. 11 shows the MoM simulations for the magnitude and phase of S_{11} for the 2×2 waveguide array. A total of $m = n = 125$ modes were utilized to simulate the array, and the cell size of slots and strips were discretized into 1 mm increments. The minimum value of -32.4 dB of S_{11} occurs at approximately 9.75 GHz.

IV. Conclusion

In this paper we presented the analysis of aperture-coupled stripline-to-waveguide transitions used in planar spatial power combining systems. The method of analysis is based on the integral equation formulation for the unknown electric and magnetic surface currents with electric and magnetic dyadic Green's functions of infinite rectangular waveguide. The method of moments discretization with piecewise sinusoidal testing

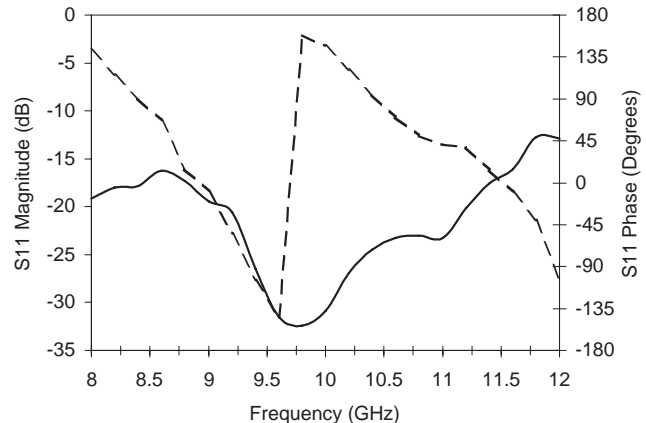


Fig. 11. MoM simulation of S_{11} for a 2×2 one lower slot, one strip, and one upper slot waveguide array. (a) Magnitude (solid line) and (b) phase (dashed line).

and basis functions reduces a coupled set of integral equations to a matrix equation. Numerical results obtained for the scattering parameters of various slot-strip-slot waveguide transitions and arrays compare well with the results calculated by the Finite Element Method commercial program (HFSS).

REFERENCES

- [1] P. F. Goldsmith, "Quasi-optical techniques at millimeter and sub-millimeter wavelengths," in *Infrared and Millimeter Waves*, K. J. Button (Ed.), New York: Academic Press, Vol. 6, pp. 277–343, 1982.
- [2] L. Wandering and V. Nalbandian, "Millimeter-wave power-combining using quasi-optical techniques," *IEEE Trans. on Microwave Theory and Techn.*, Vol. 31, pp. 189–193, February 1983.
- [3] R. A. York, Z. B. Popović *Active and Quasi-Optical Arrays for Solid-State Power Combining*, John Wiley & Sons, New York, New York, 1997.
- [4] J. C. Wiltse and J. W. Mink, "Quasi-optical power combining of solid-state sources," *Microwave Journal*, pp. 144–156, February 1992.
- [5] M. B. Steer, J. F. Harvey, J. W. Mink, M. N. Abdulla, C. E. Christoffersen, H. M. Gutierrez, P. L. Heron, C. W. Hicks, A. I. Khalil, U. A. Mughal, S. Nakazawa, T. W. Nuteson, J. Patwardhan, S. G. Skaggs, M. A. Summers, S. Wang, and A. B. Yakovlev, "Global modeling of spa-

- tially distributed microwave and millimeter-wave systems,” *IEEE Trans. Microwave Theory Tech.*, Vol. 47, pp. 830–839, June 1999.
- [6] C. T. Tai, *Dyadic Green Functions in Electromagnetics*, IEEE Press, New York, New York, 1994.
- [7] N. L. Vandenberg and P. B. Katehi, “Full-wave analysis of aperture coupled shielded microstrip lines,” *IEEE MTT-S International Microwave Symposium Digest*, Vol.1, pp. 8–10, May 1990.
- [8] C. W. Hicks, *Experimental and Electromagnetic Modeling of Waveguide-Based Spatial Power Combining Systems*, Ph.D. dissertation, North Carolina State University, Raleigh, NC, November 2002.

Chris W. Hicks received the B.S. degree in Electrical Engineering from the University of South Carolina, Columbia, in 1985, the M.S.E.E. degree from North Carolina A&T State University, Greensboro, in 1994, and the Ph.D. degree in Electrical Engineering from North Carolina State University, Raleigh, in 2002. In 1985, he joined the Naval Air Systems Command (NAVAIR), Patuxent River, MD, where he currently works for the RF Sensors Division as a Senior Engineer. His interests include electromagnetic modeling of quasi-optical and spatial power combining systems, applied computational electromagnetics, and applications of microwave and millimeter-wave devices for radar, communications, and electronic warfare applications.

Dr. Hicks was the recipient of two full-time training fellowships from NAVAIR. He is a member of the IEEE, Microwave Theory and Techniques society, and Antennas and Propagation society.

Alexander B. Yakovlev received the Ph.D. degree in Radiophysics from the Institute of Radiophysics and Electronics, National Academy of Sciences, Ukraine, in 1992, and the Ph.D. degree in Electrical Engineering from the University of Wisconsin at Milwaukee, in 1997. In summer of 2000, he joined the Department of Electrical Engineering, The University of Mississippi, University, as an Assistant Professor. His research interests include mathematical methods in applied electromagnetics, modeling of high-frequency interconnection structures and amplifier arrays for spatial and quasi-optical power combining, integrated-circuit elements and devices, theory of leaky waves, and singularity theory.

Dr. Yakovlev received the Young Scientist Award

presented at the 1992 URSI International Symposium on Electromagnetic Theory, Sydney, Australia, and the Young Scientist Award at the 1996 International Symposium on Antennas and Propagation, Chiba, Japan. He is a Senior member of the IEEE and member of URSI Commission B.

Michael B. Steer received his B.E. and Ph.D. in Electrical Engineering from the University of Queensland, Brisbane, Australia, in 1976 and 1983, respectively. Currently he is Professor of Electrical and Computer Engineering at North Carolina State University. Professor Steer is a Fellow of the Institute of Electrical and Electronic Engineers for contributions to the computer aided engineering of non-linear microwave and millimeter-wave circuits. He is active in the Microwave Theory and Techniques (MTT) Society. In 1997 he was Secretary of the Society and from 1998 to 2000 was an Elected Member of its Administrative Committee. In 1999 and 2000 he was Professor in the School of Electronic and Electrical Engineering at the University of Leeds where he held the Chair in Microwave and Millimeter-wave Electronics. He was also Director of the Institute of Microwaves and Photonics at the University of Leeds. He has authored more than 240 publications on topics related to RF, microwave and millimeter-wave systems, to high speed digital design and to RF and microwave design methodology and circuit simulation. He is coauthor of the book *Foundations of Interconnect and Microstrip Design*, John Wiley, 2000. He is a 1987 Presidential Young Investigator (USA) and in 1994, and again in 1996, he was awarded the *Bronze Medallion* by U.S. Army Research for “Outstanding Scientific Accomplishment.” He received the Alcoa Foundation Distinguished Research Award from North Carolina State University in 2003. Professor Steer is the Editor-In-Chief of the IEEE Transactions on Microwave Theory and Techniques (2003-2006).

ACCURACY OF THREE UNCONDITIONALLY-STABLE FDTD SCHEMES FOR SOLVING MAXWELL'S EQUATIONS

Guilin Sun and Christopher W. Trueman

Electromagnetic Compatibility Laboratory, Concordia University,
7141 Sherbrooke Street West, Montreal, Quebec, Canada H4B 1R6

Abstract - This paper discusses accuracy limitations due to numerical dispersion and time step size for three implicit unconditionally-stable FDTD methods: Alternate-Direction-Implicit (ADI), Crank-Nicolson (CN) and Crank-Nicolson-Douglas-Gunn (CNDG). It is shown that for a uniform mesh, the three methods have the same numerical phase velocity along the axes, but have large differences along the diagonals. The ADI method has two orders-of-magnitude larger anisotropy than that of CN and CNDG. CNDG has no anisotropy at certain Courant numbers and mesh densities. At the limit of zero spatial mesh size, the three methods have different "intrinsic temporal dispersion" for a given time step size: CN has no anisotropy; ADI has positive anisotropy and CNDG has negative anisotropy, which is much smaller than ADI. The Nyquist sampling theorem provides a fundamental upper bound on the time step size for all three methods. It is shown that for ADI and CN the practical upper bound is close to the Nyquist limit, but for CNDG is half the Nyquist limit.

Keywords - Maxwell's Equations, Finite-difference time-domain method, Alternate-Direction-Implicit method, Crank-Nicolson method, Douglas-Gunn method, numerical dispersion, numerical anisotropy, accuracy, Nyquist criterion.

I. Introduction

Yee's Finite-Difference Time-Domain (FDTD) method is popular for solving Maxwell's Equations [1]. It is second-order accurate in both time and space [2]. Since it is an explicit method [3], it is easy to program and efficient to run. However it suffers from the Courant-Friedrich-Levy (CFL) limit or the Courant limit on the time step size required for stability. For objects with fine geometrical features, using a fine mesh size greatly reduces the allowable time step size, which causes the CPU time to be prohibitively long. To eliminate the CFL limit, unconditionally-stable methods working with large Courant numbers are desirable. Early in 1984, Holland [4] proposed an implicit method but it was not completely stable. In 1995, Shang [5] developed an efficient characteristic-based algorithm and Fijany [6] proposed a parallel Crank-Nicolson (CN) method by decomposition of the eigenvalue/eigenvector for the wave equations of the second order. In 1999 and 2000, Namiki [7] and Zhen et al.

[8] suggested an Alternate-Direction-Implicit (ADI) method. In 2001, Beggs and Briley [9] reported a two-factor scheme by combining a characteristic-based approach to spatial differencing with an implicit lower-upper approximate factorization that avoids the solution of a tridiagonal system. Very recently, Sun and Trueman [10] proposed a Crank-Nicolson scheme with Douglas-Gunn algorithm (CNDG).

This paper compares the numerical dispersion and anisotropy of the ADI, CN and CNDG methods used in FDTD, and analyzes some of their common characteristics and differences. For simplicity, Yee's mesh [1] in 2D is used with a TE_z wave in a linear, isotropic, non-dispersive and lossless medium. This paper is organized as follows. In Section II, the amplification factors are listed for the three methods. In Section III, their numerical dispersion relations are given and compared for a given mesh density. In Section IV their numerical anisotropy is analyzed and compared at different Courant numbers. In Section V the time step size limits are discussed and related to the Nyquist criterion. In Section VI the accuracy limit due to dispersion is analyzed for zero spatial mesh size.

II. Amplification Factors

The update equations for the ADI-FDTD, CN-FDTD and CNDG-FDTD methods are listed in Appendices. The ADI-FDTD uses two sub-steps [7] (Appendix I). The first sub-step advances time from step n to step $n+1/2$. The field component $E_y^{n+1/2}$ is fully implicit and requires solving a tridiagonal matrix. The second sub-step advances time step from $n+1/2$ to $n+1$, and the field component E_x^{n+1} is fully implicit and also requires solving a similar tridiagonal matrix. The time step $n+1/2$ is intermediate and the field values at this step are non-physical. The amplification factors for the two sub-steps are [7,11]

$$\xi_1 = \sqrt{\frac{1+r_y^2}{1+r_x^2}} e^{-j \tan^{-1}((1+r_x^2)(1+r_y^2)-1)} \quad (1)$$

$$\xi_2 = \sqrt{\frac{1+r_x^2}{1+r_y^2}} e^{-j \tan^{-1}((1+r_x^2)(1+r_y^2)-1)} \quad (2)$$

where $j = \sqrt{-1}$, $r_x = c\Delta t \sin(\beta_x \Delta_x / 2) / \Delta_x$, $r_y = c\Delta t \sin(\beta_y \Delta_y / 2) / \Delta_y$, Δt is the time step size, $c = 1/\sqrt{\mu\epsilon}$ is the physical velocity, ϵ and μ are the permittivity and permeability of the material respectively, Δ_x and Δ_y are the spatial meshing sizes along x and y axes; $\beta_x = \beta \cos(\phi)$, $\beta_y = \beta \sin(\phi)$, $\beta^2 = \beta_x^2 + \beta_y^2$ where β is the numerical wave phase constant; and angle ϕ is the direction of travel with respect to the x axis.

The CN scheme averages the field components at time step n and $n+1$ to maintain second order accuracy in time [6, 10] (Appendix II). It has no intermediate time step. But the resulting block tridiagonal matrix is very expensive to solve by direct methods such as the Gaussian elimination or the banded matrix method, as well as by iterative methods such as Successive Over-Relaxation (SOR) or the iterative Alternate-Direction-Implicit (ADI) method [3]. Since the discretization of the Poisson Equation and heat equation also leads to such a block tridiagonal matrix, several other methods to solve it can be found in Refs. [3] and [12]. Finjany et al. [6] solve the block tridiagonal matrix by eigenvalue/eigenvector decomposition.

Different solution methods for the block tridiagonal matrix may have different amplification factors and different numerical dispersion relations. This paper assumes a direct solution method of the block tridiagonal matrix such as the Gaussian elimination for the CN-FDTD method. The amplification factor for this CN method is [10]

$$\xi_{CN} = e^{\pm j \tan^{-1} \left(\frac{\sqrt{(1+r_x^2+r_y^2)^2 - (1-r_x^2-r_y^2)^2}}{1-r_x^2-r_y^2} \right)} \quad (3)$$

Note that the magnitude of the amplification factor for the CN method is unity.

The CNDG method avoids an expensive direct solution (Appendix III). It factorizes the block tridiagonal matrix and has two sub-steps: the first sub-step finds the intermediate field value H_z^* , and the second sub-step gets the solution at the time step $n+1$ [10]. Thus, like the ADI method, the CNDG method needs to solve a tridiagonal matrix at each sub-step. The amplification factor is

$$\xi_{CNDG} = e^{\pm j \tan^{-1} \left(\frac{\sqrt{(1+r_x^2)^2(1+r_y^2)^2 - (1-r_x^2)^2(1-r_y^2)^2}}{(1-r_x^2)(1-r_y^2)} \right)} \quad (4)$$

Though ADI and CNDG both have two sub-steps, there are some differences. In CNDG, the time level of the intermediate step is unknown, and there is only one amplification factor for the two sub-steps, of unity

magnitude. On the other hand, in ADI, the intermediate time is $(n+1/2)\Delta t$, and each sub-step has its own amplification factor. The magnitudes of the two amplification factors for the two individual sub-steps are reciprocals. Their product is the magnitude of the amplification factor for one full update cycle, and is unity. Note that the unity magnitude of the amplification factors ensures that the three implicit methods are unconditionally stable and strictly non-dissipative.

III. Numerical Dispersion

The numerical dispersion relation can be written for the three methods [10, 11] as

$$\tan^2(\omega\Delta t/2) = r_x^2 + r_y^2 + gr_x^2r_y^2 \quad (5)$$

where the factor g is

$$g = \begin{cases} 1 & ADI \\ 0 & CN \\ -\tan^2(\omega\Delta t/2) & CNDG \end{cases} \quad (6)$$

Given a frequency ω , a mesh size Δ_x and Δ_y , a time step size Δt , and direction of travel ϕ , Eqn. (5) is solved implicitly for the phase constant β . For a wave to propagate β must be real. The numerical dispersion is quantified by the relative velocity that is defined as the ratio of the numerical velocity to the physical velocity.

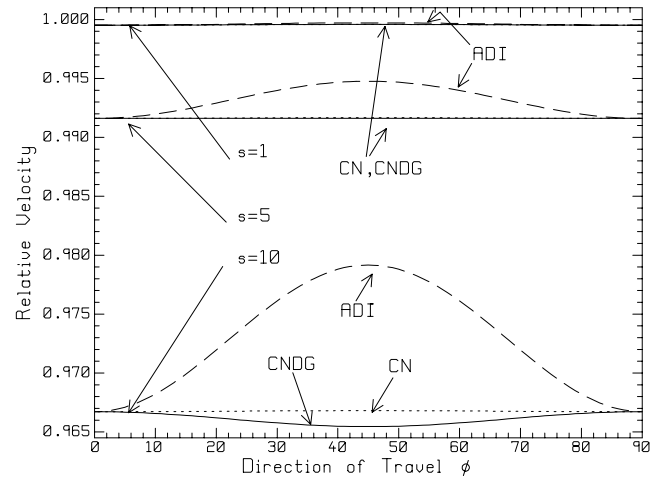


Fig. 1 Numerical dispersion with mesh density 100 and $s=1, 5$ and 10 , for ADI, CN and CNDG.

The numerical dispersion relation in Eqn. (5) for the ADI and CNDG methods has been validated with numerical experiments [10,11]. Fig.1 shows the relative velocity as a function of the direction of travel, using

$\Delta x = \Delta y$ with mesh density $N = 100$ cells per wavelength, at different Courant numbers $s = c\Delta t / \Delta x$ equal to 1, 5 and 10. Note that the numerical dispersion curves of the CN method and the CNDG method are almost identical, and are difficult to distinguish visually in Fig.1. The relative velocity along the axes is exactly the same for the three methods, but along the diagonal ADI is quite different from CN or CNDG. Thus their numerical anisotropies are significantly different, which will be discussed in the next section.

The “grid-related numerical dispersion” is defined as the dispersion at zero time step size. Since the cross term $gr_x^2 r_y^2$ in Eqn. (6) goes to zero as time step size approaches zero, the grid-related numerical dispersion is the same for the three methods, and is the same as that of Yee’s FDTD [2, 13].

IV. Numerical Anisotropy

The velocity-anisotropy error is often used to quantify the numerical anisotropy [2]. In an isotropic medium, the wavefront of a cylindrical wave is a circle, that is, the phase velocity is the same in all directions. However, in the numerical domain, the numerical wave velocity usually depends on the direction of travel. Like Yee’s FDTD with a uniform mesh, the ADI and CN methods have the largest velocity along the diagonals and slowest along the axes, as shown in Fig. 1.

However, the CNDG behaves differently from CN or ADI. At certain combinations of the mesh and time step sizes, the velocity u_{45° along the diagonals can be slower than the velocity u_{0° along the axes. To evaluate this phenomenon, the following definition of the velocity anisotropy is used for a uniform mesh

$$\Delta u = \frac{u_{45^\circ} - u_{0^\circ}}{\min\{u_{45^\circ}, u_{0^\circ}\}} \times 100\% \quad (7)$$

This error definition has the same magnitude as that Taflove and Hagness [2], but can be positive or negative, depending on which velocity is larger. Fig. 2 and Fig. 3 show the numerical anisotropy at mesh densities from 50 to 100 cells per wavelength for the ADI, CN and CNDG methods. The anisotropy of ADI is about two orders of magnitude larger than that of CN and CNDG. As the Courant number increases, the anisotropy in ADI increases significantly. The CN and CNDG have the same behaviour. For the Courant number smaller than about 11, the anisotropy of CNDG is always smaller than that of CN; for the Courant number larger than 11, the anisotropy of CNDG is larger than that of CN at coarse mesh density (for example, 50), but it quickly becomes smaller than that of CN after certain mesh densities. For instance, if the Courant number is 12, at the mesh density 50, the numerical

anisotropy is -0.148×0.01 for CNDG and 0.082×0.01 for CN; at mesh density 55, their absolute anisotropy values are the same, about 0.066×0.01 . However, at mesh density 60, CN has 0.055×0.01 but CNDG has only 0.038×0.01 .

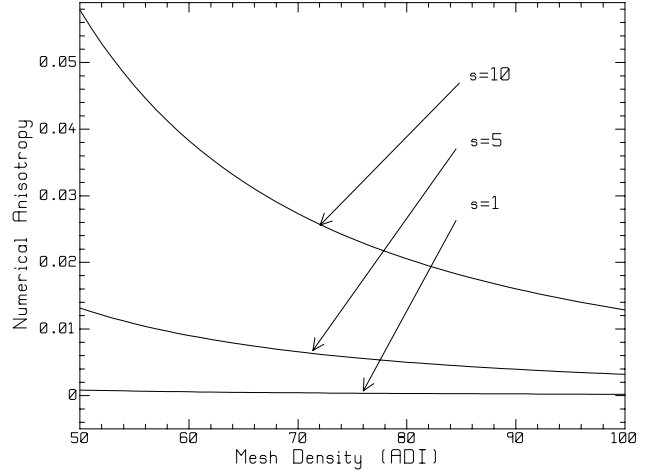


Fig. 2 Numerical anisotropy of the ADI method at Courant numbers 1, 5 and 10.

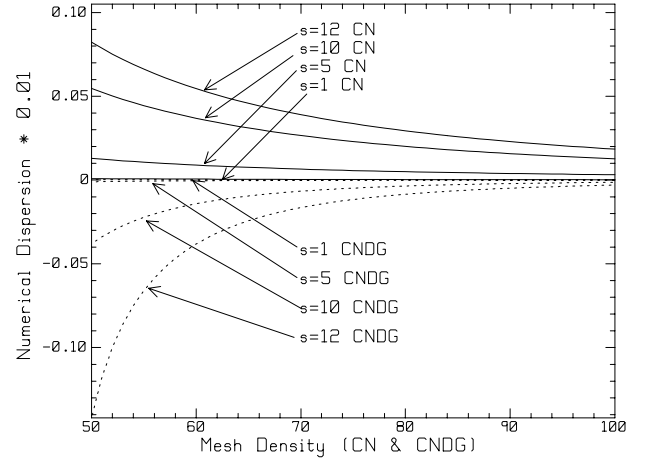


Fig. 3 Numerical anisotropy for CN and CNDG.

Notice that the anisotropy changes its sign for CNDG at certain combinations of the mesh density and Courant number. This suggests that at certain Courant numbers, a mesh may have no anisotropy. Fig. 4 shows the relation between the Courant number and mesh density with zero anisotropy. Note that neither ADI nor CN has this behavior.

V. Time Step Size Limitations

In the numerical dispersion relation of Eqn. (5), if the tangent is infinite, the phase constant becomes complex for all the three methods. This limit is reached when

$$\Delta t = \frac{1}{2f} \quad (8)$$

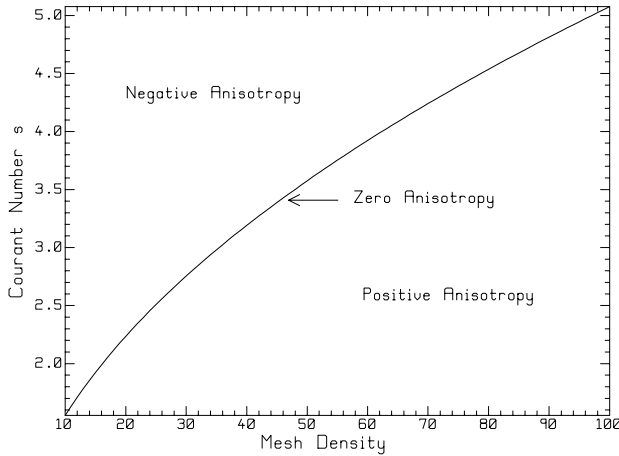


Fig. 4 The relation of the Courant number and mesh density at zero anisotropy for CNDG.

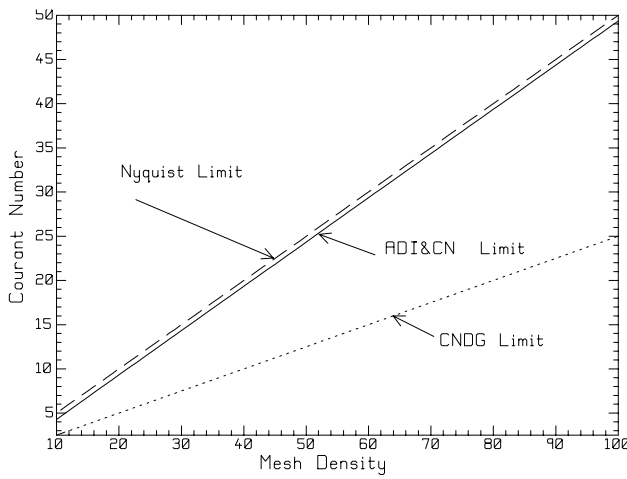


Fig. 5 Time step size limits with respect to mesh density for the three methods.

Eqn. (8) is recognized as the Nyquist limit for the time sampling. For a given mesh density N , the Nyquist limit can be written in relation to the Courant number as

$$s = \frac{N}{2} \quad (9)$$

However, Eqn. (5) implies a smaller time step size limit than the Nyquist limit. For example, along the x -axis, $\sin(\beta\Delta x/2)$ must be smaller than or equal to one if β is to be real. For the ADI and CN methods, the minimum velocity always occurs along the axes, so the limiting Courant number for a give mesh density can be found from Eqn. (5) to satisfy $\tan(\pi s/N) = s$. For the CNDG method, at larger Courant numbers, the minimum velocity is along the diagonals. For $\Delta x = \Delta y$, Eqn. (5) for the CNDG method leads to

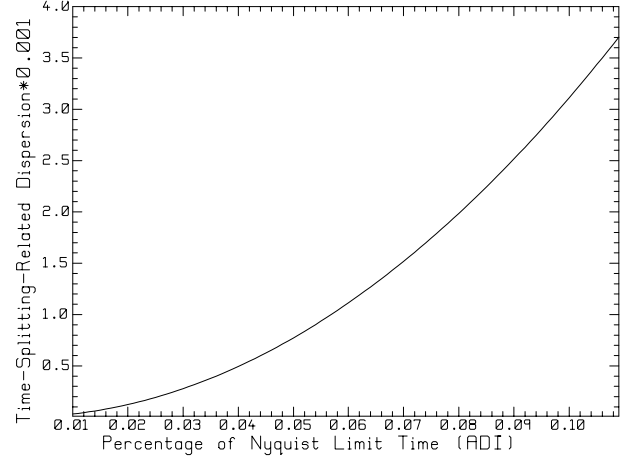


Fig. 6 Intrinsic temporal anisotropy with zero mesh size for ADI.

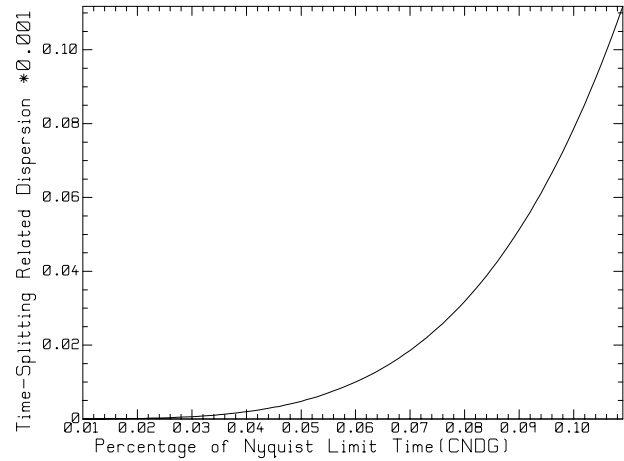


Fig. 7 Intrinsic temporal anisotropy with zero mesh size for CNDG.

$$\sin^2(\sqrt{2}\beta_{45^\circ}\Delta x/4) = \frac{1 + \sqrt{1 - \tan^4(\omega\Delta t/2)}}{(s \tan(\omega\Delta t/2))^2} \quad (10)$$

where β_{45° is the phase constant along the diagonals. If $\tan(\omega\Delta t/2) > 1$, then the phase constant β becomes a complex number. Thus $\tan(\omega\Delta t/2) = 1$ is the limit for the CNDG method. This corresponds to $s = N/4$. The three curves shown in Fig. 5 are the Nyquist limit, and the step size limits for the ADI and CN methods and for the CNDG method. If a method uses a Courant number larger than its limit shown in Fig. 5, numerical attenuation will occur, which does not correspond to the physical reality.

VI. Intrinsic Temporal Dispersion

In Yee's FDTD, as the mesh density increases, the numerical dispersion decreases. In the limit of an

infinitely-fine mesh, that is, zero spatial mesh size, there is no numerical dispersion because the Courant limit forces the time step size to be zero. Hence, Yee's method collapses to the continuous case, that is, no discretization for time and space. But for the unconditionally-stable implicit methods, because there is no Courant limit, fine mesh size can be accompanied by very large time step size and the method remains stable. Even in the limit of zero spatial mesh size, the methods are still stable for any time step size, but there is numerical dispersion. The numerical dispersion at zero mesh size is an intrinsic limitation and may be termed "intrinsic temporal dispersion", previously called "time-splitting-related dispersion" [11]. The intrinsic temporal dispersion is different for the three methods. With some manipulation, it can be written as

$$\frac{u}{c} = \frac{\omega\Delta t / 2}{\tan(\omega\Delta t / 2)} \sqrt{\frac{1 + \sqrt{1 + g(\tan(\omega\Delta t / 2) \sin 2\phi)^2}}{2}} \quad (11)$$

Numerical calculations using Eqn. (11) show that the intrinsic temporal dispersion as a function of the direction of travel is similar to that shown in Fig. 1 but smaller in magnitude. From Eqn. (11) it can be seen that the relative velocity is not a function of direction of travel for the CN method. Therefore CN's anisotropy is zero at the zero mesh size limit. But for ADI and CNDG, there is anisotropy, as shown in Fig. 6 and Fig. 7. This anisotropy is termed the "intrinsic temporal anisotropy." Note that the ADI's anisotropy is about 30 times larger than that of CNDG at the time step size of one-tenth Nyquist time step size limit.

Note that in Eqn. (11) the tangent cannot be larger than unity for CNDG method; otherwise the velocity will be a complex number. This time step size limit corresponds to

$$\Delta t \Big|_{CNDG} = \frac{1}{2} \frac{1}{2f} \quad (12)$$

This is half of the Nyquist limit, and coincides with that in Section V for the time step size limit of the CNDG method. For non-zero mesh size, the numerical velocity is always smaller than the intrinsic temporal dispersion, therefore Eqn. (11) is a fundamental accuracy limit for the three methods.

VII. Conclusion

This paper has discussed several aspects of the ADI, CN and CNDG methods. The magnitude of the overall amplification factor for all three methods is unity; hence they are all unconditionally stable. The numerical dispersion is the same along the axes for the three methods, but differs along the diagonals. The anisotropy in the ADI

method is two orders-of-magnitude larger than that of CN and CNDG. In the limit of zero mesh size, ADI and CNDG have anisotropy but the CN method does not. Different from the ADI and CN methods, the CNDG method may have slower velocity along the diagonals than along the axes, and may have zero anisotropy at certain combinations of Courant number and mesh density. The three methods have time step size limits that are smaller than the Nyquist criterion. CNDG has the smallest time step limit. The intrinsic temporal dispersion is a fundamental accuracy limit for the three methods and is much larger for ADI than for CN or CNDG along the diagonals.

APPENDIX I Update Equations for ADI-FDTD

The ADI-FDTD has two sub-steps. The first sub-step is advancing time from step n to step $n+1/2$ by use of the following update equations [7]

$$\begin{aligned} E_x^{n+1/2}(i+1/2, j) &= E_x^n(i+1/2, j) + a_1 \{ \\ &H_z^n(i+1/2, j+1/2) - H_z^n(i+1/2, j-1/2) \} / \Delta y \end{aligned} \quad (I-1)$$

$$\begin{aligned} E_y^{n+1/2}(i, j+1/2) &= E_y^n(i, j+1/2) - a_1 \{ \\ &H_z^{n+1/2}(i+1/2, j+1/2) - H_z^{n+1/2}(i-1/2, j+1/2) \} / \Delta x \end{aligned} \quad (I-2)$$

$$\begin{aligned} H_z^{n+1/2}(i+1/2, j+1/2) &= H_z^n(i+1/2, j+1/2) + a_2 \{ \\ &E_x^n(i+1/2, j+1) - E_x^n(i+1/2, j) \} / \Delta y \\ &- a_2 \{ E_y^{n+1/2}(i+1, j+1/2) - E_y^{n+1/2}(i, j+1/2) \} / \Delta x \end{aligned} \quad (I-3)$$

where $a_1 = \Delta t / 2\varepsilon$, $a_2 = \Delta t / 2\mu$, Δt is the time step size; ε and μ are the permittivity and permeability of the material respectively; Δx and Δy are the spatial meshing sizes along x and y axes; i and j are the integer-number indices of the computational cells; and n is the time step index. In this step, $E_y^{n+1/2}$ is implicit and can be found by solving a tridiagonal matrix of the form

$$\begin{aligned} E_y^{n+1/2}(i-1, j+1/2) &- \{ (\Delta x^2 / a_1 a_2 + 2) E_y^{n+1/2}(i, j+1/2) \\ &+ E_y^{n+1/2}(i+1, j+1/2) \} = -(\Delta x^2 / a_1 a_2) E_y^n(i, j+1/2) + \\ &(\Delta x / a_2) \{ H_z^n(i+1/2, j+1/2) - H_z^n(i-1/2, j+1/2) \} \\ &+ \Delta x / \Delta y \{ E_x^n(i+1/2, j+1) - E_x^n(i+1/2, j) \} + \\ &E_x^n(i-1/2, j) - E_x^n(i-1/2, j+1) \} \end{aligned} \quad (I-4)$$

The second sub-step advances time step from $n+1/2$ to $n+1$ and the update equations are

$$\begin{aligned} E_x^{n+1}(i+1/2, j) &= E_x^{n+1/2}(i+1/2, j) + a_1 \{ \\ H_z^{n+1}(i+1/2, j+1/2) - H_z^{n+1}(i+1/2, j-1/2) \} / \Delta y \end{aligned} \quad (\text{I-5})$$

$$\begin{aligned} E_y^{n+1}(i, j+1/2) &= E_y^{n+1/2}(i, j+1/2) - a_1 \{ \\ H_z^{n+1/2}(i+1/2, j+1/2) - H_z^{n+1/2}(i-1/2, j+1/2) \} / \Delta x \end{aligned} \quad (\text{I-6})$$

$$\begin{aligned} H_z^{n+1}(i+1/2, j+1/2) &= H_z^{n+1/2}(i+1/2, j+1/2) + a_2 \{ \\ E_x^{n+1}(i+1/2, j+1) - E_x^{n+1}(i+1/2, j) \} / \Delta y \\ - a_2 \{ E_y^{n+1}(i+1, j+1/2) - E_y^{n+1}(i, j+1/2) \} / \Delta x \end{aligned} \quad (\text{I-7})$$

Since E_x^{n+1} is implicit and it is found by solving a tridiagonal matrix of the form

$$\begin{aligned} E_x^{n+1}(i+1/2, j-1) - \{ \Delta y^2 / a_1 a_2 + 2 \} E_x^{n+1}(i+1/2, j) + \\ E_x^{n+1}(i+1/2, j+1) = - \{ \Delta y^2 / a_1 a_2 \} E_x^{n+1/2}(i+1/2, j) + \\ (\Delta y / a_2) \{ H_z^{n+1/2}(i+1/2, j-1/2) - \\ H_z^{n+1/2}(i+1/2, j+1/2) \} \\ + \Delta y / \Delta x \{ E_y^{n+1/2}(i+1, j+1/2) - E_y^{n+1/2}(i, j+1/2) + \\ E_y^{n+1/2}(i+1, j-1/2) - E_y^{n+1/2}(i, j-1/2) \} \end{aligned} \quad (\text{I-8})$$

APPENDIX II Update Equations for CN-FDTD

The CN scheme averages the field components at time step n and $n+1$ to maintain second order accuracy in time as follows [6, 10]

$$\begin{aligned} E_x^{n+1}(i+1/2, j) &= E_x^n(i+1/2, j) + \\ a_1 \{ H_z^{n+1}(i+1/2, j+1/2) - H_z^{n+1}(i+1/2, j-1/2) \} + \\ H_z^n(i+1/2, j+1/2) - H_z^n(i+1/2, j-1/2) \} / \Delta y \end{aligned} \quad (\text{II-1})$$

$$\begin{aligned} E_y^{n+1}(i, j+1/2) &= E_y^n(i, j+1/2) - \\ a_1 \{ H_z^{n+1}(i+1/2, j+1/2) - H_z^{n+1}(i-1/2, j+1/2) \} + \\ H_z^n(i+1/2, j+1/2) - H_z^n(i-1/2, j+1/2) \} / \Delta x \end{aligned} \quad (\text{II-2})$$

$$\begin{aligned} H_z^{n+1}(i+1/2, j+1/2) &= H_z^n(i+1/2, j+1/2) + \\ a_2 \{ E_x^{n+1}(i+1/2, j+1) - E_x^{n+1}(i+1/2, j) + \\ E_x^n(i+1/2, j+1) - E_x^n(i+1/2, j) \} / \Delta y - \\ a_2 \{ E_y^{n+1}(i+1, j+1/2) - E_y^{n+1}(i, j+1/2) + \\ E_y^n(i+1, j+1/2) - E_y^n(i, j+1/2) \} / \Delta x \end{aligned} \quad (\text{II-3})$$

The block tridiagonal matrix to be solved for the CN method is

$$\begin{aligned} H_z^{n+1}(i+1/2, j+1/2) - a_1 a_2 \{ H_z^{n+1}(i+3/2, j+1/2) + \\ H_z^{n+1}(i-1/2, j+1/2) - 2H_z^{n+1}(i+1/2, j+1/2) \} / \Delta x^2 \\ - a_1 a_2 \{ H_z^{n+1}(i+1/2, j+3/2) + H_z^{n+1}(i+1/2, j-1/2) - \\ 2H_z^{n+1}(i+1/2, j+1/2) \} / \Delta y^2 = \\ H_z^n(i+1/2, j+1/2) + a_1 a_2 \{ H_z^n(i+3/2, j+1/2) + \\ H_z^n(i-1/2, j+1/2) - 2H_z^n(i+1/2, j+1/2) \} / \Delta x^2 \\ + a_1 a_2 \{ H_z^n(i+1/2, j+3/2) + H_z^n(i+1/2, j-1/2) - \\ 2H_z^n(i+1/2, j+1/2) \} / \Delta y^2 \\ + 2a_2 \{ [E_x^n(i+1/2, j+1) - E_x^n(i+1/2, j)] / \Delta y - \\ [E_y^n(i+1, j+1/2) - E_y^n(i, j+1/2)] / \Delta x \} \end{aligned} \quad (\text{II-4})$$

APPENDIX III Update Equations for CNDG-FDTD

The update equations of CNDG-FDTD are the same as the CN method. The difference between the CN-FDTD and CNDG-FDTD is the method used to solve the block tridiagonal matrix. In CNDG-FDTD, it is factorized into two sub-steps [10]

$$\begin{aligned} H_z^*(i+1/2, j+1/2) - a_1 a_2 \{ H_z^*(i+3/2, j+1/2) + \\ H_z^*(i-1/2, j+1/2) - 2H_z^*(i+1/2, j+1/2) \} / \Delta x^2 \\ = H_z^n(i+1/2, j+1/2) + a_1 a_2 \{ H_z^n(i+3/2, j+1/2) + \\ H_z^n(i-1/2, j+1/2) - 2H_z^n(i+1/2, j+1/2) \} / \Delta x^2 \\ + a_1 a_2 \{ H_z^n(i+1/2, j+3/2) + H_z^n(i+1/2, j-1/2) - \\ 2H_z^n(i+1/2, j+1/2) \} / \Delta y^2 \\ + 2a_2 \{ [E_x^n(i+1/2, j+1) - E_x^n(i+1/2, j)] / \Delta y - \\ [E_y^n(i+1, j+1/2) - E_y^n(i, j+1/2)] / \Delta x \} \end{aligned} \quad (\text{III-1})$$

$$\begin{aligned} H_z^{n+1}(i+1/2, j+1/2) - a_1 a_2 \{ H_z^{n+1}(i+1/2, j+3/2) + \\ H_z^{n+1}(i+1/2, j-1/2) - 2H_z^{n+1}(i+1/2, j+1/2) \} / \Delta x^2 \\ = H_z^*(i+1/2, j+1/2) \end{aligned} \quad (\text{III-2})$$

At each sub-step a tridiagonal matrix must be solved. It can be seen that the ADI method solves the electric fields implicitly, but the CN and CNDG methods solve the magnetic field implicitly in the 2D TE_z case.

REFERENCES

- [1] K.S., Yee, "Numerical solution of initial boundary value problems involving Maxwell's equations in isotropic media," IEEE Trans. Antennas and Propagation, Vol.14, May, 1966, pp. 302-307.

- [2] A., Taflov, and S.C., Hagness, *Computational electrodynamics—the finite-difference time-domain method*, 2nd ed., Artech House, Boston, 2000.
- [3] J. Stoer, R. Bulirsch, “Introduction to numerical analysis,” 3rd ed, Translated by R. Bartels, W. Gautschi and C. Witzgall, Springer-Verlag, New York, 2002.
- [4] R. Holland, “Implicit three-dimensional finite differencing of Maxwell’s equations for computational electromagnetism,” IEEE Trans. Nucl. Sci., Vol. NS-31, 1984, pp. 1322-1326.
- [5] J. S. Shang, “A fractional-step method for solving 3D, time-domain Maxwell Equations,” J. of. Comput. Phys., Vol. 118, 1195, pp. 109-119.
- [6] A. Fijany, M. A. Jensen, Y. Rahmat-Samii and J. Barhen, “A massively parallel computation strategy for FDTD: time and space parallelism applied to electromagnetics problems,” IEEE Trans. Antenna and Propagation, Vol. 43, Dec., 1995, pp. 1441-1449.
- [7] T. Namiki, “A new FDTD algorithm based on alternating-direction implicit method,” IEEE Trans. Microwave Theory Tech., Vol. 47, Oct., 1999, pp. 2003-2007.
- [8] F. Zhen, Z. Chen and J. Zhang, “Toward the development of a three-dimensional unconditionally stable finite-difference time-domain method,” IEEE Trans. Microwave Theory Tech., Vol. 48, Sept., 2000, pp. 1550-1558.
- [9] J.H. Beggs and W. R. Briley, “An implicit characteristic based method for electromagnetics,” NASA/TM-2001-210862, May, 2001
- [10] G. Sun and C.W. Trueman, “Unconditionally stable Crank-Nicolson scheme for solving the two-dimensional Maxwell’s Equations,” IEE Electronics Lett., Vol. 39, April, 2003, pp. 595-597.
- [11] G. Sun, C. W. Trueman, “Analysis and Numerical Experiments on the Numerical Dispersion of Two-Dimensional ADI-FDTD”, IEEE Antennas and Wireless Propaga. Letters, to be published.
- [12] J. C. Tannehill, D. A. Anderson, R.H. Pletcher, “*Computational fluid mechanics and heat transfer*,” 2nd Ed., Taylor&Francis, Washington, DC, 1997.
- [13] Y. Liu, “Fourier analysis of numerical algorithms for the Maxwell’s Equations,” J. Comput. Phys., Vol. 124, March, 1996, pp. 396-416.



Guilin Sun was born in China in 1962, and received his B.Sc. degree from the Xi’an Institute of Technology in 1982 and his M.Sc. degree from the Beijing Institute of Technology in 1988, respectively, both in optical engineering. From 1988 to 1994 he was an assistant professor at the

Xi’an Institute of Technology. From 1994 to 2000 he was an associate professor at the Beijing Institute of Machinery.

In 1998-1999 he was a research associate at the University of Southern California, Los Angeles, working on the characterization of E/O polymers used in photonic devices. Currently he is a PhD candidate at Concordia University, Montreal, Canada.

Mr. Sun has published about 70 journal and conference papers in optical engineering and 5 papers on FDTD methods. He has won several awards and honorable titles and his name appears in Marquis “Who’s Who in the World”, 16th Edition, 1999, New Providence, NJ. Currently his interest is in computational electromagnetics, particularly in new methods of the finite-difference time-domain method in microwave and optical frequencies .



Christopher W. Trueman is a Professor in Electrical and Computer Concordia University, Montreal, Canada. He received the Ph.D. degree from McGill University in 1979 with a thesis on wire-grid modeling aircraft and their HF antennas. His research in Computational Electromagnetics

uses moment methods, the finite difference time domain method, and geometrical optics and diffraction. He has worked on EMC problems with standard broadcast antennas and high-voltage power lines, on the radiation patterns of aircraft and ship antennas, on EMC problems among the many antennas carried by aircraft, and on the calculation of the RCS of aircraft and ships. He has studied the near and far fields of cellular telephones operating near the head and hand. Recently he has been concerned indoor propagation of R.F. signals and EMI with medical equipment in hospital environments.

Accelerating Computations with a MoM-Based Computer Program using a Model-Based Parameter Estimation Algorithm

Markus Schick and Friedrich M. Landstorfer
Institut fuer Hochfrequenztechnik, Universitaet Stuttgart,
Pfaffenwaldring 47,
70550 Stuttgart, Germany
Email: schick@ihf.uni-stuttgart.de

Abstract

Electromagnetic research often requires studies within wider frequency ranges. For achieving a fine resolution in the frequency domain, the required computation time is usually high. Here the MoM-based field computation program FEKO working in frequency domain is used for this purpose. In order to reduce the computational costs by minimizing the number of sampling points used, the interpolation algorithm MPBE (Model Based Parameter Estimation) is applied to achieve a mathematically based approximation of the problem. This paper presents the acceleration of computations with FEKO using the interpolation algorithm MBPE. A short introduction to FEKO is given at the beginning. Subsequently the implementation of MBPE as well as three possible adaptive strategies for further shortening the computation time is presented. Finally examples are given that show the advantages of this implemented method.

Introduction

Research in the field of electromagnetic compatibility often requires studies over large frequency ranges. Since the scenarios to be modeled are very complex (e.g. in medical areas) and also the computation time needed for these kinds of investigations is usually very high a new approach has to be developed to fulfill all these requirements. In this paper the MoM-based field computation program FEKO is ac-

celerated using the MBPE algorithm, which is presented in the following.

The Field Computation Program FEKO

FEKO [1], [2] is a field computation program considering objects of arbitrary shape. It is based on a full wave solution of Maxwell's equations in the frequency domain. The accurate Method of Moments (MoM) formulation is used to solve for the unknown surface currents. Asymptotic techniques, Physical Optics (PO) and Uniform Theory of Diffraction (UTD) have been hybridized with the MoM in order to solve electrically large problems. The MoM has also been extended to solve problems involving multiple homogeneous dielectric bodies, thin dielectric sheets and dielectric coated wires. An approach is necessary to speed up computations over large frequency ranges. Therefore, the acceleration of FEKO with the interpolation algorithm MBPE is described in the following.

Model Based Parameter Estimation (MBPE)

In order to reduce the computational costs by minimizing the number of sampling points used, the interpolation algorithm MPBE [3], [4], [5], [6] is applied to achieve a mathematically based approximation of the problems. A function sampled in the frequency domain is approximated with MBPE to represent the original function by a reduced-order physically based approximation called a fitting model.

The application of such a fitting model means interpolating between samples to reduce the amount of data needed. First frequency f is normalized with respect to the center frequency f_c and the width of the frequency interval f_w .

$$x = \frac{f - f_c}{f_w} \quad (1)$$

Now the fitting models are described by a pole series based on the Padé approximation with rational polynomials

$$F(f) = \frac{N(f)}{D(f)} = \frac{\sum_{v=0}^n N_v f^v}{\sum_{v=0}^d D_v f^v} \quad (2)$$

with n is order of the numerator and d is order of the denominator. Basically there are three possibilities for determining parameters for fitting models, either from samples of the process to be modeled, alternatively from samples of the derivatives of the process, or from a combination of both. Since the field computation program FEKO is used here and the computational cost of derivative sampling of a process would be much higher, only function sampling is used in this paper. With sampling in frequency domain, there is no need for the samples (f_i) to be uniformly spaced as is usually the case in most time domain solutions. That means that the samples can be chosen in such a way that the yield of information for each sample is a maximum. Equation (2) leads to

$$D(f_i) \cdot F(f_i) = N(f_i), \quad i = 0, \dots, D-1 \quad (3a)$$

$$\text{where } D(f_i) = D_0 + D_1 f_i + D_2 f_i^2 + \dots + D_d f_i^d \quad (3b)$$

$$\text{and } N(f_i) = N_0 + N_1 f_i + N_2 f_i^2 + \dots + N_n f_i^n \quad (3c)$$

There are $D = d + n + 2$ unknown coefficients in the two polynomials $D(f_i)$ and $N(f_i)$. An additional condition or constraint is needed and

so $D_d = 1$ is chosen (linear predictor constraint). With now determining the $D = d + n + 1$ unknown coefficients $N_0, N_1, N_2 + \dots + N_n, D_0, D_1, D_2 + \dots + D_{d-1}$ of this equation system a function to represent the original values can be found. Now the complete frequency range is divided into different windows and for every window an equation system according to (3) is solved. In the end all fitting models are combined to give the overall solution function for the entire frequency range.

A first example (IEEE German EMC chapter: benchmark problem no. 3) for the functionality of the algorithms is given with a monopole antenna on an infinite ground plane and a nearby wire loop (see figure 1). The exciting frequency of the antenna is varied in the range from $f = 1$ MHz to 30 MHz. The resulting complex current induced in the wire loop is shown in figure 2.

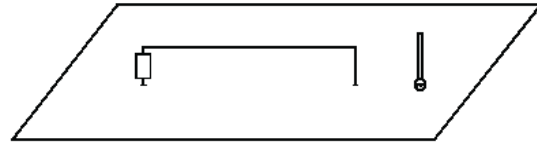


Fig. 1. Geometry in principle for the benchmark problem no. 3 defined by the German IEEE/EMC chapter.

If 30 equidistant sample points (i.e. sampling every 1 MHz) are linearly interpolated the curve shown in figure 2a results. In this case resonant peaks are cut off. An exact result can be achieved using uniformly and closely sampled points (in this case 581 samples, i.e. sampling every 50 kHz) as shown in figure 2b. The same curve results with using the 30 sample points and interpolating with MBPE (see figure 2c).

Overlapping fitting models always containing $N_N + N_D + 1 = 7$ sample points were used to approximate this problem. The orders of the polynomials for every fitting model were chosen $N_N = N_D = 3$. The first seven sample points

were used for determining the coefficients of the first model representing the first part of the solution. For the second fitting model samples 2 to 8 are used to compute its model coefficients and so on. In the end all fitting models were set together to achieve the overall solution with only 30 sample points. The computation time rises linearly with the number of sample points used in total, so in this case the overall computation was accelerated with using the MBPE algorithm by an acceleration factor of $\frac{581}{30} = 19.4$.

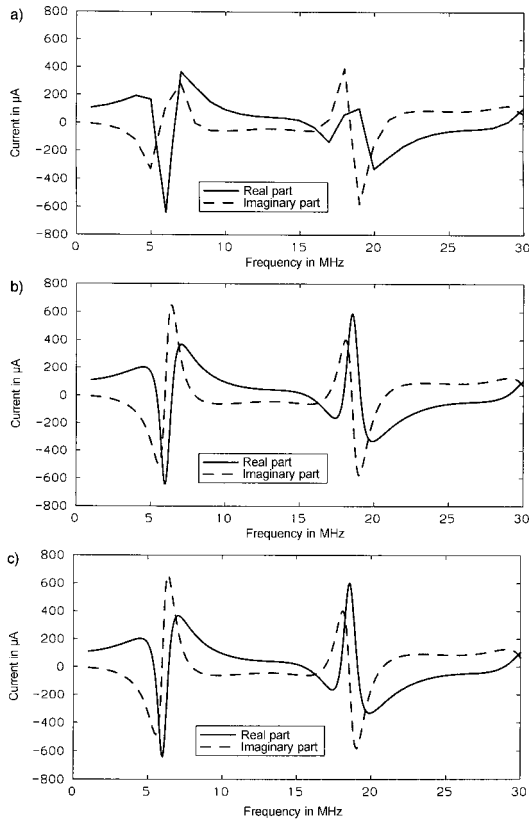


Fig. 2. Complex current induced in a wire loop.

Adaptive Sampling

With “adaptive sampling” a more flexible algorithm is applied to further minimize the number of required sample points by exploiting the fact

that in the frequency domain no uniformly spaced samples are required. The computation is started with a small set of sampling points and with these a set of overlapping windows is determined. The whole frequency range is covered by overlapping windows so that a maximum error between two fitting models

$$E_{i,j}(f_k) = \frac{|W_i(f_k) - W_j(f_k)|}{|W_i(f_k) + W_j(f_k)|} \quad (4)$$

can be determined for every frequency. Where the error is a maximum, a new sample point will be added. If a window is containing too much sample points, it will be split up into two. The algorithm is terminated when the error falls under a certain threshold.

The second adaptive sampling approach implemented is using a strategy based on Romberg’s method. The procedure starts with an interval containing five uniformly spaced samples. With these samples three trapezoidal values are computed (with samples 1,3,5; 1,2,3 and 3,4,5) and an error estimation between these values indicates whether a new sample is required in this interval. If that is the case, two new subintervals are formed from each half of the original interval and Romberg’s method is applied to both of them. If new samples are required in either of these subintervals, new sample points are added where indicated. This process is repeated until the error falls under a chosen threshold.

The third approach to reduce the number of sampling points needed is a Genetic Algorithm (GA) to find the orders of the numerator and the denominator for a fitting model representing the whole frequency range. It is started with a very simple model with low order (e.g. $N_N + N_D + 1 = 4$). There are now various possibilities for the orders of the numerator and the denominator ($N_N = 0; N_D = 3$ / $N_N = 1; N_D = 2$ / ...). If the three best models of this generation are not sufficient in representing the final result, a new sample point is added and a new set

of models (with $N_N + N_D + 1 = 5$) will be determined. In this way the number of sampling points is consequently increased during the steps of the approximation process until the error between the three best models falls under a given threshold.

Results

All three adaptive strategies are now used to achieve an accurate result with less sample points. For the benchmark problem described above the three strategies lead to the following results. The first adaptive approach needed 24 samples and achieved an accuracy of 0.01 while using four overlapping windows (window orders: $N_{N0} = 4; N_{D0} = 3$ / $N_{N1} = 5; N_{D1} = 5$ / $N_{N2} = 8; N_{D2} = 8$ and $N_{N3} = 7; N_{D3} = 6$ arranged in such a way, that always two windows are overlapping). With the second approach at first 33 samples were computed according to Romberg's method and then windows with 13 samples per window ($N_N = 6; N_D = 6$) always overlapping from sample 10 to 13 are used to get the overall function. Finally an accuracy of $6.5 \cdot 10^{-5}$ is achieved. With using the Genetic Algorithm 30 samples were computed and the achieved accuracy is $5 \cdot 10^{-3}$. The resulting three best approximation functions have the orders $N_{N0} = 14; N_{D0} = 15$ / $N_{N1} = 15; N_{D1} = 14$ and $N_{N3} = 13; N_{D3} = 16$.

In the next example [7] there is a small wire loop in a cube shaped metallic housing radiating an electromagnetic field (see figure 3). The shielding effectiveness (the electrical field radiated through the housing's front plate with four small slots in it compared to the electrical field without front plate) is shown in figure 4. Here only 84 samples were used and interpolated with MBPE (GA approach) compared to 901 for a closely and uniformly sampled function. Therefore five windows were computed (100 MHz - 309 MHz: $N_{N0} = 7; N_{D0} = 6$, 309 MHz - 418 MHz: $N_{N1} = 3; N_{D1} = 3$, 418 MHz - 550 MHz: $N_{N2} = 10; N_{D2} = 13$,

550 MHz - 760 MHz: $N_{N3} = 12; N_{D3} = 9$ 760 MHz - 1000 MHz, $N_{N4} = 12; N_{D4} = 8$) to achieve the overall solution function. There is almost no difference between the two functions (the maximum error over the whole frequency range in this case is 10^{-4}) and the factor in time saving (acceleration factor) is $901/84 = 10.7$.

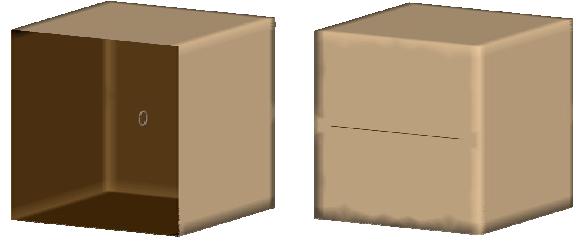


Fig. 3. Housing (without (left) and with (right) front plate) containing a small wire loop radiating an electromagnetic field.

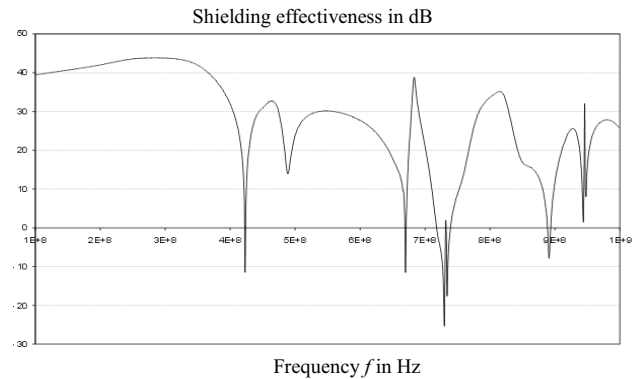


Fig. 4 Shielding effectiveness of the housing in dB.

One other examples containing also very sharp peaks is a simple dipole forked at both ends excited by an incoming plane wave. The resulting magnitude of the input impedance at its ports is depicted over frequency in figure 5. Here only 11 sample points (also shown in the figure) were necessary to interpolate this curve with an accuracy of $5.5 \cdot 10^{-5}$ compared to 1500 uniformly and closely sampled points. This means an acceleration factor of $1000/11=90.9$. One window is used to approximate the curve

with the orders $N_D = 6$ and $N_N = 4$. With a little lower accuracy this curve could be interpolated with only 10 points, which results in an acceleration factor of 100.

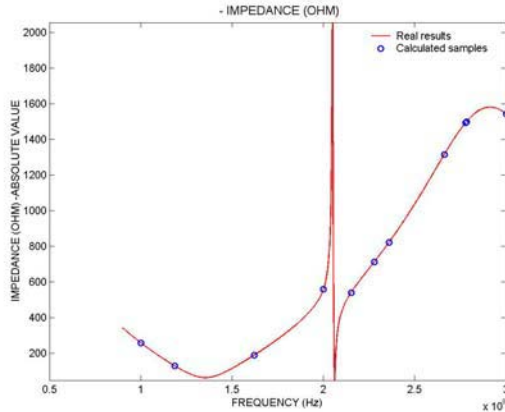


Fig. 5 Input impedance of a forked dipole antenna excited by an incoming plane wave.

Finally it can be said, that with this new approach the computation time has been much reduced and therewith parameter studies and optimizations for larger problems needing a lot of single computations can be done now with the help of this method in an acceptable time.

Conclusions

The successful implementation of Model Based Parameter Estimation and coupling with the field computation program FEKO is presented here. Adaptive sampling for speeding up computations is also described. The implemented algorithm converges and shows good accuracy in first examples, which underline the advantages of the algorithm.

Acknowledgement

The work for the paper was carried out within the scope of a project of the ‘Sonderforschungsbereich EMV’ of the ‘Deutsche Forschungsgemeinschaft (DFG)’. The authors

would like to thank the DFG for supporting their work.

References

- [1] EM Software & Systems, “FEKO User’s Manual, Suite 3.2.1”, March 2002, www.feko.co.za.
- [2] U. Jakobus, “Erweiterte Momentenmethode zur Behandlung kompliziert aufgebauter und elektrische großer elektromagnetischer Streuprobleme“, Nr. 171 in Fortschrittsberichte, Reihe 21, VDI Verlag, Düsseldorf, 1995. Dissertationsschrift.
- [3] E. K. Miller, “Model-Based Parameter Estimation in Electromagnetics: Part I. Background and Theoretical Development”, *IEEE Transactions on Antennas and Propagation*, vol. 40, no. 1, pp. 42–52, Feb. 1998.
- [4] E. K. Miller, “Model-Based Parameter Estimation in Electromagnetics: Part II. Application To EM Observables”, *IEEE Transactions on Antennas and Propagation*, vol. 40, no. 2, pp. 51–65, Apr. 1998.
- [5] E. K. Miller, “Model-Based Parameter Estimation in Electromagnetics: Part III. Applications to EM Integral Equation”, *IEEE Transactions on Antennas and Propagation*, vol. 40, no. 3, pp. 49–66, Jun. 1998.
- [6] E. K. Miller and T. K. Sarkar, “An Introduction to Model-Based Parameter Estimation in Electromagnetics”, *In Review of Radio Science 1996–1999*, International Union of Radio Science. Oxford University Press, Toronto, pp. 139–174, 1999.
- [7] F. Olysager, E. Laermans, D. De Zutter, S. Criel, R. De Smedt, N. Lietaert and A. De Clercq, “Numerical and Experimental Study of the Shielding Effectiveness of a Metallic Enclosure”, *IEEE Transactions on Electromagnetic Compatibility*, vol. 41, no. 3, pp. 202–213, Aug. 1999.



Markus Schick was born in Düsseldorf, Germany in 1973. He received the Dipl.-Ing. degree in electrical engineering from the Universität Stuttgart, Germany, in 1998.

He is now a staff member of the Institut für Hochfrequenztechnik of the Universität Stuttgart, Germany. His main interest is in solving electromagnetic problems with the Method of Moments and hybrid methods, accelerating computations over large frequency ranges as well as dealing with electromagnetic compatibility problems especially in medical areas.



Friedrich M. Landstorfer (SM'79–F'95) was born in Munich, Germany, in 1940. He received the Dipl.-Ing. and the Dr. Ing. degrees in electrical engineering from the Technical University of Munich, Germany, in 1964 and 1967, respectively.

In 1971, he became a Lecturer and in 1976 he became a Professor at the Technical University of Munich, Germany. In 1986 he moved to Stuttgart to become Professor and head of the RF-institute at the University of Stuttgart, Germany. His research interests include antennas, microwaves, electromagnetic theory, wave propagation in connection with mobile communication, navigation, and electromagnetic compatibility.

Dr. Landstorfer received the award of the NTG (Nachrichtentechnische Gesellschaft im VDE, now ITG) for the optimization of wire antennas in 1977 and was Chairman of the 21st European Microwave Conference in Stuttgart, Germany, in 1991. For eight years he headed the antenna group of the NTG/ITG and has been a member of URSI. He was awarded Honorary Professor of Jiaotong University in Chengdu, China, in 1993.

Performance of Preconditioned Krylov Iterative Methods for Solving Hybrid Integral Equations in Electromagnetics *

Jeonghwa Lee^{1†}, Jun Zhang^{1‡}, and Cai-Cheng Lu^{2§}

¹Laboratory for High Performance Scientific Computing and Computer Simulation, Department of Computer Science, University of Kentucky, Lexington, KY 40506-0046, USA

² Department of Electrical and Computer Engineering, University of Kentucky, Lexington, KY 40506-0046, USA

Abstract

In solving systems of linear equations arising from practical engineering models such as the electromagnetic wave scattering problems, it is critical to choose a fast and robust solver. Due to the large scale of those problems, preconditioned Krylov iterative methods are most suitable. The Krylov iterative methods require the computation of matrix-vector product operations at each iteration, which account for the major computational cost of this class of methods. We use the multilevel fast multipole algorithm (MLFMA) to reduce the computational complexity of the matrix-vector product operations. We conduct an experimental study on the behavior of three Krylov iterative methods, BiCG, BiCGSTAB, and TFQMR, and of two preconditioners, the ILUT preconditioner, and the sparse approximate inverse (SAI) preconditioner. The preconditioners are constructed by using the near part matrix numerically generated in the MLFMA. Our experimental results indicate that a well chosen preconditioned Krylov iterative method maintains the computational complexity of the MLFMA and effectively

reduces the overall simulation time.

1 Introduction

The hybrid integral equation approach combines the volume integral equation and the surface integral equation to model the scattering and radiation by mixed dielectric and conducting structures [12]. For example, when a radome is applied to an antenna, the combined system consists of both dielectrics and conductors. Hence, the hybrid surface-volume integral equation is ideal for this problem [3]. The volume integral equation is applied to the material region (V) and the surface integral equation is enforced over the conducting surface (S). The hybrid surface-volume integral equations for electromagnetic scattering problems can be formally written as follows,

$$\begin{aligned} \{L_S(r, r') \cdot J_S(r') + L_V(r, r') \cdot J_V(r')\}_{\tan} \\ = -E_{\tan}^{\text{inc}}(r), \quad r \in S, \\ -E + L_S(r, r') \cdot J_S(r') + L_V(r, r') \cdot J_V(r') \\ = -E^{\text{inc}}(r), \quad r \in V, \end{aligned}$$

where E^{inc} stands for the excitation field produced by an instant radar, the subscript “tan” stands for taking the tangent component from the vector it applies to, and L_Ω , ($\Omega = S, V$), is an integral operator that maps the source J_Ω to electric field $E(r)$ and it is defined as

$$L_\Omega(r, r') \cdot J_\Omega(r') =$$

*This research work was supported in part by NSF under grants CCR-9902022, CCR-9988165, CCR-0092532, ACI-0202934, and ECS-0093692, by DOE under grant DE-FG02-02ER45961, by ONR under grant N00014-00-1-0605, by RIST (Japan), and by the University of Kentucky Research Committee.

[†]leejh@engr.uky.edu, <http://www.csr.uky.edu/~leejh>.

[‡]jzhang@cs.uky.edu, <http://www.cs.uky.edu/~jzhang>.

[§]cclu@engr.uky.edu, <http://www.engr.uky.edu/~cclu>.

$$i\omega\mu_b \int_{\Omega'} (I + k_b^{-2}\nabla\nabla) G(r, r') \cdot J_{\Omega}(r') d\Omega'.$$

Here $G(r, r') = e^{ik_b|r-r'|}/(4\pi|r-r'|)$ is the 3D scalar Green's function for the background media, and $i = \sqrt{-1}$. It should be pointed out that E is related to J_V in the above integral equations by $J_V = i\omega(\epsilon_b - \epsilon)E$.

We follow the general steps of the method of moments (MoM) [17] to discretize the hybrid surface-volume integral equations, and solve the resultant matrix equation by a multilevel fast multipole algorithm (MLFMA), which is a multilevel implementation of the fast multipole method (FMM). A matrix equation is given as the form

$$\begin{bmatrix} Z^{SS} & Z^{SV} \\ Z^{VS} & Z^{VV} \end{bmatrix} \cdot \begin{bmatrix} a^S \\ a^V \end{bmatrix} = \begin{bmatrix} U^S \\ U^V \end{bmatrix}, \quad (1)$$

where a^S and a^V stand for the vectors of the expansion coefficients for the surface current and the volume function, respectively [3, 12], and the matrix elements can be generally written as

$$Z_{jl} = i\omega\mu_b \int_{\Omega} d\Omega f_j^{\Omega}(r) \cdot \int_{\Omega'} d\Omega' (I + k_b^{-2}\nabla\nabla) G(r, r') \cdot \chi(r') f_l^{\Omega'}.$$

The material function $\chi(r') = 1$ if Ω' is a surface patch, and $\chi = (\epsilon/\epsilon_b - 1)$ if Ω' is a volume cell. It can be seen that the coefficient matrix arising from discretized hybrid integral equations is nonsymmetric. Once the matrix equation (1) is solved by numerical matrix equation solvers, the expansion coefficients a^S and a^V can be used to calculate the scattered field and radar cross section. In antenna analysis problems the coefficients can be used to retrieve the antenna's input impedance and calculate the antenna's radiation pattern. In the following, we use A to denote the coefficient matrix in Equation (1), $x = [a^S, a^V]^T$, and $b = [U^S, U^V]^T$ for simplicity.

The basic idea of the FMM is to convert the interaction of element-to-element to the interaction of group-to-group. Using the addition theorem for the free-space scalar Green's function, the matrix-vector product Ax can be written as

$$Ax = (A_D + A_N)x + V_f \Lambda V_s x,$$

where V_f , Λ , and V_s are sparse matrices. We denote $B_N = (A_D + A_N)$ for simplicity. The FMM

speeds up the matrix-vector product operations and reduces the computational complexity of a matrix-vector product from $O(N^2)$ to $O(N^{1.5})$, where N is the order of the matrix [4]. The computational complexity is further reduced to $O(N \log N)$ with the multilevel fast multipole algorithm (MLFMA) [3]. As the level of the MLFMA decreases, we find that the number of nonzeros in the near part matrix B_N increases significantly. The accuracy of the computed solution is strongly related to the number of levels of the MLFMA [11]. That is, as the number of the MLFMA levels decreases, the computed solution is close to the exact solution, but the near part matrix B_N becomes denser. It is well-known that the MLFMA is an approximation method.

A matrix problem involving N unknowns may be solved in $CN^{\text{iter}}N^{Ax}$ floating point operations, where C is a constant depending on the implementation of a particular iterative method [2, 4, 5, 15], and N^{Ax} is the floating point operations needed for each matrix-vector multiplication. For many realistic problems, N^{iter} depends on both the iterative solver and the target properties (shape and material). For example, a problem with an open-ended cavity needs much more iterations than that with a solid conducting box of the same size. Since N^{iter} is a proportional factor in the CPU counter, to further reduce the total CPU time, it is necessary to reduce the number of iterations of the iterative solvers. Hence preconditioning techniques, which may speed up the convergence rate of the Krylov iterative methods, are needed in this application.

We iteratively solve the linear system of the form $Ax = b$, where the coefficient matrix A is a large scale, dense, and complex valued matrix for electrically large targets. The biconjugate gradient (BiCG) method [9], the biconjugate gradient stabilized method (BiCGSTAB) [16], and the transpose-free variant of the quasi-minimum residual method (TFQMR) [6] are some of the well-known Krylov iterative methods which are applicable to non-Hermitian matrices. In our experimental tests, we use these three methods as the iterative solver, coupled with different preconditioning strategies to solve a few study cases of representative electromagnetic scattering problems. We propose to use an incomplete lower-upper

(ILU) triangular factorization with a dual dropping strategy [11, 14] and a sparse approximate inverse (SAI) technique [8, 10, 19] to construct a preconditioner from the near part matrix (B_N) in the MLFMA implementation. We mainly compare the performance difference of different Krylov iterative methods combined with different preconditioners.

2 Preconditioned Krylov Iterative Methods

Krylov iterative methods are considered to be the most effective iterative solution methods currently available [1, 7, 15]. The complexity of these methods is on the order of $O(N^{\text{iter}}N^2)$ if the convergence is achieved in N^{iter} iterations. The Krylov iterative methods such as BiCG require the computation of some matrix-vector product operations at each iteration, which account for the major computational cost of this class of methods.

In our experiments, we observe that the convergence behavior of BiCG is irregular. Few theoretical results are known about the convergence of BiCG [2]. BiCG requires two matrix-vector products (one with A and one with A^H , the complex conjugate transpose of A) at each step of iteration. BiCGSTAB is one of variant of BiCG to avoid the irregular convergence patterns of BiCG. A residual vector is minimized locally and it has substantially smoother convergence behavior. Each iteration step of BiCGSTAB also requires two matrix-vector products (both with A). TFQMR is also chosen to get a smoother convergence behavior. TFQMR requires two matrix-vector products (both with A) at each iteration. All of three solvers designed to solve non-Hermitian linear systems. Every related algorithm which is implemented in our program originally comes from [2, 6, 15].

The convergence behavior of the Krylov methods depends on the distribution of the eigenvalues and on the condition number of the coefficient matrix. By applying a good preconditioner we may achieve better spectrum and smaller condition number compared to those of the original coefficient matrix. Therefore, the convergence behavior of the Krylov iterative method can be improved by a good pre-

conditioner. In our previous papers [10, 11] we show that the ILUT and the SAI preconditioned BiCG method has tight spectrum around 1 and small condition numbers with little extra CPU time to construct the preconditioners and small extra memory to store the preconditioner matrix. For some problems, iterative methods without a preconditioner might not converge. Hence, preconditioning techniques should be used in practical applications with the Krylov iterative method to reduce the number of iterations. Most preconditioning techniques, such as the ILU(0), rely on a fixed sparsity pattern, obtained from the sparsified coefficient matrix by dropping small magnitude entries. Some SAI techniques need access to the full coefficient matrix (to construct a sparsified matrix), which is not available in the FMM.

The purpose of the preconditioning is to make the preconditioned matrix MA as close to the identity matrix I as possible. To this end, we try to construct a matrix M that approximates the matrix A^{-1} . It is difficult to make the matrix M sparse, since in most cases the inverse of a matrix A is dense even if A is sparse. We evaluate three different Krylov iterative methods with two preconditioners, the ILU preconditioner with a dual dropping strategy (ILUT) (with a fill-in parameter p and a drop tolerance τ) [11, 14] and the SAI preconditioner [10, 19], using the non-preconditioning case as comparison. In the MLFMA implementation, the global matrix A is not numerically available, but the near part matrix B_N is. We thus construct the ILUT and the SAI preconditioners with respect to the matrix B_N . The total storage of the ILUT preconditioner is bounded by $2pN$. Here the parameter τ controls the computational cost, and the parameter p controls the memory cost. We use a static sparsity pattern strategy for constructing the SAI preconditioner M . For SAI, we construct a sparsified matrix \tilde{B}_N from the near part matrix B_N . Here the matrix \tilde{B}_N is obtained from B_N by removing some small magnitude entries of B_N with respect to a threshold parameter ϵ_1 . The computational procedure is given in [10], in which ϵ_1 , ϵ_2 , and ϵ_3 are three user provided threshold drop tolerance parameters chosen by a heuristic process. By judiciously choosing those parameters, we are able to construct both preconditioners that are effective and do not use much memory space. We

use the notation of $\text{ILUT}(\tau, p)$ and $\text{SAI}(\epsilon_1, \epsilon_2, \epsilon_3)$ for simplicity, see [10, 11].

3 Numerical Experiments

The major cost of the preconditioned iterative solvers is the matrix-vector product with both the coefficient matrix and the preconditioner [18]. There are two matrix-vector products at each iteration of BiCG, BiCGSTAB, and TFQMR. A number of numerical examples are presented to demonstrate the performance of the preconditioned Krylov iterative methods.¹ Note that the examples are different from the ones in our previous two papers [10, 11] with different incident angles.

We examine the convergence behavior based on the number of preconditioned iterations. We compare three different Krylov iterative methods (BiCG, BiCGSTAB, and TFQMR) with the ILUT preconditioner, the SAI preconditioner, and no preconditioner one and another. The efficiency of the ILU preconditioner with a dual dropping strategy (ILUT) and the SAI preconditioner (with BiCG) is reported in [10, 11]. Since both ILUT and SAI preconditioners have been shown to be efficient for solving the dense complex linear systems from electromagnetic wave scattering problems, we mainly compare the performance difference of three Krylov iterative methods, BiCG, BiCGSTAB, and TFQMR.

We calculate the radar cross section (RCS) to demonstrate the performance of our preconditioned Krylov iterative solvers for different conducting geometries with and without coating. The geometries considered include plates, antenna arrays, and cavities (see Table 1). The mesh sizes for all the test structures are about one tenth of a wavelength.

The test problems are described in Table 1 and some numerical results are listed in Table 2. In Tables 1 and 2, “level” indicates the number of levels in the multilevel fast multipole algorithm, “setup” the setup CPU time in seconds for constructing

a preconditioner, “#it” the number of the (preconditioned) Krylov iterations, and “total” the CPU time in seconds for both the setup and the iteration phase. The notations used for “case” are 0=BiCG, 1=BiCGSTAB, 2=TFQMR, N=NONE, I=ILUT, and S=SAI. Thus, “P3C2S” means that the P3C case is solved by using TFQMR with the SAI preconditioner.

Due to space limit, we report one set of parameters for the ILUT and the SAI preconditioners. In our experiments, we use $\text{ILUT}(10^{-3}, 30)$ for the P1C and P3C cases, $\text{ILUT}(10^{-3}, 130)$ for the C1C case, and $\text{SAI}(0.03, 0.04, 0.05)$ for all test cases.

According to the total CPU time for solving a problem, BiCGSTAB with the SAI and the ILUT preconditioners seems to converge very fast for most cases (see Table 2). Without a preconditioner, the results are various depending on cases. For the problem which has a small number of unknowns (say, less than 1000), the iterative solver with the SAI preconditioner takes more time than with the ILUT preconditioner, mainly due to the higher cost in constructing the SAI preconditioner.

Figures 1 – 3 show the number of iterations of (a) BiCG with three different preconditioners, (b) BiCGSTAB with three different preconditioners, (c) TFQMR with three different preconditioners, (d) NONE-preconditioned three different solvers, (e) ILUT preconditioned three different solvers, and (f) SAI preconditioned three different solvers.

In the P1C case, we observe that all three iterative solvers with the SAI preconditioner converge faster than the other two, and without a preconditioner are the slowest. Without a preconditioner, BiCG is the fastest one and TFQMR is the slowest. With the ILUT preconditioner, BiCGSTAB is the fastest one and BiCG is the slowest. With the SAI preconditioner, BiCGSTAB is the fastest one and the BiCG is the slowest.

In the C1C case, we see that BiCG and BiCGSTAB iterative solvers with the SAI preconditioner converge faster than the other two, and without a preconditioner are the slowest. TFQMR with the ILUT preconditioner is the fastest one and that without preconditioner are the slowest. Without a preconditioner, TFQMR is the fastest one and BiCG is the slowest. With

¹All cases are tested on one processor of an HP Superdome cluster at the University of Kentucky. The processor has 2 GB local memory and runs at 750 MHz. The code is written in Fortran 77 and is run in single precision. The computation terminates when the 2-norm residual is reduced by 10^{-3} , or the number of iterations exceeds 2,000.

Table 1: Information about the matrices used in the experiments (all length units are in λ_0 , the wavelength in free-space).

case	level	unknowns	matrix	nonzeros	target size and description
P1C	4	1,416	A	2,005,056	Dielectric plate over conducting plate $2.98824 \times 2 \times 0.1$ frequency = 200MHz
			A_D	66,384	
			B_N	155,616	
C1C	5	20,176	A	407,070,976	Cavity $3 \times 1 \times 0.5$ frequency = 1GHz
			A_D	1,565,032	
			B_N	3,728,842	
P3C	7	100,800	A	10,160,640,000	Patch array (30×30) Array size: 22.25×22.25 frequency = 300MHz
			A_D	3,571,808	
			B_N	7,211,632	

Table 2: Numerical results with different test cases.

case	setup	#it	total	case	setup	#it	total	case	setup	#it	total
P1C0N		973	112.3	C1C0N		812	1431.1	P3C0N		347	2499.9
P1C1N	-	1044	118.4	C1C1N	-	751	1310.3	P3C1N	-	201	1450.9
P1C2N		2000	225.9	C1C2N		509	893.2	P3C2N		216	1529.1
P1C0I		40	5.4	C1C0I		367	1028.4	P3C0I		37	414.5
P1C1I	0.3	24	3.3	C1C1I	67.5	112	327.6	P3C1I	111.5	12	205.7
P1C2I		30	4.3	C1C2I		179	577.5	P3C2I		20	275.9
P1C0S		29	11.5	C1C0S		322	714.9	P3C0S		41	376.0
P1C1S	8.0	15	9.7	C1C1S	110.9	120	326.2	P3C1S	64.2	17	189.6
P1C2S		17	10.1	C1C2S		199	476.4	P3C2S		26	254.7

the ILUT preconditioner, BiCGSTAB is the fastest one and BiCG is the slowest. With the SAI preconditioner, BiCGSTAB is the fastest one and the BiCG is the slowest.

In the P3C case, we find that all three iterative solvers with the ILUT preconditioner converge faster than the other two, and without a preconditioner are the slowest. With all three different preconditioners, BiCGSTAB is the fastest one and BiCG is the slowest.

Although a general iterative solver for solving some categories of problems efficiently might not exist [13], according to the results from our numerical experiments, we can see that BiCGSTAB with the SAI or the ILUT preconditioners is robust and converges very fast for solving three dimensional model cases from electromagnetic scattering simulations. In all cases, these Krylov iterative methods without a preconditioner are much less efficient.

4 Conclusions

We conducted a few numerical tests to show that the Krylov iterative methods coupled with the

ILUT and the SAI preconditioners are efficient to solve the problems arising from electromagnetic scattering.

Our numerical results indicate that, solving the large non-Hermitian dense linear system arising from the electromagnetic scattering by using the BiCGSTAB method with the ILUT preconditioner and the SAI preconditioner achieves faster convergence in most cases. The ILUT and the SAI preconditioned Krylov iterative solvers (BiCG, BiCGSTAB, and TFQMR) maintain the computational complexity of the MLFMA, and consequently reduces the total CPU time. Our experimental experience may help researchers and engineers choose suitable robust solvers in practical large scale electromagnetic simulations.

References

- [1] O. Axelsson. *Iterative Solution Methods*. Cambridge Univ. Press, Cambridge, 1994.
- [2] R. Barrett, M. Berry, T. F. Chan, J. Demmel, J. Donato, J. Dongarra, V. Eijkhout, R. Pozo, C. Romine, and H. Van der Vorst.

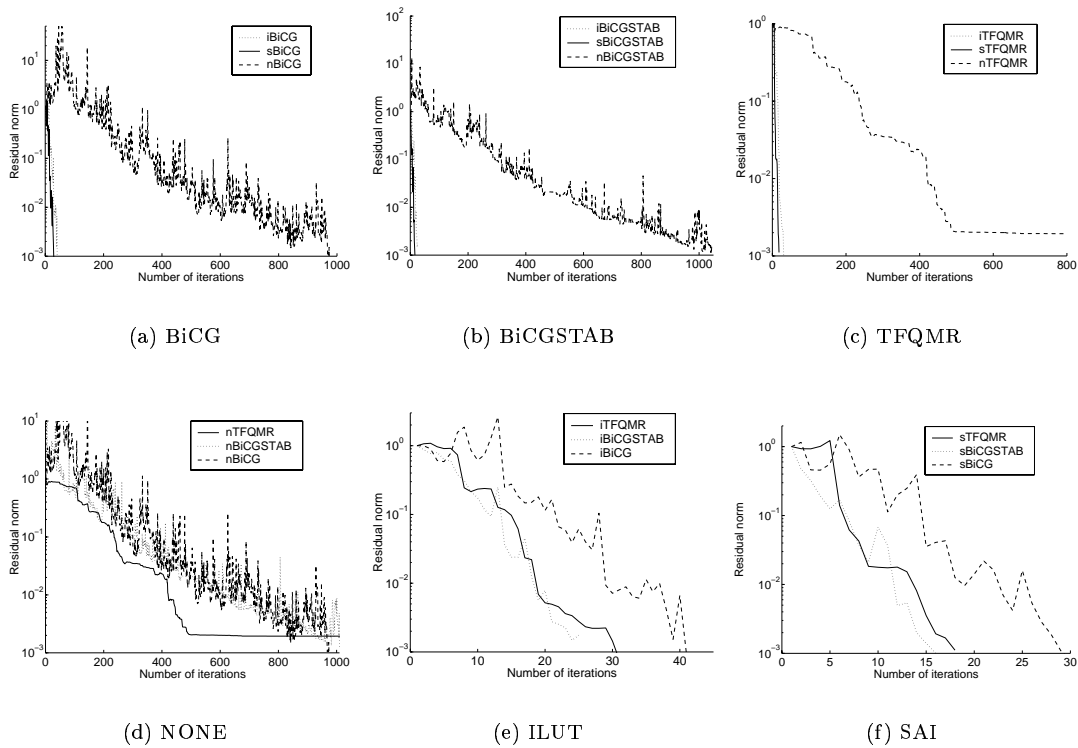


Figure 1: Convergence history for the P1C case.

- Templates for the Solution of Linear Systems: Building Blocks for Iterative Methods, 2nd Edition.* SIAM, Philadelphia, PA, 1994.
- [3] W. C. Chew, J. M. Jin, E. Mideielsen, and J. M. Song. *Fast and Efficient Algorithms in Computational Electromagnetics.* Artech House, Boston, MA, 2001.
- [4] R. Coifman, V. Rokhlin, and S. Wandzura. The fast multipole method for the wave equation: a pedestrian prescription. *IEEE Antennas Propagat. Mag.*, 35(3):7–12, 1993.
- [5] E. Darve. The fast multipole method: numerical implementation. *J. Comput. Phys.*, 160:195–240, 2000.
- [6] R. W. Freund. A transpose-free quasi-minimum residual algorithm for non-Hermitian linear systems. *SIAM J. Sci. Comput.*, 14:470–482, 1993.
- [7] A. Greenbaum. *Iterative Methods for Solving Linear Systems.* SIAM, Philadelphia, 1997.
- [8] L. Y. Kolotilina. Explicit preconditioning of systems of linear algebraic equations with dense matrices. *J. Sov. Math.*, 43:2566–2573, 1988.
- [9] C. Lanczos. Solution of systems of linear equations by minimized iterations. *J. Research National Bureau Standards*, 49:33–53, 1952.
- [10] J. Lee, J. Zhang, and C. C. Lu. Sparse inverse preconditioning of multilevel fast multipole algorithm for hybrid integral equations in electromagnetics. Technical Report No. 363-02, Department of Computer Science University of Kentucky, Lexington, KY, 2002.
- [11] J. Lee, J. Zhang, and C. C. Lu. Incomplete LU preconditioning for large scale dense

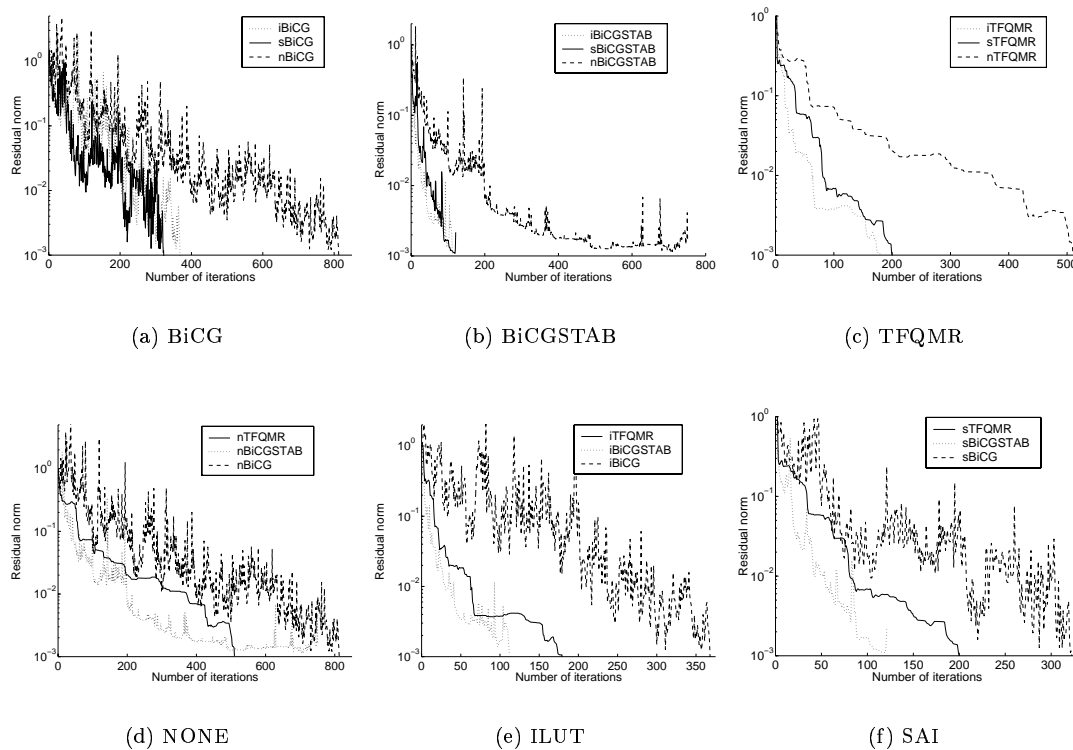


Figure 2: Convergence history for the C1C case.

- complex linear systems from electromagnetic wave scattering problems. *J. Comput. Phys.*, 185(1):158–175, 2003.
- [12] C. C. Lu and W. C. Chew. A coupled surface-volume integral equation approach for the calculation of electromagnetic scattering from composite metallic and material targets. *IEEE Trans. Antennas Propag.*, 48(12):1866–1868, 2000.
- [13] N. M. Nachtigal, S. C. Reddy, and L. N. Trefethen. How fast are nonsymmetric matrix iterations? *SIAM Matrix Anal. Appl.*, 13(3):778–795, 1992.
- [14] Y. Saad. ILUT: a dual threshold incomplete LU preconditioner. *Numer. Linear Algebra Appl.*, 1(4):387–402, 1994.
- [15] Y. Saad. *Iterative Methods for Sparse Linear Systems*. PWS Publishing, New York, NY, 1996.
- [16] H. van der Vorst. Bi-CGSTAB: a fast and smoothly converging variant of Bi-CG for the solution of nonsymmetric linear systems. *SIAM J. Sci. Stat. Comput.*, 13:631–644, 1992.
- [17] Y. V. Vorobyev. *Method of Moments in Applied Mathematics*. Gordon And Breach Science Publishers, New York, 1965.
- [18] J. Zhang. Preconditioned Krylov subspace methods for solving nonsymmetric matrices from CFD applications. *Comput. Methods Appl. Mech. Engrg.*, 189(3):825–840, 2000.
- [19] J. Zhang. Sparse approximate inverse and multilevel block ILU preconditioning techniques for general sparse matrices. *Appl. Numer. Math.*, 35(1):67–86, 2000.

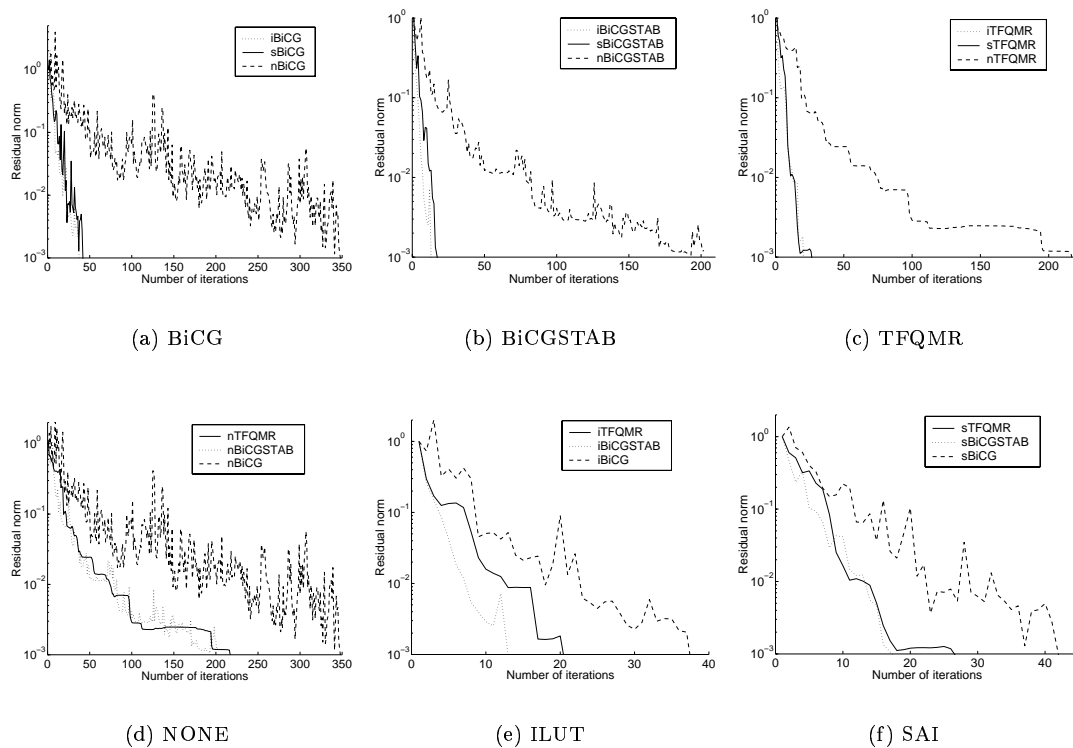


Figure 3: Convergence history for the P3C case.

Short Biography

Jeonghwa Lee received an M.S. in Mathematics from Chonnam National University, South Korea. She is currently a Ph.D. student of Computer Science at the University of Kentucky. Her research interests include large scale parallel and scientific computing, iterative and preconditioning techniques for large scale matrix computation, and computational electromagnetics.

Jun Zhang received a Ph.D. from The George Washington University in 1997. He is an Associate Professor of Computer Science and Director of the Laboratory for High Performance Scientific Computing and Computer Simulation at the University of Kentucky. His research interests include large scale parallel and scientific computing, numerical simulation, iterative and preconditioning techniques for large scale matrix computation. Dr. Zhang is associate editor and on the editorial boards of three international journals in computer simulation and computational mathematics, and is on the program com-

mittees of a few international conferences. His research work is currently funded by the U.S. National Science Foundation and the Department of Energy. He is recipient of National Science Foundation CAREER Award and several other awards.

Cai-Cheng Lu got his Ph.D. degree from University of Illinois at Urbana Champaign in 1995, and now he is an assistant professor in the Department of Electrical and Computer Engineering at the University of Kentucky. Prior to join University of Kentucky, he was with Demaco, Inc. (now SAIC) where he worked on a number of new features for the Xpatch code. His research interests are in wave scattering, microwave circuit simulation, and antenna analysis. He is especially experienced in fast algorithms for computational electromagnetics and is one of the authors for a CEM code FISC. He is a recipient of the 2000 Yong Investigator Award from the Office of Naval Research, and a CAREER Award from the National Science Foundation. Dr. Lu is a senior member of IEEE.

Analysis of Scattering Problems by MOM with Intervallic Wavelets and Operators

Sami Barmada, Marco Raugi
 Dipartimento Sistemi Elettrici e Automazione,
 Via Diotallevi 2 56126 Pisa Italy.
 Phone +39 050 565312 Fax +39 050 565333
 E-mail: sami.barmada@dsea.unipi.it

Abstract— In this paper a method for the solution of scattering problems is proposed. In particular the EFIE is solved by a collocation point procedure, where the unknown current density is expanded by Daubechies wavelets on the interval and the integration is performed in the wavelet domain by the integral operator, hence without the use of any quadrature formula. Comparison with induced currents calculated by a standard MoM and with fields calculated by a FEM code are reported.

I. INTRODUCTION

Wavelet Expansion (WE) has become a widely used tool in electromagnetic analysis. The main reasons can be found in the strong interpolating properties of the wavelet functions and to the fact that WE and reconstruction can be performed by the use of fast algorithms (see for example [1] - [3]).

The analysis of scattering problems can be carried out expanding the unknown functions in terms of a chosen wavelet basis and performing a Galerkin procedure using the same wavelet functions as test functions (see [4] - [6]). The integration is then performed by the use of quadrature formulae.

In this paper the EFIE for the scattering on a conductive body is solved in a different way. By utilizing Daubechies wavelets on the interval the unknown current is expanded, then a collocation point method is used and the integration is performed by the use of the integral operator for Daubechies wavelets on the interval developed by the authors (see [8]). In this way the need of quadrature formulae is avoided; furthermore the well known capability of the wavelet functions of representing irregular signals with few coefficients, allows us to use bases of low dimension (if compared with the number of unknowns of a standard MoM); for these reasons both accuracy and CPU time saving are achieved.

II. WAVELETS ON THE INTERVAL AND OPERATORS

The concepts of scaling functions, wavelets, time-scale analysis, multiresolution analysis are here considered known [1]; there are many wavelet bases available in the literature, and we chose the Daubechies Wavelets on the interval [2] for their numerical properties. In particular the choice of wavelets that "survive" only on intervals is adopted because we are interested in the solution of a boundary value problem.

From the wavelet theory we know that WE must be performed starting from a signal known at a dyadic number of samples. This number is equal to the dimension of the basis on which we perform the WE; hence a signal represented by $n = 2^m$ samples when expanded in the wavelet domain leads to a number of 2^m coefficients. For the compact support wavelet there is an important relation that allows a straight computation of the coefficients at the higher resolution of a generic function: it is possible to obtain them from the samples of the functions itself according to the relation $\langle \phi_{J,k}, f \rangle = 2^{J/2} f(2^J k)$, where $\phi_{J,k}$ is the scaling function of order J, k of the adopted wavelet basis. Then, the vector of wavelet coefficients \mathbf{g} representing the wavelet transform of a function $g(x)$ can be obtained by multiplying a matrix \mathbf{W} related to the adopted wavelet basis and the samples $g(x_j)$ corresponding to 2^m equally spaced points in the interval $[0, 1]$. Further details about wavelet numerical computation can be found in [3].

When performing WE of a function, the notation that will be used throughout the paper is the following:

$$f(t) = \sum_i f_i b_i(x) = \mathbf{b}(x) \mathbf{f} \quad (1)$$

where $\mathbf{b}(x) = [b_1(x), \dots, b_n(x)]$ is the wavelet basis

and $\mathbf{f} = [f_1, \dots, f_n]^T$ is the vector of coefficients constituting the wavelet expansion of the signal.

Also operators can be represented in the wavelet domain, as described in [7]. The authors have obtained the representation of the integral operator for the Daubechies wavelets on the interval (see for example [8]). The convenience in using operators in the wavelet domain is that the integral of a function $f(x)$ can be calculated by the matrix-vector product \mathbf{Tf} where \mathbf{T} is the constant sparse matrix representing the operator in the wavelet domain and \mathbf{f} is the wavelet expansion of the function $f(x)$. In the previous operation the result is the primitive function of f . In order to better understand the previous statement let us define $f(x) = x^3$; we can write that

$$\int_{[0,1]} f(x)dx = \int_{[0,1]} x^3 dx = \frac{1}{4}x^4 = g(x) \quad (2)$$

where the integral limit $[0, 1]$ indicates that we are considering the interval $[0, 1]$. Expanding (2) according to (1) in the wavelet domain we can write that

$$\int_{[0,1]} \mathbf{b}(x)\mathbf{f}dx = \mathbf{b}(x)\mathbf{g} \quad (3)$$

where \mathbf{f} and \mathbf{g} are the wavelet expansion of the two functions. Left multiplying by $\mathbf{b}(x)^T$ and taking into account the definition of the integral operator ($\mathbf{T} = \langle \mathbf{b}(x), \int \mathbf{b}(x) \rangle$) and the orthogonality properties of the wavelet basis ($\mathbf{I}_d = \langle \mathbf{b}(x), \mathbf{b}(x) \rangle$, with \mathbf{I}_d being the identity matrix) we can write that

$$\mathbf{Tf} = \mathbf{g} \quad (4)$$

Hence as clearly stated in equation (4) the calculation of function $g(x)$ can be performed in the wavelet domain by multiplying matrix \mathbf{T} by vector \mathbf{f} , the wavelet expansion of the function $f(x)$; then the result, vector \mathbf{g} , is inverse transformed, obtaining the function $g(x)$.

In order to compute a definite integration directly in the wavelet domain, two new (row) vectors must be introduced: vectors $\mathbf{b}_0 = \mathbf{b}(0)$ and $\mathbf{b}_1 = \mathbf{b}(1)$ that are the values of the basis functions on the left and right border, respectively, of the interval $[0, 1]$. The meaning of these two vectors is the following: given a function $f(x)$, its left border value $f(0)$ can be obtained by the coefficients of its WE simply by the use of the vector \mathbf{b}_0 as $f(0) = \mathbf{b}_0\mathbf{f}$.

Suppose that we want to compute

$$\int_0^1 f(x)dx = \int_0^1 x^3 dx = \frac{1}{4}x^4|_0^1 = g(x)|_0^1 = \frac{1}{4} \quad (5)$$

Then starting from equation (4) it must be considered that the primitive function (\mathbf{g}) is already calculated, and we only need to evaluate it on the borders of the interval. Hence it yields

$$\int_0^1 f(x)dx = \mathbf{b}_1\mathbf{g} - \mathbf{b}_0\mathbf{g} \quad (6)$$

which can be rewritten as

$$\int_0^1 f(x)dx = \mathbf{b}_1\mathbf{Tf} - \mathbf{b}_0\mathbf{Tf} \quad (7)$$

As evidenced in equation (7) the calculation of the definite integral of a function $f(x)$ can be performed knowing its WE \mathbf{f} , the integral operator matrix \mathbf{T} and the border vectors. The quantities \mathbf{T} , \mathbf{b}_0 and \mathbf{b}_1 are known once a wavelet basis has been chosen, so they need to be computed only once, and not at any analysis.

III. METHOD OF MOMENTS AND WAVELET EXPANSION

A. General Considerations

In the study of scattering from conducting cylinders, an integral equation can be formulated, which in general has the form of

$$\begin{aligned} & j\frac{\eta}{\beta} \left[\beta^2 \int_S \int_S \mathbf{J}_s(\mathbf{r}')\mathbf{G}(\mathbf{r}_s, \mathbf{r}')d\mathbf{s}' + \right. \\ & \left. + \nabla \int_S \nabla' \cdot \mathbf{J}_s(\mathbf{r}')\mathbf{G}(\mathbf{r}_s, \mathbf{r}')d\mathbf{s}' \right] = \mathbf{E}_t^i(\mathbf{r} = \mathbf{r}_s) \end{aligned} \quad (8)$$

where $\eta = \sqrt{(\mu/\epsilon)}$ and $\beta^2 = \omega^2\mu\epsilon$; \mathbf{J}_s is the current density induced on the scatterer, \mathbf{G} is the green function for the three dimensional scatterer, \mathbf{r}' and \mathbf{r}_s are respectively the integration variable and the observation point, both on the surface scatterer; and \mathbf{E}_t^i is the incident field.

In a simpler way and in one dimension equation (8) can be in general rewritten as

$$\int g(x')K(x, x')dx' + c(x)g(x) = h(x) \quad (9)$$

where $g(x)$ is our unknown function. In the literature [5], function g is expanded in the wavelet

domain, and the expansion is substituted in (9). In order to obtain a linear system for the unknown coefficients, the resultant equation is tested with the same expansion functions (Galerkin's method). Quadrature formulae available in the literature for wavelets and scaling functions are used, and a square system is obtained, which solved gives the unknown coefficients.

Due to the high interpolating properties of the Daubechies wavelets on the interval, we have adopted this family of wavelets, for which the authors have developed the representation of the integral operator. Wavelets on the interval (and so operators in the wavelet domain) are defined on $[0, 1]$, hence the contour of the scatterer must be mapped into the interval $[0, 1]$. As it is suggested in [6] for an arbitrary contour of the scatterer two steps must be performed:

- The contour of the scatterer is discretized in boundary elements and then each boundary element (simply a first order element) is mapped into one dimensional standard element through shape functions or interpolation functions.
- The standard elements are mapped into corresponding portions of the interval $[0, 1]$.

In this way the basis functions are defined in a standard way on the interval $[0, 1]$, since the contour has been mapped on this interval.

B. Scattering from a Conductive Body

In case of a two dimensional problem with TM^z polarization the EFIE equation is the following:

$$\frac{\eta\beta}{4} \int_C J_z(\rho') H_0^{(2)}(\beta|\rho_m - \rho'|) d\rho' = E_z^i(\rho_m) \quad (10)$$

where ρ_m is any observation point on the scatterer, ρ' is any source point on the scatterer and C is the contour of the scatterer.

After the mapping on the elemental interval $[0, 1]$ (described in the previous section) is performed, we perform a classical collocation point procedure: we evaluate equation (10) at a particular point $\bar{\rho}_m$ of the contour; hence equation (10) can be rewritten as

$$k \int_0^1 f(x)g(x)dx = h \quad (11)$$

where $k = \frac{\eta\beta}{4}$, $f(x) = H_0^{(2)}(\beta|\rho_m - \rho'|)$ and $g(x) = J_z(\rho')$.

Then the wavelet expansion in the space domain is performed. It has to be noticed that in equation

(11) there is the product between two functions, in particular one of them is known ($f(x)$) while the other is our unknown. As explained in [8] it is possible to obtain the wavelet expansion of a the product between two functions $y(x) = f(x)g(x)$ as the product between a constant diagonal matrix \mathbf{F} and a vector \mathbf{g} , where \mathbf{g} is the wavelet expansion of the function $g(x)$ and \mathbf{F} is a diagonal matrix whose entries are the samples at $n = 2^m$ equally spaced points of the values of $f(x)$ in the interval. This approximation is as much accurate as the number of samples is high, hence as the resolution of the chosen basis increases. In case the two functions are know the above described procedure is useless, since the expansion of $y(x)$ can be performed directly. But in the cases when one of the two functions is unknown then the procedure is fundamental, since it allows to keep \mathbf{g} as the unknown vector and anyway perform the wavelet expansion. Hence equation (11) can be expressed in the wavelet domain as

$$k \int_0^1 \mathbf{b}(x)\mathbf{F}\mathbf{g}dx = \mathbf{b}(x)\mathbf{h} \quad (12)$$

where \mathbf{F} is the diagonal matrix with the samples of the Hankel function, \mathbf{g} is the vector of unknown coefficients and \mathbf{h} is the expansion of constant h on the interval $[0, 1]$ i.e. considered as a constant function on the whole interval. By left multiplying equation (12) by $\mathbf{b}(x)^T$ we obtain

$$k\mathbf{b}(x)^T \int_0^1 \mathbf{b}(x)dx\mathbf{F}\mathbf{g} = \mathbf{b}(x)^T\mathbf{b}(x)\mathbf{h} \quad (13)$$

and taking into account the definition of the integral operator and the orthogonality properties of the chosen basis we obtain

$$k\mathbf{T}\mathbf{F}\mathbf{g} = \mathbf{h} \quad (14)$$

In this way equation (14) establishes a relation between the primitive of the product $f(x)g(x)$ and the constant function $h(x) = constant$. This is actually something different from what we want, hence the two vectors \mathbf{b}_0 and \mathbf{b}_1 (introduced in section II) must be employed. Hence we can write that

$$\mathbf{b}_1 k\mathbf{T}\mathbf{F}\mathbf{g} - \mathbf{b}_0 k\mathbf{T}\mathbf{F}\mathbf{g} = \mathbf{h} \quad (15)$$

Equation (15) is characterized by known matrices \mathbf{T} and \mathbf{F} and known vectors \mathbf{b}_0 and \mathbf{b}_1 and by the unknown vector of coefficients \mathbf{g} . Once the resolution of the wavelet basis is chosen the number of

basis functions is consequently fixed, hence equation (15) must be written for a number of n points on the interval itself. This leads to a sparse linear square system whose unknowns are the coefficients \mathbf{g} and which can be solved in low CPU time.

IV. NUMERICAL RESULTS

The numerical results presented here are relative to the scattering of a square conductive object illuminated by a polarized TM_z field. The geometry of the system and the input signal are reported in figures 1 and 2.

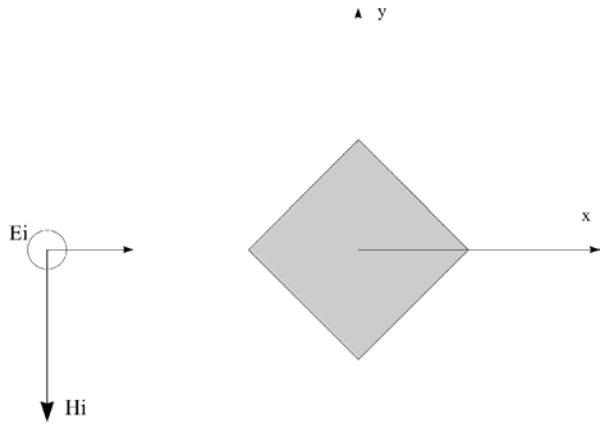


Fig. 1. Geometry of the system

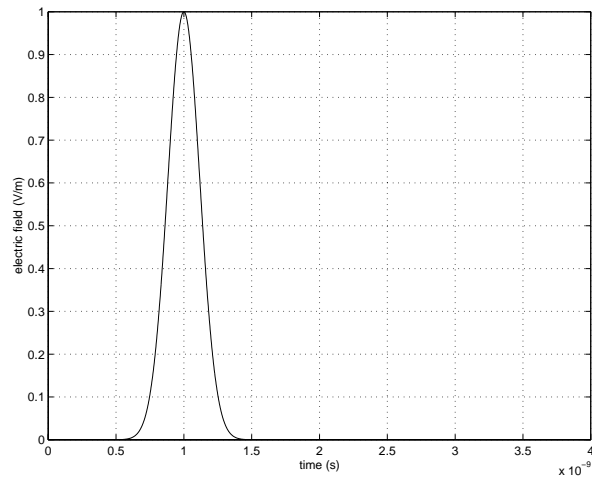


Fig. 2. Input signal

The diagonal of the scatterer is of 0.2m and the frequency content of the input signal is of the order of GHz. FFT has been used in order to obtain the behavior in the time domain. Figures 3 - 5 show the

calculated current density on the surface scatterer for a number of 64, 128 and 256 wavelet functions for a frequency of 1 GHz.

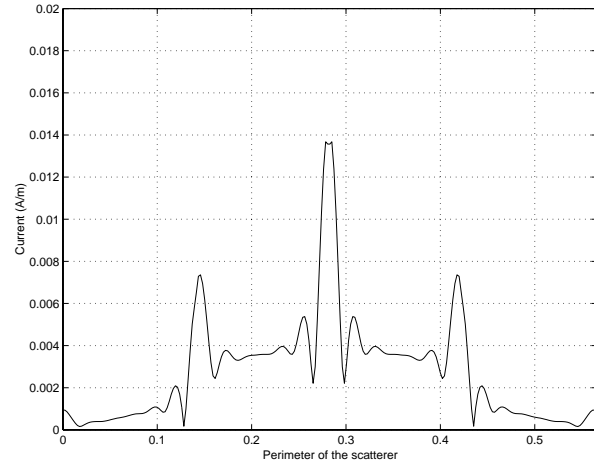


Fig. 3. Current density on the scatterer calculated by the use of 64 wavelets

It is evident that together with the increase of the resolution from 64 to 256, the accuracy of the results becoming higher. Nevertheless even at lower resolutions the obtained current (at a very low CPU time cost) is consistent with the problem.

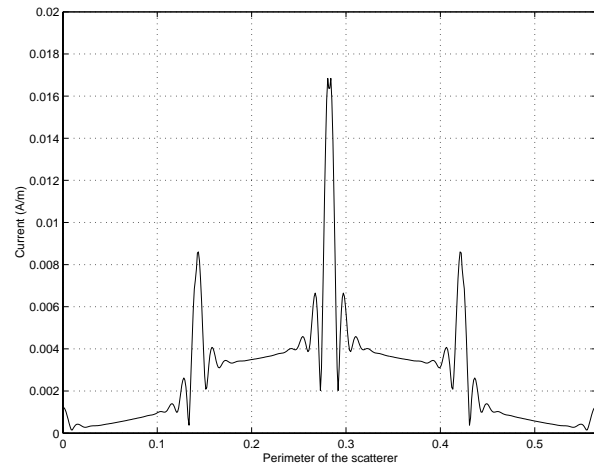


Fig. 4. Current density on the scatterer calculated by the use of 128 wavelets

Figure 6 shows the comparison between the calculations performed by the proposed method with a resolution of 256 wavelets and a standard MoM (with collocation point) technique with 500 points on the whole perimeter. It can be seen the very good agreement between the two different methods.

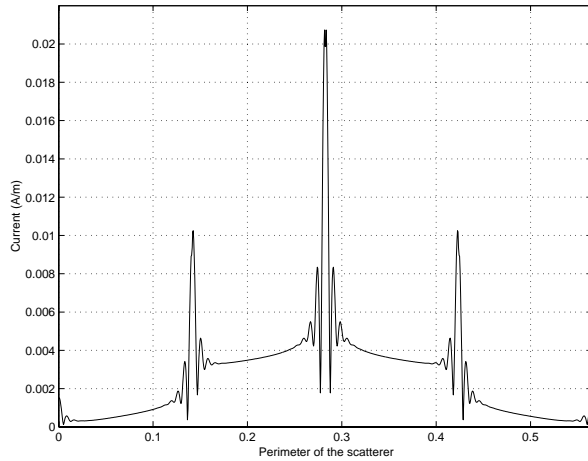


Fig. 5. Current density on the scatterer calculated by the use of 256

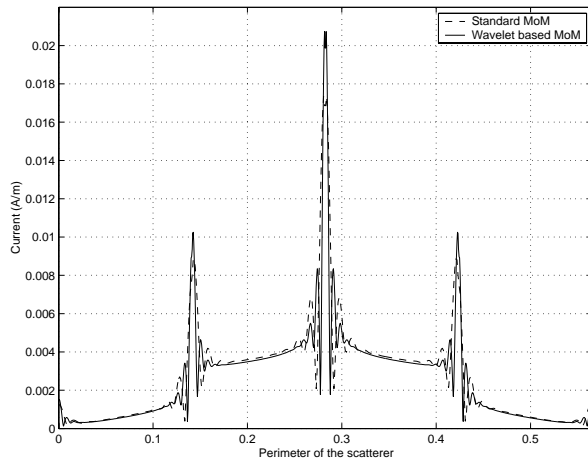


Fig. 6. Current density on the scatterer calculated by the use wavelets and MoM

As for the CPU time the method proposed is of the order of 2-4 times faster than the standard MoM, due to the high numerical efficiency of the wavelet expansion and integration, as described in the previous sections: the construction of the integral operator matrix and the border vectors is done only once and can be seen as a pre processing activity, while the integration is performed by a simple matrix - vector product, without the need of any quadrature formula. Furthermore the well known numerical properties of the wavelet functions (well addressed in the literature) allow the choice of bases of small dimensions in order to obtain accurate results.

Since the calculation of the current density is not

the only important result from an engineering point of view, a comparison with results obtained by the use of a FEM code of the total field are also reported. In figures 7 and 8 the electric field in point $P \equiv (-0.2, 0)$ and $P \equiv (0, -0.2)$ are reported, evaluated by the FEM code and by the proposed method, by using a wavelet basis of 256 functions.

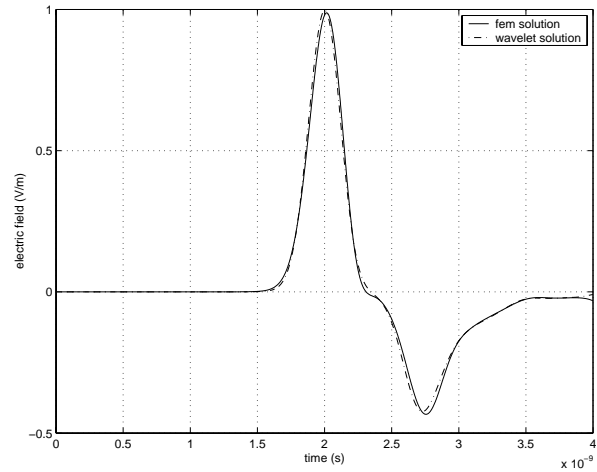


Fig. 7. Electric field evaluated at point $P \equiv (-0.2, 0)$

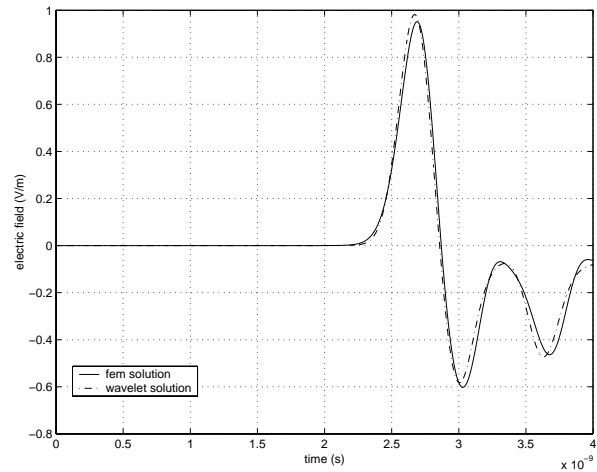


Fig. 8. Electric field evaluated at point $P \equiv (0, -0.2)$

Figure 9 reports the comparison between two solutions obtained by the proposed method at different resolutions, in particular with 64 and 256 wavelets, and shows the robustness of the method in terms of calculated fields

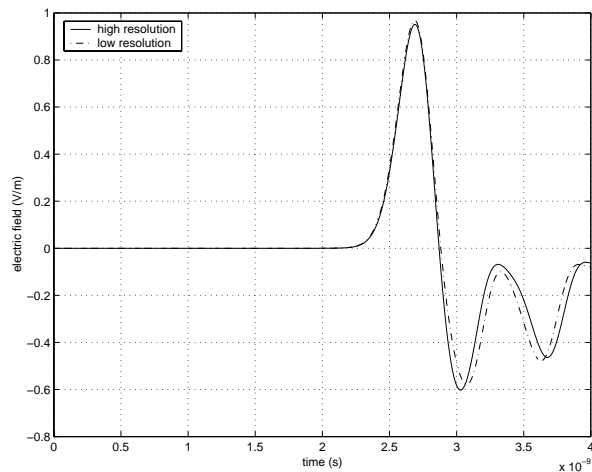


Fig. 9. Comparison at different resolutions of Electric field evaluated at point $P \equiv (0, -0.2)$

V. CONCLUSION

The method proposed here performs the analysis of scattering problems by the use of a MoM technique numerically implemented by wavelet expansion. In particular the use of the integral operator in the wavelet domain makes it possible to obtain the unknown current without the use of quadrature formulae, and the high interpolating properties of the chosen wavelet basis gives results with low CPU time. The good quality of the results is demonstrated by comparisons with standard MoM and FEM computations.

REFERENCES

- [1] C. K. Chui, "Wavelets: a Tutorial in Theory and Applications" *New York, Academic Press, 1992*
- [2] A. Cohen, I. Daubechies, B. Jawerth, P. Vial, "Multiresolution analysis wavelets and fast algorithms on the interval" *C. R. Acad. Sci. Paris ser. i Math. Vol. 316, 1992, pp. 417-421*
- [3] T. K. Sarkar, M. Salazar-Palma, M. C. Wicks, "Wavelet Applications in Engineering Electromagnetics" *Artech House 2002*
- [4] Y. Shifman, Y. Leviatan "Scattering by a Groove in a Conductiong Plane - A PO-MoM Hybrid Formulation and Wavelet Analysis" *IEEE trans. Antennas and Propagation vol. 349, n. 12. December 2001, pp. 1807 - 1811*
- [5] G. Pan "Orthogonal Wavelets with Applications in Electromagnetics" *IEEE trans. Mag. vol. 32, n. 3. May 1996, pp. 975 - 983*
- [6] G. Wang, G. Pan, B. K. Gilbert "A Hybrid Wavelet Expansion and Boundary Element Analysis for Multi-conductor Transmission Lines in Multilayered Dielectric Media" *IEEE trans. MTT. vol. 43, n. 3, March 1995 pp. 664 - 675*
- [7] G. Beylkin "Wavelets and Fast Numerical Algorithms" *Proc. of Symposia in Applied Math. Vol. 47, 1993*
- [8] S. Barmada, M. Raugi, "Transient Numerical Solutions

of Nonuniform MTL Equations with Nonlinear Loads by Wavelet Expansion in Time or Space Domain" " *IEEE Transactions on Circuits and Systems August 2000, Vol. 47, n. 8, pp. 1178 - 1190*



Sami Barmada was born in Livorno, Italy on November 18, 1970. He received his master degree in Electrical Engineering from the University of Pisa in 1995. He worked from 1995 to 1997 at ABB Teknolog (Oslo, Norway), on distribution network analysis and optimization.

In 2001 he received the Ph. D. in Electrical Engineering at the department of Electrical System and Automation of the University of Pisa. He is currently assistant professor in the same department and he is working on numerical computation of electromagnetic fields, in particular on the modeling of MTL and to the application of the wavelet expansion to computational electromagnetics.



Marco Raugi received the degree in Electronic Engineering from the University of Pisa in 1985 and the Ph. D. in Electrical Engineering from the Department of Electrical Systems and Automation in 1990. He is currently a full professor of Electrical Engineering. His research activity is in the numerical methods for the

analysis of electromagnetic fields in linear and non-linear media. Main applications have been devoted to Non Destructive Testing, Electromagnetic compatibility in transmission lines, electromagnetic launchers. He is author of around 100 papers on international journals and conferences. He is the general chairman of the International conference PIERS (Progress In Electromagnetic Research Symposium) 28-31 March 2004 in Pisa. He has been chairman of the Editorial Boards and he served as chairman and session organizer of international conferences. He has been recipient of the IEEE-IndustryApplicationSociety 2002 Melcher Prize Paper Award.

On the Construction and Use of Two-Dimensional Wavelet-Like Basis Functions

W. Elliott Hutchcraft and Richard K. Gordon
 Department of Electrical Engineering
 Anderson Hall Box 7
 University of Mississippi
 University, MS 38677 USA
eweh@olemiss.edu, egordon@olemiss.edu

Abstract: An alternative method for generating higher dimensional wavelet-like basis functions is proposed in this paper. One method that has been used was to derive the two-dimensional wavelet-like basis from the two-dimensional traditional finite element basis. However, in this paper, products of one-dimensional wavelet-like functions are used as two-dimensional wavelet-like basis functions. The generation of linear wavelet-like functions is discussed in detail and the use of linear and higher order wavelet-like functions is also investigated. The advantages and disadvantages of this technique for deriving wavelet-like basis functions will be discussed.

Keywords: Wavelets, Iterative Techniques, Finite Element Methods

I. INTRODUCTION

Wavelets and wavelet analysis have recently become increasingly important in the computational sciences. Wavelets have many applications in areas such as signal analysis, image compression, and the numerical solution of partial differential equations and integral equations. Only rather recently, however, have wavelets begun being used in computational electromagnetics. The multiresolution time domain technique (MRTD), developed by Katehi et. al, has attracted abundant interest in the use of wavelets as basis functions [1]. Gordon has used wavelet-like basis functions in the numerical solution of elliptic partial differential equations

[2]. The wavelet-like functions have also been used as the basis for a finite element time-domain algorithm [3]. Although the wavelet-like functions are not true wavelets, they do exhibit some of the benefits that have caused wavelets to receive attention. One advantage that will be discussed in detail in this paper is that wavelet-like basis functions have good stability and convergence properties.

II. GENERATION OF BASIS FUNCTIONS

The method for generating the wavelet-like basis was first discussed by Jaffard in [4]. Consider the generation of linear wavelet-like functions for which the domain, Ω , is the line segment $0 \leq x \leq 1$. Assume that the problem under consideration has Dirichlet boundary conditions so that the value of the solution is specified at both endpoints of the problem domain. This eliminates the necessity of nodes at the endpoints of the domain. To begin the multiresolution analysis (MRA) for the generation of the linear wavelet-like basis functions, an initial discretization is chosen such that there is a single node placed at the midpoint of the domain (Fig. 1). This corresponds to beginning with two segments in the initial discretization; one segment from $0 \leq x \leq 0.5$, and another segment from $0.5 \leq x \leq 1$. This particular discretization is not a requirement; a very simple or extremely complex segmentation may be used as the initial discretization of the problem domain.

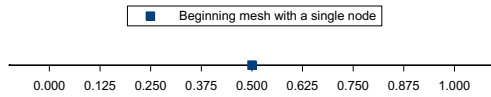


Fig. 1. Initial discretization with a single node in the mesh.

This beginning discretization is chosen for ease of illustration of the MRA. The traditional linear basis function associated with the node at $x = 0.5$ is normalized (Fig. 2).

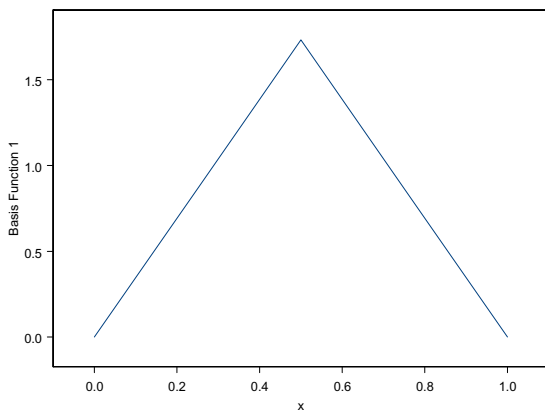


Fig. 2. Wavelet-like function from the first level of the MRA.

The first level of the MRA has now been completed and this function is considered to be the first wavelet-like basis function. To begin the second level of the MRA, each of the two segments from the first level is divided into two equal segments. After doing this, there are now four segments in the domain: one segment from $0 \leq x \leq 0.25$, another segment from $0.25 \leq x \leq 0.5$, another from $0.5 \leq x \leq 0.75$, and another from $0.75 \leq x \leq 1.0$. The node at $x = 0.5$ is not a new node, and the function associated with it is discarded. The nodes located at $x = 0.25$ and at $x = 0.75$ are new nodes (Fig. 3). Therefore, these two nodes need to be considered in the analysis. Next, the traditional basis functions that are associated with the two nodes are orthogonalized against the wavelet-like function from the first level; then, the resulting

functions will be orthonormalized against each other.

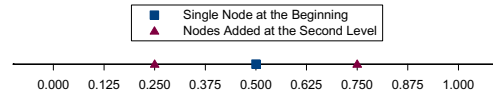


Fig. 3. Initial discretization with added nodes from second level of the MRA.

After the orthonormalization, the two functions can be added to the wavelet-like basis. Now the second level of the MRA is complete and there are three wavelet-like functions in the basis. The wavelet-like function associated with the node at $x = 0.25$ is shown in Fig. 4.

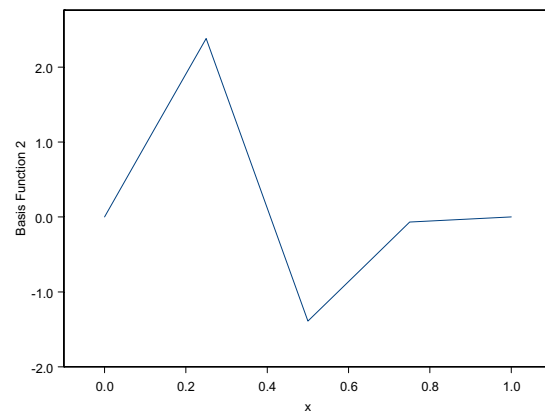


Fig. 4. Wavelet-like function added at the second level of the MRA.

The process of subdividing the segments and orthogonalizing traditional basis functions against previous wavelet-like basis functions and then orthonormalizing the resulting functions can be continued until the desired level of discretization is reached. Figures 5, 6, and 7 show the progression of the subdivision of the line segment from the third level to the fifth level of the analysis. Also, the linear wavelet-like basis function associated with the node at $x = 0.375$, which was added during the third level of the MRA, is shown in Fig. 8.

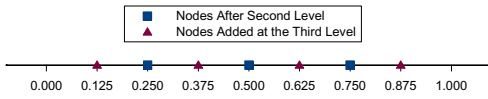


Fig. 5. Second Level discretization with added nodes from the third level.

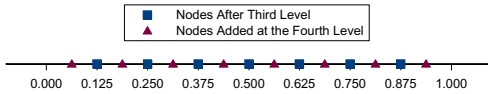


Fig. 6. Third level discretization with added nodes from the fourth level.

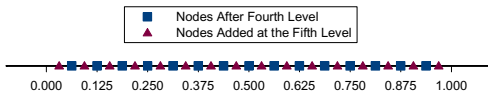


Fig. 7. Fourth level discretization with added nodes from the fifth level.

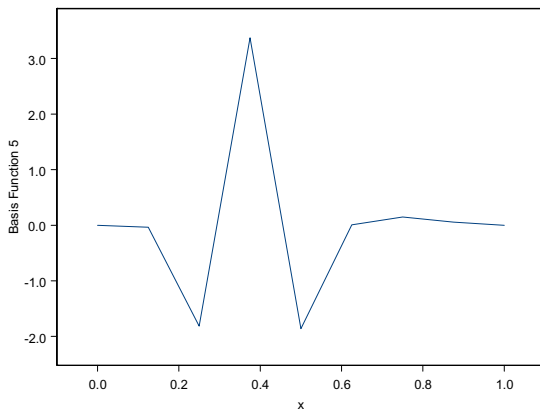


Fig. 8. Wavelet-like function added at the third level of the MRA.

This concludes the discussion of the generation of one-dimensional linear wavelet-like functions. Now there will be a brief discussion of the generation of higher dimensional and higher order wavelet-like functions.

There are two methods that have been used to generate higher dimensional wavelet-like functions. One possibility is to generate them from their higher dimensional traditional finite element counterparts. For example, a piecewise linear two-dimensional wavelet-like basis can be generated from the traditional two-dimensional tetrahedral basis. However, this is not how higher dimensional wavelets are typically created. Instead, they are generally formed from products of one-dimensional wavelets [5]. In two dimensions, this yields

$$\Psi_{m,n}(x,y) = \Psi_m(x)\Psi_n(y) \quad (1)$$

Hutchcraft and Gordon have shown that this technique can also be employed using products of wavelet-like functions [6].

Just as higher dimensional wavelet-like functions can be generated using their traditional counterparts, so can higher order wavelet-like functions. These functions have been used by Hutchcraft and Gordon in the numerical solution of a one-dimensional problem in [7] in which the traditional piecewise cubic basis functions are used to generate piecewise cubic wavelet-like basis functions. Implementing both of these concepts, higher order, higher-dimensional wavelet-like functions can be generated by forming products of one-dimensional higher order wavelet-like functions.

III. EXAMPLES OF ONE AND TWO-DIMENSIONAL BASIS FUNCTIONS

Consider a rectangular region as the domain for a two-dimensional problem. To obtain a two-dimensional wavelet-like basis, one-dimensional wavelet-like functions need to be generated in both the x- and y-directions by the method outlined previously. For the two-dimensional wavelet-like basis, all products of a wavelet-like function in the x-direction with a wavelet-like function in the y-direction will be considered a two-dimensional wavelet-like basis function; thus, the total number of wavelet-like functions

generated by this procedure will be the total number of wavelet-like functions in the x-direction multiplied by the total number of wavelet-like functions in the y-direction.

To aid in the visualization of these functions, Figs. 9-16 show several one- and two-dimensional linear and cubic wavelet-like functions. First, Figs. 9 and 10 illustrate one-dimensional cubic wavelet-like functions. In Fig. 10, the more slowly varying of the two functions is from the first level of the MRA. It has a single piecewise cubic representation over the entire domain. The other function in Fig. 10 is from the second level in the MRA. It is also piecewise cubic, but it has two different representations; one representation for the segment $0 \leq x \leq 0.5$ and another representation for the segment from $0.5 \leq x \leq 1.0$.

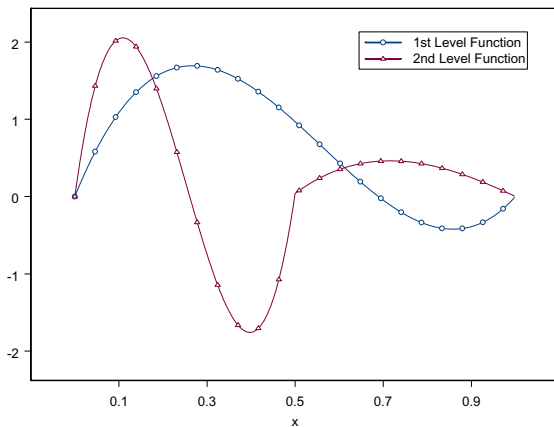


Fig. 9. Third order wavelet-like basis functions from the 1st and 2nd levels.

As discussed previously, two-dimensional wavelet-like functions are obtained by forming products of one-dimensional wavelet-like functions. Figure 11 shows a two-dimensional linear wavelet-like function. The linear wavelet-like function $B_6(x,y)$, which could also be written as $B_2(x)B_3(y)$ to denote that it is derived from the product of the 2nd basis function in the x-direction and the 3rd basis function in the y-direction, is formed from a function from the second level of the MRA in the x-direction and a

function from the second level of the MRA in the y-direction.

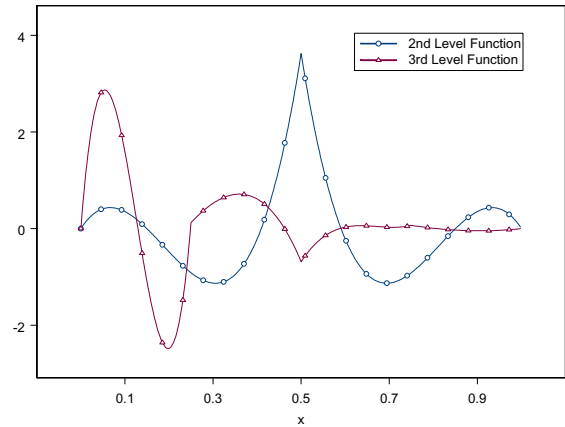


Fig. 10. Third order wavelet-like basis functions from the 2nd and 3rd levels.

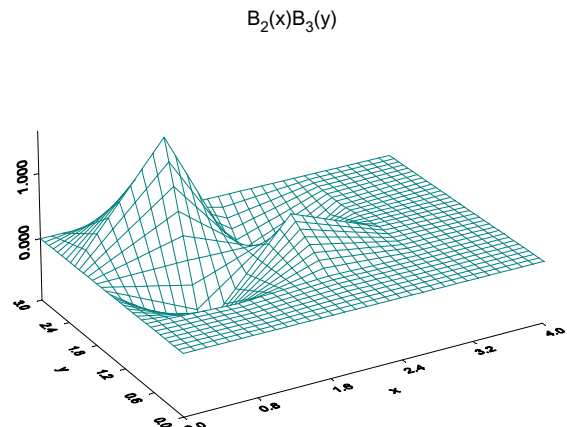


Fig. 11. Linear wavelet-like basis function obtained from a 2nd level x and 2nd level y function.

Plots of several two-dimensional cubic wavelet-like basis functions are shown in Figs. 12, 13, 14, and 15. $B_1(x,y)$ is a cubic wavelet-like basis function that is generated from the first level in both the x- and y-directions (Fig. 12). As can be seen from the figure, this function is nonzero over most of the domain. It is also a piecewise cubic polynomial in the x-direction and a piecewise cubic polynomial in the y-direction. $B_5(x,y)$ and $B_{10}(x,y)$ are both generated from the first level of the MRA in the y-direction and the

second level of the MRA in the x-direction (Figs. 13 and 14). In the x-direction, each of these two functions has two different piecewise cubic representations; on the other hand, both of these functions have a single representation in the y-direction. Specifically, in the x-direction, there is one piecewise cubic representation for the segment $0 \leq x \leq 2.0$, and another piecewise cubic representation for the segment $2.0 \leq x \leq 4.0$. $B_{15}(x,y)$ is a basis function that is obtained from a second level x-directed function and a second level y-directed function (Fig. 15). This function has two different piecewise cubic representations in both the x- and y-directions.

$B_1(x,y)$

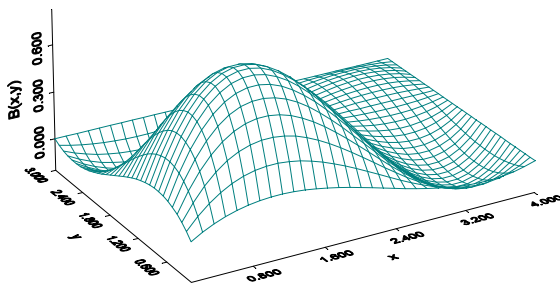


Fig. 12. Cubic wavelet-like basis function obtained from a 1st level x and 1st level y function.

$B_5(x,y)$

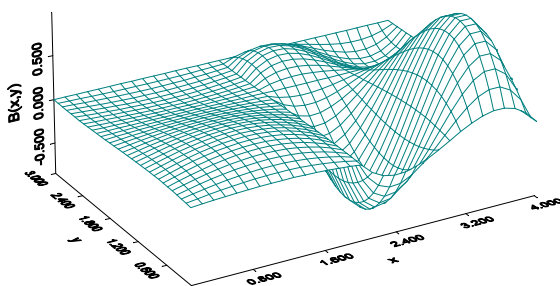


Fig. 13. Cubic wavelet-like basis function obtained from a 2nd level x and 1st level y function.

$B_{10}(x,y)$

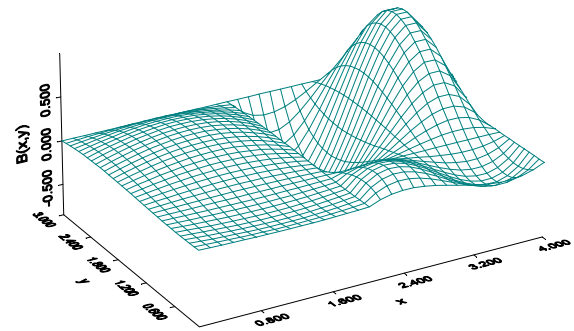


Fig. 14. Cubic wavelet-like basis function obtained from a 2nd level x and 1st level y function.

$B_{15}(x,y)$

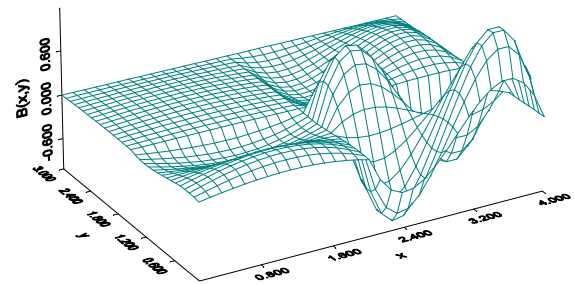


Fig. 15. Cubic wavelet-like basis function obtained from a 2nd level x and 2nd level y function.

With wavelet analysis, as levels in the MRA are added, the wavelets become more localized. As can be seen from these figures, the wavelet-like basis functions also possess this property; they have a large magnitude in a smaller portion of the domain as the level in the MRA for either (or both) the x- or y-directions increases. $B_1(x,y)$ has a rather large magnitude over the entire domain. Again, $B_5(x,y)$ and $B_{10}(x,y)$ are from the second level in the x-direction and the first level in the y-direction; notice that these two functions have a large value only in half of the region. $B_{15}(x,y)$ is a function from the second

level in both the x - and y -directions and its value is large only in one-quarter of the domain.

IV. EXAMPLE PROBLEM

As an example of the use of the wavelet-like basis functions, consider the following differential equation

$$-\nabla \cdot (a(x,y)\nabla u(x,y)) + b(x,y)u(x,y) = g(x,y) \quad (2)$$

in which the domain is the rectangular region from $x=0.0$ to $x=4.0$ and from $y=0.0$ to $y=3.0$. Laplace's equation can be obtained by choosing the following: $a(x,y)=-1.0$, $b(x,y)=0.0$, and $g(x,y)=0.0$. An illustration of the problem domain along with the boundary conditions is shown in Fig. 16.

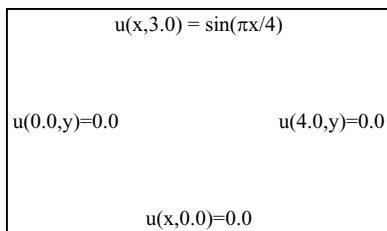


Fig. 16. Problem domain.

Solutions were obtained using the traditional two-dimensional basis functions, two-dimensional basis functions that were products of linear wavelet-like basis functions, and two-dimensional basis functions that were products of cubic wavelet-like basis functions. A comparison of the analytic solution and the numerical solution, which was found using 961 linear wavelet-like basis functions, is made along the line $x=1.5$ (Fig. 17). The numerical solution in this case corresponds to 31 wavelet-like functions in each direction ($31 \times 31 = 961$ total basis functions). To illustrate the accuracy when the linear wavelet-like basis is used, the curves for the numerical solution and the analytic solution lie on top of each other. To illustrate that an accurate solution is also obtained when the cubic wavelet-like basis functions is used, the analytic solution and the numerical solution,

which was obtained with 55 cubic wavelet-like basis functions, are compared along the line $y=1.5$ (Fig. 18). Again, these two curves are indistinguishable on the graph. The numerical solution obtained with only 25 cubic wavelet-like basis functions is plotted in figure 19. For this graph, five cubic wavelet-like functions in each direction were used as the two-dimensional basis. As expected, very few cubic basis functions are necessary to obtain an accurate solution. From these figures, it is seen that the solutions obtained are accurate when either cubic or linear wavelet-like basis functions are used.

Although the ability of any basis function to accurately model an arbitrary function is quite important, the wavelet-like basis also has other advantages. Previously, wavelet-like functions have been shown to have extremely good convergence and stability properties. After diagonal preconditioning, the condition number of the system matrix was calculated. Figure 20 illustrates how the condition number varies as the number of basis functions is increased. Because the condition number of the system matrix is much smaller for the wavelet-like bases in comparison with the rapidly rising condition number when the traditional basis is used, the condition numbers when the linear and cubic wavelet-like basis functions are used are shown separate in Fig. 21. The benefits of this low condition number are especially evident when looking at the number of steps required for convergence of the conjugate gradient method. In Fig. 22, the number of steps required for convergence of the conjugate gradient method is plotted as the number of basis functions is increased. With approximately 225 basis functions, the traditional basis requires 78 steps for convergence; this is in contrast to only 34 for 225 linear wavelet-like basis functions and only 18 for 253 cubic wavelet-like basis functions.

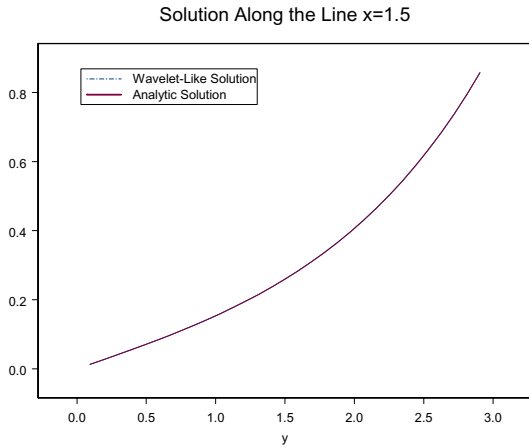


Fig. 17. Numerical (with 961 linear 2D wavelet-like basis) and analytic solutions along the line $x = 1.5$.

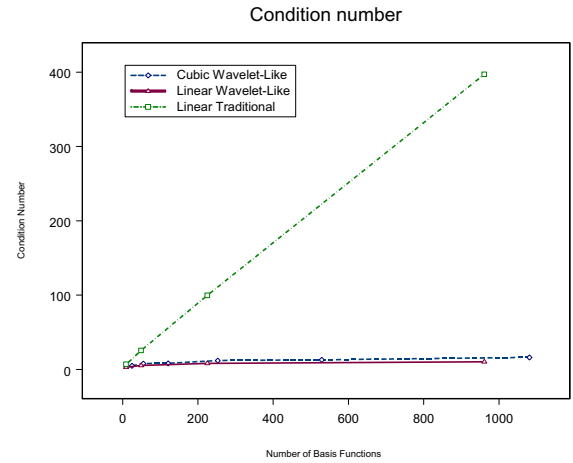


Fig. 20. Condition number comparison of wavelet-like and traditional basis.

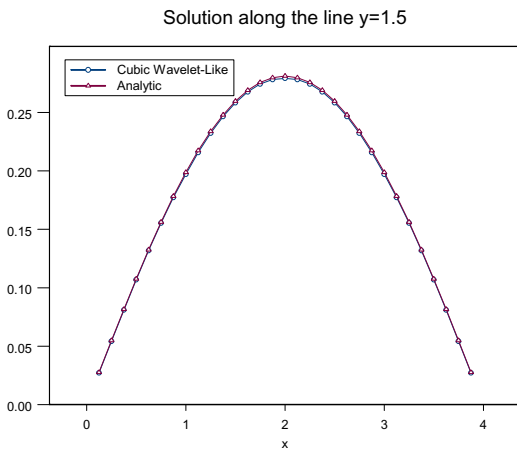


Fig. 18. Numerical and analytic solution along the line $y=1.5$.

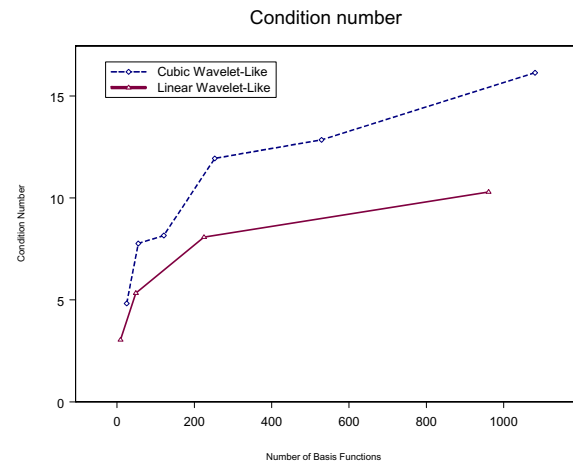


Fig. 21. Condition number when wavelet-like bases are used.

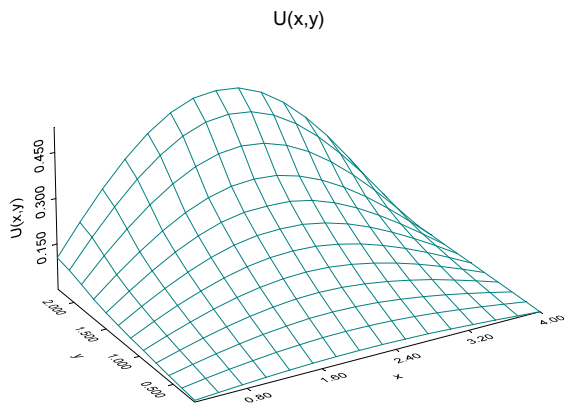


Fig.19. Numerical solution when 25 cubic wavelet-like functions are used.

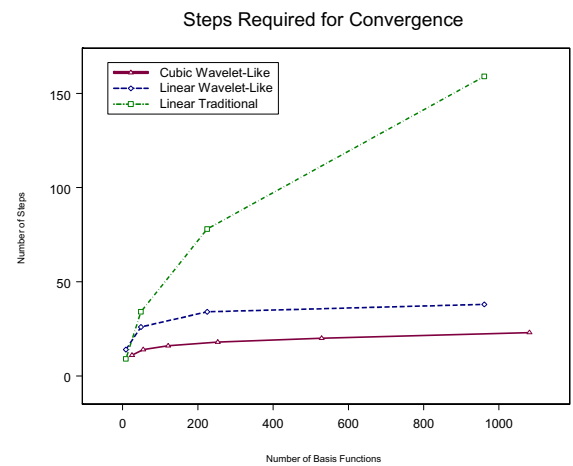


Fig. 22. Steps required for convergence.

V. CONCLUSION

It has been shown that one-dimensional wavelet-like basis functions can be multiplied to obtain two-dimensional basis functions that give accurate results when they are used to obtain numerical solutions. The stability of the condition number and the rapid convergence when the conjugate gradient method is used have also been shown to be two advantages of using either linear or higher order wavelet-like rather than traditional basis functions. As is the case with higher order traditional basis functions, fewer cubic wavelet-like basis functions are required for high accuracy. One disadvantage of this method is that the mesh would resemble more of a finite difference mesh rather than the triangular patches that are typically associated with the finite element method; however, non-uniform spacing is still rather easily accomplished with the wavelet-like method.

VI. REFERENCES

- [1] M. Krumpholz and L. P. B. Katehi, "MRTD: New Time Domain Schemes Based on Multiresolution Analysis," *IEEE Transactions on Microwave Theory and Techniques*, Vol. 44, No. 4, pp. 555-571, April 1996.
- [2] Richard K. Gordon, "On the use of wavelet-like basis functions in the finite element analysis of elliptic problems," *Proceedings of the Eleventh Annual Review of Progress in Applied Computational Electromagnetics*, pp. 559-567, Monterey, CA, March 1995.
- [3] W. Elliott Hutchcraft, Richard K. Gordon, and Jin-Fa Lee, "A Finite Element Time Domain Method Using Wavelet-Like Basis Functions", *Proceedings of The Thirty-First Southeastern Symposium on System Theory*, pp. 310-314, Vol. 1, March 1999.
- [4] Stephane Jaffard, "Wavelet methods for fast resolution of elliptic problems," *SIAM Journal on Numerical Analysis*, vol. 29, num. 4, pp. 965-986, August 1992.
- [5] I. Daubechies, "Orthonormal bases of compactly supported wavelets," *Commun. Pure Appl. Math.*, vol. 41, pp. 909-996, November 1988.
- [6] W. Elliott Hutchcraft and Richard K. Gordon, "On the Generation of Two-dimensional Wavelet-Like Basis Functions", *Proceedings of The Thirty-Third Southeastern Symposium on System Theory*, pp. 387-390, March 2001.
- [7] W. Elliott Hutchcraft and Richard K. Gordon, "Higher Order Wavelet-Like Basis Functions in the Numerical Solution of Partial Differential Equations using the Finite Element Method", *Proceedings of The Thirty-Third Southeastern Symposium on System Theory*, pp. 391-394, March 2001.
- [9] Y.W. Cheong, Y. M. Lee, and K. H. Ra et al., "Wavelet-Galerkin scheme of time-dependent inhomogeneous electromagnetic problems," *IEEE Microwave Guided Wave Lett.*, vol 9, pp. 297-299, August 1999.
- [10] Ben Zion Steinberg and Yehuda Leviatan, "On the use of wavelet expansions in the method of moments," *IEEE Transactions on Antennas and Propagation*, vol. 41, no. 5, pp. 610-619, May 1993.
- [11] T. K. Sarkar, L. E. Garcia-Castillo, and M. S. Salazar-Palma, "Utilization of wavelet concepts in finite elements for efficient solution of Maxwell's equation," *1994 Digest of the IEEE Antennas and Propagation Society International Symposium*, vol. 1, p. 7, June 1994.
- [12] H. C. Schweinler and E. P. Wigner, "Orthogonalization methods," *Journal of Mathematical Physics*, pp. 1693-1694, May 1970.
- [13] Gene H. Golub and Charles F. Van Loan, *Matrix Computations*, Second Edition, p. 554, The Johns Hopkins University Press, 1989.



W. Elliott Hutchcraft received his BS degree from the University of Mississippi in 1996, his MS degree from the University of Mississippi in 1998 and his PhD degree from the University of Mississippi in 2003. He is a member of IEEE, Eta Kappa

Nu and Tau Beta Pi. He is joining the faculty at the University of Mississippi in the fall of 2003. His research interests include the use of wavelets in computational methods, acoustics, microwave and antenna measurements, and parallel and distributed computing.



Richard K. Gordon received his BS degree in physics from Birmingham-Southern College in 1983, his MS degree in applied mathematics from the University of Illinois Urbana in 1986 and his PhD degree in electrical engineering from

the University of Illinois Urbana in 1990. He is presently an Associate Professor at the University of Mississippi. His research interests include mathematical methods, numerical techniques, scattering problems, and parallel computing.

Transient Modeling of Magnetoelastic Problems in Electric Machinery

O. A. Mohammed¹, T.E. Calvert², L. Petersen² and R. McConnell³

¹Florida International University, ECE Department, Miami, FL 33174 (e-mail: mohammed@fiu.edu)

²Office of Naval Research, ONR Code 334, Arlington VA

³Naval Surface Warfare Center, Carderock Division, Machinery R&D Directorate, Philadelphia, PA.

Abstract-- This paper investigates some aspects on noise and vibrations of electrical machinery based upon the coupling between the magnetic field and the mechanical deformation in the stator. This coupling is typically considered by using reluctance forces. Since the deformations occurring are small compared to the machine's dimensions, there is no feedback to the magnetic system in numerical models. However, stator deformations are caused not only by reluctance forces, but also by magnetostriction effect of the stator iron. Magnetostriction is one of the main causes of noise in electromagnetic systems particularly when the flux density is above 1.5 Teslas. Here, we develop numerical models that incorporate magnetostriction effects and all other possible electromechanical forces and related material interactions. Magnetostriction presents a problem at all levels of frequencies. At frequencies, particularly 2E, magnetostrictive forces are undesirable and can be large as well as generate acoustic noise, which can impede the system's performance.

The magnetostrictive deformations can be calculated based upon the magnetic field. If the magnetostrictive deformations are slightly higher than the magnitude of the deformations caused by the reluctance forces, there will be a need for feedback to the magnetic system. In order to account for this effect, the magnetostriction characteristic of iron $\lambda(H)$ is needed. The dependency of permeability on mechanical stress must be accounted for and be built into a strong coupling scheme. Implementation results on a 2-hp, permanent magnet motor indicate that magnetostrictive forces are significant and must be accounted for in the electromagnetic system's design stage.

Index Terms— Coupled problems, transient FE formulation, magnetoelastic problem, Magnetostriction.

I. INTRODUCTION

A numerical 2-D tensor finite element model for coupled magneto-mechanical problems is presented. The developed model can be used to evaluate force components in electromagnetic devices including those due to the magnetostrictive phenomenon. Magnetostriction is a property of ferrous alloys in which the material will exhibit strain in the presence of magnetic field. This strain is in addition to any other strains that might exist as a result of electrical and/or mechanical forces in devices. At low frequencies, magnetostrictive forces are undesirable. They can be large and generate acoustic noise in electromagnetic systems [1].

Magnetostriction is built into the coupled system using a force distribution that is added to magnetic forces. Magnetostriction forces mean the set of forces that induce the same strain in the material as magnetostriction does. The numerical implementation of this approach is similar to the way thermal stresses are applied. To evaluate thermal stresses, the thermal expansion of the free body is calculated based upon the temperature distribution [2]. The thermal stresses are found by deforming the expanded body back into its original shape. Magnetostriction forces are calculated by expansion of the free body due to magnetostriction based upon the magnetic flux density. The magnetostriction forces are found as the reaction to the forces needed to deform the expanded body back into the original boundary conditions.

In finite element models, this can be performed for each element through the element's nodal displacements with respect to the element's centre point using the element's flux density and the magnetostriction characteristic of the material, $\lambda(H)$. The element's strains are converted into nodal displacements considering the center of the element as a fixed point.

Magnetostriction in magnetic materials, such as electrical silicon steel sheets, is one of the main causes of noise and vibration in electric machinery and equipment for which there is no proven remedy. It is an important factor in governing the magnetic properties of magnetic materials. In order to achieve lower losses and noise levels in electrical machines, we need to know the magnetostrictive effects in the design stage. Some studies have been done on the reduction of magnetostriction and in orienting the steel sheet in the same direction as the applied tension to generate 180° domains in the direction. Even with such an effort, the improvements in noise and loss levels in actual equipment are only marginal especially under rotating field conditions where the effects of magnetostriction are greater. If the magnetic flux changes direction or is rotating, \mathbf{B} and \mathbf{H} will not be parallel and therefore tensor values of magnetic reluctivities should replace

the single values. Furthermore, it is possible that the magnetostriction itself or the accompanying material property changes, may be small in one direction, they can significantly vary when the domain structure changes in the magnetic flux direction [3, 4].

Magnetization characteristics data available from electrical steel manufacturers today are usually available for lower field levels (typically around 1.5 T in test samples) and such data *do not exist* under any stress level. The magnetic field causes elastic deformation and the mechanical stress changes the magnetization curve and the hysteresis loop. An initial effort on magnetostriction measurement was conducted on test samples to obtain magnetization curves under several stress levels were obtained [5, 6]. The obtained curves are subsequently used in the numerical models described here. Implementation results on a 2-hp, permanent magnet motor indicate that magnetostrictive forces are significant and amount to more than 50% force level increase.

II. DEVELOPMENT OF THE NUMERICAL MODEL

Implementing the finite element discretization, we can obtain the numerical solution of Maxwell's equations. As a result of the finite element discretization, the following matrix equations for both the electromagnetic and mechanical problems obtained [1]:

$$[\mathbf{S}] [A] = [J_e] \quad (1)$$

$$[\mathbf{K}] [U] = [F] \quad (2)$$

where \mathbf{S} and \mathbf{K} are the electromagnetic and mechanical stiffness matrices and F is the force vector.

Solving equations (1) and (2) yields the magnetic vector potential, A and the displacement U . One could easily notice that equations (1) and (2) are coupled through; a) the magnetic force and, b) the variation of the material permeability with stress [4-6]. Therefore a coupled solution model is necessary. Utilizing the coupled solution, the magnetic force in the direction of the displacement, U is equal to the variation of the magnetic energy with respect to U while the magnetic flux is held constant. When implementing the virtual work method [7], holding the magnetic flux constant is done by holding the difference of the magnetic vector potential between two nodes constant. In one element,

the contribution to the force acting on a given node is as follows:

$$F^e = - \int_{\text{Re}} [(H^T \cdot \frac{\partial B}{\partial U}) |G| + (\int_0^B H^T \cdot dB) \frac{\partial |G|}{\partial U} + (\int_0^B \frac{\partial}{\partial \sigma} (H^T) \cdot dB) \frac{\partial \sigma}{\partial U} |G|] dx dy \quad (3)$$

where Re is the element area, $|G|$ is the determinant the local Jacobian derivatives matrix G .

The variation of the permeability with mechanical stress is taken into consideration in the third term of equation (3). This corresponds to the force component of magnetostriction origin. The third term in equation (3) is the force component due to the magnetostriction phenomenon in one element acting on a given node is re-written as:

$$F_{ms}^e = - \int_{\text{Re}} [(\int_0^B \frac{\partial}{\partial \sigma} (H^T) \cdot dB) (\frac{E}{(1+\nu)(1-2\nu)}) |G|] dx dy \quad (4)$$

The total effect on a given part in the device can be calculated by adding the elemental contributions. It should be noticed that in evaluating the force equations, the permeability changes with stress must be taken into consideration in computing the field. This equation, equation (3), gives only the force component due to magnetostriction in one element. All other forces (electromagnetic, mechanical, etc.) must be calculated in the standard way given by the problem.

For the full reluctivity tensor model, the magnetostrictive force term with tensor reluctivity is written as follows [1, 5, 6]:

$$F_{ms}^e = - \int_{\text{Re}} \{ [v'_{xx}(\sigma_u) B_x^2] (\frac{E}{(1+\nu)(1-2\nu)}) |G| \} dx dy - \int_{\text{Re}} \{ [v'_{xy}(\sigma_u) B_x B_y] (\frac{E}{(1+\nu)(1-2\nu)}) |G| \} dx dy - \int_{\text{Re}} \{ [v'_{yx}(\sigma_u) B_x B_y] (\frac{E}{(1+\nu)(1-2\nu)}) |G| \} dx dy - \int_{\text{Re}} \{ [v'_{yy}(\sigma_u) B_y^2] (\frac{E}{(1+\nu)(1-2\nu)}) |G| \} dx dy \quad (5)$$

where E is the Young's modulus and ν is the Poisson's ratio. $|G|$ is the determinant of the local Jacobian matrix [1].

Results from an initial effort [1, 5, 6] on the measurement of magnetization curves under

mechanical stress were used in the implementation to the 2-hp motor given here. From the measurements and at a given value of flux density, within the proportional limit of ferrous materials, the permeability will increase as the applied stress increases. However, a reduction in the material permeability will occur as the stress increases further. The reduction in permeability will continue as the stress on the material passes through the elastic limit. A more pronounced reduction in permeability would occur as the increase in stress takes the material beyond the elastic limit (plastic range up to the yield point). At each level of stress, permeability versus magnetic field will vary. This would also mean that the hysteresis loop would shift affecting the behavior of the device and cause a noticeable and/or a permanent change in performance.

III. IMPLEMENTATION AND RESULTS

The numerical model was implemented on a 6-pole, three-phase, 2-hp surface mounted permanent magnet motor. One pole of this motor is shown in figure (1). The figure also shows the winding arrangement in the double-layered slots. Three-phase excitation is applied to the winding and the half slot

current density in the windings. A 360-degree model for the motor was used in developing the strongly coupled transient solution. The transient solution was obtained by rotating the rotor every quarter degree for a whole pole-pitch.

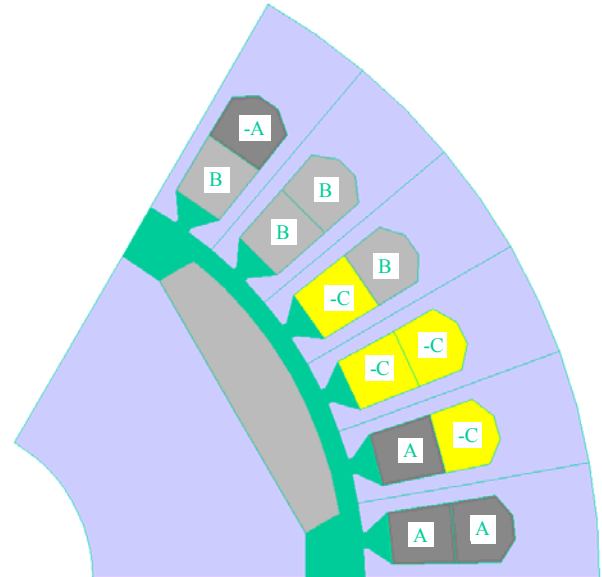


Fig. (1) One pole of the 2-hp Motor

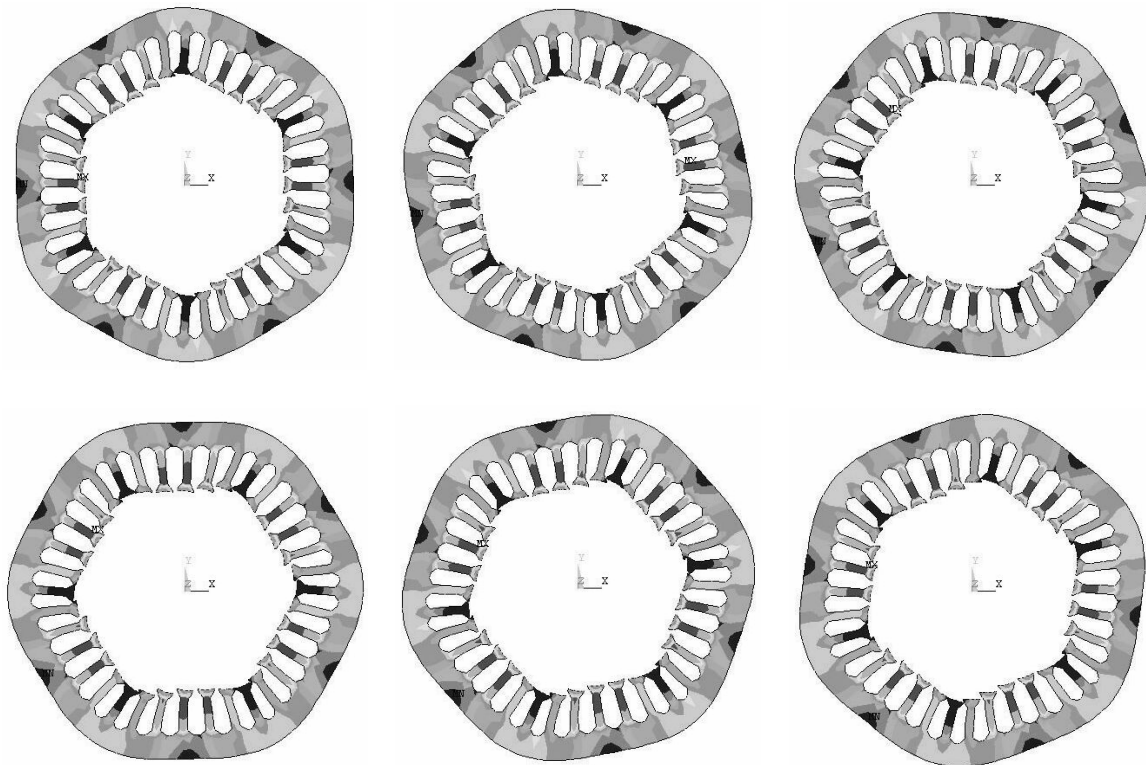


Fig. (2) Flux density on deformed shape from transient solution without Magnetostrictive forces.

Sample flux density solutions at various rotor positions are shown in figure (2). The measured magnetization curves under stress levels were used in the numerical model. Magnetostriction was included by utilizing the curves and the stress levels obtained from the numerical solution and a table look-up

procedure incorporating the measured curves. Figure (2) shows the flux density on the deformed shape at six instances from the transient solution without the magnetostriction forces included. On the other hand, figure (3) shows the flux density on the deformed shape with the magnetostriction forces added.

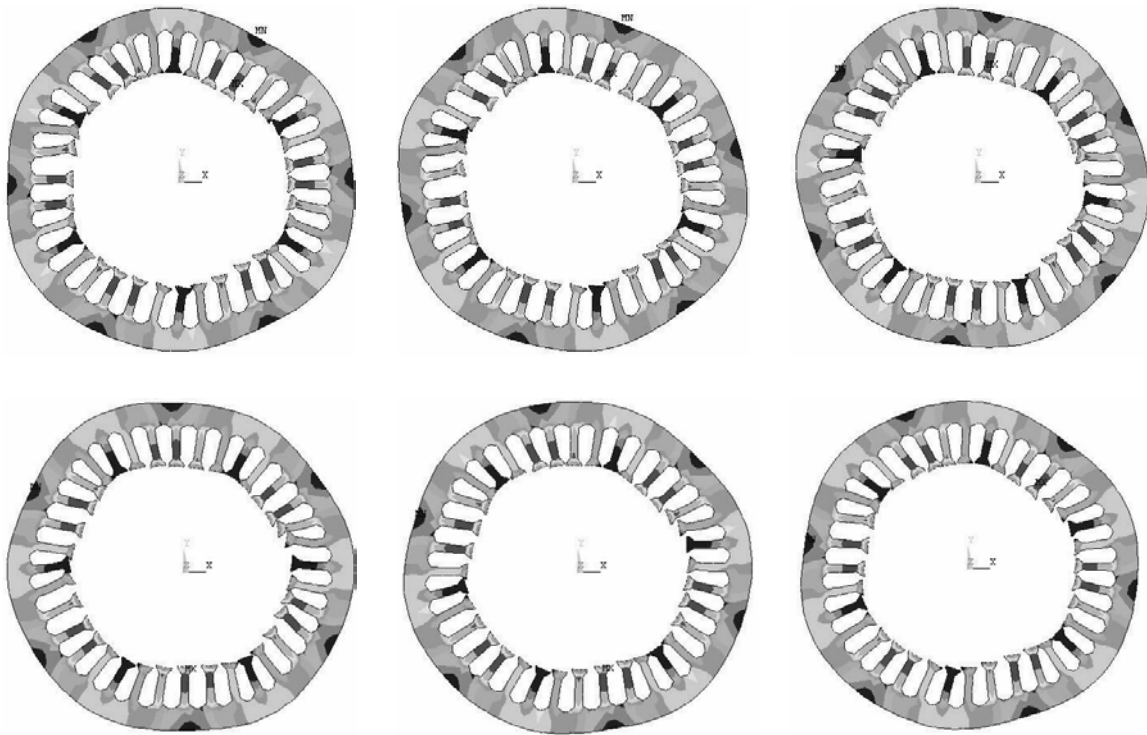


Fig. (3) Flux density on deformed shape from transient solution with Magnetostrictive forces.

Sample flux density solutions at various rotor positions are shown in figure (2). The measured magnetization curves under stress levels were used in the numerical model. Magnetostriction was included by utilizing the curves and the stress levels obtained from the numerical solution and a table look-up procedure incorporating the measured curves. figure (2) shows the flux density on the deformed shape at six instances from the transient solution without the magnetostriction forces included. On the other hand, Figure (3) shows the flux density on the deformed shape with the magnetostriction forces added.

The nodal forces at several nodes on the stator are shown in figures (4) and (5). It can be easily seen from

these two figures that the magnetostriction force values are significant and include additional pulsation as an indication that the magnetostriction effect adds more noise. These magnetostriction forces are significant and cause additional deformations in the iron and contribute added noise. These forces represent nearly 50% force value increase due to magnetostriction. This is significant and must be accounted for in the design and analysis stages in electric machinery. Furthermore, the torque pulsation has increased as can be depicted in figure (6). This figure shows the torque from the transient solution with and without magnetostriction.

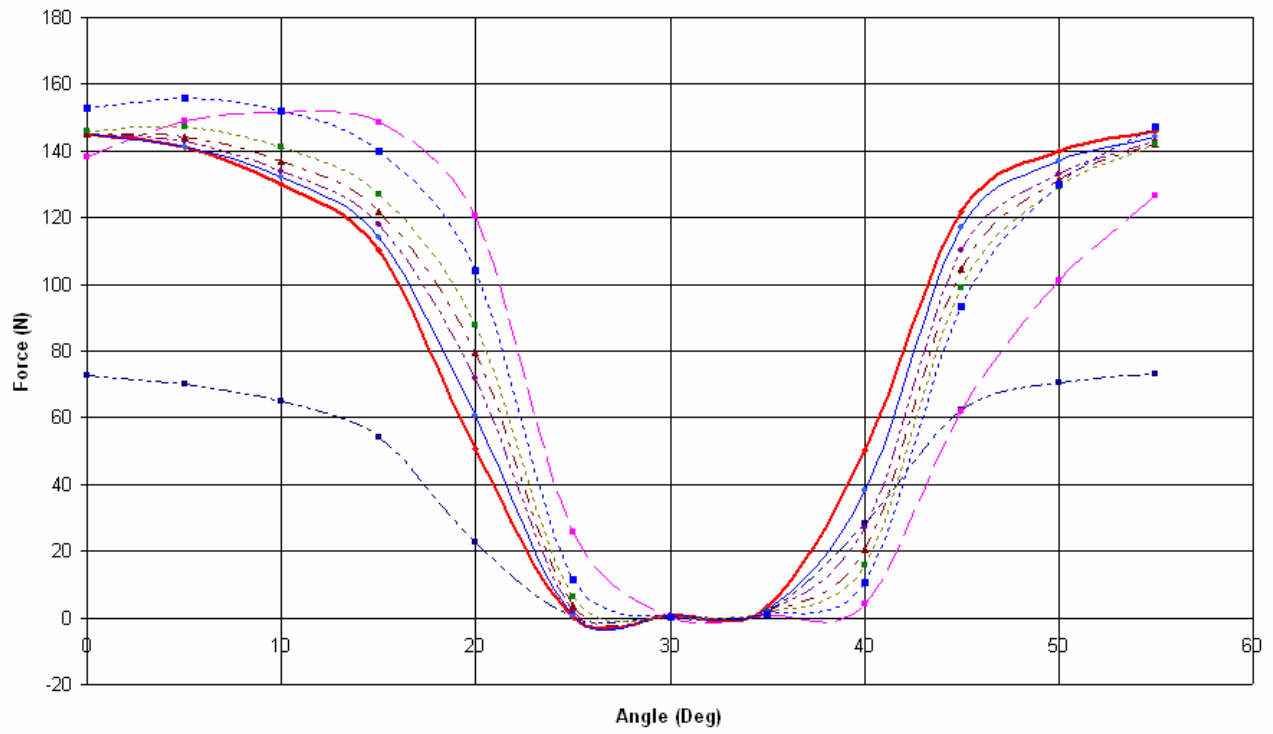


Fig. (4) Force values at selected points on stator without the Magnetostriction effect.

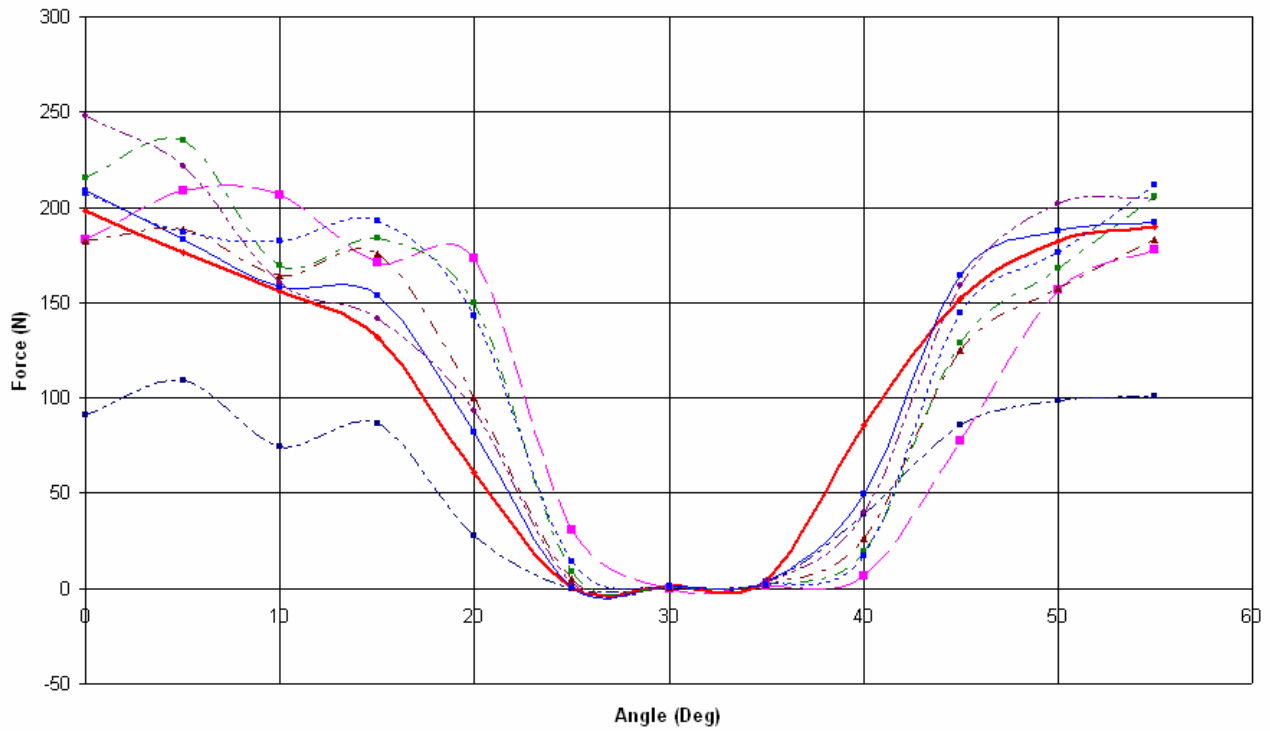


Fig. (5) Force values at selected points on stator with the Magnetostriction effect.

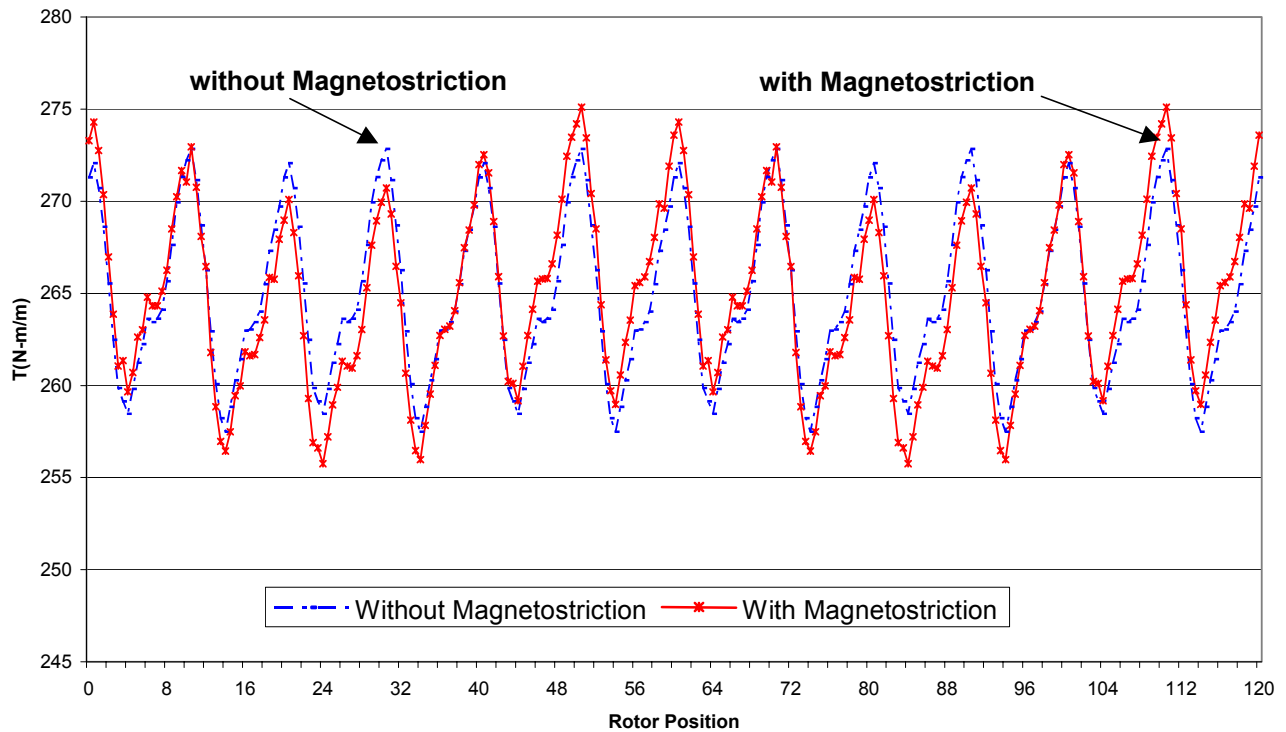


Fig. (6) Torque pulsation with and without Magnetostriction effect.

IV. CONCLUSION

We presented an investigation on the causes of noise and vibrations of electrical machinery based upon a strongly coupled numerical model comprising magnetic field and the mechanical deformation in the stator. The deformations in the stator are caused not only by reluctance forces, but also by magnetostriction effect of the stator iron. We noticed an increase in the deformations in the back iron and the force values causing it.

Measured data on magnetization curves under stress levels were used in obtaining the nonlinear transient numerical solutions presented here. A feedback to the magnetic system was performed utilizing the dependence of permeability on mechanical stress from the measured data. In order to account for this effect, the magnetostriction characteristic of iron $\lambda(H)$ was used. The dependency of permeability on mechanical stress was accounted for and built into the strong coupling scheme. Implementation results on a 2-hp, permanent magnet motor indicate that magnetostrictive forces are significant and must be considered design stage.

V. ACKNOWLEDGMENT

This work is supported by the Office of Naval Research.

VI. REFERENCES

- [1] Mohammed O. A., Calvert, T. E. and McConnell, R. "Coupled Magnetoelastic Finite Element Formulation Including Anisotropic Reluctivity Tensor and Magnetostriction Effects for Machinery Applications," *IEEE Transactions on Magnetics*, Vol. 37, No. 5, P.P. 3388-3392, September 2001.
- [2] Jiles, D. *Introduction to Magnetism and Magnetic Materials*, Chapman & Hall, London 1991.
- [3] Enokizono, M., Todaka, T. and Kanao, S., "Two-dimensional Magnetic Properties of Silicon Steel Sheet Subjected to a Rotating Field," *IEEE Transactions on Magnetics*, Vol. 29, No. 6, November 1993.
- [4] Enokizono, M. and Mori, S., "A Treatment of the Magnetic Reluctivity Tensor for Rotating Magnetic Field," *IEEE Transactions on Magnetics*, Vol. MAG-33, No. 2, March 1997.
- [5] Mohammed, O. A., Calvert, T., and McConnell, R. "Numerical Prediction of Magnetostrictive Behavior in Non-oriented Electrical Steel Sheets," *IEEE Conference on Electromagnetic Field Computation, IEEE CEFC'2000*, p.p. 419, June 2000.
- [6] Mohammed, O. A., Calvert, T. and McConnell, R., "A Model for Magnetostriction in Coupled Nonlinear Finite Element Magneto-elastic Problems in Electrical Machines," *Proceedings of the IEEE International Electric Machines and Drives Conference, Seattle, WA*, pp. 201-207, May 1999.

- [7] Coulomb, J. L. "A Methodology for the Determination of Global Electromechanical Quantities from Finite Element Analysis and its Application to the Evaluation of Magnetic Forces, Torque and Stiffness," IEEE Transactions on Magnetics, Vol. Mag-19, No.6, Nov. 1983.
- [8] Armco Non-oriented Electrical Steels, Armco Data 1997.
- [9] Tremolet de Lacheisserie, Etienne du, Magnetostriction Theory and Applications of Magnetoelasticity, CRC Press, 1993.



Dr. Osama A. Mohammed is a Professor and Associate Chairman of electrical and computer engineering at Florida International University, Miami, Florida, USA. He has many years of teaching, curriculum development, research and industrial consulting experience. He specializes in Electrical Energy Systems, Design Optimization of Electromagnetic Devices, and Artificial Intelligence Applications to Energy Systems as well as Electromagnetic Field Computations in Nonlinear Systems. Dr. Mohammed has been successful in obtaining a number of research contracts and grants from industries and government agencies. Professor Mohammed is a Fellow of IEEE and has authored and co-authored more than 200 technical papers in the archival literature as well as in National and International Conference records in addition to numerous technical reports and monographs.

He received many awards for excellence in research, teaching and service to the profession. Professor Mohammed has chaired sessions and programs in numerous International Conferences and has delivered numerous invited lectures at scientific organizations in North and South America, Europe and Asia. He was the General Chairman of the 1993 COMPUMAG International Conference and was the Vice-Chairman of COMPUMAG-RIO, November 3-7, 1997. He was also the General Chairman of the 1996 International Conference on Intelligent Systems Applications to Power Systems (ISAP'96), Orlando, Florida as well as the General Chairman of the 1994 IEEE Southeastcon, Miami, Florida. He also was a member of the technical program committee for the 1996 IEEE/CEFC conference, Okayama, Japan, and a member of the International Steering Committee for the ISEM conferences and the 1997 International Electric Machines and Drives Conference (IEEE-IEMDC), Milwaukee, Wisconsin, May 18-21, 1997. He was the Technical Program and Editorial Board Chairman for the IEEE/CEFC2000, Milwaukee, WI, June 4-7, 2000, in addition to several other technical programs and editorial boards of International Conferences. Dr. Mohammed has also organized and taught many short courses on power systems, electromagnetics and intelligent systems as well as educational techniques in the U.S.A and abroad.

He is a member of the IEEE/Power Engineering Society Governing Board and Chairman of its Constitution and Bylaws Committee. He is also the vice chairman of the electrical machinery committee. Dr. Mohammed is the

current Chairman of the Miami Section of IEEE. He also serves as chairman, officer or as an active member on several IEEE Power Engineering Society committees, sub-committees and technical working groups. Currently Professor Mohammed is the President of the Applied Computational Electromagnetic Society (ACES).



Thomas E. Calvert graduated in 1970 from Drexel University with a B.S. degree in electrical engineering. In 2003 he retired from the Naval Surface Warfare Center Carderock Division after 38+ years of federal service. His experience is primarily naval ship technology development and application, including machinery acoustics and advanced technology ship propulsion systems. His present position is Senior Principal Engineer with Anteon Corporation. He is supporting the Office of Naval Research All Electric Ship advanced technology programs.



Lynn J. Petersen is the deputy to the Program Officer for Submarine Science and Technology, at the Office of Naval Research (ONR), Arlington, VA. He is responsible for the funding, execution and management of US Navy motor and motor controller programs for ONR. Mr. Petersen has conducted investigations into motor and motor drive technologies and has written and presented numerous papers and reports in this field. He earned the Bachelors of Science Degree in Mathematics from the United States Naval Academy, Annapolis, MD in 1986 and earned the Masters of Science Degree in Mechanical Engineering in 1994 from the Naval Postgraduate School, Monterey, CA. Additionally, he is an Engineering Duty Officer Commander in the US Navy Reserve. Mr. Petersen is married and has two children.



Richard McConnell joined Naval Surface Warfare Center Carderock Division in 1983. He has spent his entire career analyzing and modeling electric machinery for naval applications, with a particular interest in using finite element methods for acoustic analysis. He holds a BS degree in Engineering Science & Mechanics from Virginia Polytechnic Institute and State University and an MS degree in Electric Power Engineering from Rensselaer Polytechnic Institute.

Multimode Hybrid Junctions

M. Hamid

Department of Electrical and Computer Engineering
University of South Alabama
Mobile, Alabama 36688, U.S.A.
mhamid@usouthal.edu

Abstract: The design, construction and testing of new hybrid junctions to perform the usual functions of summation and subtraction of incoming signals, not only over the fundamental mode but also to include the first few higher order modes, are important tasks for both military and civilian applications. The performance of the proposed junctions is evaluated experimentally and their relevance for a variety of microwave measurements and tracking radars suggested.

Keywords: Microwave Hybrid Junctions, Radar, Higher Order Modes

1. Introduction

Hybrid junctions or combining circuits are primarily magic tees, hybrid rings and directional couplers that are employed in a variety of electromagnetic engineering applications for duplexing and mixing of signals as well as impedance measurements. They are also used for signal sampling as well as amplitude-phase bridge networks for on-line monitoring and quality control of physical and dielectric properties of sheet materials during the manufacturing and processing stages [1-2].

The operation of these junctions is based on the principle that analog signals incident at some ports are added in or out of phase at other “sum” and “difference” ports, respectively. Thus it is possible to redirect signals to some ports and

isolate others. This is particularly important in radar systems as will be discussed later.

Applying the reciprocity principle to the four port magic tee shown schematically in Fig. 1a, we see how signals incoming at the collinear ports 3 and 4 add in phase at port 1 (parallel arm or P arm) and out of phase at port 2 (shunt arm or S arm). Conversely, a signal fed into port 1 splits equally between ports 3 and 4 with the outputs equal in amplitude and opposite in phase. On the other hand, a signal fed into port 2 also splits between ports 3 and 4 with the outputs equal in amplitude and phase. Thus two transmitters with equal power connected to ports 2 and 1 will produce twice as much power at port 4 and none at port 3.

The hybrid ring shown in Fig. 1b operates on similar principles where signals add in phase if they are an even number of half waveguide wavelengths ($\lambda_g/2$) apart and out of phase if they are an odd number of half waveguide wavelengths ($\lambda_g/2$) apart. With a signal fed into port 1, two outputs with equal amplitude and opposite phase will appear at ports 3 and 4 and zero output at port 2. On the other hand, a signal fed into port 2 produces two signals of equal amplitude and phase at ports 3 and 4 and cancels out at port 1. Also a signal fed into port 3 splits with equal amplitude and phase at ports 2 and 1, and no signal appears at port 4. Similarly, a signal fed into port 4 splits with equal and opposite phase at ports 1 and 2 and no signal appears at port 3.

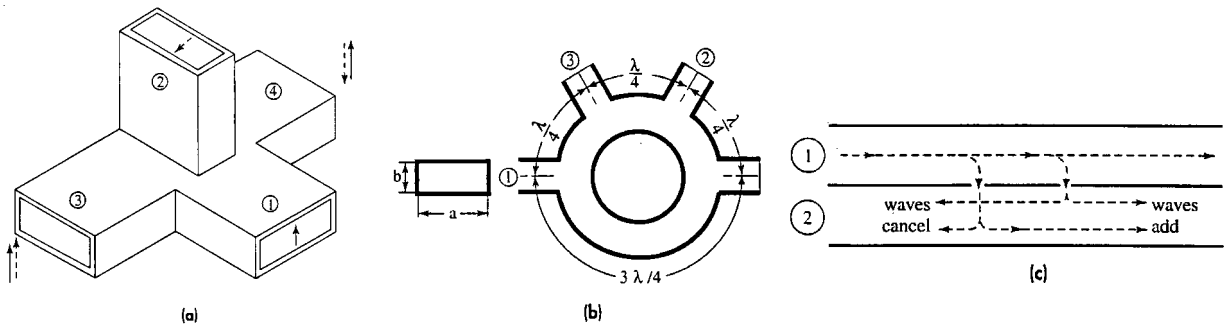


Figure 1. Schematic Diagram of Four-Port Hybrid Junctions.
 (a) Magic Tee (b) Hybrid Ring (c) Directional Coupler

The two hole directional coupler shown in Fig. 1c has two identical sampling holes between the primary and secondary waveguides so that forward signals add in phase at port 4 and cancel in port 2, and so on.

The disadvantages of all three hybrid junctions in the rectangular waveguides shown in Fig. 1 is the residual or leakage coupling between the collinear arms which are supposed to be isolated from each other at the design frequency or within the passband of the waveguide. At frequencies higher than the design frequency, but still above the cutoff frequency f_c of the fundamental TE or TM mode of the waveguide, this coupling increases so dramatically that the “magic tee” loses its “magic power”. In such

cases, higher order modes are excited in all three types of hybrid junctions, and a solution needs to be found for both rectangular and circular waveguide hybrid junctions.

The problem of redesigning hybrid junctions to perform analog sum and difference signals over the fundamental as well as higher order modes is very critical in certain types of tracking radars which are described in detail elsewhere [3]. As a review example, the conventional amplitude-comparison monopulse tracking radar for a single angle coordinate employs two squinted antenna feeds which are connected to a magic tee so that the sum (Σ) and difference (Δ) signals appear at the two output ports as shown in Fig. 2, [3]. On reception, the outputs of the sum and difference

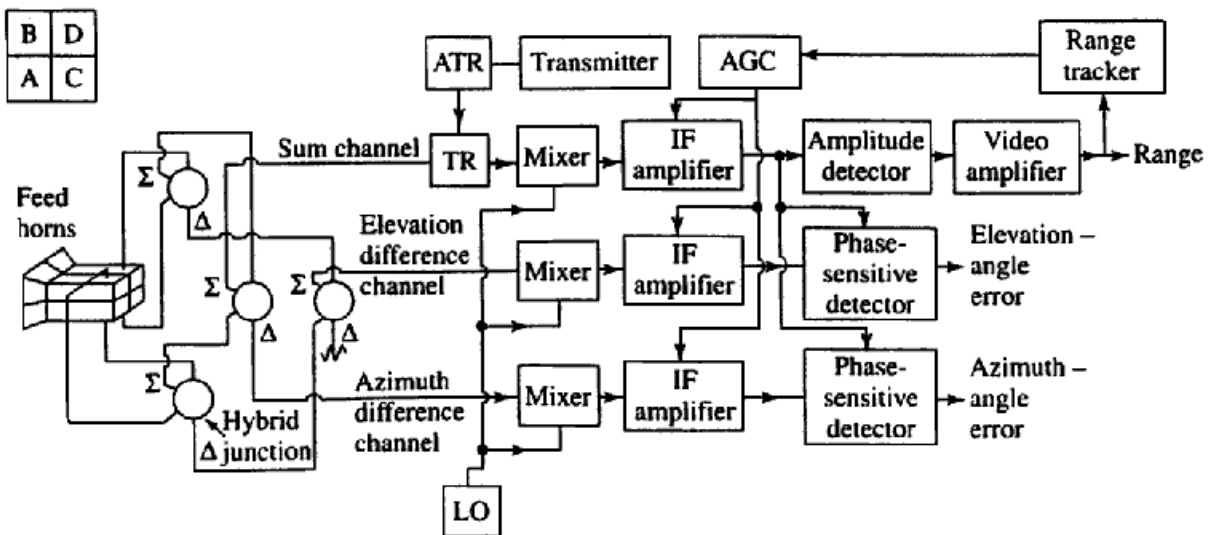


Figure 2. Schematic Diagram of Two-Coordinate (Azimuth and Elevation) Amplitude-Comparison Monopulse Tracking

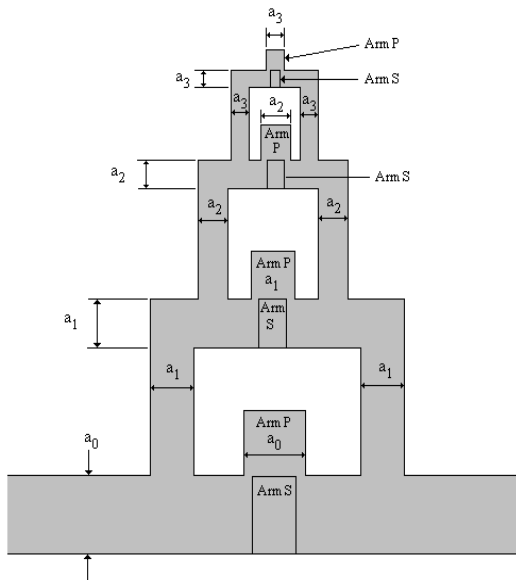
ports are each heterodyned to an intermediate frequency (IF) and amplified in a super heterodyne receiver where the local oscillator (LO) is shared by the two channels which are maintained with the same amplitude and phase characteristics. The transmitter is connected to the sum port of the hybrid junction while a duplexer is inserted in the sum channel to protect the sum channel receiver. The outputs of the sum and difference channels are inputted to a phase sensitive detector which is a nonlinear device that compares the two signals at the same frequency. The output of this detector is the angle-error signal θ_q whose magnitude is proportional to the difference between the target and boresight angles, while the polarity of the output indicates the direction of the angle error relative to the boresight. This technique is extended to two-angle coordinate measurement by employing a cluster of four (A, B, C and D) feed horns (feeding a cassegrain dish or space-fed phased array) which generate four partially overlapping (squinted) beams as shown schematically in Fig. 2. The sum pattern is found from $(A+B+C+D)$ while the azimuth difference pattern is obtained from $(A+B) - (C+D)$ and for the elevation plane the difference pattern is found from $(B+D) - (A+C)$. Range information is extracted from the output of the sum channel after envelope detection and is employed for range tracking.

Although the four-horn feed system is simple, it cannot provide the sum and difference patterns that are independently optimized. The sum pattern should have maximum gain on axis which requires uniform aperture illumination. On the other hand, the difference pattern should have an aperture illumination which results in a large slope of the error signal at the beam crossover. For this, some improvement has been incorporated in some precision tracking radars by using a five-horn feed consisting of one horn in the middle to produce the sum pattern surrounded by four horns to generate the difference patterns. The analysis in the literature indicates that the sizes of the four horns generating the difference pattern should be twice as big as the central horn

generating the sum pattern. Instead of further improvement by adopting a twelve-horn design to satisfy the optimization criteria and avoid complexity, it has been the practice in many types of radar to use higher order waveguide modes to obtain better control of the sum and difference patterns. An example of such systems is the AN/MPS-39 for multiple missile tracking or the MOTR (Multiple Object Tracking Radar) which employ a four-horn triple-mode feed. For these multimode feed systems and for other systems, which employ multiple frequencies or frequency agility/diversity to smooth out the angle error due to glint, it is necessary to develop new multimode hybrid junctions to produce the sum and difference patterns which is the main purpose of this paper.

2. Outline of Proposed Hybrid Junctions

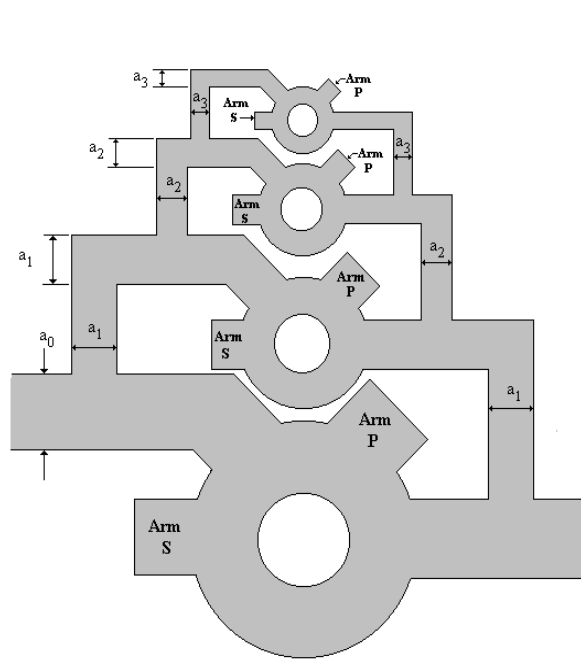
The primary objective of this project is to design and develop new types of multimode hybrid junctions in rectangular and circular waveguides which permit the extraction of separate sum and difference signals for the fundamental as well as higher order TE and TM modes in multimode signals. These are shown schematically in Fig. 3 for rectangular and circular waveguides. The basic approach is to use cascaded hybrid junctions, one for each mode of interest, so that the sum and difference signals can be displayed and processed separately for each mode. Starting with Fig. 3a, we see that the collinear arms of the magic tee in the primary rectangular waveguide accommodate the fundamental as well as all the higher order modes excited above frequencies f_c relative to $(f_c)_{TE_{10}}$ of the fundamental mode. A second mode magic tee is inserted in cascade with its collinear arms coupled to the primary waveguide so as to extract the second and all higher order modes, but not the primary mode, since its dimensions are such that the primary mode is below cutoff. Only the second mode is processed in the second mode magic tee since the third and higher order modes are extracted in the third mode magic tee prior to



H-plane dimensions $a_0 > a_1 > a_2 > a_3$ for the parallel (P), summing arms of the magic tees

Some E-plane dimensions for the series (S), difference arms of the magic tees may be equal, depending on the mode selected. The difference arms are perpendicular to the plane of the paper.

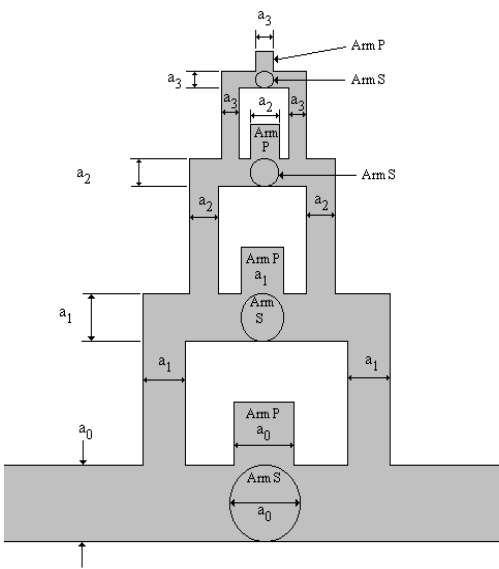
Figure 3.a. Cascaded Mode-Selective Rectangular WG Magic Tees



H-plane dimensions $a_0 > a_1 > a_2 > a_3$ for the parallel (P), summing arms of the hybrid junctions.

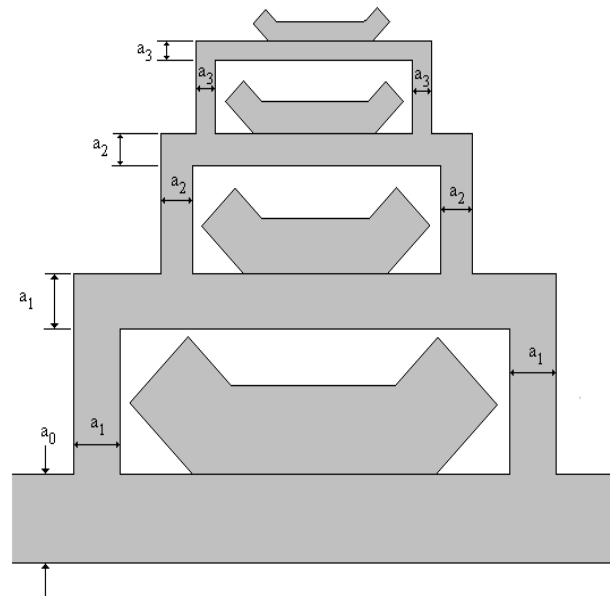
Some E-plane dimensions for the series (S), difference arms of the hybrid junctions may be equal, depending on the mode selected.

Figure 3.c. Cascaded Mode-Selective Hybrid Junctions



Diameters $a_0 > a_1 > a_2 > a_3$ provide selection of successively higher modes in a manner similar to cascading high-pass filters with successively higher cut-off frequencies.

Figure 3.b. Cascaded Mode-Selective Circular WG Magic Tees



H-plane dimensions $a_0 > a_1 > a_2 > a_3$ for the parallel (P), summing arms of the hybrid junctions.

Some E-plane dimensions for the series (S), difference arms of the hybrid junctions may be equal, depending on the mode selected.

Figure 3.d. Cascaded Mode-Selective Directional Couplers

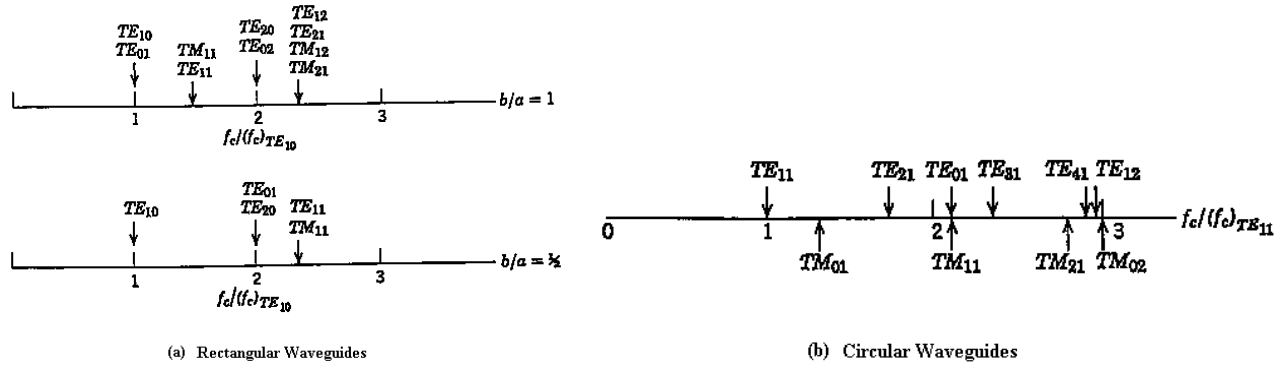


Figure 4. Relative Cutoff Frequencies of Higher Order Modes in Waveguides

processing, etc. It is obvious that the waveguide dimensions decrease as the selected mode to the primary waveguide so as to extract the second and all higher order modes, but not the primary mode, since its dimensions are such that the primary mode is below cutoff. Only the second mode is processed in the second mode magic tee since the third and higher order modes are extracted in the third mode magic tee prior to

processing, etc. It is obvious that the waveguide dimensions decrease as the selected mode number increases so that the procedure will be limited to only the first few modes to avoid network complexity. The actual modes to be selected depend on the usual rectangular waveguide dimensions (a and b) as illustrated in Fig. 4a while Fig. 4b shows a similar spectrum for circular waveguide modes to which the technique will be extended later. The initial

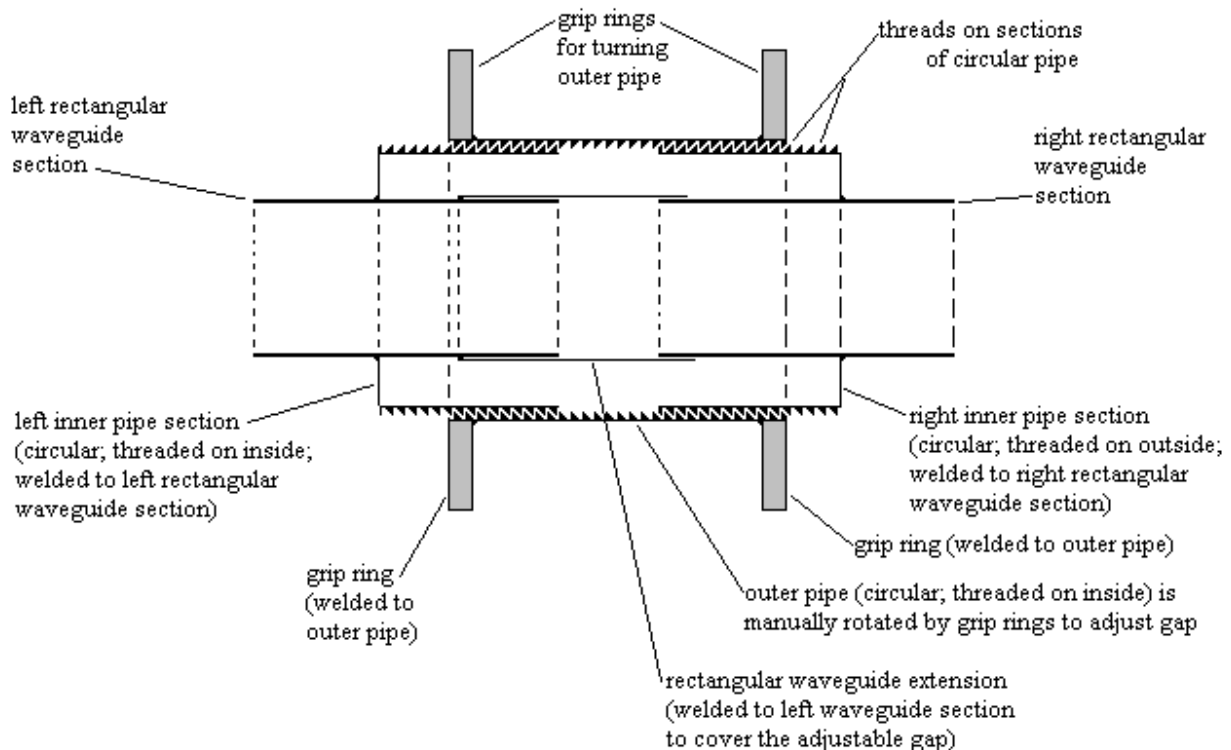


Figure 5. Schematic Diagram of Adjustable Length Rectangular Waveguide

design will therefore concentrate on the rectangular waveguide dimensions (a and b) of each magic tee such that all few modes of interest are excited within the available frequency band of the sweep oscillator.

One drawback of the proposed technique is the effect of the added junctions on the voltage standing wave ratio (VSWR) in the primary and branch waveguides of the multimode hybrid junctions [3]. Although slide screw tuners as well as rotary vane, ferrite or other types of phase shifters can be used to minimize the VSWR, an alternative method is proposed to avoid heating of tuning elements or power leakage from rotary vane slots, particularly in high power radar applications. This is shown schematically in Fig. 5 where the waveguide length is varied by a sliding mechanical technique which provides adequate phase shift. A threaded sleeve, which is turned using two outer rings attached to a circular pipe, introduces spacing between two adjacent waveguides which slide inside an outer waveguide provided for that purpose. This adjustable waveguide length method is novel and useful for testing the proposed hybrid junctions for each mode.

3. Experimental Procedure and Results

The three hybrid junctions were constructed and tested only for the fundamental TE_{10} as well the first higher TE_{20} modes only. The testing procedure employed a 2-18.6 GHz Hewlett Packard sweep oscillator whose output was displayed on a spectrum analyzer to determine the amplitude of each mode excited in the passband of the main feed waveguide. This output was then fed into the collinear arms of each hybrid junction and the signals at the sum and difference arms of each junction were then measured and compared with the expected values of the higher order mode. Slotted waveguides and two-way directional couplers were inserted in series with the collinear arms of each junction to measure the VSWR with and

without the adjustable length waveguide. The main test frequencies were 3, 6, 9 and 18 GHz, although secondary frequencies were employed as well. The maximum VSWR observed was 1.12 while the maximum deviation of the TE_{20} mode amplitude from the expected value was 7.6% for the rectangular magic tee, 9.1% for the hybrid rind and 6.9% for the directional coupler.

4. Conclusions

New hybrid junctions were designed, constructed and tested for the first two propagating modes in rectangular waveguides for standard laboratory measurements as well as radar applications. The design of the various waveguide sections will be optimized in the future using the method of moments [4] while the proposed variable-length waveguide proved helpful in the proposed hybrid junctions to minimize mismatch losses. The extension of multimode hybrid junctions to circular waveguides will be investigated separately once the rectangular waveguide multimode junctions are tested over several modes.

Acknowledgement

The author wishes to acknowledge the financial assistance of the Faculty of Graduate Studies of the University of South Alabama which made this research possible. Thanks are also due to David Vanlandingham and Heath Parker for their assistance in preparing the illustrations and formatting the paper.

References

- [1] H. Reich, P. Ordung, H. Krauss and J. Skalnik, "Microwave Theory and Techniques", Chapter 6, Van Nostrand, 1953.
- [2] T. Ishii, "Microwave Engineering", second Edition, Harcourt Brace Jovanovich Publishers, Chapter 6, 1989.

- [3] M. Skolnik, "Radar Systems", Chapter 4, McGraw-Hill, 2001.
- [4] A. K. Hamid, I. R. Ciric and M. Hamid, "A Generalized Network Formulation for Symmetric Double-Step Waveguide Discontinuities", *Int'l Journal of Electronics*, Vol. 67, No. 3, pp. 427-435, Sept. 1989.



Michael Hamid Graduated from McGill University in Montreal with a B.Eng. degree in 1960, a M.Eng. degree in 1962 and from the University of Toronto with a Ph.D. degree in 1966, all in Electrical Engineering. He joined the University of Manitoba in 1965 where he became a Professor of Electrical Engineering and head of

the Antenna Laboratory. He was a Visiting Professor at the Universities of California Davis and Central Florida and is presently a Professor of Electrical Engineering at the University of South Alabama. He is a past president of the International Microwave Power Institute, a Fellow of IEE and IEEE and published 307 referred articles and 25 patents.

Electromagnetic Scattering by a System of Dielectric Spheres Coated With a Dielectric Shell

A-K. Hamid
Department of Electrical and
Computer Engineering
University of Sharjah
P.O. Box 27272, Sharjah, U.A.E
email: akhamid@Sharjah.ac.ae

M. I. Hussein
Department of Electrical Engineering
United Arab Emirates University
P.O. Box 17555, Al-Ain, United Arab
Emirates
email: MIHussein@uaeu.ac.ae

M. Hamid
Department of Electrical Engineering
University of South Alabama
Mobile, AL 36688, U.S.A
email: mhamid@usouthal.edu

Abstract

Analytical solution is derived to the problem of scattering of electromagnetic plane wave by an array of dielectric spheres each coated with a dielectric shell. The incident, scattered and transmitted electric and magnetic fields are expressed in terms of the vector spherical wave functions. The vector spherical translation addition theorem is applied to impose the boundary conditions on the surface of various layers. Numerical results are computed and presented graphically for the radar cross sections of several configurations of spheres system with multi dielectric layers.

1. Introduction

Many authors have studied the scattering of electromagnetic plane wave by a dielectric sphere coated with a dielectric shell. Aden and Kerker [1] obtained analytical expressions to the scattering of electromagnetic plane wave by a dielectric sphere coated with a concentric spherical shell of different dielectric materials, while Scharfman [2] presented numerical results for the special case of a small electrical radius ($ka < 1$) dielectric coated conducting sphere. It was found in those early studies that the presence of dielectric coatings leads to substantial increase in the backscattering cross section for an appropriate choice of the dielectric constant and thickness of the coating relative to that of uncoated sphere. Further, Wait has extended the solution to the case of scattering by a radially inhomogeneous sphere [3], while a numerical solution using the method of moments obtained by Medgyesi-Mitschang and Putnam for the case of dielectric-coated concentric sphere [4]. More recently, an exact solution of electromagnetic plane wave scattering by an eccentric multilayered sphere was developed by Lim and Lee [5]. Numerous papers on the scattering from systems of spheres of various natures in close proximity have been treated by numerous researchers [6-11].

Up to now, there has been no analytical or numerical solution to the problem of scattering of electromagnetic plane wave by an array of conducting spheres each coated

with a dielectric layer. In this paper, we extend the solution of scattering by two dielectric spheres covered with a dielectric shell [9] to the case of scattering by a system of dielectric spheres each covered with a dielectric shell. The solution to this problem has many practical applications since, for example, it may be used to study the scattering by complex objects simulated by a collection of spheres [12], and it may also be used to check the accuracy of numerical solutions.

From the design point of view, the backscattering cross section of an array of N dielectric coated spheres can be controlled to exploit multiple resonances by optimizing the multivariables of the system. These include the size and location of each sphere, number of dielectric layers coating each sphere as well as the thickness and relative dielectric constant of each layer as already done for conducting cylinders [13].

2. Formulation of the Problem

Consider a linear array of N dielectric spheres each coated with a dielectric shell and having different radii and unequal spacing with centers lying along the z axis, as shown in Fig. 1. Electromagnetic plane wave of unit electric field intensity, whose propagation vector \bar{K} lies in the x-z plane and makes an angle α with the z-axis, is assumed to be incident on the spheres. Its incident electric and magnetic fields are

$$\bar{E}_i = e^{j\bar{k} \cdot \bar{r}} \hat{y} \quad (1)$$

$$\bar{H}_i = -\frac{1}{\eta} e^{j\bar{k} \cdot \bar{r}} (\cos \alpha \hat{x} - \sin \alpha \hat{z}) \quad (2)$$

with k being the wave number, \hat{x} , \hat{y} , and \hat{z} are the unit vectors along the x, y and z axes, respectively, and η is the surrounding medium intrinsic impedance. The incident electric and magnetic fields may be expanded in terms of spherical vector wave functions around the center of the p^{th} sphere as

$$\bar{E}_i(r_p, \theta_p, \phi_p) = \frac{\sum_{n=1}^{\infty} \sum_{m=-n}^{m=n} [P_p(m, n) \bar{N}_{mn}^{(1)}(r_p, \theta_p, \phi_p) + Q_p(m, n) \bar{M}_{mn}^{(1)}(r_p, \theta_p, \phi_p)]}{\quad} \quad (3)$$

$$\eta \bar{H}_i(r_p, \theta_p, \phi_p) = j \frac{\sum_{n=1}^{\infty} \sum_{m=-n}^{m=n} [P_p(m, n) \bar{M}_{mn}^{(1)}(r_p, \theta_p, \phi_p) + Q_p(m, n) \bar{N}_{mn}^{(1)}(r_p, \theta_p, \phi_p)]}{\quad} \quad (4)$$

where $\bar{M}_{mn}^{(1)}$ and $\bar{N}_{mn}^{(1)}$ are the spherical vector wave functions of the first kind representing incoming waves associated with the spherical Bessel function, while $P_p(m, n)$ and $Q_p(m, n)$ are the incident field expansion coefficients defined in [7-8,14]. The field in the region II can be also expressed in terms of the vector spherical wave functions of the first and third kinds. Hence the electric and magnetic fields may be written as

$$\bar{E}_{II}(r_p, \theta_p, \phi_p) = \frac{\sum_{n=1}^{\infty} \sum_{m=-n}^{m=n} [A'_{Ep}(m, n) \bar{N}_{mn}^{(1)}(r_p, \theta_p, \phi_p) + A''_{Ep}(m, n) \bar{N}_{mn}^{(3)}(r_p, \theta_p, \phi_p) + A'_{Mp}(m, n) \bar{M}_{mn}^{(1)}(r_p, \theta_p, \phi_p) + A''_{Mp}(m, n) \bar{M}_{mn}^{(3)}(r_p, \theta_p, \phi_p)]}{\quad} \quad (5)$$

$$\eta \bar{H}_{II}(r_p, \theta_p, \phi_p) = j \frac{\sum_{n=1}^{\infty} \sum_{m=-n}^{m=n} [A'_{Ep}(m, n) \bar{M}_{mn}^{(1)}(r_p, \theta_p, \phi_p) + A''_{Ep}(m, n) \bar{M}_{mn}^{(3)}(r_p, \theta_p, \phi_p) + A'_{Mp}(m, n) \bar{N}_{mn}^{(1)}(r_p, \theta_p, \phi_p) + A''_{Mp}(m, n) \bar{N}_{mn}^{(3)}(r_p, \theta_p, \phi_p)]}{\quad} \quad (6)$$

where $A'_{pE}(m, n)$, $A'_{pM}(m, n)$, $A''_{pE}(m, n)$, and $A''_{pM}(m, n)$ are the field expansion coefficients, while $\bar{M}_{mn}^{(3)}$ and $\bar{N}_{mn}^{(3)}$ are the vector spherical wave functions of the third kind representing outgoing waves associated with the spherical Hankel function. The subscripts E and M denote transverse magnetic (TM) and transverse electric waves (TE), respectively. The field in region I of the p th sphere may be written in terms of the vector wave functions of the first kind, i.e.,

$$\bar{E}_I(r_p, \theta_p, \phi_p) = \frac{\sum_{n=1}^{\infty} \sum_{m=-n}^{m=n} [A_{EP}(m, n) \bar{N}_{mn}^{(1)}(r_p, \theta_p, \phi_p) + A_{MP}(m, n) \bar{M}_{mn}^{(1)}(r_p, \theta_p, \phi_p)]}{\quad} \quad (7)$$

$$\bar{H}_I(r_p, \theta_p, \phi_p) = \frac{\sum_{n=1}^{\infty} \sum_{m=-n}^{m=n} [A_{EP}(m, n) \bar{M}_{mn}^{(1)}(r_p, \theta_p, \phi_p) + A_{MP}(m, n) \bar{N}_{mn}^{(1)}(r_p, \theta_p, \phi_p)]}{\quad} \quad (8)$$

where A_{EP} and A_{MP} are the unknown transmitted coefficients. Finally, the scattered electric and magnetic fields from the p th sphere are expanded as

$$\bar{E}^s(r_p, \theta_p, \phi_p) = \frac{\sum_{n=1}^{\infty} \sum_{m=-n}^{m=n} [A_{Ep}(m, n) \bar{N}_{mn}^{(3)}(r_p, \theta_p, \phi_p) + A_{Mp}(m, n) \bar{M}_{mn}^{(3)}(r_p, \theta_p, \phi_p)]}{\quad} \quad (9)$$

$$\eta \bar{H}^s(r_p, \theta_p, \phi_p) = j \frac{\sum_{n=1}^{\infty} \sum_{m=-n}^{m=n} [A_{Ep}(m, n) \bar{M}_{mn}^{(3)}(r_p, \theta_p, \phi_p) + A_{Mp}(m, n) \bar{N}_{mn}^{(3)}(r_p, \theta_p, \phi_p)]}{\quad} \quad (10)$$

where $A_{EP}(m, n)$, $A_{MP}(m, n)$ are the unknown scattered field coefficients. To express the scattered fields from the q th sphere in the coordinate system of the p th sphere, we apply the spherical vector translation addition theorem for translation along the z -axis [15], i.e.,

$$\bar{M}_{mn}^{(3)}(r_q, \theta_q, \phi_q) = \frac{\sum_{v=1}^{\infty} [A_{mn}^{mv}(d_{pq}) \bar{M}_{mv}^{(1)}(r_p, \theta_p, \phi_p) + B_{mn}^{mv}(d_{pq}) \bar{N}_{mn}^{(1)}(r_p, \theta_p, \phi_p)]}{\quad} \quad (11)$$

$$\bar{N}_{mn}^{(3)}(r_q, \theta_q, \phi_q) = \frac{\sum_{v=1}^{\infty} [A_{mn}^{mv}(d_{pq}) \bar{N}_{mv}^{(1)}(r_p, \theta_p, \phi_p) + B_{mn}^{mv}(d_{pq}) \bar{M}_{mn}^{(1)}(r_p, \theta_p, \phi_p)]}{\quad} \quad (12)$$

where $A_{mn}^{mv}(d_{pq})$ and $B_{mn}^{mv}(d_{pq})$ are the translation coefficients of the spherical vector translation addition theorem. To determine the unknown scattered field coefficients, we apply the boundary conditions on the various interfaces, i.e.,

$$\bar{r}_p \times \left[\bar{E}_i(b_p, \theta_p, \phi_p) + \sum_{p=1}^N \bar{E}^s(b_p, \theta_p, \phi_p) \right] = \bar{r}_p \times \bar{E}_{II}(b_p, \theta_p, \phi_p) \quad (13)$$

$$\bar{r}_p \times \left[\bar{H}_i(b_p, \theta_p, \phi_p) + \sum_{p=1}^N \bar{H}^s(b_p, \theta_p, \phi_p) \right] = \bar{r}_p \times \bar{H}_{II}(b_p, \theta_p, \phi_p) \quad (14)$$

$$\bar{r}_p \times \bar{E}_{II}(a_p, \theta_p, \phi_p) = \bar{r}_p \times \bar{E}_I(a_p, \theta_p, \phi_p) \quad (15)$$

$$\bar{r}_p \times \bar{H}_{II}(a_p, \theta_p, \phi_p) = \bar{r}_p \times \bar{H}_I(a_p, \theta_p, \phi_p) \quad (16)$$

Substituting the appropriate field expansion expressions in equations (13) to (16), and applying the orthogonality properties of spherical vector wave functions and eliminating the transmission coefficients we obtain

$$A_{EP}(m, n) = v_n(\rho_p) P_p(m, n) + \sum_{\substack{q=1 \\ q \neq p}}^N \sum_{v=1}^{\infty} [A_{mn}^{mv}(dpq) A_{EP}(m, v) + B_{mn}^{mv}(dpq) A_{MP}(m, v)] \quad (17)$$

$$A_{Mp}(m, n) = u_n(\rho_p) Q_p(m, n) + \sum_{\substack{q=1 \\ q \neq p}}^N \sum_{v=1}^{\infty} [A_{mn}^{mv}(dpq) A_{Mp}(m, v) + B_{mn}^{mv}(dpq) A_{Ep}(m, v)] \quad (18)$$

where $v_n(\rho_p)$ and $u_n(\rho_p)$ are the electric and magnetic scattered field coefficients for a single dielectric sphere coated with a dielectric layer [1,9]. Equations (17) and (18) may be written in matrix form for the purpose of computing the scattered field coefficients, i.e.

$$\bar{A} = \bar{L} + T \bar{A} \quad (19)$$

where \bar{A} and \bar{L} are column matrices for the unknown scattered and incident field coefficients, respectively, and T is a square matrix which contains the translation addition coefficients.

Once the scattered field is computed from equation (19), the normalized bistatic cross section can be obtained as in [16].

3. Numerical Results

In order to check the validity of our computer program, several numerical tests were conducted and the results compared favorably with previously published results [7-8,11]. These tests included the limiting cases of (i) an array of dielectric spheres obtained by setting $kb \approx ka$, $\epsilon_{lr} = 1$ or $\epsilon_{lr} = \epsilon_r$ (ii) an array of conducting spheres each coated with a single dielectric layer obtained by setting $\epsilon_r = \infty$ and (iii) an array of conducting spheres obtained by setting $\epsilon_r = \infty$ and $kb \approx ka$ or $\epsilon_{lr} = 1$.

In this paper, we presented numerical results for different sphere arrays to show the dependence of the radar cross section on various parameters characterizing the geometry, material properties, and incidence angles. Fig. 2 shows the normalized bistatic cross section versus the scattering angle θ for a system of three identical spheres in the E and H-planes. The electrical radii of the outer and inner spheres are $ka=2.0$ and $kb=2.5$, respectively, while the electrical separation between successive spheres is $kd=7.0$, and the relative dielectric permittivity of the inner dielectric layer is 3.0 and the outer is air. The purpose of this comparison is to check the accuracy of the computer code for the dielectric sphere case [8] as a special case of the dielectric spheres except the relative dielectric permittivity of the dielectric layer is set equal to unity. The parameters of Fig. 3 are similar to Fig. 2 except that the dielectric layer has a value of 2. We can see that the number of resonances in E plane is increased. Figs. 4 and 5 have the same parameters as in Fig. 3 except that the number of spheres is increased to five and eight, respectively. We can see that the number of resonances also increases with the number of spheres.

Fig. 6 shows the normalized backscattering cross section versus the electrical distance (kd), which ranges from 8 (touching) to 15.5 for end fire incidence and the number of spheres is five. The electrical radii of outer and inner spheres are $ka=4.0$ and $kb=3.0$, respectively, while the relative dielectric permittivity of the inner dielectric layer is 3.0 and for the outer layer is 2. Fig. 7 is similar to Fig. 6 except the number of spheres is increased to 8. We can see that the location of the maximum peaks did not change by increasing the number of spheres for both cases. Furthermore, the magnitude of the normalized backscattering cross section at the maximum peaks increased with increasing number of spheres.

In Figs. 8 and 9 we have plotted the normalized backscattering cross as a function of the angle of incidence α , which ranges from 0 to 90 degrees for a system of three and eight spheres. The electrical radii of the outer and inner spheres are $ka=1.5$ and $kb=1.0$, respectively, while the relative permittivity of the inner dielectric layer is 4 while

for the outer layer is 3 and the electrical separation between the centers of the spheres is 3.0 (touching).

4. CONCLUSIONS

We have obtained an analytic solution of the problem of scattering by an array of dielectric spheres each coated with a dielectric shell. The boundary conditions are satisfied at various interfaces with the help of the vector translation addition theorem. The system of equations was written in matrix form while the scattered field coefficients were obtained by matrix inversion. Numerical results were presented for different numbers of spheres, angles of incidence, electrical separation, and relative dielectric constant. For the general case of spheres orientation, the reader may find more details in [8].

ACKNOWLEDGMENT

The first author wishes to acknowledge the support provided by University of Sharjah. The second author wishes to acknowledge the support of the United Arab Emirates University, while the third author wishes to acknowledge the financial support of the University of South Alabama and the National Science Foundation.

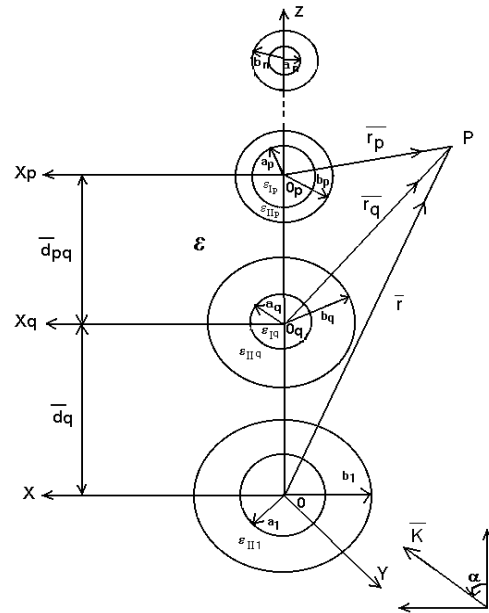


Fig. 1: Geometry of the scattering problem.

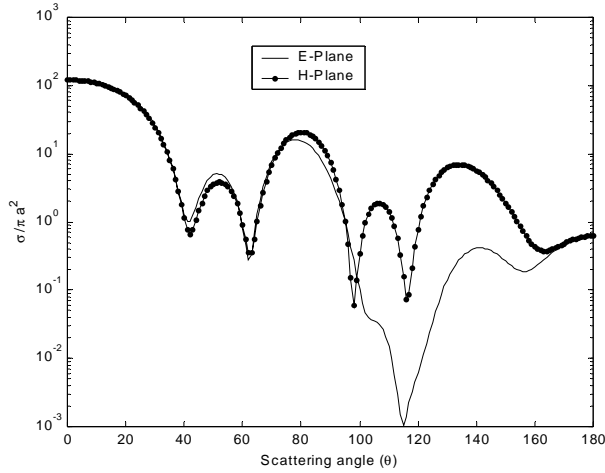


Fig. 2: Normalized bistatic cross section patterns for three identical dielectric spheres each covered with dielectric layer with $ka=2.0$, $kb=2.5$, $kd=7.0$, $\alpha=0$, $\mathcal{E}_{I_r}=3.0$, and $\mathcal{E}_{II_r}=1.0$. In the E-plane ($\phi = \pi/2$) and H-plane ($\phi = 0$).

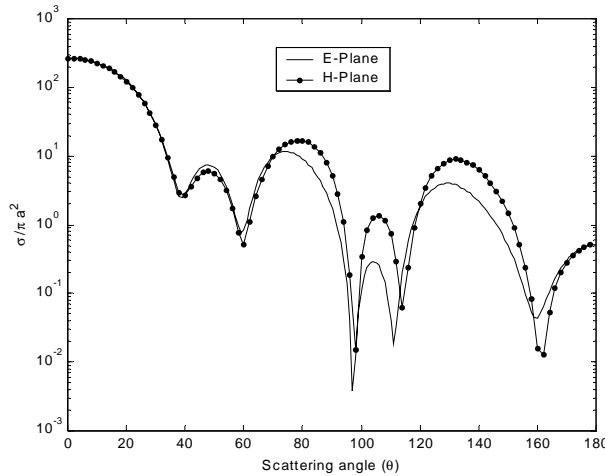


Fig. 3: Normalized bistatic cross section patterns for three identical dielectric spheres each covered with dielectric layer with $ka=2.0$, $kb=2.5$, $kd=7.0$, $\alpha=0$, $\mathcal{E}_{I_r}=3.0$, and $\mathcal{E}_{II_r}=2.0$.

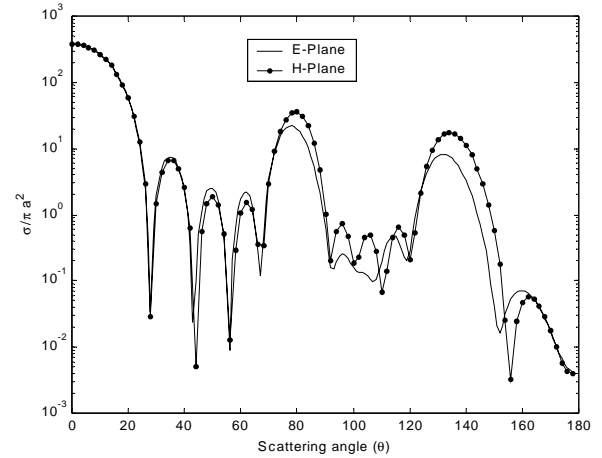


Fig. 4: Normalized bistatic cross section patterns for five identical dielectric spheres each covered with a dielectric layer with $ka=2.0$, $kb=2.5$, $kd=7.0$, $\alpha=0$, $\mathcal{E}_{I_r}=3.0$, and $\mathcal{E}_{II_r}=2$.

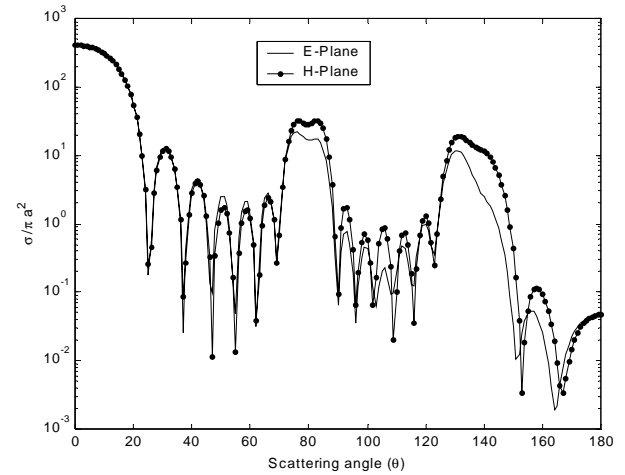


Fig. 5: Normalized bistatic cross-section patterns for eight identical dielectric spheres each covered with a dielectric layer with $ka=2.0$, $kb=2.5$, $kd=7.0$, $\alpha=0$, $\mathcal{E}_{I_r}=3.0$, and $\mathcal{E}_{II_r}=2.0$.

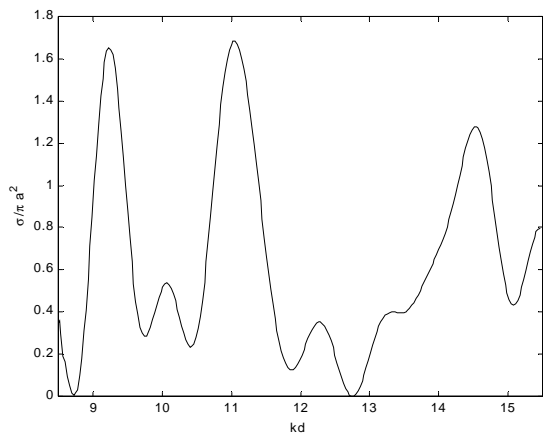


Fig. 6: Normalized backscattering cross section versus electrical separation (kd) for end-fire incidence and a linear array of five identical dielectric spheres each covered with a dielectric layer with: $ka=4.0$, $kb=3.0$, $\alpha = 0.0$, $\epsilon_{lr}=3.0$, and $\epsilon_{llr}=2.0$.

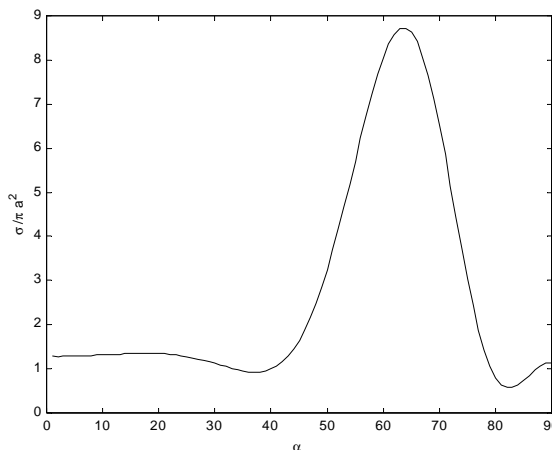


Fig. 8: Normalized backscattering cross section versus aspect angle α for a linear array of three identical dielectric spheres each covered with a dielectric layer with $ka=1.5$, $kb=1.0$, $kd=3.0$, $\epsilon_{lr}=4.0$, and $\epsilon_{llr}=3.0$.

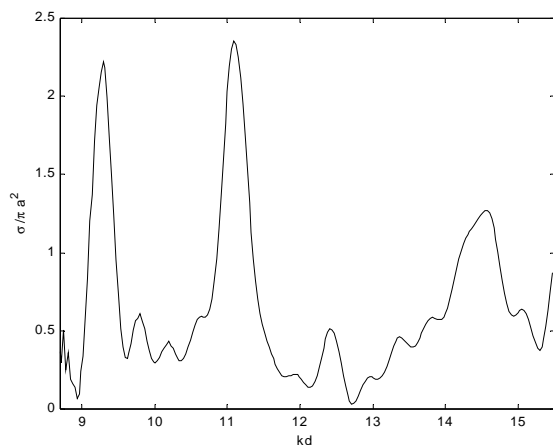


Fig. 7: Normalized backscattering cross section versus electrical separation (kd) for end-fire incidence and a linear array of eight identical dielectric spheres each covered with a dielectric layer with: $ka=4.0$, $kb=3.0$, $\alpha = 0.0$, $\epsilon_{lr}=3.0$, and $\epsilon_{llr}=2.0$.

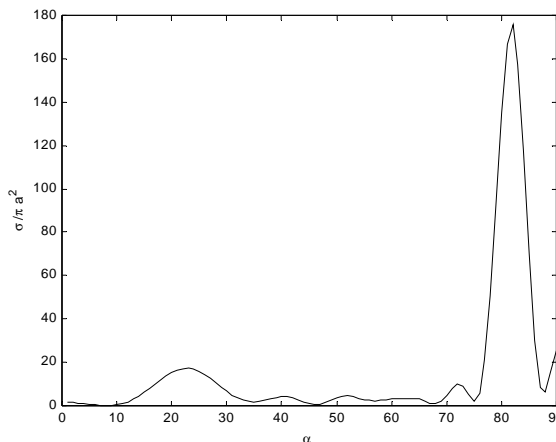


Fig. 9: Normalized backscattering cross section versus aspect angle α for a linear array of eight identical dielectric spheres each covered with a dielectric layer with $ka=1.5$, $kb=1.0$, $kd=3.0$, $\epsilon_{lr}=4.0$, and $\epsilon_{llr}=3.0$.

REFERENCES

1. Aden, A.L., and Kerker, M., "Scattering of electromagnetic waves from two concentric spheres", J. Appl. Phys., 22, pp. 1242-1246, 1951.
2. Scharfman, H, "Scattering from dielectric coated spheres in the region of the first resonance", J. Appl. Phys., 25, pp. 1352-1356, 1954.
3. Wait, J.R., "Electromagnetic scattering from a radially inhomogeneous spheres," Appl. Sci. Res., vol. 10, p. 441, 1963.

4. Medgyesi-Mitschang, L.N, and Putnam, J.M., "Electromagnetic scattering from axially inhomogeneous bodies of revolution," IEEE Trans. Antennes Propag., vol. AP-32, no. 8, pp. 797-806, 1984.
5. Kyutae, L., and Lee, S.L., "Analysis of Electromagnetic scattering from an eccentric multilayered sphere," IEEE Trans. Antennes Propag., vol. AP-43, no. 11, pp. 1325-1328, 1995.
6. Bruning, J. H., and Lo, Y., 1971, "Multiple scattering of EM waves by spheres: Parts I

- and II", IEEE Trans., AP-19, pp. 378-400, 1971.
7. Hamid, A-K., Ciric I.R., and Hamid, M., "Multiple scattering by a linear array of conducting spheres", Can. J. Phys., vol. 68, pp. 1157-1165, 1990.
 8. Hamid, A-K., Ciric I.R., and Hamid, M., "Iterative Solution of The Scattering by an Arbitrary Configuration of Conducting or Dielectric Spheres", IEE Proc., Part H, vol. 148, pp. 565-572, 1991.
 9. Hamid, A-K., Ciric I.R., and Hamid, M., "Analytic Solutions of The Scattering by Two Multilayered Dielectric Spheres", Can. J. Phys., vol. 70, pp. 696-705, 1992.
 10. Comberg, U., and Wriedt, T. " Comparison of scattering calculations for aggregated particles based on different models," J. of Quantitative Spectroscopy and Radiative Transfer, vol. 63, pp. 149-162, 1999.
 11. A-K. Hamid, M.I. Hussein, and M. Hamid, "Radar Cross Section of a System of Conducting Spheres Each Coated with a Dielectric Layer," J. of Electromagnetic Waves and Applications, vol. 17, pp. 431-445, 2003.
 12. Hamid, A-K., " Modeling the Scattering from a Dielectric Spheroid by System of Dielectric Spheres", J. of Electromagnetic Waves and Applications, vol.10, no.5, pp. 723-729, 1996.
 13. Hamid, M., and Rao, T.C.K., " Scattering by a multilayered dielectric-coated conducting cylinder", International J. of Electronics, vol. 38, pp. 667-673, 1975.
 14. Stratton, J.A., "Electromagnetic Theory", (McGraw Hill, New York), 1941.
 15. Cruzan, O.R., "Translational addition theorems for spherical wave functions", Quart. Appl. Math. , 20, pp. 33-40, 1962.
 16. Hamid, A-K., Hussein, M.I., and Hamid, M., "Bistatic Cross Section of an Array of Dielectric Spheres Each Covered with a Dielectric Shell," the 19th Annual Review of Progress in Applied Computational Electromagnetics, Naval Postgraduate School, Monterey, California, U.S.A., pp. 77-81, March 2003.

A.-K. Hamid was born in Tulkarm, West Bank, on Sept. 9, 1963. He received the B.Sc. degree in Electrical Engineering from West Virginia Tech, West Virginia, U.S.A. in 1985. He received the M.Sc. and Ph.D. degrees from the university of Manitoba, Winnipeg, Manitoba, Canada in 1988 and 1991, respectively, both in Electrical Engineering. From 1991-1993, he was with Quantic Laboratories Inc., Winnipeg, Manitoba, Canada, developing two and three dimensional electromagnetic field solvers using boundary integral method. From 1994-

2000 he was with the faculty of electrical engineering at King Fahd University of Petroleum and Minerals, Dhahran, Saudi Arabia. Since Sept. 2000 he has been an associate Prof. in the electrical\electronics and computer engineering department at the University of Sharjah, Sharjah, United Arab Emirates. His research interest includes EM wave scattering from two and three dimensional bodies, propagation along waveguides with discontinuities, FDTD simulation of cellular phones, and inverse scattering using Neural Networks.

Mousa I. Hussein received the B.Sc. degree in electrical engineering from West Virginia Tech, USA, 1985, M.Sc. and Ph.D. degrees from University of Manitoba, Winnipeg, MB, Canada, in 1992 and 1995, respectively, both in electrical engineering. From 1995 to 1997, he was with research and development group at Integrated Engineering Software Inc., Winnipeg, Canada, working on developing EM specialized software based on the Boundary Element method. In 1997 he joined the faculty of engineering at Amman University, Amman, Jordan, as an Assistant Professor. Currently Dr. Hussein is an Associate Professor with the Electrical Engineering Dept. at the United Arab Emirates University. Dr. Hussein research interests include computational electromagnetics, electromagnetic scattering, antenna analysis and design, EMI and signal integrity. microstrip antennas, phased arrays, slot and open ended waveguide antennas.

Michael Hamid Graduated from McGill University in Montreal with a B.Eng. degree in 1960, a M.Eng. degree in 1962 and from the University of Toronto with a Ph.D. degree in 1966, all in Electrical Engineering. He joined the University of Manitoba in 1965 where he became a Professor of Electrical Engineering and head of the Antenna Laboratory. He was a visiting Professor at the Naval Postgraduate School as well as the universities of California Davis and Central Florida and is presently a Professor of Electrical Engineering at the University of South Alabama. He is a past president of the International Microwave Power Institute, a Fellow of IEE and IEEE and published 307 referred articles and 25 patents.

A Fast Forward Model for Simulating EMI Scattering with Realistic Sensors and Elongated Objects

K. Sun ⁽¹⁾, K O'Neill ^(1,2), I. Shamatava ⁽¹⁾, F. Shubitidze ⁽¹⁾, K. D. Paulsen ⁽¹⁾

(1) Thayer School of Engineering, Dartmouth College,
Cummings Hall, HB 8000, Hanover NH, 03755, USA

(2) USA ERDC Cold Regions Research and Engineering Laboratory
72 Lyme Road, Hanover NH, 03755, USA

Keli.sun@dartmouth.edu

Abstract Fast solutions for UWB electromagnetic induction (EMI) scattering from fundamental object shapes are of longstanding interest for sensing of metallic objects, e.g. underground unexploded ordnance (UXO) detection and discrimination. Researchers have recently developed the general formulation for an analytical solution for EMI scattering from a spheroid. The specialization based on Small Penetration Assumption (SPA) is designed to attack the high frequency difficulties that challenge many numerical techniques. This paper uses the new analytical techniques to explore scattering from spheroids and other objects, with excitation complicated by non-uniform fields. To perform the necessary decomposition of the transmitted primary field into spheroidal modes, we represent the transmitter by a set of magnetic dipoles, which dramatically increases efficiency. The performance of the SPA solution is evaluated by comparison with results from other numerical techniques and measured data. Comparison with measured data also indicates that EMI signals from some complicated objects can be approximated by those from spheroids with similar proportions, which is promising for applications requiring fast solutions, such as inversion processing.

Keywords spheroid, EMI, scattering, SPA, GEM-3, non-uniform field, spheroidal modes

1. Introduction and review of spheroid solutions

In terms of their physical responses, some complicated but reasonably smooth, elongated objects can be approximated by a representative spheroid, when observed from some distance. The idea of approximate spheroid representation has been applied in fluid mechanics [1] and magnetic field analysis [2-4]. In the EMI frequency range (~ 10 's of Hz up to ~ 100 's of kHz) we are particularly attracted to the possibility, because in this band the smaller details of shape may not be important.

A great deal of work has been done in electromagnetic scattering by spheroids and analytically shaped particles, with both exact [5,6] and approximate methods [7-10]. Physical optics approximations have been used to model large particle scattering [11,12]. For scattering from more than a single particle, addition theorems were employed [13,14]. The EMI problem we are studying here is different from the previously treated problems in that (1) the frequency is very low so that the field is magneto-quasistatic (2) the scatterer is metallic, with conductivity much higher than that of the surrounding media. Tractable analytical and numerical solutions for the general EMI problem have not been available until recently [15-20]. New analytical solutions for the secondary (scattered) field from prolate spheroids were presented in [15,16], including high frequency approximations, with specialization for the SPA readily extended to oblate cases as well [17]. For our applications here, we only pursue the prolate case.

In the magneto-quasistatic EMI realm, only a scalar potential Ψ is usually required for the region surrounding a metallic scatterer. The transmitted primary (ψ^{pr}) and received secondary fields (ψ^s) can be expressed in that region as [16]

$$\begin{aligned}\psi^{pr} &= \frac{H_0 d}{2} \sum_m \sum_{n=m}^{\infty} \sum_{p=0}^1 b_{pmn} P_n^m(\eta) P_n^m(\xi) T_{pm}(\phi) \\ \psi^s &= \frac{H_0 d}{2} \sum_m \sum_{n=m}^{\infty} \sum_{p=0}^1 B_{pmn} P_n^m(\eta) Q_n^m(\xi) T_{pm}(\phi)\end{aligned}\quad (1)$$

where (η, ξ, ϕ) are the standard spheroidal coordinates, d is the inter-focal distance, P_n^m and Q_n^m are Associated Legendre functions, $T_{pm}(\phi)$ is $\cos(m\phi)$ for $p = 0$ and is $\sin(m\phi)$ for $p = 1$. The coefficients b_{pmn} for the primary field are known (readily calculated), and the unknown B_{pmn} must be solved for.

For high induction numbers (small skin depth) cases, one can derive relations reminiscent of impedance boundary conditions to treat the effects of internal fields. Different approaches to this are possible, the most general involving use of the magnetic field divergence equation and the normal field components and derivatives, e.g. [18,20] in the numerical realm. Alternatively, for analytical solution, all higher order terms are neglected in the governing double curl equation in [16], mostly involving tangential gradients inside the object. Then to derive an applicable gradient condition just below the scatterer's surface, the tangential field components are assumed to have functional dependencies as in a 1-D frequency domain solution with respect to the normal component, i.e. $\sim \exp\{i\alpha_n k n\}$, where k is the equivalent of wave number, here equal to $\sqrt{i\omega\sigma\mu}$ for angular frequency, electrical conductivity, and magnetic permeabilities ω , σ , and μ , respectively. In the specific case of the spheroids, α_n is unity for the azimuthal component and can be solved for analytically for the angular component H_η . With these approximations, one can solve a simple algebraic system for the unknown B_{pmm} , corresponding only to an exterior problem in the scalar potential, with no expressions involving the problematical spheroidal wave functions in the object interior. The resulting spheroid solutions for a spatially uniform primary field indicate that the SPA may produce accurate results over the entire EMI broadband, in particular where magnetic permeability μ is high, as for steel, whether skin depth is small or not. See [15,16,23] for more details.

2. Fast Decomposition of the primary field into spheroidal modes

To solve the EMI scattering problem for a spheroid using our algorithm, the key task is to decompose the known primary field Ψ^{pr} into spheroidal modes (i.e. find b_{pmm} in (1)). This is easily done for a uniform field, but otherwise may require new analytical expressions or numerical computation. In our approach, one multiplies both sides of (1) by $T_{pm}(\phi) P_n^m(\eta)$ and then integrates, using established orthogonality relations for the Legendre functions to obtain

$$b_{pmm} = \frac{\int_{-1}^1 P_n^m(\eta) \int_0^{2\pi} T_{pm}(\phi) \Psi^{pr}(\eta, \xi_0, \phi) d\phi d\eta}{\frac{\alpha\pi H_0 d}{2n+1} P_n^m(\xi_0) \frac{(n+m)!}{(n-m)!}} \quad (2)$$

where $\alpha = 1$ for $m \geq 0, p = 1$ or $m \geq 1, p = 0$, and $\alpha = 2$ for $m = 0, p = 0$. $\xi = \xi_0$ is the surface of the spheroid. At some distance away from the sensor head, the excitation field produced by most EMI transmitters can be approximated using dipole sources. For a magnetic dipole with dipole moment $\mathbf{m} = (m_x, m_y, m_z)$ at location $\mathbf{R}_0 = (x_0, y_0, z_0)$, the potential and magnetic field will be [21]

$$\begin{aligned} \psi &= \frac{\mathbf{m} \cdot (\mathbf{R} - \mathbf{R}_0)}{4\pi |\mathbf{R} - \mathbf{R}_0|^3} \\ \mathbf{H} &= \frac{1}{4\pi |\mathbf{R} - \mathbf{R}_0|^3} \left(\frac{3(\mathbf{R} - \mathbf{R}_0)(\mathbf{R} - \mathbf{R}_0)}{|\mathbf{R} - \mathbf{R}_0|^2} - \mathbf{I} \right) \cdot \mathbf{m} \end{aligned} \quad (3)$$

At this point the potential ψ can be translated into spheroidal coordinates and be decomposed according to (2), through numerical integration.

Lab measurements were obtained using the Geophex GEM-3 broadband EMI sensor [22]. The sensor head contains two transmitting current loops with radii approximately 20cm and 10cm. The current in the inner loop is about half of that in the outer loop and it flows in the opposite direction, so that the primary field at the receiver in the head center is near zero. The primary field near the sensor is complicated and cannot be calculated analytically, so at any point of interest \mathbf{H} must be calculated according to the Biot-Savart Law [21]. The potential can then be computed by integration of the magnetic field along an arbitrary path. After the values of potential on the spheroid surface are obtained, the field can be decomposed into spheroidal modes according to (2).

For a complicated Ψ^{pr} such as that in the GEM-3 near field, decomposition requires numerical integration in several steps, which are too time consuming for our inversion calculations when the potential is computed as described above. Therefore we approximate the actual source by a superposition of some basic fictitious sources (i.e. point magnetic charges or dipoles), whose potential and magnetic field can be specified analytically. In keeping with the geometry of the GEM-3 sensor, the sources are distributed with azimuthal symmetry. The sensor produces fields like a magnetic dipole in the far field, and the magnetic field direction near the sensor is mainly perpendicular to its broad surfaces. Therefore we distribute the magnetic dipole sources only on the sensor surface, such that the dipoles only have a component perpendicular to the sensor head. The source distribution

contains M_1 at $\mathbf{R}_{s1}=(0,0,0)$, and M_i at $\mathbf{R}_{sij}=(\rho_i \cos(\theta_j), \rho_i \sin(\theta_j), 0)$ for $i=2,3,\dots,N_M$, $j=1,2,3,\dots,N_i$, where M_i are magnitudes of point dipoles and N_M and N_i are the number of rings and number of sources in each ring, respectively (Figure 1). The basic idea is to distribute the dipoles symmetrically, with different numbers at different radii. The magnetic field at position \mathbf{R} will be $\mathbf{H} = \sum_{i=1}^{N_M} \frac{M_i}{4\pi} \mathbf{A}_i$ with

$$\mathbf{A}_i = \sum_{j=1}^{N_i} \frac{1}{|\mathbf{R} - \mathbf{R}_{sij}|^3} \left(\frac{3(\mathbf{R} - \mathbf{R}_{sij})(R_z - R_{sijz})}{|\mathbf{R} - \mathbf{R}_{sij}|^2} - \hat{\mathbf{z}} \right) \quad (4)$$

and $N_1 = 1$, subscripts “s” and “z” refer to source and z component.

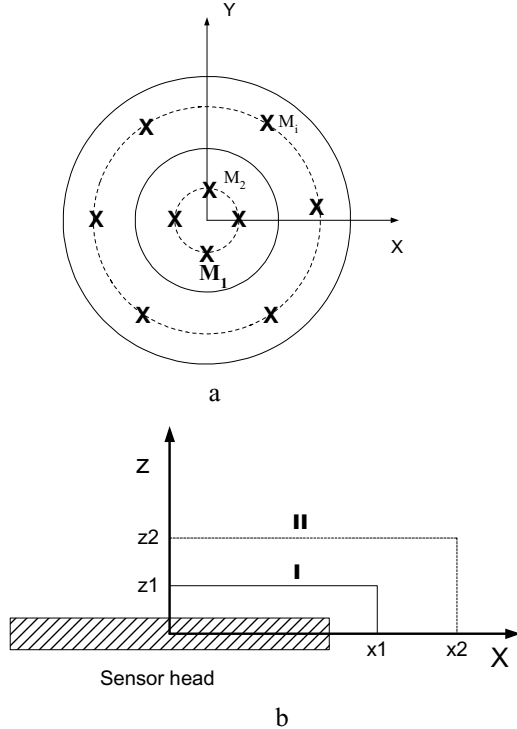


Figure 1. a) Set of dipole sources (X's); the two solid lines are the inner and outer current loop of the GEM-3 sensor. b) Control surface (I) employed to determine dipole sources and the testing surface (II) used for evaluating the accuracy of the field from these sources.

For given magnetic field at control points (on the control surface in Figure 1 b), a mean least square was employed to determine M_i , i.e. by minimizing the difference between

the primary magnetic field determined by the fully detailed representation of the sensor loops and that obtained from the set of dipole sources. Then the transmitted potential of GEM-3 can be approximated by Figure 2

$$\psi^{pr} = \sum_{i=1}^{N_M} \sum_{j=1}^{N_i} \frac{M_i}{4\pi} \left(\frac{R_z - R_{sijz}}{|\mathbf{R} - \mathbf{R}_{sij}|^3} \right) \quad (5)$$

and decomposed according to (2)

3. Results and discussion

3.1 Accuracy of SPA results

The accuracy of spheroidal SPA solutions under a uniform primary field has been well studied [16,23]. As we will show below, the field from the GEM-3 sensor can be accurately represented by a set of point dipoles. So we begin here by studying the performance of SPA algorithm for objects under the non-uniform fields from dipole sources. Figure 2 shows results for a spherical object and for a 1x4 prolate spheroid, where the induction number $|k|a = \sqrt{\omega\mu\sigma}a$.

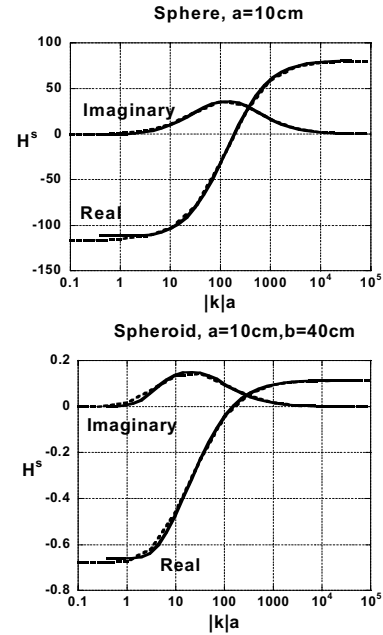


Figure 2. Scattered field from the sphere and 1x4 spheroid under dipole excitation. $\mu = 50\mu_0$. The solid lines are results obtained using the MAS and dashed lines are from the SPA.

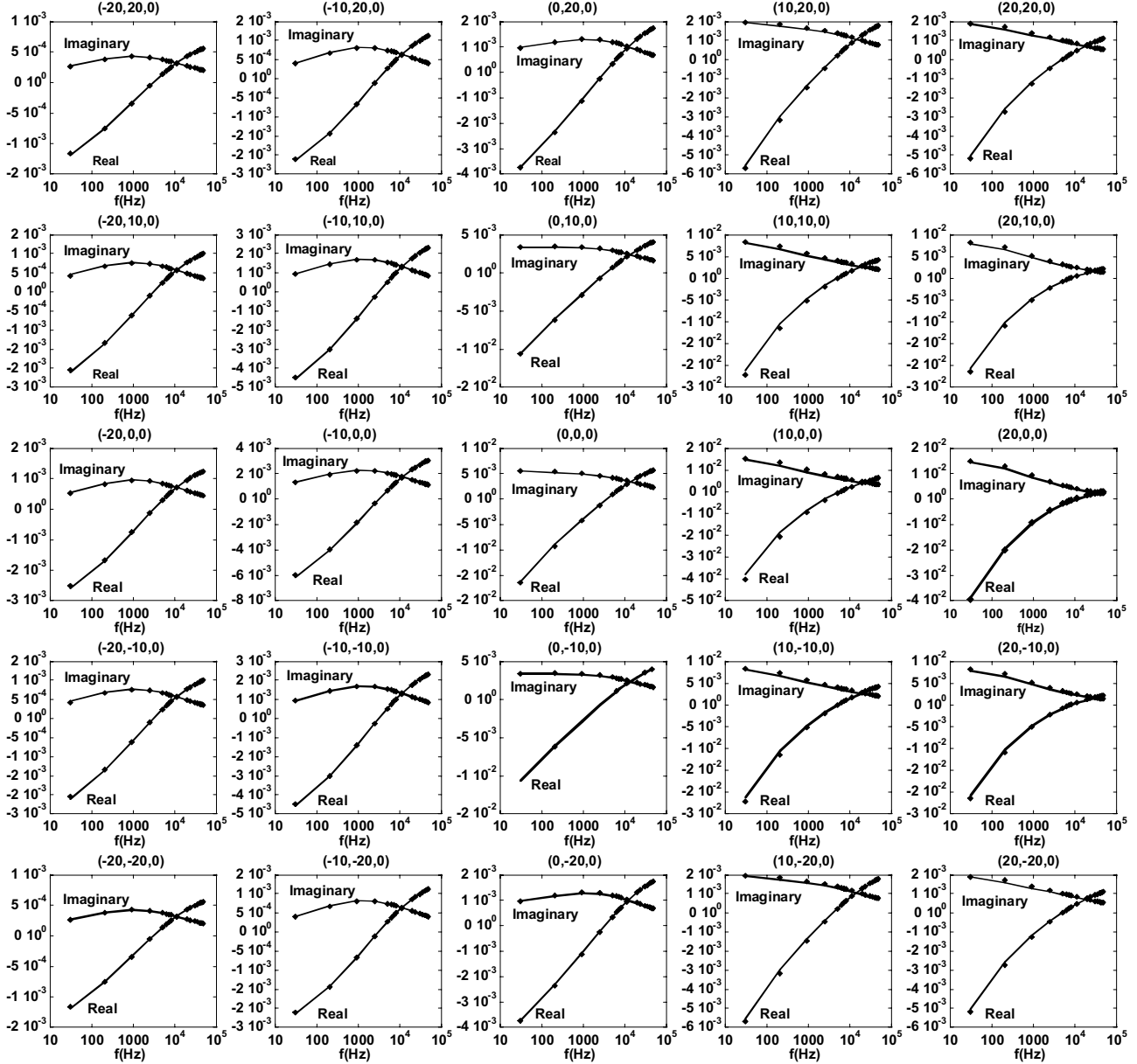


Figure 3 Comparison of SPA (markers) and MAS (lines) values (H_z^s) for a prolate spheroid ($a=4\text{cm}$, $b=24\text{cm}$) in a 5×5 grid of sensor locations. $\sigma = 4 \times 10^6$, $\mu_r = 100$, $x_0 = y_0 = 0$, $z_0 = -30\text{cm}$, $\phi_0 = 0$, $\theta_0 = \pi/4$.

Results are compared with those from a verified and complete numerical approach, namely the MAS-TSA algorithm [20] and are displayed in terms of received components in phase with the primary field (real component) and those in phase quadrature with it (imaginary component). The radius of the sphere is 10cm, the dipole is 15cm away from its center, and the scattered field was determined at the same position as the dipole transmitter. Similarly, the 1×4 prolate spheroid has the same diameter but greater length ($a=10\text{cm}$, $b=40\text{cm}$), and

the dipole is at position $(0,0,60\text{cm})$. Although the field around the target is non-uniform, the SPA result still works very well over a wide frequency range.

To test the accuracy of SPA results for more general cases, we consider a real EMI sensor (GEM-3 developed by Geophex, Ltd.); center of the sensor is moved over a 5×5 grid on a surface above the target. The total size of the grid is 50cm by 50cm. A global coordinate system (x, y, z) on the grid has its origin at the center and z axis perpendicular

to the surface. The target center is at $(x_0, y_0, z_0) = (0, 0, z_0)$ in the global system, with units in centimeters. The orientation is described by θ_0 (the angle with z axis) and ϕ_0 (angle with x axis of the grid). At each grid point the data were calculated for 17 frequencies (distributed from 30Hz to 47,970Hz), for both real and imaginary components. An example is shown in Figure 3, with MAS results as reference [20]. Results indicate that the SPA routine is generally reliable in the frequency range studied, for non-uniform source fields, at least for these smooth and regular target shapes.

3.2 Representing the GEM-3 field with magnetic dipoles

Next we test the accuracy of the GEM-3 primary field represented by point dipoles. The "exact" magnetic field on the control and testing surfaces was calculated from direct integration around the current loops [21,22], and field values on the control surface were employed to determine point dipoles needed to represent the overall source field. Then the approximate transmitted field was compared on testing surface with that calculated from direct integration. For this example we choose the control surfaces at $z = 10$ cm and $x = 30$ cm (they are in fact only lines because of the symmetry properties). The testing surfaces are at $z = 15$ cm and $x = 45$ cm. As described above, we distribute the dipole of sources in several rings. The first dipole is at the center, then the i^{th} (for $i \geq 2$)

ring has radius of $\rho_i = \frac{i-1}{N_M-1} \times 20$ cm, where N_M is the

total number of rings of sources, the number of sources in the i^{th} ring is $2i$. Figure 4 shows the comparison of approximated field with the "exact" one (namely calculated directly from current loops) on the testing surfaces. The approximated field converges to the exact one as the number of sources increases. For this case, 6 or 8 rings of dipole sources is sufficient to describe the field outside of the testing surface.

3.3 Representing complicated objects with spheroids

For EMI sensing, an arbitrary scatterer can be approximated by one or a few magnetic dipoles when viewed in the far field. However, this approximation becomes less accurate as the sensor gets closer, and in much UXO sensing we must operate in the very near field. Over most of the near field, a prolate spheroid of finite extent may be a better representative of the object than a small number of infinitesimal dipoles. To investigate the applicability of spheroidal representations for more

irregular objects, we consider the response of a jagged, non-BOR piece of elongated metal scrap (Figure 5). This ordnance fragment was collected at a UXO cleanup test site. Note that the target geometry is complicated, with jagged appurtenances and different profiles in different rotations about its long axis.

Figure 6 shows the comparison between measured GEM-3 data from the piece of ordnance scrap and simulation for a best-fit prolate spheroid. The distance between the object center and the sensor is 10 cm, approximately the same as the target length. Despite the irregularities and asymmetry of the target, it produces an EMI signature similar to that of a prolate spheroid with approximately the same overall proportions. The object's lack of rotational symmetry has some effect on the signature in the orientation transverse to the primary field, but strikingly little. These results encourage further exploration of equivalent spheroid use for UXO discrimination. The scheme would rest on the assumption that one can find a sufficiently equivalent spheroid for UXO of interest and apply this equivalence in model-based inversion algorithms. For given measured EMI data, one would identify a spheroid that produces similar EMI signals by doing inversion or optimization, given that we have fast algorithm for calculating the forward EMI solution from spheroids. We expect that the scale and proportions of the spheroid will reflect the geometrical information of the measured object. One can also calculate derivatives of the forward problem solution analytically, for use in Jacobians required for inversion processing.

Pursuing this, Figure 7 shows an example real UXO, composed of a main body (magnetic), a copper band, and fins and tail with different steel. With the UXO beneath the measurement grid as shown in Figure 7, its EMI responses were measured along X and Y axis (9 points along each line) using the GEM-3 sensor and a representative spheroid was found by fitting the measured data. The EMI data from the representative spheroid are shown in Figure 8. The first 9 figures (the first and second lines) are data along X axis ($y=z=0$), and the second 9 figures are data along Y axis ($x=z=0$). Comparison with the measurement data shows that even for this complicated composite object, over an array of viewing angles by the sensor, it was still possible to find a representative spheroid which produces similar EMI response. One should note that this is a cooperative case because the steel part is much larger than other parts, and is close to the sensor, so that it dominates the response. In other orientations in which different sensor positions highlight the tail of the UXO, we expect more difficulty in matching it with a single spheroid. See [24] regarding other treatments of this same target. Overall, the very good fit observed here may not always be obtained for general composites in highly non-symmetric targets.

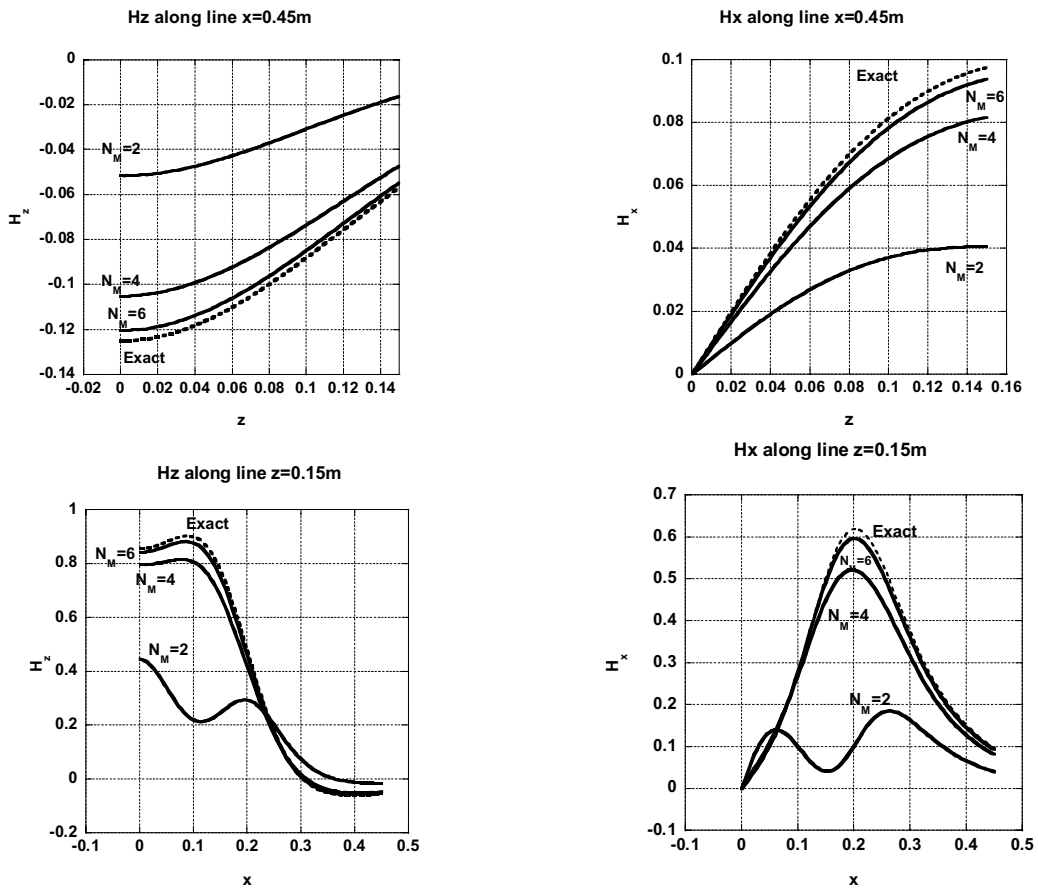


Figure 4. Convergence of the approximate field from the transmitter to the exact one, over the testing surfaces.



Figure 5. Piece of ordnance scrap on which measurements were performed, with length about 10 cm, width in one transverse direction 3~4 cm and about 2cm in the other.

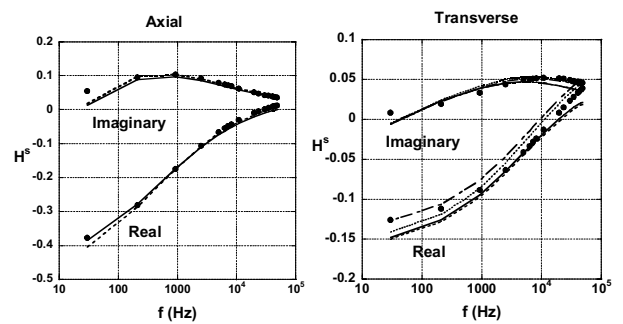


Figure 6. Comparison of the measured EMI signal from the fragment in Figure 5 (lines) with that calculated for a prolate spheroid with $a = 1.25$ cm, $b = 5$ cm, $\sigma = 2.6 \times 10^6$ (S/m), $\mu = 36\mu_0$ (dots). Different line types are for measurements from different views (i.e. up and down for the axial case, and four 90° rotations about the axis for the transverse case).

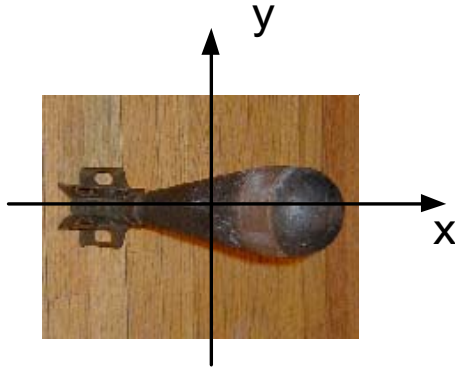


Figure 7. UXO 28 cm in length and about 8.3 cm in diameter at its widest point. Measurements are along X and Y axis, which is on a surface 22cm above the target.

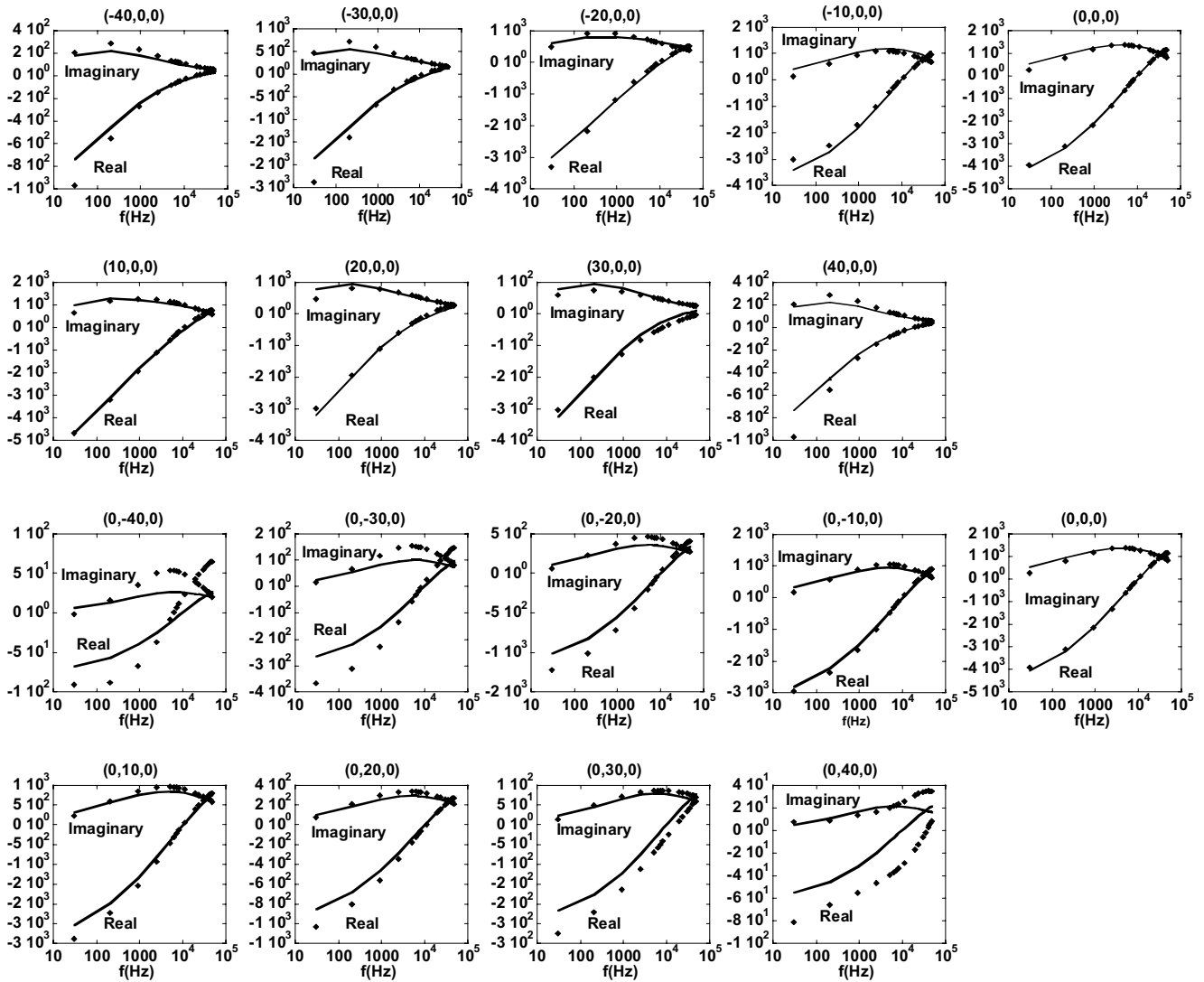


Figure 8. Scattered field H_z (in ppm) of UXO (markers) and its representative spheroid ($a = 2.2\text{ cm}$, $b = 14\text{ cm}$) along X and Y axis. $\sigma = 4 \times 10^6$, $\mu_r = 227$, $x_0 = 3.8\text{ cm}$, $y_0 = -0.93\text{ cm}$, $z_0 = -22\text{ cm}$, $\phi_0 = 0$, $\theta_0 = \pi/2$.

4. Concluding Discussion

The results presented here contribute to the computational capabilities necessary for inversion of EMI measurements, in applications such as discrimination of UXO from scrap [25-27]. To approach that problem, we must be able to model both targets of interest as well as clutter. With great economy, the formulations above represent the primary field from a real sensor, using distributions of magnetic dipoles. This source construction is particularly beneficial because one can readily decompose the primary field from each contributing source into spheroidal components. For each of these, in turn, fast analytical solutions can be obtained, for steel objects. Comparison of EMI measurements and simulations suggests that even some rather irregular scatterers may be represented well by spheroidal shapes. Some limitations of the SPA type formulations can appear at low frequencies, especially for objects with low permeability [20,23]. Ultimately, this problem can be overcome by using the emerging full analytical spheroid solution, as opposed to the SPA [28, 29]. While a great many targets of interest can be idealized as bodies of revolution, future work should attack similar development of solutions for ellipsoidal shapes. With three different principal axis dimensions and correspondingly different directional scattering, they would provide the most flexible tool for inversion calculations.

Acknowledgment: This work was sponsored in part by the Strategic Environmental Research and Development Program and US Army CoE ERDC BT25 and AF25 programs. Computations were based on modifications of C. O. Ao's SPA program for uniform primary field.

References:

1. K. Sun and W. Wu, "Electrophoresis of two arbitrary axisymmetric prolate particles," *Int. J. Multiphase Flow*, Vol. 21, No.4, pp. 705-714, 1995.
2. S. D. Billings, J. M. Stanley and C. Youmans, "Magnetic discrimination that will satisfy regulators," UXO Forum 2002, Orlando, September 3-6, 2002.
3. K. Sun, K. O'Neill, I. Shamatava, F. Shubitidze, "Application of prolate Spheroid Solutions in Simulation of EMI Scattering with Realistic Sensors and Objects," ACES conference, Monterey, CA, pp531-537, Mar 24-28, 2003
4. K. Sun, K. O'Neill, L. liu, F. Shubitidze, I. Shamatava, K. D. Paulsen, "Analytical solutions for EMI scattering from general spheroids with application in signal inversion for UXO discrimination," *Detection and Remediation Technologies for Mines and Minelike Targets VIII (or48)*, Part of SPIE's 17th Annual International Symposium on AeroSense, Orlando, Florida, 21-25 April 2003.
5. SH. Asano, G. Yamamoto, "Light scattering by a spheroidal particle," *Appl. Opt.*, v.14, p. 29-49, 1975.
6. V.G. Farafonv, "Difraktsiya ploskoj e'lektromagnitnoj volny na die'lektricheskom sferoide," *Diffrents. Uravn.*, v. 109, pp. 30-43,1983.
7. R. Pecora (Ed.), "Dynamic light scattering. Application of photo correlation spectroscopy," New York: Plenum press, 1985.
8. Van de Hulst H., "Light scattering by small particles," J. Wiley & Sons, NY,1957.
9. J.D. Klett, R.A. Sutherland, "Approximate methods for modeling the scattering properties of nonspherical particles: evaluation of the Wentzel-Kramers-Brillouin method," *Appl. Opt.*, v.31, pp. 373-386,1992.
10. P. Latimer, "Predicated scattering by spheroids: comparison of approximate and exact methods," *Photochem. Photobiol.*, v.19, pp.3039-3041,1980.
11. J. C. Ravey, P. Mazon, "Light scattering in the physical optics approximation: application to large spheroids," *J. Optics*, v.13,pp.273-282,1982.
12. J. C. Ravey, P. Mazon, "Light scattering by large spheroids in the physical optics approximation: numerical comparison with other approximate and exact results," *J. Optics*, v. 14, pp.29-41, 1983.
13. Bateshwar P. Sinha, Robet H. Macphie, "Translational additional theorems for spheroidal scaler and vector wave functions," *Quart. Appl. Math.*, v. 38, pp. 143-158, 1980.
14. M.F.R. Cooray, I.R. Ciric, "Electromagnetic wave scattering by a system of two spheroids of arbitrary orientation," *Antennas and Propagation, IEEE Transactions on*, v. 37, pp. 608-618,1989.
15. H. Braunisch, C. O. Ao, K. O'Neill and J. A. Kong, "Magneto-quasistatic response of conducting and permeable prolate spheroid under axial excitation," *IEEE Trans. Geosci. Remote Sensing*, vol. 39, pp. 2689-2701, 2001.
16. C. O. Ao, H. Braunisch, K. O'Neill and J. A. Kong "Quasi magnetostatic solution for a conducting and permeable spheroid with arbitrary excitation", *IEEE Trans, Geosci. Rem. Sens.*, Vol. 40, pp. 887-897, April, 2002.
17. C.O.Ao, H.Braunisch, K.O 'Neill, J.A.Kong, L.Tsang, and J.T.Johnson, "Broadband electromagnetic induction response from conducting and permeable spheroids," *Proc. SPIE*, vol. 4394: *Detection and Remediation Technologies for Mines and Minelike Targets VI*, Orlando, pp 1304-1315, April 16-20, 2001.
18. K. Sun, K. O'Neill, F. Shubitidze, S. A. Haider, and K. D. Paulsen, "Simulation of electromagnetic induction scattering from targets with negligible to moderate penetration by primary fields," *IEEE Trans. Geosci. Remote Sensing*, Vol. 40, pp.910-927, Apr. 2002.

19. F. Shubitidze, K. O'Neill, S. Haider, K. Sun, and K.D. Paulsen, "Application of a generalized formulation of the method of auxiliary sources to the wideband electromagnetic induction problem," *IEEE Trans. Geosci. Remote Sensing*, Vol. 40, pp.928-942, Apr. 2002.
20. F. Shubitidze, K O'Neill , K. Sun, I. Shamatava and K.D. Paulsen, "A combined MAS-TSA algorithm for broadband electromagnetic induction problems," *ACES conference*, Monterey, CA. pp566-572, Mar. 24-28,2003.
21. D. J. Jackson, "Classical electrodynamics," Wiley, New York, 3rd Edition, 1999.
22. I. J. Won, D. A. Keiswetter, D. R. Hanson, E. Novikova and T. M. Hall, "GEM-3: a monostatic broadband electromagnetic induction sensor," *Jour. Envir. Eng. Geophysics*, Vol. 2, No. 1, pp53-64, 1997.
23. I. Shamatava, K. O'Neill, F. Shubitidze, K. Sun and C.O. Ao, "Evaluation of approximate analytical solutions for EMI scattering from finite objects of different shapes and properties," *IEEE International Geosciences and Remote Sensing Symposium and the 24th Canadian Symposium on Remote Sensing*, pp1550-1552, 2002
24. F. Shubitidze, K O'Neill, I. Shamatava, K. Sun and K.D. Paulsen, "Analysis of EMI scattering to support UXO discrimination: heterogeneous and multiple objects," *Detection and Remediation Technologies for Mines and Minelike Targets VIII (or48)*, Part of SPIE's 17th Annual International Symposium on AeroSense, , Orlando, Florida, 21–25 April 2003.
25. K. Sun, K. O'Neill, L. Liu, F. Shubitidze, I. Shamatava, "Application of Bayesian inversion of electromagnetic induction data for UXO discrimination," *Symposium on the application of geophysics to environmental and engineering problems (SAGEEP03)*, San Antonio, TX, pp 1469-1478, April 6-10, 2003
26. K. O'Neill, K. Sun, F. Shubitidze, I. Shamatava, L. Liu, K. D. Paulsen, "Dealing with clutter in inversion and classification schemes for buried UXO discrimination," *Detection and Remediation Technologies for Mines and Minelike Targets VIII (or48)*, Part of SPIE's 17 th Annual International Symposium on AeroSense, Orlando, Florida, 21–25 April 2003.
27. K. Sun, K. O'Neill, L. Liu, F. Shubitidze, and I. Shamatava, "Application of Bayesian inversion of scatterer shape from EMI data," *IEEE International Symposium on Antennas and Propagation*, Columbus, OH, June 22-27, 2003
28. B. E. Barrowes, K. O'Neill, T. M. Grzegorzczuk, X. Chen and J. A. Kong, "Broadband electromagnetic induction solution for a conducting and permeable spheroid," *IEEE Trans. Geosci. Remote Sensing*, submitted for publication, 2003.
29. B. E. Barrowes, K. O'Neill, T. M. Grzegorzczuk, J. A. Kong, "Asymptotic expansions of the prolate angular spheroidal wave function for complex size parameter," *Studies in Applied Mathematics*, submitted for publication, 2003



Keli Sun received his B.S., M.S. and Ph.D. degrees in Computational and Biofluid Mechanics from the Department of Mechanics and Engineering Sciences, Peking University, Beijing, P. R. China, in 1991, 1994 and 1997 respectively. As an exchange student, he also worked in the School of Pure and

Applied Sciences, Tokyo University, Tokyo, Japan, from December 1995 to December 1996, studying the mobility and mechanical properties of membrane proteins in living cells. After getting his Ph.D. degree in 1997, he worked on the faculty of Tsinghua University, Beijing, P.R. China performing research and teaching biomechanics. He obtained a second Master of Science degree in Computational Electromagnetics in May 2001 from the Thayer School of Engineering at Dartmouth College in Hanover, NH. Dr. Sun is currently employed as a Research Associate in the Numerical Methods Laboratory in the Thayer School furthering his research in Computational Electromagnetics and its applications in remote sensing.



Kevin O'Neill received the B.A. magna cum laude from Cornell University, followed by M.A., M.S.E., and Ph.D. degrees from Princeton University, Department of Civil Engineering. After an NSF postdoctoral fellowship at the Thayer School of Engineering at Dartmouth

College and the U.S. Army Cold Regions Research and Engineering Laboratory (CRREL), he joined CRREL as a Research Civil Engineer. His research has focused on numerical modeling of porous media transport phenomena and of geotechnically relevant electromagnetic problems. He has been a Visiting Fellow in the Department of Agronomy at Cornell University, continues since 1989 as a Visiting Scientist at the Center for Electromagnetic Theory and Applications at MIT, and since 1984 has been on the adjunct faculty of the Thayer School. Current work centers on electromagnetic remote sensing of surfaces, layers, and especially buried objects such as unexploded ordnance.



Irma Shamatava received the degree of Diploma radio physicist (M.S) from the Sukhumi branch of Tbilisi State University, Republic of Georgia, in 1994. Beginning in 1997 she joined the Staff of the Computer center, Sukhumi branch of Tbilisi State

University, Republic of Georgia. During the same period she joined Department of Physics and Mathematics, as an assistant teacher. She is currently working as researcher at the Thayer School of Engineering, Dartmouth College, Hanover NH. Her research interests focus on analytical and numerical modeling of electromagnetic scattering by subsurface metallic objects.



Fridon Shubitidze received the degree of Diploma radio physicist (M.S) from the Sukhumi branch of Tbilisi State University, Republic of Georgia, in 1994 and Candidate of Sciences Ph.D degree in radio physics (applied electromagnetics) from its physics department, Tbilisi State

University, Republic of Georgia, in 1997. Beginning in 1994 he was on the Research Staff of the Laboratory of Applied Electrodynamics, Tbilisi State University, Department of Physics, Republic of Georgia. At the same time he joined department of physics and mathematics, Sukhumi branch of Tbilisi State University as a senior teacher and became Associate Professor there in 1998. From 1998 to 1999 he held a postdoctoral fellowship in National Technical University of Athens, Greece, performing research in connection with computer simulation of electrostatic discharge, electrodynamic aspects of EMC, numerical modeling of conformal antennas, electromagnetic wave scattering, field visualization and identification of objects by scattered field analysis, investigation of wave propagation through anisotropy, plasma and chiral media; and innovative numerical methods. He is currently, working as Senior Research Associate at the Thayer School of Engineering, Dartmouth College, Hanover NH. His current work interests focus on numerical modeling of electromagnetic scattering by subsurface metallic objects.



Keith D. Paulsen received a B.S. from Duke University and M.S. and Ph.D. degrees from the Thayer School of Engineering, Dartmouth College, all in biomedical engineering. He was an assistant professor in electrical and computer engineering at the University of

Arizona and jointly, an assistant professor in radiation oncology at the University of Arizona Health Sciences Center, and is now a professor of engineering at the Thayer School. A recipient of numerous academic and research awards and fellowships, he has carried out sponsored research for the National Science Foundation, the National Cancer Institute, the Whitaker Foundation, and the National Institute of Health. He has served on more than 10 advisory committees for the National Cancer Institute, and has chaired or organized five symposia on hyperthermic cancer treatment. He has published over 60 journal articles, over three dozen conference presentations, abstracts, and papers, and contributed chapters on electromagnetic power deposition patterns to five books. At Thayer School he is co-founder and co-manager of the Numerical Methods Laboratory. He performs research and teaches courses in computational methods for engineering and scientific problems, with particular applications in electromagnetics, subsurface object sensing, and biomedical engineering.

Computation of SAR in Cell Culture Flasks Exposed to 900 MHz GSM Type Signals in a Modified TEM Cell

Robert L McIntosh, Raymond J McKenzie, Steve Iskra, Amico Carratelli, and Paul Standaert
Telstra Research Laboratories, Clayton, Victoria, 3168, Australia
robert.l.mcintosh@team.telstra.com

Abstract: In order to provide rigorous dosimetry for *in vitro* studies, Telstra Research Laboratories has developed a modified transverse electromagnetic cell exposure system. The system acts as a chamber for experiments in which a human cell culture exists as a very thin monolayer adhered to the bottom of a plastic culture flask under a layer of several millimetres of RPMI nutrient medium while incubated in a controlled atmosphere. A key to the rigour of any experiment seeking to investigate possible effects of electromagnetic energy on living systems is to ensure that the exposures used are accurately known, and to achieve this, numerical methods for the challenging task of characterising the SAR profile in the medium have been developed. This paper describes salient aspects of the development and analysis of the system.

Keywords: FDTD modelling; RF exposure; TEM cell; SAR; GSM

1. Introduction

To enable the future investigation of possible biological effects of mobile phone exposure, this paper considers an experimental setup where a human cell culture can be exposed to 900 MHz GSM type radiofrequency (RF) signals. The exposure system consists of a modified Crawford transverse electromagnetic (TEM) cell (Crawford 1974), which is supplied with a simulated GSM mobile phone type signal at 20 W peak power (900 MHz RF signal pulsed at 1/8 duty cycle for 2.5 W average power). The cell culture is placed in the TEM cell in standard *Falcon*TM 25 cm³ plastic culture flasks and resides as a very thin monolayer (a few microns) at the bottom of 6 mm of the nutrient RPMI-1640 (Roswell Park Memorial Institute) while incubated in a 37 °C CO₂ atmosphere. This setup is similar to that discussed in French and Blood 2002 which investigated possible gene expression changes in live human astrocytes.

For this situation, the specific energy absorption rate (SAR) (W/kg) is commonly accepted to be the most appropriate metric for determining RF exposure. SAR can be determined at any point in a medium from the *E*-field (V/m) at that point:

$$SAR = \frac{\sigma |E|^2}{\rho} \quad (1)$$

where σ is the conductivity (S/m) and ρ is the mass density (kg/m³).

Many RF exposure systems rely on measurements of average absorption within the target material to determine the SAR. In a TEM cell, the actual SAR at any given point in the exposed medium will differ markedly from the average value. The geometry used here, where the height (*h*) of the medium coincides with the direction of the incident electric (*E*) field, ensures that there is the essential uniformity in SAR on the bottom layer of the RPMI medium where the cell culture resides. However, it also means that SAR typically varies quadratically with *h* within the medium (see Burkhardt et al. 1996, Guy et al. 1999, Samaras et al. 2000, and Schönborn et al. 2001). This makes it critical that accurate computational techniques are used to provide a good estimate of SAR (especially on the bottom layer).

2. Choice and Design of Exposure Chamber

To achieve well controlled and characterised RF exposures has been a concern in many previous studies. References Guy et al. 1999, Kuster and Schönborn 2000, and Schönborn et al. 2000 and 2001, discuss exposure requirements and the merits of various exposure systems. Such systems include waveguides, radial transmission lines (RTL), TEM cells, Gigahertz TEM (GTEM) cells, and free-field exposure in anechoic chambers.

Based on considerations of physical size, experimental needs, and required field characteristics, a TEM cell was chosen. A TEM cell provides uniform incident plane wave exposure conditions, useful for simplifying analysis, as long as each culture flask is placed in a central position and the absorbing medium is not too thick (see Crawford and Workman 1979, Burkhardt et al. 1996, Popovic et al. 1998, and Schönborn et al. 2001) (Figure 1). Modifications included provision of adequate ventilation in the 37 °C CO₂ incubator (Figure 2); access ports and inserts to allow placement of the two flasks at the midpoint of the top half of the TEM cell (Figure 3); and fixtures to allow

ingress and accurate location of fluoroptic temperature probes (Figure 4). The measured return loss of the input signal was greater than 30 dB. To ensure CO₂ diffusion and suitable power efficiency the height of the RPMI was chosen to be 6 mm. Total absorbed power with the TEM cell loaded with two flasks containing the RPMI was less than 4% of forward power, indicating that the TEM field conditions were maintained within the TEM cell.

3. Determination of SAR

The commercially available computational software XFDTD (Remcom 2003) was used to determine the SAR profile in the RPMI (Figure 5). The SAR was used to report the background energy level in which the cell culture was placed and also to validate the setup through the resultant temperature estimation. XFDTD uses the finite-difference method (see, for example, Kunz and

Luebbers 1993). A computational mesh of the 6 mm medium was constructed with cubical cells of length 0.5 mm. The conductivity of RPMI was set at 1.8 S/m, relative permittivity 73.2, and density 1000 kg/m³. The incident field frequency was 900 MHz with the *E*-field polarised in the vertical direction.

For the supplied plane wave signal (*E*-field 214 V/m peak amplitude, equivalent to 2.5 W average power in the TEM cell), the calculated peak SAR on the bottom of the medium was 0.20 W/kg. The average SAR on this level was found to be 0.18 W/kg. Figure 5 highlights the uniformity of SAR on the bottom layer, and the non-uniformity in the 6 mm vertical direction (this profile is consistent with published results Burkhardt et al. 1996, Guy et al. 1999, Pickard et al. 1999, Samaras et al. 2000, and Schönborn et al. 2001).

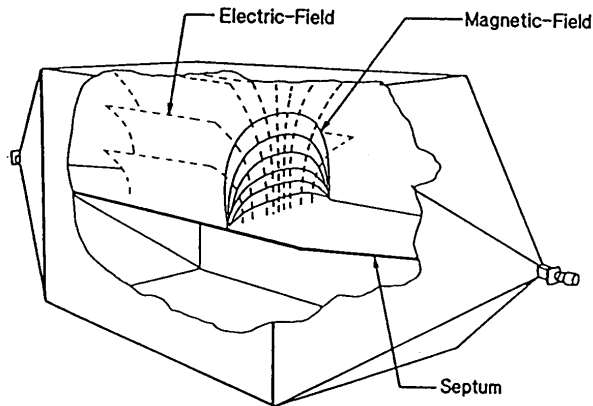


Figure 1. The electric and magnetic fields within a TEM cell, with a plane wave type structure at the midpoint of the top half.

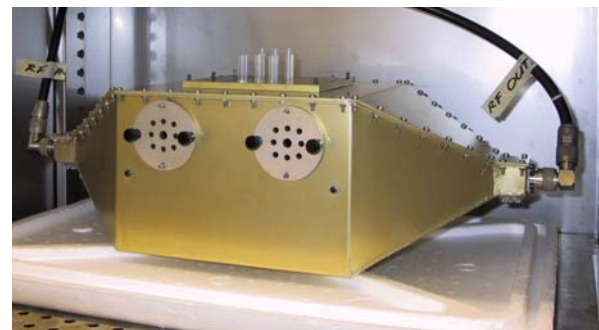


Figure 2. TEM Cell placed in the incubator (with ventilation holes shown).

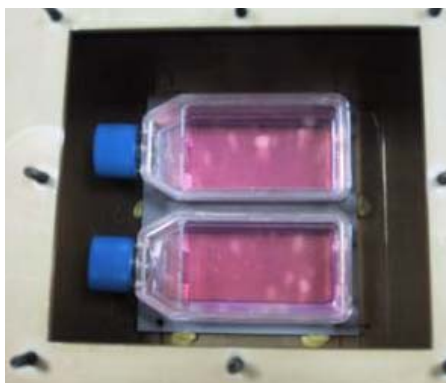


Figure 3. Two culture flasks, each filled with 6 mm of RPMI, placed in the middle of the top half of the TEM cell.

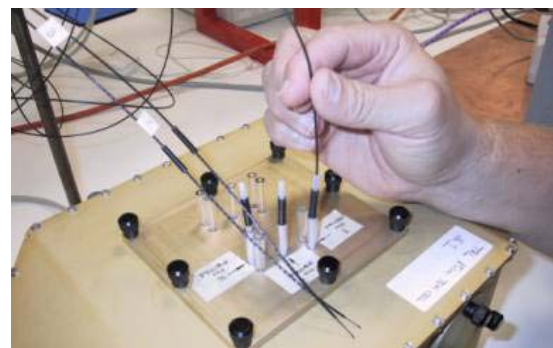


Figure 4. The placement of fluoroptic temperature probes. Three probes were placed at distinct regions of one flask. Each tip was situated in the medium, 0.5 mm above the flask bottom.

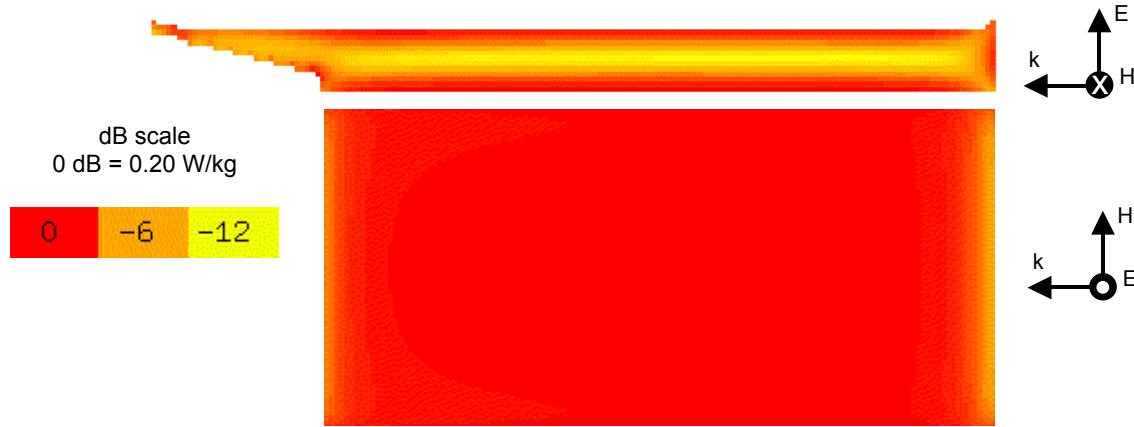


Figure 5. SAR profile in the RPMI medium. top: Slice through the middle (note the medium in the neck of the flask on the left). bottom: Bottom layer where cell culture resides.

An uncertainty analysis suggested the actual SAR values should agree with these values to within $\pm 35\%$. The main contributing factors to the possible error are the input power (accurate to within $\pm 25\%$; has a linear influence on the calculated SAR), height of the medium (accurate to within ± 0.5 mm resulting in a possible $\pm 17\%$ error; quadratic), and the conductivity ($\pm 10\%$; approximately linear). The modelling has also highlighted the significant influence of the meniscus due to the E -field polarisation (see also Guy et al. 1999, Schönborn et al. 2001, and Schuderer and Kuster 2003). The addition of the meniscus, 1 mm high and 1 mm in from the edge, as shown in the top right of Figure 5, lead to a 5% increase in SAR on the bottom layer.

Note that SAR has only been determined in the nutrient medium. The method of determining SAR without including the cell culture layer itself is consistent with work by other investigators in this field (see, for example, Schönborn et al. 2000 and 2001). To also determine SAR in the actual cell culture is a difficult task since the height of this layer is just a few microns. If the cell culture (assumed to be human brain cells) is included in the model as an infinitely thin planar layer at the bottom of the medium (with conductivity 0.77 S/m and relative permittivity 45.8 as for average brain (Gabriel 1996)) then the peak SAR at the bottom is reduced to 0.14 W/kg. If instead, the cell culture is modelled by the bottom 0.5 mm layer of mesh cells, then the peak is 0.10 W/kg. The actual value is likely to lie somewhere in this range, so long as the dielectric values for the cell culture have been appropriately chosen in the models. Better consideration of this issue of the SAR at the cell culture layer may be possible as improved modelling techniques become available.

The efficacy of using a plane wave incident field to simplify the analysis was confirmed by an XFDTD

model of the rectangular central portion of the TEM cell (using a ‘TEM Excitation Plane’). The resultant electromagnetic fields have the required plane wave type structure at the position of the flasks.

4. Comparison with, and Application of, the Burkhardt Formula

In Burkhardt et al. 1996, an analytical formulation is derived that provides SAR as a function of height (thickness), h , of the medium (which is taken to be in the direction of the incident field E). It is assumed that the geometry can be simplified to that of a thin conductive sheet. This enables a “... separation between ‘capacitive’ and ‘inductive’ coupling ... the capacitively induced part of the E -field [E_{cap}] is normal and the inductively induced part [E_{ind}] is parallel to the surface of the [sheet].” The formula is

$$\begin{aligned} SAR(z') &= \frac{\sigma}{\rho} (|E_{ind}|^2 + |E_{cap}|^2) \\ &= \frac{\sigma}{\rho} |E|^2 \left(\left(\frac{\mu\omega z'}{Z_0} \right)^2 + \frac{1}{|\epsilon_k|^2} \right) \end{aligned} \quad (2)$$

where it is assumed that the centre of the bottom of the sheet (lying in the x - y plane) is at the origin of a Cartesian coordinate system, and $z' = z - h/2$, $\omega = 2\pi f$, f is the frequency, $\epsilon_k = \epsilon_r - i\sigma/(\epsilon_0 \omega)$, and $Z_0 = 377 \Omega$.

To consider the accuracy of the Burkhardt formula with h , XFDTD models of finite sheets were constructed at a series of values. In each XFDTD model, the sheet was of dimensions 100 mm \times 100 mm and was 12 mesh cells high, and the material and field properties were

identical to those above. For each method, the SAR values at the bottom of the sheet (centrally placed in the XFDTD model) were compared. The comparison indicated that there was close agreement for a 4 mm high sheet (Burkhardt 0.0648 W/kg, XFDTD 0.0634 W/kg), around a 10% difference at 6 mm (0.138 W/kg, 0.152 W/kg), with the accuracy diminishing at 12 mm (0.535 W/kg, 1.30 W/kg). The analysis also highlighted that the desired uniformity over the bottom layer also diminishes significantly as h increases.

The formula thus provides a coarse validation method for checking the results from an XFDTD analysis of the SAR in a flask. In particular, at 6 mm, the Burkhardt formula gives the value of 0.138 W/kg (the sheet is the only possible analytic geometry) compared with the XFDTD value 0.20 W/kg (calculated above for the flask).

However, the formula offers a very prompt method to calculate approximate SAR values (an XFDTD calculation takes a few hours), which is useful in initial experimental design. It can also be used to test the sensitivity of input parameters. For example, the formula indicates that SAR varies quadratically with h (closely approximating the profile of the vertical slice in Figure 5). Since the cells reside on the bottom of the medium, this emphasises the need to choose and measure this parameter with great care.

5. SAR Validation through Temperature Measurement and Modelling

The efficacy of using XFDTD to determine the SAR profile was also confirmed through comparison of physical measurements of the resultant thermal rise in the medium with numerically calculated estimates based on the predicted SAR. Thermal RF dosimetry is based upon the equation

$$\rho c \frac{\partial T}{\partial t} = K \nabla^2 T + \rho SAR \quad (3)$$

where c is the specific heat capacity, and K is the thermal conductivity.

A standard approach in the determination of SAR is to ignore the conduction term $K \nabla^2 T$ in equation 2 and measure the initial rate of temperature increase $\partial T/\partial t$ (see, for example, Rowley and Anderson 1999). However, this approach is not possible in this case due to the high vertical SAR gradient, unless either highly sensitive temperature probes are used or the input power is significantly increased (see Moros and Pickard 1999, Pickard et al. 1999, and Samaras et al. 2000). (An alternative is to use equation 1 and use an E -field probe with a tip that is small enough and positioned so that it does not disrupt the exposure (Schönborn et al. 2000).)

In the validation measurements, the input power to the TEM cell was set at 113.5 W. Fluoroptic immersion temperature probes (Luxtron unit 790, probe type SFF) were chosen, as there are no metallic components to produce interference with the E -field. Measurements were performed when the two flasks, each filled with 6 mm high medium were placed in the TEM cell, and then again when the two flasks each had 12 mm of medium. The medium consisted of RPMI in a gelled form (using Natrosol 250 HR, 7.4% by mass) to reduce the effect of thermal diffusion due to convection (no cell culture was present). The measured electrical conductivity of the gel (with added common salt, 0.21% by mass, to obtain comparable conductivity to liquid RPMI) was 2.05 S/m and the relative permittivity 72.6. The measurements were performed in an environment that was not temperature controlled. These conditions were not sufficient to accurately determine local SAR from $\partial T/\partial t$ alone, since the chosen temperature probes have inadequate sensitivity at this power level.

Thermal modelling was undertaken through the development of a finite-difference temperature modelling environment based on equation 3 (using the numerical formulation in Wang and Fujiwara 1999, with the XFDTD mesh), and where, in addition, the thermal conditions at the surface are modelled as a convective boundary:

$$K \frac{\partial T}{\partial n} = -h(T - T_a) \quad (4)$$

where h is the convection coefficient, and T_a is the ambient temperature. For the RPMI gel, the specific heat capacity, c , was set at 4174 J/(kg °C), and the thermal conductivity, K , was set at 0.60 W/(m °C) (as for water). The convection coefficient, h , was set at 10.5 W/(m² °C) (see Kritikos et al. 1981, and Wang and Fujiwara 1999). The increase in ambient temperature in the TEM cell, T_a , was accounted for (for empty flasks, measurements showed a 0.16 °C increase over 360 s).

The input SAR profile is first calculated in XFDTD. As well as the mesh described previously for the 6 mm high medium, a second mesh was created for a 12 mm high medium (with cubical cells of length 1.0 mm). The measured values for the conductivity and relative permittivity of the RPMI gel were used. The calculations found that, with an input of 113.5 W, the peak SAR on the bottom of the 6 mm and 12 mm medium is 9.25 W/kg and 67.59 W/kg, respectively. The SAR profile was then input to the thermal model.

Figure 6 presents a comparison of two temperature measurements with the temperatures calculated by the model. The agreement between the results provides confidence in the accuracy of the SAR values. Other measurements gave consistent results. Due to thermal

conduction processes, the temperature rise profile at any given height in the medium has a similar shape over the 360 s period to that shown in Figure 6 (apart from the deviation in the first few seconds due to the particular SAR at that position, which cannot be resolved in our measurements) (see also Pickard et al. 1999 and Samaras et al. 2000). However, this type of long term comparison does confirm the average SAR value, and by using this as a reference, also confirms the value of SAR

throughout the height (given our confidence in the shape of the vertical profile as discussed above).

The temperature program was also used to confirm that for 2.5 W input, the exposure is under what is deemed ‘athermal’ conditions (the peak steady-state temperature rise is estimated to be only 0.013°C).

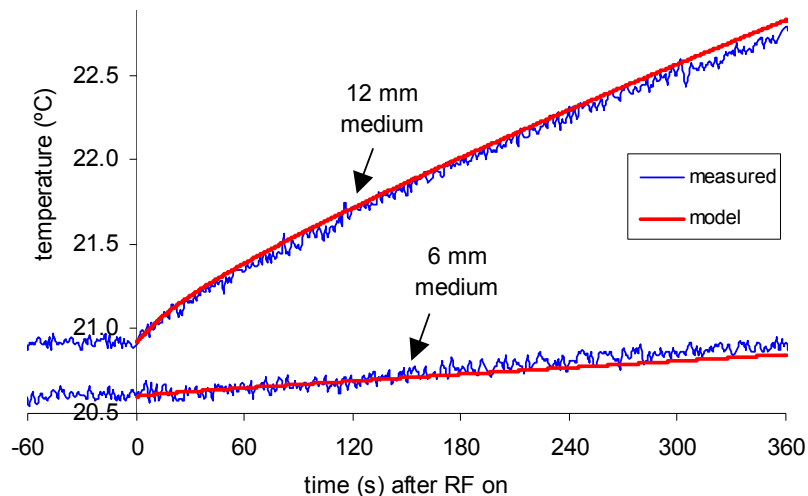


Figure 6. Comparison of measured and model temperature rise (0.5 mm off the bottom in the centre) for 113.5 W input

6. Conclusions

In vitro studies present a significant challenge to researchers in ensuring that the SAR of the exposed cell culture is accurately characterised. A TEM cell exposure chamber provides a useful system for *in vitro* studies due to the uniform layer in the medium where the cell culture resides. However, due to the highly non-uniform SAR profile in the vertical direction in the medium, it is critical that accurate techniques are employed to obtain an accurate estimate of the SAR. This paper has shown how this can be provided through the development of SAR and temperature computational analysis methods, both in the estimation and validation process.

References

- Burkhardt M, Pokovic K, Gnos M, Schmid T, and Kuster N, “Numerical and Experimental Dosimetry of Petri Dish Exposure Setups”, *Bioelectromagnetics*, Vol 17, pp483-493, 1996.
- Crawford M L, “Generation of Standard EM Fields using TEM Transmission Cells”, *IEEE Transact EMC*, Vol 16, No 4, pp189-195, 1974.
- Crawford M L, and Workman J L, “Using a TEM Cell for EMC Measurements of Electronic Equipment”, *US Department of Commerce, National Bureau of Standards, Technical Note 1013*, Apr 1979.
- French P W, and Blood A, “Characterisation of Molecular Changes Induced by Simulated Mobile Phone Radiofrequency Radiation Exposure”, *2nd Intl Workshop on Biological Effects of EMFs*, Greece, 2002.
- Gabriel C, “Compilation of the Dielectric Properties of Body Tissues at RF and Microwave Frequencies”, *Brooks Air Force Technical Report AL/OE-TR-1996-0037* (see <http://www.fcc.gov/fcc-bin/dielec.sh>, accessed July 2003).
- Guy A W, Chou C K, and McDougall J A, “A Quarter Century of *in vitro* Research: A New Look at Exposure Methods”, *Bioelectromagnetics*, Vol 20, pp21-39, 1999.
- Kritikos H N, Foster K R, and Schwan H P, “Temperature Profiles in Spheres Due to Electromagnetic Heating”, *J Microwave Power*, Vol 16, No 3-4, pp327-344, 1981.
- Kunz K S, and Luebbers R J, “The Finite Difference Time Domain Method for Electromagnetics”, *CRC Press*, 1993.

Kuster N, and Schönborn F, "Recommended Minimal Requirements and Development Guidelines for Exposure Setups of Bio-Experiments Addressing the Health Risk Concern of Wireless Communication", *Bioelectromagnetics*, Vol 21, pp508-514, 2000

Moros E G, and Pickard W F, "On the Assumption of Negligible Heat Diffusion during the Thermal Measurement of a Nonuniform Specific Absorption Rate", *Rad Res*, Vol 152, pp312-320, 1999

Pickard W F, Straube W L, Moros E G, and Fan X, "Simplified Model and Measurement of a Specific Absorption Rate Distribution in a Culture Flask Within a Transverse Electromagnetic Mode Exposure System", *Bioelectromagnetics*, Vol 20, pp183-193, 1999.

Popovic M, Hagness S C, and Taflove A, "Finite-Difference Time-Domain Analysis of a Complete Transverse Electromagnetic Cell Loaded with Liquid Biological Media in Culture Dishes", *IEEE Trans Biomedical Eng*, Vol 45, No 8, Aug 1998.

Remcom, Inc. website <http://www.remcom.com>. Accessed July 2003.

Rowley J T, and Anderson V, "A Critical Review of Resonant Cavities for Experimental *in vitro* Exposure to Radiofrequency Fields", *Inaugural Conf of IEEE EMBS Australia*, pp150-153, Feb 1999.

Samaras T, Regli P, and Kuster N, "Electromagnetic and Heat Transfer Computations for Non-ionizing Radiation Dosimetry", *Phys Med Biol*, Vol 45, pp2233-2246, 2000.

Schönborn F, Pokovic K, Burkhardt M, and Kuster N, "Basis for Optimization of *in vitro* Exposure Apparatus for Health Hazard Evaluations of Mobile Phone Communications", *Bioelectromagnetics*, Vol 22, pp547-559, 2001.

Schönborn F, Pokovic K, Wobus A M, and Kuster N, "Design, Optimisation, Realization, and Analysis of an In Vitro System for the Exposure of Embryonic Stem Cells at 1.71 GHz", *Bioelectromagnetics*, Vol 21, pp372-384, 2000.

Schuderer J, and Kuster N, "Effect of the Meniscus at the Solid/Liquid Interface on the SAR Distribution in Petri Dishes and Flasks", *Bioelectromagnetics*, Vol 24, pp103-108, 2003.

Wang J, and Fujiwara O, "FDTD Computation of Temperature Rise in the Human Head for Portable Phones", *IEEE Trans Microwave Theory and Techniques*, Vol 47, No 8, Aug 1999, pp1528-1534.



Robert McIntosh obtained his PhD in Mathematics at the Australian National University in 1989 in the area of PDEs. He has been a member of the Electromagnetic Energy (EME) Safety Research team at Telstra Research since 1999, developing and applying a numerical modelling environment for the study of RF dosimetry and human body absorption. Between 1989 and 1999, he worked at the BHP Research Laboratories on the development of electromagnetic levitation, pumping, and braking devices for liquid metal, and new techniques in noise reduction in electromagnetic geophysics. Robert is a member of the Australian Mathematical Society.



Ray McKenzie is the Project Leader of the EME Safety Research Group at the Telstra Research Laboratories (TRL), where he leads a team of researchers investigating the effects of human exposure to electromagnetic energy (EME). He specialises in electromagnetic propagation and physical interactions, in particular the dosimetry and measurement of ambient fields and SAR, as well as computational electromagnetic modelling. He has spent 13 years in the area of electromagnetic energy and is in his 20th year at TRL. He gained his Bachelor of Applied Science with first class honours in Physics from RMIT University in 1996, and currently undertakes postgraduate research in radon dosimetry at the Whole Body Facility of the Australian Radiation Protection and Nuclear Safety Agency (ARPANSA). He currently serves on specialist working committees of the Australian Communications Authority (ACA), the Australian Communications Industry Forum (ACIF), the Australian Mobile Telephone Association (AMTA) and the IEEE International Committee on Electromagnetic Safety (ICES) Standards Committee 4. Ray is a member of the Applied Computational Electromagnetic Society (ACES) and the Bioelectromagnetics Society (BEMS).



Steve Iskra received the B.E. (Hon.) degree in electrical engineering from the University of Melbourne, Australia in 1982. In 1982 he joined the Telstra Research Laboratories and has specialised in the areas of EMC and in the interaction of radio waves on the human body and on medical devices. He is a member of the International Special Committee on Radio Interference (CISPR) and Committee TE/3,

Electromagnetic Interference, of Standards Australia.



Amico Carratelli is a senior technical officer in the EME Safety Group at the Telstra Research Laboratories. Amico received an Associate Diploma in Mechanical Engineering in 1991 and has also completed Certificate of Technology courses in Mechanical Design (1974) and Structural Design (1980).

Amico has extensive research and development experience in the design/manufacture and analytical assessments of mechanical and electromechanical systems. He has lead project teams in evaluation of new telecommunications technologies and technology deployment across the company. Amico is currently assisting research teams with the main focus being SAR measurement techniques and SAR hardware development and implementation.



Paul Standaert received an Honours Degree in Electrical Engineering from Deakin University in 1982. He started work with the then Telecom Australia Research Laboratories as a Research Engineer in 1982.

Paul has worked in designing automated measurement instrumentation, has run the laboratories asset acquisition programme, and has also assisted in the development of optical standards for Telstra. His current research interests are in speech quality in communication systems as well as EME general research and measurement systems.

ACES COPYRIGHT FORM

This form is intended for original, previously unpublished manuscripts submitted to ACES periodicals and conference publications. The signed form, appropriately completed, MUST ACCOMPANY any paper in order to be published by ACES. PLEASE READ REVERSE SIDE OF THIS FORM FOR FURTHER DETAILS.

TITLE OF PAPER:

RETURN FORM TO:

Dr. Atef Z. Elsherbeni
University of Mississippi
Dept. of Electrical Engineering
Anderson Hall Box 13
University, MS 38677 USA

AUTHORS(S)

PUBLICATION TITLE/DATE:

PART A - COPYRIGHT TRANSFER FORM

(NOTE: Company or other forms may not be substituted for this form. U.S. Government employees whose work is not subject to copyright may so certify by signing Part B below. Authors whose work is subject to Crown Copyright may sign Part C overleaf).

The undersigned, desiring to publish the above paper in a publication of ACES, hereby transfer their copyrights in the above paper to The Applied Computational Electromagnetics Society (ACES). The undersigned hereby represents and warrants that the paper is original and that he/she is the author of the paper or otherwise has the power and authority to make and execute this assignment.

Returned Rights: In return for these rights, ACES hereby grants to the above authors, and the employers for whom the work was performed, royalty-free permission to:

1. Retain all proprietary rights other than copyright, such as patent rights.

2. Reuse all or portions of the above paper in other works.

3. Reproduce, or have reproduced, the above paper for the author's personal use or for internal company use provided that (a) the source and ACES copyright are indicated, (b) the copies are not used in a way that implies ACES endorsement of a product or service of an employer, and (c) the copies per se are not offered for sale.

4. Make limited distribution of all or portions of the above paper prior to publication.

5. In the case of work performed under U.S. Government contract, ACES grants the U.S. Government royalty-free permission to reproduce all or portions of the above paper, and to authorize others to do so, for U.S. Government purposes only.

ACES Obligations: In exercising its rights under copyright, ACES will make all reasonable efforts to act in the interests of the authors and employers as well as in its own interest. In particular, ACES REQUIRES that:

1. The consent of the first-named author be sought as a condition in granting re-publication permission to others.

2. The consent of the undersigned employer be obtained as a condition in granting permission to others to reuse all or portions of the paper for promotion or marketing purposes.

In the event the above paper is not accepted and published by ACES or is withdrawn by the author(s) before acceptance by ACES, this agreement becomes null and void.

AUTHORIZED SIGNATURE

TITLE (IF NOT AUTHOR)

EMPLOYER FOR WHOM WORK WAS PERFORMED

DATE FORM SIGNED

Part B - U.S. GOVERNMENT EMPLOYEE CERTIFICATION

(NOTE: if your work was performed under Government contract but you are not a Government employee, sign transfer form above and see item 5 under Returned Rights).

This certifies that all authors of the above paper are employees of the U.S. Government and performed this work as part of their employment and that the paper is therefor not subject to U.S. copyright protection.

AUTHORIZED SIGNATURE

TITLE (IF NOT AUTHOR)

NAME OF GOVERNMENT ORGANIZATION

DATE FORM SIGNED

PART C - CROWN COPYRIGHT

(NOTE: ACES recognizes and will honor Crown Copyright as it does U.S. Copyright. It is understood that, in asserting Crown Copyright, ACES in no way diminishes its rights as publisher. Sign only if *ALL* authors are subject to Crown Copyright).

This certifies that all authors of the above Paper are subject to Crown Copyright. (Appropriate documentation and instructions regarding form of Crown Copyright notice may be attached).

AUTHORIZED SIGNATURE

TITLE OF SIGNEE

NAME OF GOVERNMENT BRANCH

DATE FORM SIGNED

Information to Authors

ACES POLICY

ACES distributes its technical publications throughout the world, and it may be necessary to translate and abstract its publications, and articles contained therein, for inclusion in various compendiums and similar publications, etc. When an article is submitted for publication by ACES, acceptance of the article implies that ACES has the rights to do all of the things it normally does with such an article.

In connection with its publishing activities, it is the policy of ACES to own the copyrights in its technical publications, and to the contributions contained therein, in order to protect the interests of ACES, its authors and their employers, and at the same time to facilitate the appropriate re-use of this material by others.

The new United States copyright law requires that the transfer of copyrights in each contribution from the author to ACES be confirmed in writing. It is therefore necessary that you execute either Part A-Copyright Transfer Form or Part B-U.S. Government Employee Certification or Part C-Crown Copyright on this sheet and return it to the Managing Editor (or person who supplied this sheet) as promptly as possible.

CLEARANCE OF PAPERS

ACES must of necessity assume that materials presented at its meetings or submitted to its publications is properly available for general dissemination to the audiences these activities are organized to serve. It is the responsibility of the authors, not ACES, to determine whether disclosure of their material requires the prior consent of other parties and if so, to obtain it. Furthermore, ACES must assume that, if an author uses within his/her article previously published and/or copyrighted material that permission has been obtained for such use and that any required credit lines, copyright notices, etc. are duly noted.

AUTHOR/COMPANY RIGHTS

If you are employed and you prepared your paper as a part of your job, the rights to your paper initially rest with your employer. In that case, when you sign the copyright form, we assume you are authorized to do so by your employer and that your employer has consented to all of the terms and conditions of this form. If not, it should be signed by someone so authorized.

NOTE RE RETURNED RIGHTS: Just as ACES now requires a signed copyright transfer form in order to do "business as usual", it is the intent of this form to return rights to the author and employer so that they too may do "business as usual". If further clarification is required, please contact: The Managing Editor, R. W. Adler, Naval Postgraduate School, Code EC/AB, Monterey, CA, 93943, USA (408)656-2352.

Please note that, although authors are permitted to re-use all or portions of their ACES copyrighted material in other works, this does not include granting third party requests for reprinting, republishing, or other types of re-use.

JOINT AUTHORSHIP

For jointly authored papers, only one signature is required, but we assume all authors have been advised and have consented to the terms of this form.

U.S. GOVERNMENT EMPLOYEES

Authors who are U.S. Government employees are not required to sign the Copyright Transfer Form (Part A), but any co-authors outside the Government are.

Part B of the form is to be used instead of Part A only if all authors are U.S. Government employees and prepared the paper as part of their job.

NOTE RE GOVERNMENT CONTRACT WORK: Authors whose work was performed under a U.S. Government contract but who are not Government employees are required so sign Part A-Copyright Transfer Form. However, item 5 of the form returns reproduction rights to the U. S. Government when required, even though ACES copyright policy is in effect with respect to the reuse of material by the general public.

January 2002

INFORMATION FOR AUTHORS

PUBLICATION CRITERIA

Each paper is required to manifest some relation to applied computational electromagnetics. **Papers may address general issues in applied computational electromagnetics, or they may focus on specific applications, techniques, codes, or computational issues.** While the following list is not exhaustive, each paper will generally relate to at least one of these areas:

1. **Code validation.** This is done using internal checks or experimental, analytical or other computational data. Measured data of potential utility to code validation efforts will also be considered for publication.
2. **Code performance analysis.** This usually involves identification of numerical accuracy or other limitations, solution convergence, numerical and physical modeling error, and parameter tradeoffs. However, it is also permissible to address issues such as ease-of-use, set-up time, run time, special outputs, or other special features.
3. **Computational studies of basic physics.** This involves using a code, algorithm, or computational technique to simulate reality in such a way that better, or new physical insight or understanding, is achieved.
4. **New computational techniques,** or new applications for existing computational techniques or codes.
5. **“Tricks of the trade”** in selecting and applying codes and techniques.
6. **New codes, algorithms, code enhancement, and code fixes.** This category is self-explanatory, but includes significant changes to existing codes, such as applicability extensions, algorithm optimization, problem correction, limitation removal, or other performance improvement. **Note: Code (or algorithm) capability descriptions are not acceptable, unless they contain sufficient technical material to justify consideration.**
7. **Code input/output issues.** This normally involves innovations in input (such as input geometry standardization, automatic mesh generation, or computer-aided design) or in output (whether it be tabular, graphical, statistical, Fourier-transformed, or otherwise signal-processed). Material dealing with input/output database management, output interpretation, or other input/output issues will also be considered for publication.
8. **Computer hardware issues.** This is the category for analysis of hardware capabilities and limitations of various types of electromagnetics computational requirements. Vector and parallel computational techniques and implementation are of particular interest.

Applications of interest include, but are not limited to, antennas (and their electromagnetic environments), networks, static fields, radar cross section, shielding, radiation hazards, biological effects, electromagnetic pulse (EMP), electromagnetic interference (EMI), electromagnetic compatibility (EMC), power transmission, charge transport, dielectric, magnetic and nonlinear materials, microwave components, MEMS technology, MMIC technology, remote sensing and geometrical and physical optics, radar and communications systems, fiber optics, plasmas, particle accelerators, generators and motors, electromagnetic wave propagation, non-destructive evaluation, eddy currents, and inverse scattering.

Techniques of interest include frequency-domain and time-domain techniques, integral equation and differential equation techniques, diffraction theories, physical optics, moment methods, finite differences and finite element techniques, modal expansions, perturbation methods, and hybrid methods. This list is not exhaustive.

A unique feature of the Journal is the publication of unsuccessful efforts in applied computational electromagnetics. Publication of such material provides a means to discuss problem areas in electromagnetic modeling. Material representing an unsuccessful application or negative results in computational electromagnetics will be considered for publication only if a reasonable expectation of success (and a reasonable effort) are reflected. Moreover, such material must represent a problem area of potential interest to the ACES membership.

Where possible and appropriate, authors are required to provide statements of quantitative accuracy for measured and/or computed data. This issue is discussed in “Accuracy & Publication: Requiring, quantitative accuracy statements to accompany data,” by E. K. Miller, *ACES Newsletter*, Vol. 9, No. 3, pp. 23-29, 1994, ISBN 1056-9170.

EDITORIAL REVIEW

In order to ensure an appropriate level of quality control, papers are peer reviewed. They are reviewed both for technical correctness and for adherence to the listed guidelines regarding information content.

JOURNAL CAMERA-READY SUBMISSION DATES

March issue	deadline 8 January
July issue	deadline 20 May
November issue	deadline 20 September

Uploading an acceptable camera-ready article after the deadlines will result in a delay in publishing this article.

STYLE FOR CAMERA-READY COPY

The ACES Journal is flexible, within reason, in regard to style. However, certain requirements are in effect:

1. The paper title should NOT be placed on a separate page. The title, author(s), abstract, and (space permitting) beginning of the paper itself should all be on the first page. The title, author(s), and author affiliations should be centered (center-justified) on the first page.
2. An abstract is REQUIRED. The abstract should be a brief summary of the work described in the paper. It should state the computer codes, computational techniques, and applications discussed in the paper (as applicable) and should otherwise be usable by technical abstracting and indexing services.
3. Either British English or American English spellings may be used, provided that each word is spelled consistently throughout the paper.
4. Any commonly-accepted format for referencing is permitted, provided that internal consistency of format is maintained. As a guideline for authors who have no other preference, we recommend that references be given by author(s) name and year in the body of the paper (with alphabetical listing of all references at the end of the paper). Titles of Journals, monographs, and similar publications should be in italic font or should be underlined. Titles of papers or articles should be in quotation marks.
5. Internal consistency shall also be maintained for other elements of style, such as equation numbering. As a guideline for authors who have no other preference, we suggest that equation numbers be placed in parentheses at the right column margin.
6. The intent and meaning of all text must be clear. For authors who are NOT masters of the English language, the ACES Editorial Staff will provide assistance with grammar (subject to clarity of intent and meaning).
7. Unused space should be minimized. Sections and subsections should not normally begin on a new page.

PAPER FORMAT

The preferred format for initial submission and camera-ready manuscripts is 12 point Times Roman font, single line spacing and double column format, similar to that used here, with top, bottom, left, and right 1 inch margins. Manuscripts should be prepared on standard 8.5x11 inch paper.

Only camera-ready electronic files are accepted for publication. The term “**camera-ready**” means that the material is neat, legible, and reproducible. Full details can be found on ACES site, Journal section.

ACES reserves the right to edit any uploaded material, however, this is not generally done. It is the author(s)

responsibility to provide acceptable camera-ready pdf files. Incompatible or incomplete pdf files will not be processed, and authors will be requested to re-upload a revised acceptable version.

SUBMITTAL PROCEDURE

All submissions should be uploaded to ACES server through ACES web site (<http://aces.ee.olemiss.edu>) by using the upload button, journal section. Only pdf files are accepted for submission. The file size should not be larger than 5MB, otherwise permission from the Editor-in-Chief should be obtained first. The Editor-in-Chief will acknowledge the electronic submission after the upload process is successfully completed.

COPYRIGHTS AND RELEASES

Each primary author must sign a copyright form and obtain a release from his/her organization vesting the copyright with ACES. Copyright forms are available at ACES, web site (<http://aces.ee.olemiss.edu>). To shorten the review process time, the executed copyright form should be forwarded to the Editor-in-Chief immediately after the completion of the upload (electronic submission) process. Both the author and his/her organization are allowed to use the copyrighted material freely for their own private purposes.

Permission is granted to quote short passages and reproduce figures and tables from and ACES Journal issue provided the source is cited. Copies of ACES Journal articles may be made in accordance with usage permitted by Sections 107 or 108 of the U.S. Copyright Law. This consent does not extend to other kinds of copying, such as for general distribution, for advertising or promotional purposes, for creating new collective works, or for resale. The reproduction of multiple copies and the use of articles or extracts for commercial purposes require the consent of the author and specific permission from ACES. Institutional members are allowed to copy any ACES Journal issue for their internal distribution only.

PUBLICATION CHARGES

ACES members are allowed 12 printed pages per paper without charge; non-members are allowed 8 printed pages per paper without charge. Mandatory page charges of \$75 a page apply to all pages in excess of 12 for members or 8 for non-members. Voluntary page charges are requested for the free (12 or 8) pages, but are NOT mandatory or required for publication. A priority courtesy guideline, which favors members, applies to paper backlogs. Authors are entitled to 15 free reprints of their articles and must request these from the Managing Editor. Additional reprints are available to authors, and reprints available to non-authors, for a nominal fee.

ACES Journal is abstracted in INSPEC, in Engineering Index, and in DTIC.